High Temperature Transducers for Online Monitoring of Microstructure Evolution

Nuclear Energy Enabling Technologies

Dr. Cliff Lissenden
Pennsylvania State University

Suibel Schuppner, Federal POC
Pradeep Ramuhalli, Technical POC

NEUP | Nuclear Energy University Programs

U.S. Department of Energy

Project Title: High Temperature Transducers for Online Monitoring of Microstructure Evolution 11-3046

Period: October 1, 2011 through December 30, 2014

Report Date: March 30, 2015

Recipient: Pennsylvania State University

Award No.: 00120237

PI: Cliff Lissenden, (814) 863-5754, Lissenden@psu.edu

Co-PI: Bernhard Tittmann, brtesm@engr.psu.edu

TABLE OF CONTENTS

PART I. ABSTRACT

A critical technology gap exists relative to online condition monitoring (CM) of advanced nuclear plant components for damage accumulation; there are not capable sensors and infrastructure available for the high temperature environment. The sensory system, monitoring methodology, data acquisition, and damage characterization algorithm that comprise a CM system are investigated here. Thus this work supports the DOE mission to develop a fundamental understanding of advanced sensors to improve physical measurement accuracy and reduce uncertainty. The research involves a concept viability assessment, a detailed technology gap analysis, and a technology development roadmap.

Condition monitoring with ultrasound is enabled by development and processing of piezoelectric materials that have the unique capability to function at high temperatures. Bismuth titanate/lithium niobate composites have been shown to generate and receive ultrasound signals at temperatures up to 1000°C. Thus it is assessed for CM applications in the NGNP. Lead zirconate titanate/bismuth titanate is investigated for light water reactor applications at more moderate temperatures. Of course there is more to a CM system than just the sensor material; instrumentation and monitoring methodology play key roles and are investigated. Innovative transducer designs are employed that are based on the generation of ultrasonic guided waves to monitor significant volumes of material, rather than simply at the transducer location. Furthermore, detection of macroscale damage often occurs too late in the life of the component to enable effective operations management. Thus, it is very beneficial to track microstructure evolution and the development of precursors to macroscale damage, which is possible through detection of higher harmonics.

Three test cases are investigated to concretely demonstrate the online CM capabilities. Comb transducers for tubular heat exchanger structures are spray-deposited and successfully tested. Second, methods to deposit and process spray-on transducers in the field are developed. Lastly, the feasibility of spray-on transducers for condition monitoring of a compact intermediate heat exchanger design is demonstrated.

PART II. OBJECTIVES, EFFORT, AND ACCOMPLISHMENTS

1. FULL STATEMENT OF OBJECTIVES

A critical technology gap exists relative to online condition monitoring (CM) of advanced nuclear plant components for damage accumulation; there are not capable sensors and infrastructure available for the high temperature environment. The sensory system, monitoring methodology, data acquisition, and damage characterization algorithm that comprise a CM system are proposed. Thus the project supports the DOE mission to develop a fundamental understanding of advanced sensors to improve physical measurement accuracy and reduce uncertainty. The project aims to: (1) demonstrate ultrasonic transducer capabilities, (2) detect and characterize macroscale defects in tubular structures, (3) demonstrate field implementation of transducers, (4) prove that ultrasonic transducers can generate and receive higher harmonics under operating conditions, (5) link higher harmonics to incipient damage, and (6) show feasibility of the online CM system for a compact intermediate heat exchanger. The research plan involves a concept viability assessment, a detailed technology gap analysis, and a comprehensive technology development roadmap.

Condition monitoring with ultrasound will be enabled by development and processing of piezoelectric materials that have the unique capability to function at high temperatures. Bismuth titanate/lithium niobate composites have been shown to generate and receive ultrasound signals at temperatures up to 1000°C. The capabilities of this and other high temperature piezoelectrics will be assessed for CM applications in the NGNP. Light water reactor applications at more moderate temperatures will also be explored. Of course there is more to a CM system than just the sensor material; instrumentation, data acquisition, and monitoring methodology all play key roles and will be investigated. Innovative transducer designs will be employed that are based on the generation of ultrasonic guided waves to monitor significant volumes of material, rather than simply at the transducer location. Furthermore, detection of macroscale damage often occurs too late in the life of the component to enable effective operations management. Thus, it is very beneficial to track microstructure evolution and the development of precursors to macroscale damage, which is possible through detection of higher harmonics. A CM system would be incomplete without prognostic modeling to guide decision making. In this project prognostics will focus on microstructure evolution leading to initiation and growth of a macroscale crack.

Three test cases are investigated to concretely demonstrate aspects of the online CM capabilities. A comb transducer for tubular heat exchanger structures is tested at high temperature. Second, a methodology to spray-deposit and process transducers on large structural components in the field is developed. Lastly, the feasibility of spray-on transducers to monitor diffusion bonds in a compact intermediate heat exchanger is evaluated.

2. DESCRIPTION OF EFFORT PERFORMED

This section summarizes the key elements of the work performed over the course of the project. It is separated into seven subsections based on the project milestones. Subsection 1 merges milestones 1 and 2 together because they became intrinsically linked during the performance of the work. Thus, the numbering of subsections 2-7 actually corresponds to milestones 3-8. The following subsections are taken from the project milestone reports, but in cases have deletions for conciseness or additions based on knowledge gained after the submission of the milestone report.

2.1 Viability of High Temperature Piezoelectric Materials and Instrumentation

Of the many challenges associated with condition monitoring of tubing, pipes, and pressure vessels in nuclear power plants perhaps temperature resistance, transducer coupling, surface curvature, damage sensitivity, and the size of the material domain to be monitored are the most critical. This project investigates a condition monitoring system that addresses each of these challenges. Temperature resistant piezoelectric materials (having high Curie temperatures) are sprayed onto a structural component. Spray deposition is very amenable to curved surfaces and adhesion of the sprayed material to the component obviates the need for couplant. Furthermore, the geometry of the sprayed transducer can be manipulated in such a way to control the generation of ultrasonic guided waves that can travel reasonably long distances in components such as pipes and pressure vessels. And if the signal to noise ratio is large enough, then higher harmonic generation can be correlated with microstructural changes in the material that precede macroscale damage in order to provide unprecedented damage sensitivity. This subsection describes the achievement of project milestones 1 and 2, which are:

1. Demonstrate viability of high temperature piezoelectric materials;

2. Demonstrate functionality provided by instrumentation.

The research has focused on two distinct applications: (i) service temperatures up to 400°C, such as could occur in a number of light water reactor components, and (ii) service temperatures up to 950°C, such as is expected for the very high temperature reactor type of next generation nuclear plant. Different piezoceramic composites are proposed for these applications; PZT (lead zirconate titanate) transducers doped with bismuth titanate, which we will denote PZT/BT, are tested at 400°C and bismuth titanate - lithium niobate composite transducers, which we will denote BT/LN, are tested at 850°C. Herein the transducer processing

methodology, instrumentation, and demonstration of capabilities are reported. Results of proof tests on the mechanical integrity and functionality after long term exposure and thermal cycling are presented.

2.1.1 Transducer Processing Methodology

PZT/BT

The spray-on process that we use was first developed by Kobayashi et al. [2000]. The process described here was also reported by Cyphers [2012] and more recently by Orr [2015]. This section is based substantially on the description in Orr's [2015] thesis.

The composite transducers fabricated in this work have two main components: a sol-gel solution and a powder. The sol-gel solution is fabricated from a series of chemical reactions that form a ceramic suspended in an organic solution. This solution is combined with a powder, mixed and sprayed onto a metal substrate. Following the deposition, the substrate is placed on a hot plate for pyrolization. Then the ceramic is densified using various techniques. After densification a conductive electrode is deposited onto the ceramic, and the ceramic is poled. In naming the composites, e.g., PZT/BT, the first constituent (PZT in this case) is the sol-gel, and the second constituent (bismuth titanate) is the added ceramic powder.

The complete process, as described below, is shown in the flow chart in Figure 1.1.
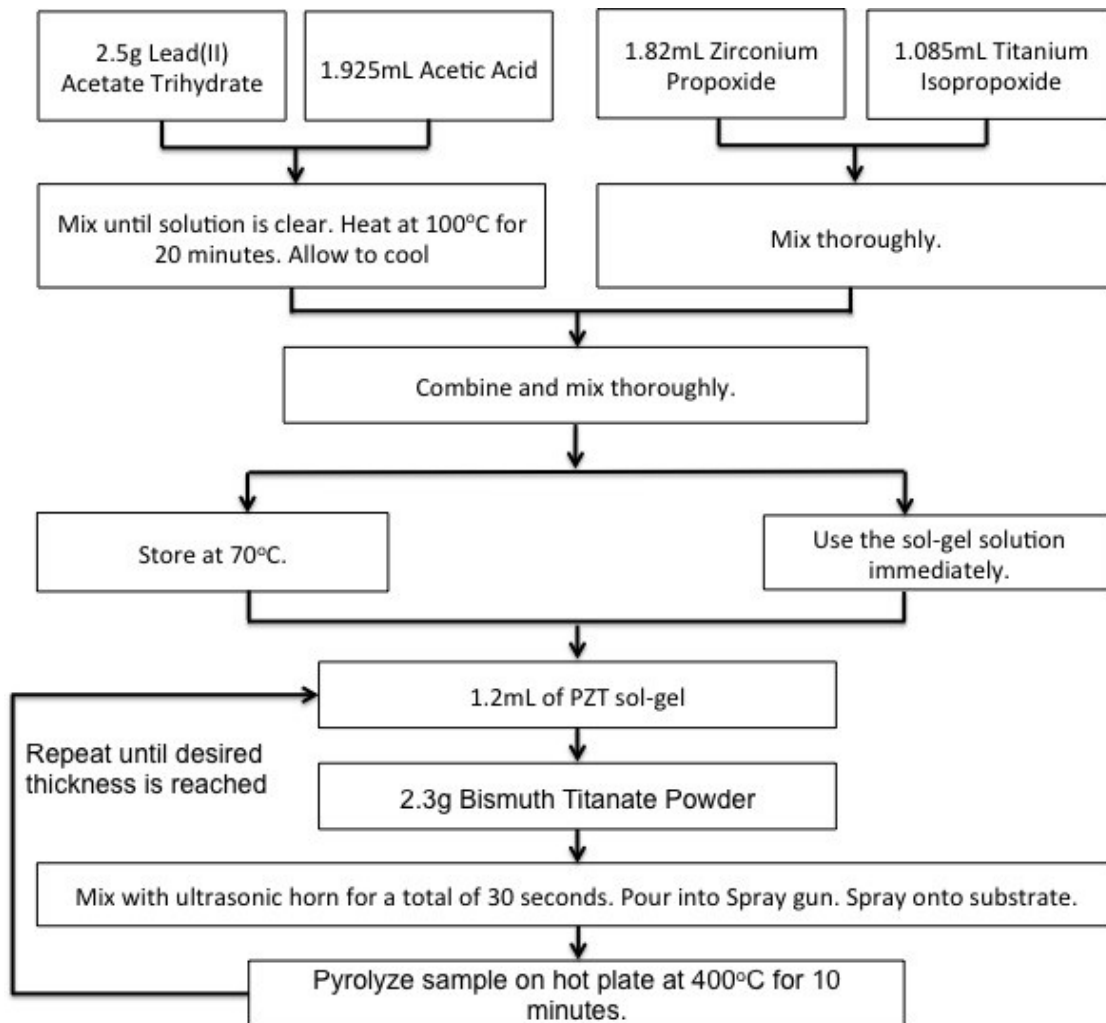
Figure 1.1. *The spray-on process for sol-gel PZT/BT transducers.*

2.1.1.1 Sample Preparation

Before a sample can be sprayed with the composite ceramic mixture, there are a few cleaning and preparation steps that must be taken to ensure good adhesion between the surface of the substrate and the ceramic. First, the surface of the substrate must be roughened to increase the surface area of the substrate. The substrate is cleaned with industrial cleaner and water to remove any dirt that may have been left behind by the sandpaper. The substrate is then cleaned with acetone and isopropyl alcohol to degrease the surface. Cleanliness cannot be overstressed throughout this process because any contamination could cause adhesion problems, and jeopardize the transducer's performance.

2.1.1.2 Preparation of the Sol-Gel Solution

The PZT sol-gel is produced using a two-step process. The first precursor solution is formed by dissolving lead acetate in acetic acid at 100°C. The solution is left on a hot plate at 100°C for approximately 20 minutes, during which the solution should slightly boil to ensure the lead is completely dissolved. The second precursor solution is formed by combining zirconium propoxide with titanium isopropoxide. When the lead/acetic acid solution is cooled, the two solutions are combined. Thorough stirring is critical during this step to ensure the completion of the chemical reaction. Distilled water is then added to the solution to stabilize it. The solution can be used at this point, or it can be stored at 70°C for later use. Careful consideration must be taken when not using the solution immediately, as the temperature of the sol-gel solution should not go below 30°C. If the temperature of the solution cools below 30°C, it will start to form a crystalized solid and therefore cannot be used.

When the solution is ready to be deposited, the PZT solution is doped with bismuth titanate powder. The formation of the two materials allows for the favorable characteristics of each material to be available, namely the excellent signal strength of PZT and the high-temperature capabilities of bismuth titanate. Traditionally, the powder and sol-gel solutions are mixed using a ball milling process; however, the use of an ultrasonic horn, shown in Figure 1.2, is much faster and just as effective. The horn, when excited at its resonant frequency, injects a significant amount of energy into the solution in a short period of time through a complex cavitation process [Sinding, 2014]. The ultrasonic horn is used for three short cycles of 10-15 seconds each. This causes energy to go into the solution with minimal heating, as heating may have negative effects on the solution.

Figure 1.2. *The ultrasonic horn used to combine the PZT sol-gel with the bismuth titanate powder.*

Once the solution is thoroughly mixed, the porosity is conducive to air gun spraying, and is poured into a Kobalt low-gravity feed spray gun, which is connected to a compressed air supply. The resulting mixture is sprayed onto the substrate at a low pressure from a distance of approximately 1 foot [Sinding, 2014] as shown in Figure 1.3. A single spray application results in a coating thickness of approximately 20 microns. Uniform spray application on a cylindrical surface is achieved by placing the cylinder on a rotary stage.

Figure 1.3. *Spray gun deposition of PZT/BT coating on the end of a cylindrical sample.*

2.1.1.3 Pyrolization

Pyrolization is a heat treatment used to drive out the organic compounds from the acetic acid that was used in the precursor solutions to fabricate the sol-gel. This process is critical to the final microstructure of the transducer, as the pyrolysis step significantly reduces the volume of the composite by removing the organics. In thick-films (approximately 20 microns per spray), the volume reduction causes microcracking.

The pyrolization step is carried out after each spray deposition. The substrate is placed on a hotplate at 400°C; however, the actual pyrolization temperature that the ceramic is exposed to is about 200°C due to the thickness of the substrate. This temperature is in reasonable agreement with what Yi et al., [1988] found. The spray-on deposition and pyrolization processes are repeated until the desired coating thickness is reached.

2.1.1.4 Densification

The densification process plays a large role in determining the microstructure of the final composite ceramic. Sintering is a heat treatment process that is intended to allow solid-state diffusion to occur, which results in the combination and densification of the ceramic. Before densifying, the grains in the ceramic only feel forces on one side from neighboring atoms inside of the grain because the distance between grain boundaries is large enough that the forces from atoms on the opposite side of the grain are negligible. As the temperature increases during densification or sintering, the grains expand because the atoms become more energetic due to the added energy. After sufficient heating, the sintering process is deemed complete, and there is one interface between the grains due to a large amount of atomic motion stimulating crystal bonding at the interface between the particles [Xu, 1991; Uchino, 2010]. However, in our processing only partial densification is achieved, which is why we do not refer to it as sintering.

For this project densification has been performed in a tube furnace, in a microwave oven, with a blowtorch, and with an induction heater. Earlier transducers were sintered in a microwave oven, but that oven is shared between many research groups and has multiple purposes. It became contaminated with carbon and was henceforth ineffective for our project. Even though temperature parameters are not closely controlled with the blowtorch, it has provided consistent results on flat substrates and it is very amenable for field use. On the other hand the tube furnace is not practical for in-situ densification. Blowtorch densification was used due to its ease of use and accessibility. We followed a procedure developed for composite transducers deposited on metallic substrates [Searfass, 2008]. The sample is placed on a hotplate at 400°C for at least 10 minutes to heat up the substrate and reduce the possibility of thermal shock when exposed to the flame. The sample is taken off the hotplate and placed on a ceramic block and the center cone of the flame is applied to the side of the substrate. The flame is kept away from the ceramic because rapid heating of the ceramic may cause thermal shock and result in cracking. The sample is heated for 12-15 minutes, until the substrate is glowing orange, as shown in Figure 1.4. Then the blowtorch is removed and the sample is allowed to cool.

Figure 1.4*. Blow torch densification of spray-on ceramic transducers. Notice how the metal substrate is starting to glow.*

Blowtorch and microwave densification methods can sometimes destroy the ceramic coating. Microwave densification is susceptible to thermal runaway, and the blowtorch is either on or off making temperature control difficult. Thus, an induction heater with coils that wrap around the pipe or cylindrical substrate as shown in Figure 1.5 is used to densify the ceramic coating by heating the substrate. Induction heating is controlled by a thermocouple, which is spot welded to the substrate. Temperature, heating rate, and cooling rate are adjusted with the power settings of the Ambrell induction heating system. Sintering is intended to increase grain size and ceramic density, but we have found through experimentation that a sintered ceramic is not a prerequisite for piezoelectricity.

Induction heating provides a more controllable densification method that is amenable to field use. A new Ambrell induction heating system, shown in Figure 1.6, has been setup in the hood in our laboratory in order to densify piezoceramic coatings. The induction coils heat the metal substrate, which then densify the coating.

The significant challenge associated with densifying the sprayed-on piezoceramic is cracking of the ceramic due to a mismatch of the coefficient of thermal expansion (CTE) between the ceramic and a metallic substrate. The stresses induced by this mismatch can exceed the tensile strength of the ceramic and cause fracture of the ceramic material [Sinding, 2014]. For this reason, the densification temperature is reduced from approximately 850°C, which is typical for a ferroelectric material fabricated through a powder pressing process, to 550°C. However, if the substrate is exposed to 550°C for an extended time (longer than 15 minutes), cracking will most likely occur.
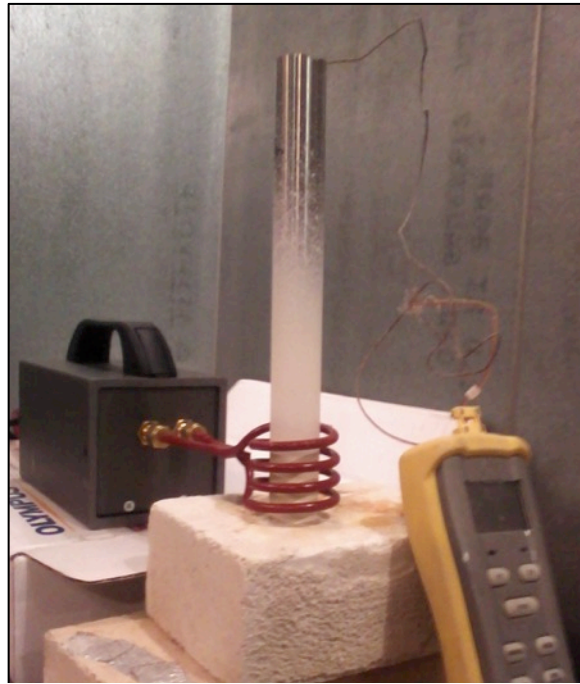
Figure 1.5. *Induction heating coils and thermocouple display to control sintering of a PZT/BT transducer deposited on a stainless steel pipe.*

Due to the lower temperature and reduced time at temperature, the ceramic does not fully densify and there is uncertainty about how much sintering occurs. Thus, the ceramic has significant porosity [Boch and Philippe, 2007]. It is interesting to note that we have found that piezoelectric functionality does not require sintering to occur.
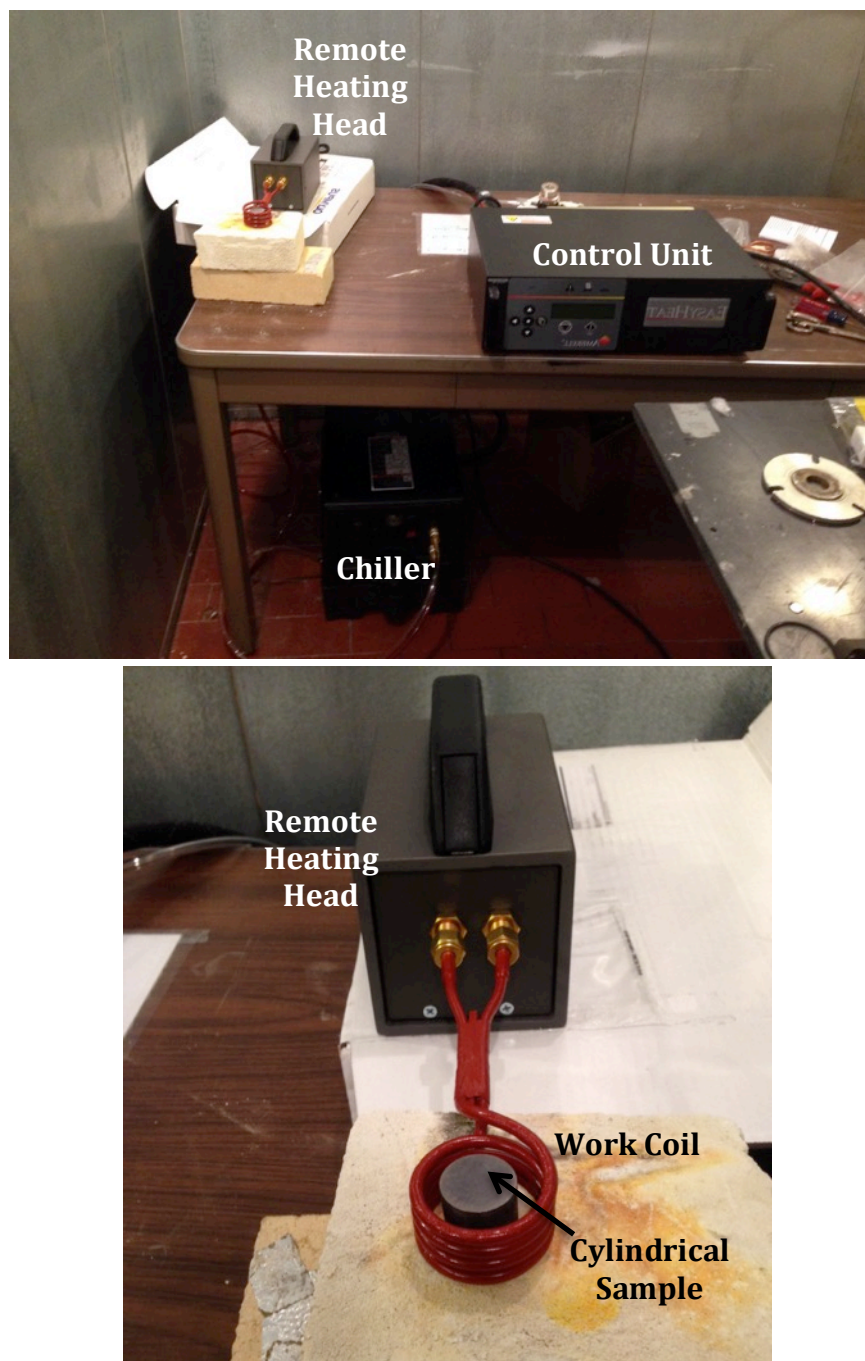
Figure 1.6. *Ambrell induction heating system for sintering piezoceramic coatings.*

BT/LN

Processing of BT/LN composite transducers is similar to PZT/BT except that the sol-gel is bismuth titanate and lithium niobate powder is added to form a composite. Procuring lithium niobate powder turned out to be an issue. First, there was an 8-week lead time, then they sent a crystalline form of the powder rather than a fine powder. The crystalline powder did not dissolve in the sol-gel solution

because the surface area was insufficient. The solution was to ball mill the crystalline powder, which is time consuming.

A persistent inability to pole BT/LN coatings deposited on 25 mm diameter pipe with a 2 mm wall thickness spurred an investigation of the as-densified microstructure. Optical micrographs in Figure 1.7 show that cracking around lithium niobate particles is pervasive throughout. In these images the coating was densified using a blow torch. Initially, during development of densification procedures we found that the mechanical integrity of the coating could be compromised if the wrong procedures were employed. Here however, from a macroscopic view the mechanical integrity is sufficient, but the microcracking prevents the coating from being poled. A sauereisen coating was deposited atop the BT/LN in an attempt to seal the microcracks. Platinum electrodes were then painted on top of the sauereisen. However, the thickness of the sauereisen was quite nonuniform and there were gaps in the coverage as shown in Figure 1.8, and thus the trial was unsuccessful.

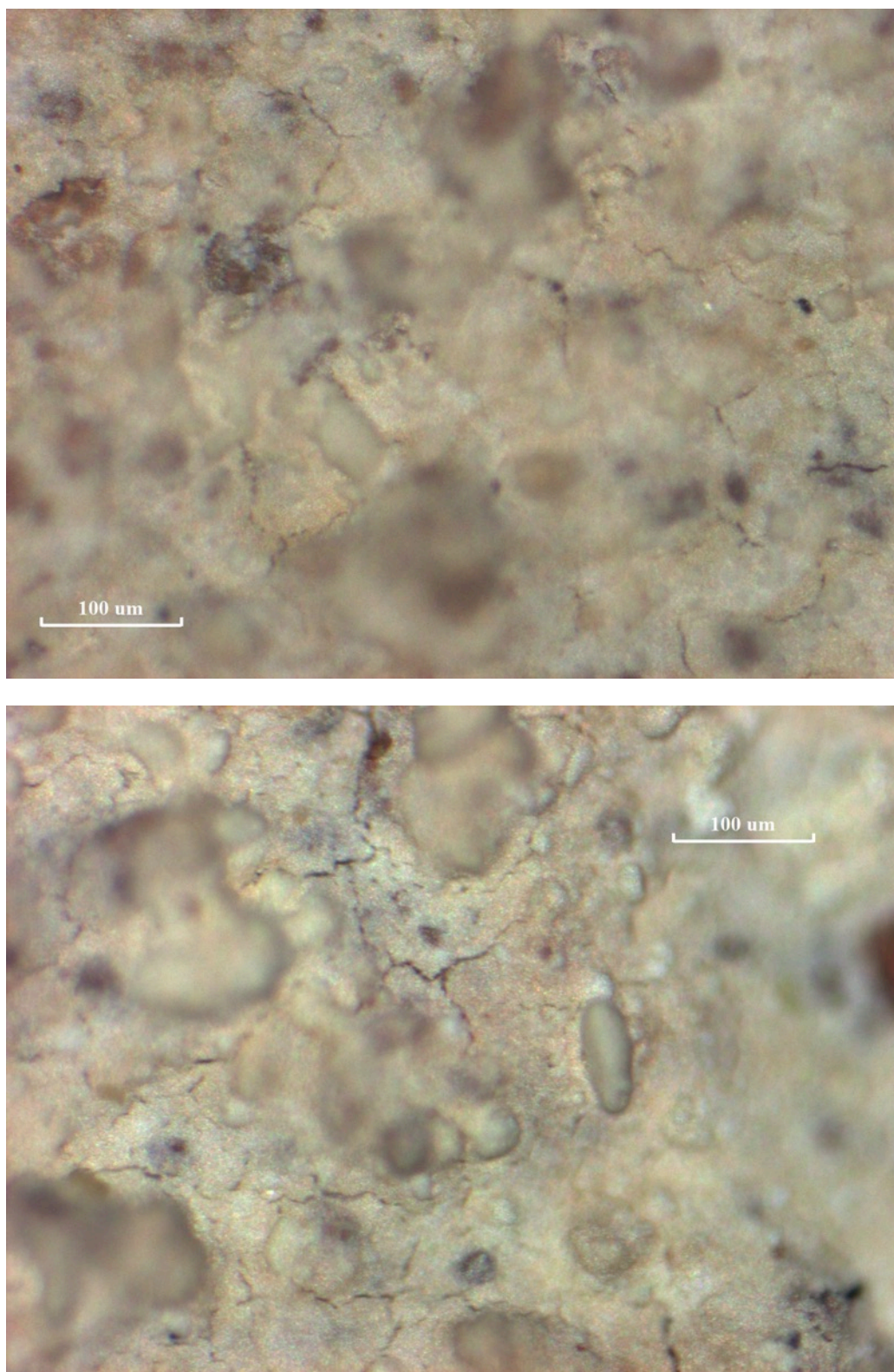***Figure 1.7****. Optical micrographs of BTLN coating densified by blow torch. The substrate is curved and the depth of field small, leading to parts of image being out of focus. Randomly oriented cracks around lithium niobate particles are evident.*
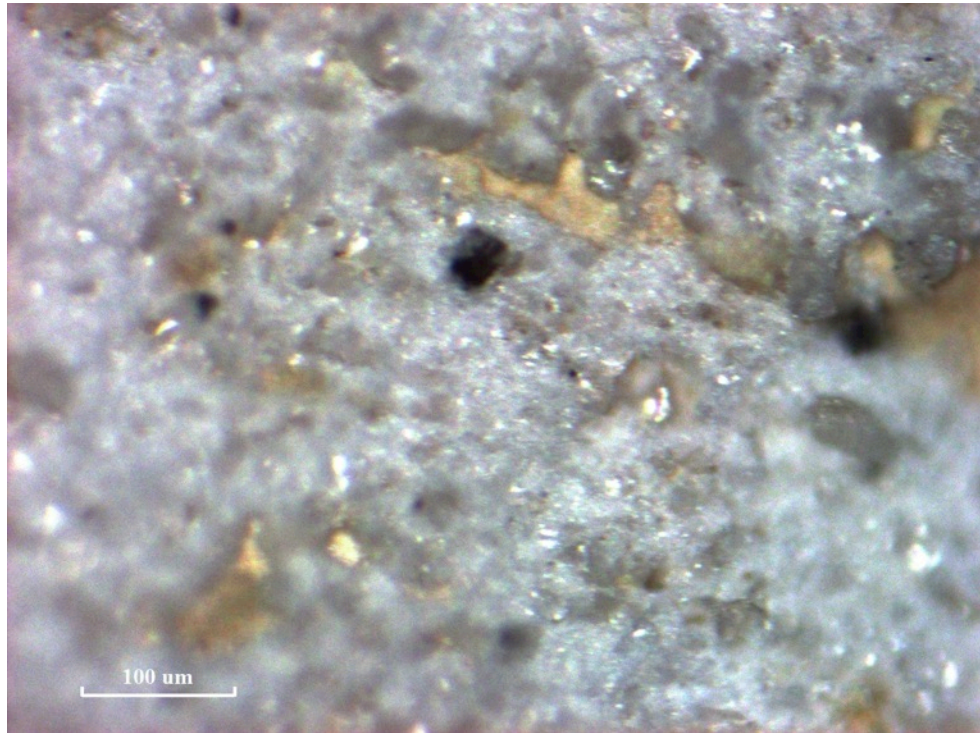
Figure 1.8. *Optical micrograph of sauereisen on BT/LN coating. Gaps in the sauereisen coverage are evident.*

2.1.2 Instrumentation

For the purposes of this project we identify the instrumentation as everything other than the piezoceramic coating described in subsection 2.1.1; that includes the electrodes, lead wires, polarization process, and pulser/receiver. Perhaps surprisingly, it is the electrodes that proved to be the most problematic. The reasons that electrodes turn out to be the biggest challenge are (i) that they are the part of the instrumentation that directly touches the piezoelectric coating and (ii) they need to be temperature resistant.

2.1.2.1 Electrodes

The electrodes enable an electric field to be applied to, and received from, the piezoelectric material. Only one electrode needs to be applied to the top of piezoelectric coating since the metallic substrate serves as the ground. Platinum is a good electrode material due to its temperature resistance, although it is quite expensive. A thin (~300 nm) sputter deposited layer of platinum does not use much material and has worked well with our transducers applied to small samples. An example is shown in Figure 1.9.
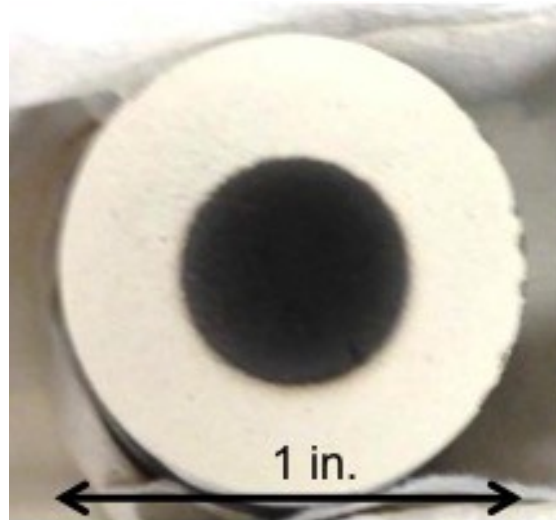
Figure 1.9. *Platinum sputtered electrode. The dark center circle is the electrode, and the light colored outer portion is excess sprayed-on ceramic material.*

Sputter coatings are applied in small vacuum chambers in the laboratory, which makes the process not very amenable for larger pipe samples or for field use. Our end goal is to be able to apply these transducers in the field, thus other methods to deposit electrodes onto the ceramic were explored. Painting platinum electrodes was the initial obvious solution, despite the high cost of platinum paint. However, this turned out to be far more challenging than expected.

The selection of platinum was driven by the high temperature application (850-950°C), however for 20-400°C platinum is not necessary. Nickel paste was investigated, but eliminated from consideration since at elevated temperatures (~100°C) the nickel draws oxygen from the porous ceramic microstructure removing the ferroelectric property from the ceramic. We obtained functioning transducers by painting first a layer of gold and then a layer of silver for the electrode. The gold layer helps to seal the porous piezoceramic and keeps the small silver atoms from penetrating into and through the ceramic.

In order to confirm that the transducer functionality issues described above are associated with the electrode application and not the coating, other electroding techniques were assessed. Trial one was sputtering platinum onto the coating surface. This worked well for samples small enough for the sputter chamber. Trial two was to use an evaporation chamber, which is significantly larger than the sputter chamber. However, unlike sputtering, evaporation is a line of sight deposition technique so pores are more easily filled than bridged. Trial three was simply placing copper tape on top of the ceramic coating around the circumference of a coated pipe. An issue with a tape electrode is that oil from the oil bath penetrates between the electrode and the piezoceramic making poling more difficult. Only sputtered electrodes functioned reliably at elevated temperature.

Another aspect of this project, but not included in these two milestones, is the control of ultrasonic guided waves generated by these spray-on transducers. The control is provided by patterning the

electrodes, which can be done by methods such as painting electrode stripes or laser ablation. This will be described in detail in subsection 2.2.

2.1.2.2 Lead Wires

For high temperature applications coaxial cable lead wires connected to the transducer electrode and the substrate (ground) via silver paint as shown in Figure 1.10 have proved to be very reliable.
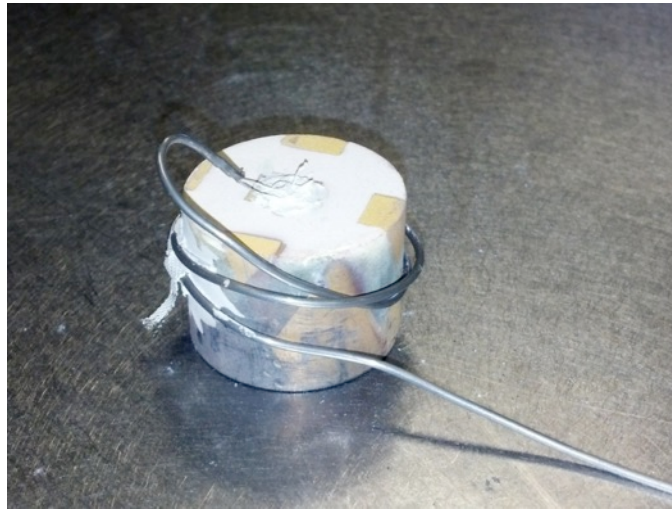

Figure 1.10. BT/LN transducer on an Alloy 617 sample showing the lead wire.

2.1.2.3 Polarization

The net polarization of a polycrystalline piezoceramic is very low because the grains are randomly oriented. To create a net polarization in the material, the material must be *poled*. In this process, the domains of the internal dipoles, which are originally randomly oriented, are aligned and produce a net polarization. During the poling process, the material is brought to a temperature between 100°C and 200°C while applying a large electric field. The elevated temperature provides enough thermal energy so that when the electric field is applied, the atoms within each grain will displace in the proper direction with respect to the electric field. The material is held at elevated temperature with the high electric field for a predetermined amount of time. The electric field is held as the material cools back down to room temperature and a net polarization is then induced in the material because not enough thermal energy is present to allow the atoms to reorient themselves to their original position. Generally, the alignment of the grains achieves 80-90% of the single crystal value [Searfass, 2008].

The poling process used in this work is conducted in a silicon oil bath, which insulates and provides resistance to internal discharge breakdown. The oil is circulated in a bath which is held at 150°C during the entire process to help heat the material. The convection of the oil over the surface of the ceramic

reduces the heat stored in the layer, reducing the possibility of thermal breakdown. A high voltage, approximately 50 kV/cm, is applied to the electrode, and the substrate is grounded. The high voltage is applied to the ceramic for approximately 15 minutes and then the ceramic is taken out of the oil to cool, and the electric field is reapplied as it cools. The poling process takes about 35 minutes to complete. The poling apparatus is shown in Figure 1.11.

(a)   (b)

Figure 1.11. (a) Poling probes used to apply high voltage to the samples. The beige probes can be moved up and down to fit the samples underneath. (b) the poling bath with the heater.

Once the ceramic is cooled, the fabrication process is complete, and the resultant ceramic is a composite ferroelectric transducer. After fabrication, capacitance and $\tan\delta$ are measured at 1kHz and 1V on a Stanford LCR meter, and d33 is measured on a Berlincourt d33 meter. This machine applies a mechanical stress and measures the output charge developed by the film in order to calculate the d33 coefficient. The failure of a transducer to pole is an indicator that some aspect of the spraying or electroding parts of the fabrication process went awry.

For the fabricated sol-gel composite transducers, the d33 typically ranges from 10-20 pC/N, capacitance is on the order of pF, and $\tan\delta$ is less than 0.05. The d33 and capacitance values are low relative to PZT, but the composite is approximately 90% bismuth titanate and 10% PZT. Since bismuth titanate has a d33 of approximately 14 pC/N, the range of the d33 values seems reasonable.

2.1.2.4 Transducer Protection

Regardless of the results of our transducer durability assessment described in subsection 2.1.3 below, which does not include additional protection for the transducer, we believe that a protective coating is an important element to improve transducer reliability. The coating is intended to prevent accidental handling harm, eliminate wear, erosion, and reaction with the environment, and maintain a positive connection of the lead wires. It is intended to encapsulate the transducer with sauereisen. Figure 1.12 shows a sauereisen coating, that when applied properly without leaving gaps, would protect the piezoceramic, the electrodes, and the lead wire connection.
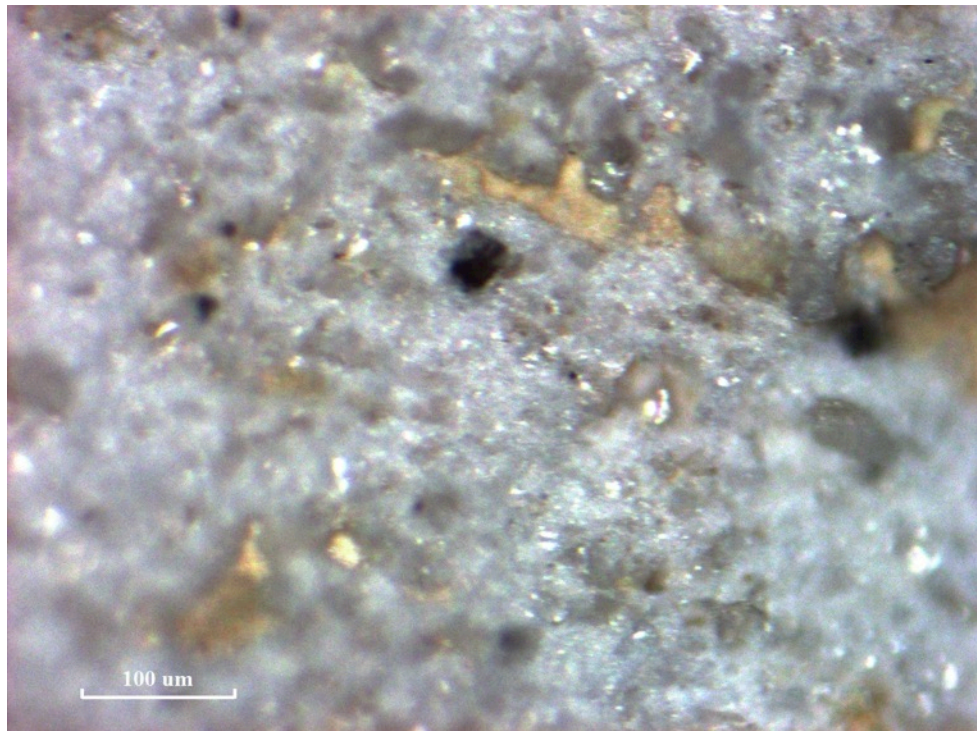
Figure 1.12. *Optical micrograph of sauereisen on BT/LN coating. Gaps in the sauereisen coverage are evident.*

2.1.3 Demonstration

The transducers that we fabricated are approximately 90% bismuth titanate and 10% PZT. The highest density a sol-gel fabricated transducer can acheive may be 80%. However, the transducers are not expected to be fully densified based upon the processing employed. Another limitation of the PZT/BT composite transducers is the high mechanical Q. When tested with an HP Network Analyzer to find the resonant frequencies, no resonances are visible due to the high Q.

Micromechanical modeling of composite piezoelectric transducers using the generalized method of cells has been conducted to predict transducer functionality over a wide range of temperatures based on the constituent properties. Weight fractions of powders are input and transducer properties can be estimated as a function of temperature, which enables optimal powder mixtures to be designed. The details of this modeling effort are presented in Kyle Sinding's thesis [Sinding, 2014].

2.1.3.1 Functionality During Initial Exposure

PZT/BT Transducers

PZT transducers are expected to provide a high signal strength, but have limited resistance to high-temperature based on their Curie temperature. Previous work by Kobayashi [private communication] has shown that bismuth titanate doped PZT transducers can achieve temperatures around 450°C before losing amplitude. In contrast, here results are presented on PZT/BT transducers that give measurable signals up to about 690°C.

A PZT/BT transducer was deposited on the end of a short cylinder and used in pulse-echo mode. The Ultran pulser was set at a gain of 20 dB and a pulse voltage of 200 V. Figure 1.13 shows the measured peak-to-peak amplitude of the time domain signal of the first echo versus temperature, while Figure 1.14 shows the frequency spectrum of the first back wall echo at several selected temperatures.
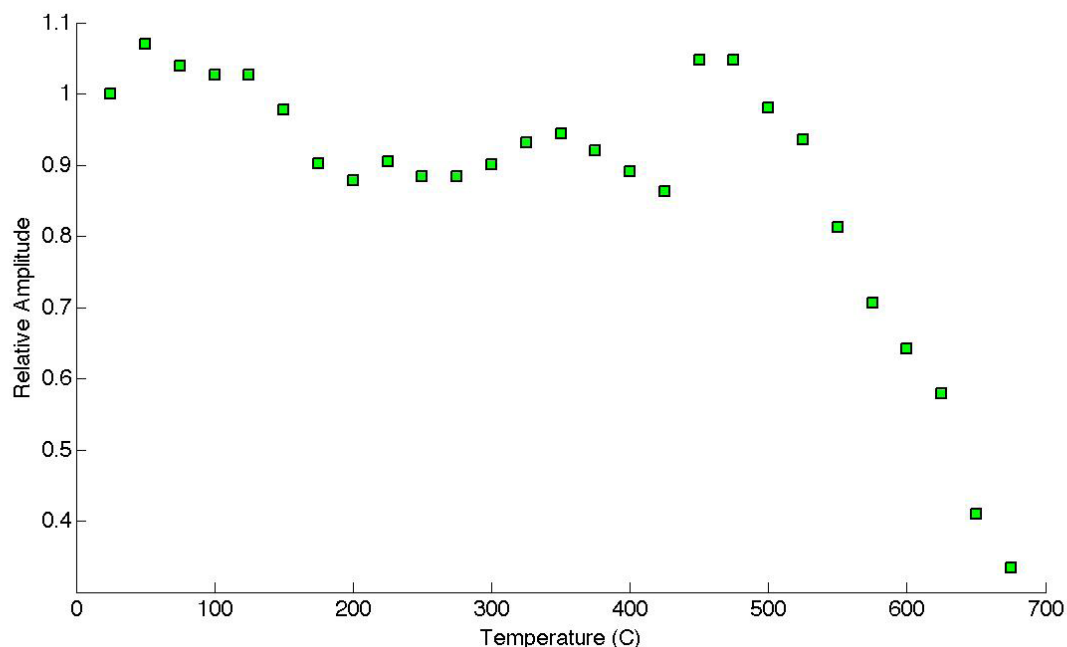
Figure 1.13. *Peak-to-peak amplitude as a function of temperature (25-675°C) for PZT/BT transducer.*
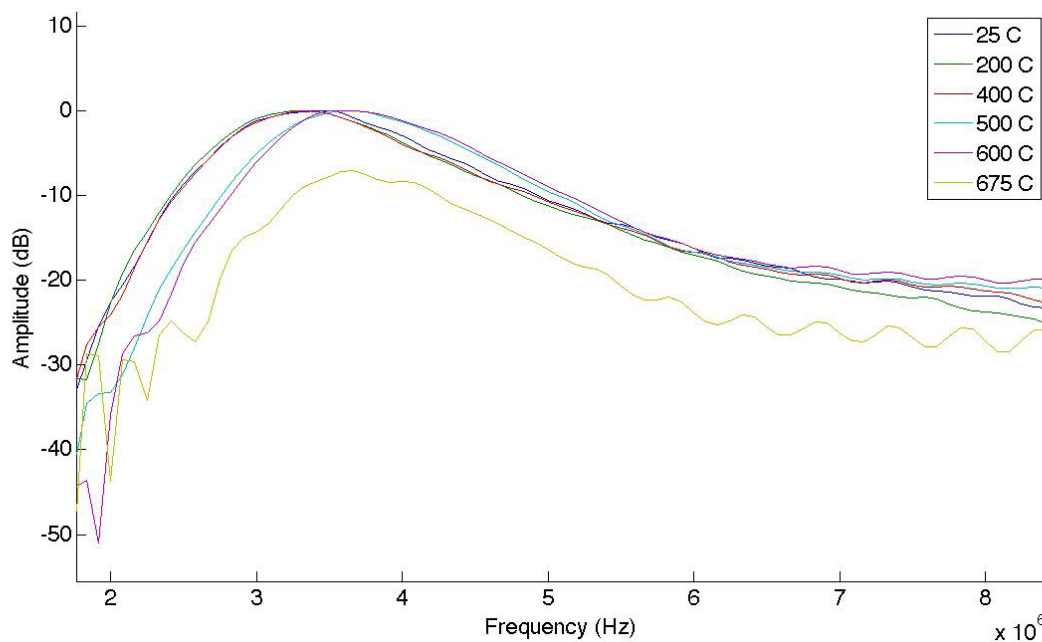
Figure 1.14. *Frequency spectra of the first backwall echo at selected temperatures for PZT/BT transducers.*

BT/LN Transducers

Two BT/LN transducers were sprayed onto Alloy 617 substrates. One of the samples, shown in Figure 1.15, was subjected to a high temperature test in which the signal amplitude was monitored as the sample was heated from room temperature to 1000°C. A conventional tube furnace, which is shown in Figure 1.16, was used to raise the temperature at as steady a rate as possible, and the sample was allowed to soak at each target temperature in an attempt to ensure that the sample be as uniform as possible.

Figure 1.15. *Alloy 617 sample having a BT/LN transducer sprayed onto one end.*
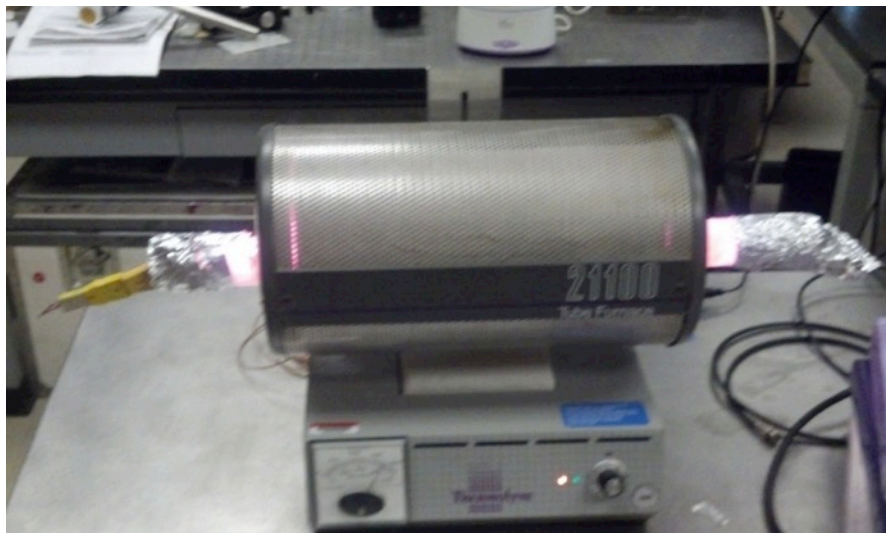
Figure 1.16. *Tube furnace heating Alloy 617 sample.*

The transducer was continuously pulsed throughout the run with a toneburst sine wave. The transducer was operating in pulse-echo mode. The first and second echoes from the back wall of the cylinder were visible. These echoes were confirmed to be from the back wall by a simple time of flight calculation. The longitudinal wave speed is reported to be 5820 m/s and the length of the cylinder was measured to be 20 mm. The time of flight from transducer to the back wall and back is computed as,

$$time\ of\ flight = \frac{distance}{velocity} = \frac{0.04\ m}{5820\ ^m/_s} = 6.87\ \text{μs}.$$

The time measured on the oscilloscope for the reflections was approximately 6.7 μs, which is approximately equal to the computed time of flight and confirms that the wave speed is reasonably accurate.

Peak-to-peak amplitude measurements of the back wall echo were taken in intervals of 50°C. An averaging (256) data acquisition mode was used on the oscilloscope. The data from this run are plotted in Figure 1.17. Overall, the signal amplitude increases approximately 200 mVpp from 200-750°C. The signal amplitude then gradually decreases until the sample was between 900 – 950°C, where a very large drop in amplitude was observed. As the transducer approached 1000°C the amplitude continued to decrease until it was barely detectable. At this point the furnace was turned off and the sample was allowed to cool. The transducer continued to be pulsed even as it cooled and within a few minutes the signal amplitude slowly began to increase. After about 20 minutes the sample was around 650°C and the signal amplitude was back to 260 mV indicating that the transducer survived the 1000°C temperature and was still operational, although at a reduced strength. This is where signal monitoring ceased and the sample was allowed to cool to room temperature. When the sample was retrieved the next day, the transducer had turned a greenish tint and delaminated from the substrate. This transducer actually retained its signal strength to a higher temperature than past BT/LN transducers that we processed and evaluated. These results demonstrate that BT/LN transducers can function up to the upper end target temperature of 950°C. However, the aging and durability of BT/LN transducers still needs to be assessed. Clearly, a protective coating could prove to be very beneficial in this regard.
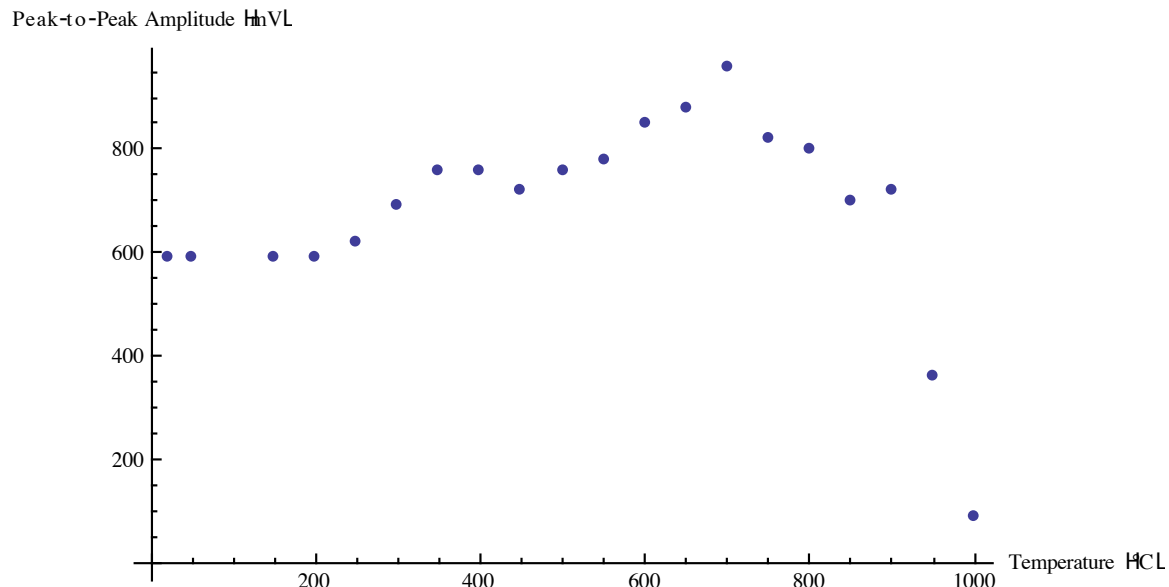

Figure 1.17. *Peak-to-peak amplitude (in mV) as a function of temperature (°C) for BT/LN transducer.*

2.1.3.2 Mechanical Integrity

Durability of PZT/BT at 400°C

A PZT/BT coating was spray deposited and then densified onto a 25.4 mm diameter stainless steel pipe. The pipe was then thermally cycled to 400°C in a furnace. The first ten cycles each had a duration of 4 hours, while next ten cycles each had a duration of 20 minutes. No degradation was visible after cycling. A PZT/BT coating was also spray deposited and then densified onto a flat steel dogbone specimen. This sample was fatigued in load control and no degradation was visible after mechanical cycling.

Durability of BT/LN at 850°C

BT/LN coatings were sprayed onto two stainless steel pipe sections. These coatings consist of 6 sprays. The BT/LN coatings were densified with a blow torch, but not electroded. These pipe sections were then thermally cycled in a tube furnace between room temperature and 850°C. Ten thermal cycles were performed on the first sample over a two-day period without removing the pipe from the furnace. After 10 cycles the stainless steel was severely oxidized and the BT/LN coating was essentially gone. Clearly 850°C is too high a temperature for stainless steel in terms of hot corrosion. The second sample was therefore visually observed after each cycle. Photographs are shown in Figures 1.18 and 1.19. While discolored, the coating is intact and exhibits no visible cracks. It is apparent however, that there is less of the coating. Since coating loss was not an issue in previous high temperature testing of BT/LN transducers mounted on a nickel base alloy substrate it is probable that it is associated with oxidation of the stainless steel. The value of a protective coating for the BTLN is evident for this type of environment. However, the good news from these results is that the BT/LN coating did not flake or spall off and there was no evidence of cracking.
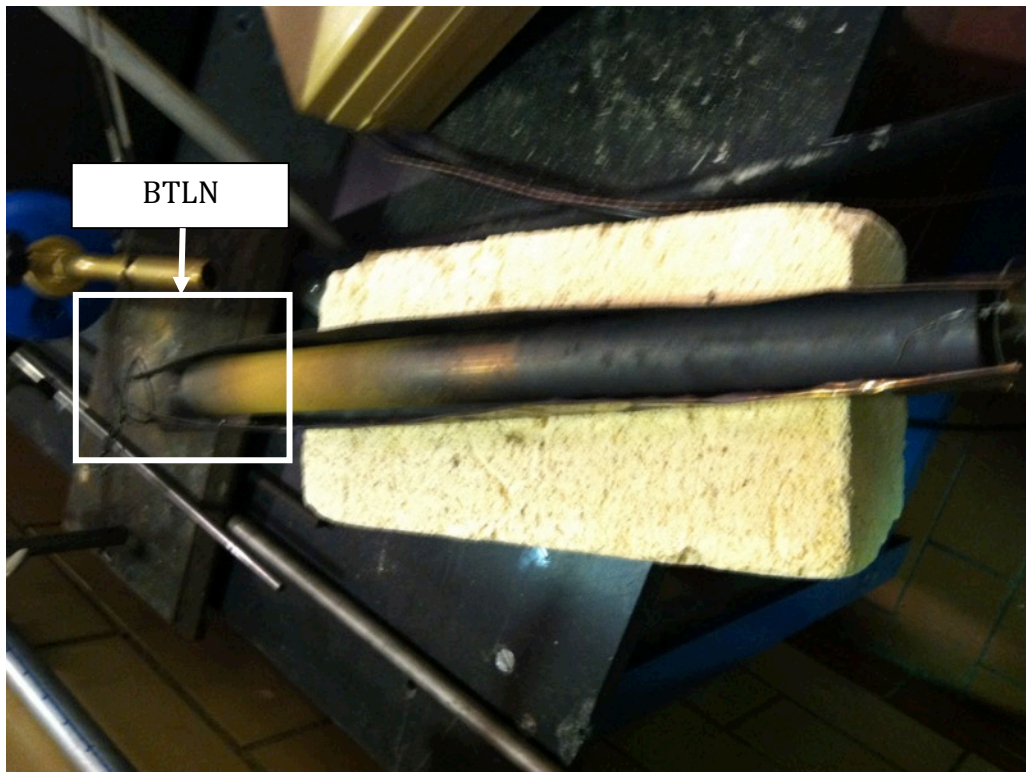
Figure 1.18. BT/LN coating on stainless steel pipe after one thermal cycle to 850°C.

Figure 1.19. BT/LN coating on stainless steel pipe after two thermal cycles to 850°C.

2.1.3.3 Functionality

Typically, this demonstration involved propagating a high frequency (1-7 MHz) bulk wave through a 25mm thick stainless steel disk.

Tests were performed on stainless steel disks (Figure 1.20) in a Lindbergh tube furnace. While our successful previous high-temperature test samples used sputtered gold or platinum electrodes, in more recent experiments SPI silver paint electrodes were brushed directly on the piezoceramic coating. Painted electrodes are deemed to be much more practical and economical for field deposition since a vacuum chamber is not required. Initial high temperature tests of painted electrodes on pipe samples were conducted with induction heating to raise the temperature of the pipe inner diameter to 400°C for 20 minutes. This temperature applied for this duration did not measurably degrade the ultrasonic signal strength.

Figure 1.20. *PZT/BT samples for 400°C tests: one-cycle (20 minutes) test result on left, two-week duration test result on right. The oxidized silver electrode from the long duration test developed a discolored, non-conducting surface.*

To test long-term exposure, the first transducers were placed in the furnace at 410°C for two weeks. After that extended immersion in air at high temperatures, the ceramic delaminated from the steel and the silver electrode oxidized as shown in Figure 1.20. In a second test, new transducers were only kept in the furnace at 410°C for one hour. After this time, the visibly unchanged samples were retested for high frequency bulk wave generation. Despite no visible degradation, the pulse-echo signal amplitudes and d_{33} decreased by 67% as shown in Figure 1.21 and Table I.
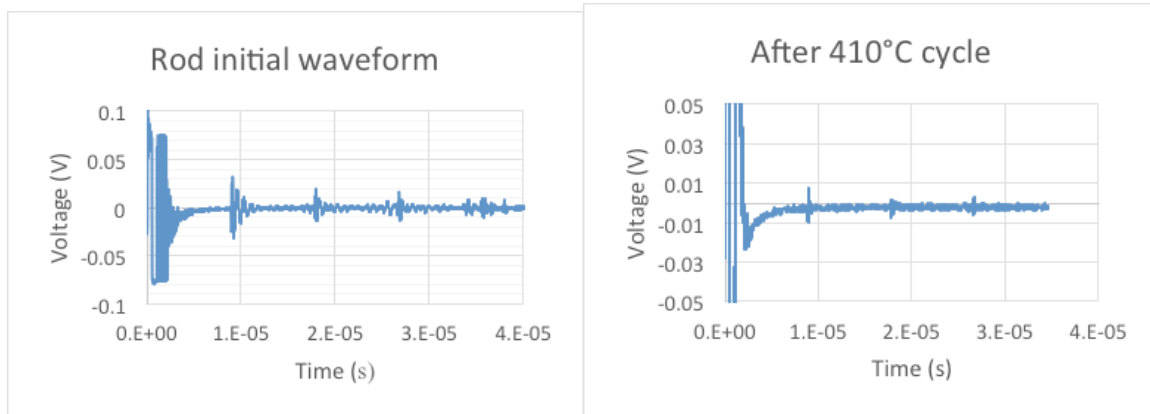
Figure 1.21. *Pulse-echo waveforms before and after one thermal cycle in furnace.*

Table I. *Transducer properties before and after one thermal cycle in furnace. Capacitance and tanδ were measured by LCR meter, and the d_{33} by Berlincourt d_{33} meter.*

	before	after
1st echo (V_{pp})	0.06	0.02
d33 (pC/N)	3	1
Capacitance (pF)	130	90
tanδ	0.02	0.002

The electrical data offers clues as to how the samples degraded. Because the capacitance dropped below all previous values, 130pF for poled and 140pF for virgin PZT/BT, the ceramic likely did not simply depole or relax its electrical domains. Additionally, the low tanδ value given in Table 1.1 suggests that silver from the electrode did not seep through cracks in the ceramic all the way to the steel, unlike what we reported for the transducers described in the quarterly report for Year 2 Quarter 4. However, it appears that metal paint for electrodes tends to seep into the inherit porosity of the spray-on piezoceramic, while sputtered metal electrodes appears to seal the porosity. Previous studies using optical microscopy reveal that the sintered ceramic contains many microcracks that are roughly 1 micron wide at the surface. We suspect that SPI silver paint penetrates these microcracks as the paint solvent evaporates. When the sample temperature rises to 410°C, the silver may then act as a reducing agent, pulling oxygen away from the piezoelectric and altering its chemistry.

Gold and platinum painted electrodes behaved the same as the silver painted ones. The only transducers that did not suffer significant performance degradation over time at temperature are ones with sputtered electrodes with lead wires attached by silver paint. Thus, we conclude that the deposition process of sputtering seals the porosity, while the metal particles in the paint become free to migrate into the porous piezoceramic as the organics are burned off at elevated temperature. These particles may chemically react with the piezoceramic, effectively changing its properties for the worse.

Clearly, sputter deposition of electrodes works well, but a deposition method more amenable to field installation of coatings for condition monitoring of existing structures is part of the technology readiness plan.

2.1.4 Conclusions About Viability

The demonstration of PZT/BT and BT/LN composite transducer and instrumentation capabilities indicates that they have potential for condition monitoring for high temperature applications in nuclear power plants. The transducers are deposited by air-spray of a sol-gel and then densified using methods appropriate for field installation. Field application of electrodes will be part of the technology development roadmap in that only sputter-coated electrodes functioned properly at high temperature.

2.1.5 References

Boch, J.C., Philippe, N., 2007, *Ceramic Materials: Processes, Properties and Applications*, London, ISTE.

Cyphers, R.L., 2012, Research on low frequency composite transducers fabricated using a sol-gel spray-on method, Master of Science thesis in Engineering Mechanics, The Pennsylvania State University, University Park, PA.

Durruthy-Rodríguez, A M. D., Yáñez-Limón A J. M., 2011, Photoluminescence in Doped PZT Ferroelectric Ceramic System, In: *Ferroelectrics - Physical Effects*, 6773.

Eitel, R.E., 2003, Novel piezoelectric ceramics: development of high temperature, high performance piezoelectrics on the basis of structure, Thesis*,* The Pennsylvania State University, University Park, PA.

Kobayashi, M., Olding, T.R., Zou, L., Sayer, M., Jen, C.K., Rehmen, A.U., 2000, "Piezoelectric thick film ultrasonic transducers fabricated by a spray technique," 2000 *IEEE Ultrasonics Symp. Proc.*, 985-989.

Orr, A., 2015, A bond stiffness study of sol-gel spray-on transducers, Master of Science thesis in Acoustics, The Pennsylvania State University, University Park, PA.

Searfass, C.T., 2008, Fabrication and testing of piezoelectric bismuth titanate for use as a high temperature ultrasonic transducer, Master of Science thesis in Engineering Science, The Pennsylvania State University, University Park, PA.

Sinding, K., 2014, The effect of weight percent on the properties of ultrasonic transducers fabricated through a sol-gel deposition process, Honors thesis in Engineering Science, The Pennsylvania State University, University Park, PA.

Uchino, K., 2010, *Ferroelectric Devices*, 2 ed., CRC Press.

Xu, Y*.*, 1991, *Ferroelectric Materials and Their Applications*, Amsterdam.

Yi, G ., Wu, Z., Sayer, M., 1988, "Preparation of Pb(Zr,Ti)O3 thin films by sol gel processing: electrical, optical, and electro-optic properties," *J. Appl. Phys.* 64(5):2717-2724*.*

2.2 Transducer Capabilities on Tubing

Tubing is an integral part of heat exchangers. For the intermediate heat exchanger in the proposed very high temperature reactor the operating temperature could be as high as 950°C. In light water reactors the operating temperatures of piping systems could be as high as 400°C. Condition monitoring of these passive systems would enable improvements in management of maintenance actions and operating procedures. Ultrasonic guided waves have the ability to propagate tens of meters in pipes and are sensitive to cracking and corrosion. It is greatly desirable to do the condition monitoring online, which means that the transducers need to be resistant to high temperature. PZT/BT and BT/LN composite transducers were developed for these and similar applications. Comb transducers to preferentially send and receive ultrasonic guided wave modes are described and demonstrated. Comb transducers for axisymmetric guided waves in pipes and tubing are rings spaced equally to match the wavelength of the desired wave mode.

Transducers were deposited on 304 stainless steel (c_L = 5.96 mm/us, c_T = 3.23 mm/us, ρ = 7932 kg/m^3) 1" schedule 40 pipe (r_o = 12.7 mm, r_i = 10.6 mm, d = 2.1 mm). The dispersion curves that show the propagating wave modes are shown in Figure 2.1.
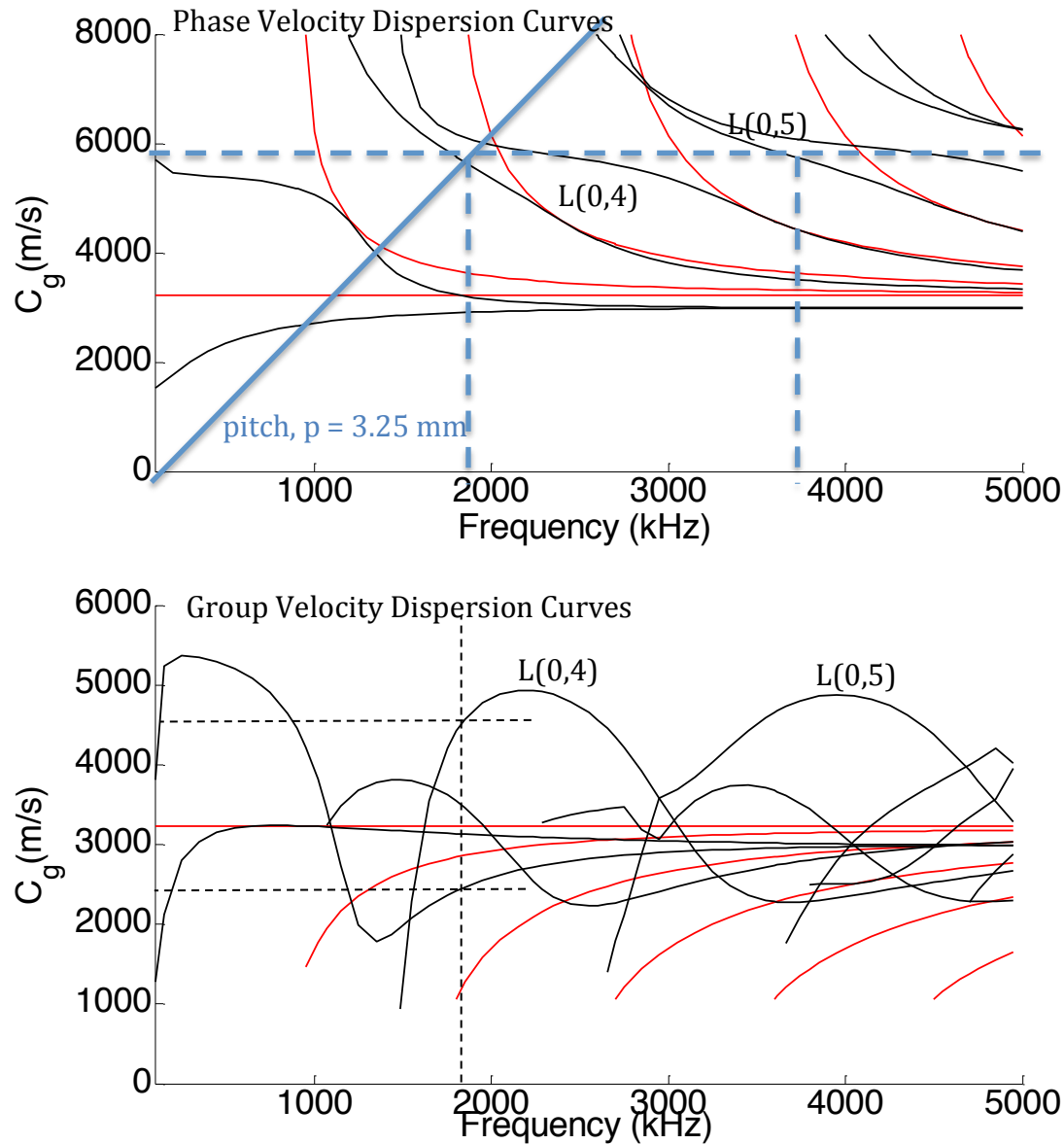
Figure 2.1. *Dispersion curves for r_o = 12.7 mm, d = 2.1 mm stainless steel pipe. Phase velocity (above) and group velocity (below) are shown for the axisymmetric modes; black lines indicate longitudinal modes and red line indicate torsional modes. The activation line for a comb transducer with a 3.25 mm pitch is also shown on the phase velocity dispersion curve plot.*

The transducer was designed to activate the longitudinal mode L(0,4) at c_p = c_L with fd = 3.85 MHz-mm, f = 1.83 MHz, λ = 3.25 mm, w = 1.625 mm. Here:

c_p = phase velocity

c_L = longitudinal wave speed

f = central excitation frequency

λ = wavelength

w = width of active elements

This mode was selected because it generates a cumulative second harmonic mode: L(0,5) at c_p = c_L with fd = 7.7 MHz-mm, f = 3.67 MHz, λ = 1.62 mm, w = 0.81 mm. Second harmonic generation is not measured for this milestone, but it is part of milestone 4 (subsection 2.1.3). A schematic of the multiple elements in a comb transducer is shown in Figure 2.2. The pitch of the elements is matched to the wavelength λ of the mode to preferentially actuate. Figure 2.1 indicates that a comb transducer with a pitch of 3.25 mm activated at 1.83 MHz will preferentially generate the L(0,4) longitudinal mode and the phase velocity will be equal to c_L.

Figure 2.2. Patterned transducer electrodes for controlled generation of ultrasonic guided waves.
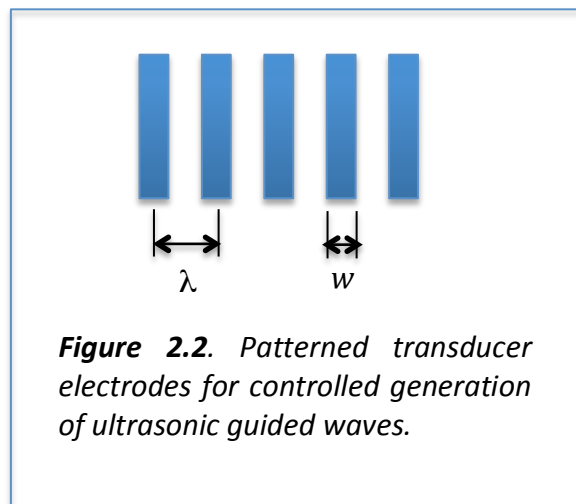
2.2.1 Transducer processing

Both PZT/BT and BT/LN piezoceramic multilayer coatings have been air-sprayed onto pipes using the methods described in subsection 2.1. After deposition of multiple layers, the coating is densified with an induction heating system as shown in Figure 2.3. The heating coils induce eddy currents in the pipe that cause the pipe to be heated, which consolidates the piezoceramic coating. For field deposition the coils could be formed in the field, or a different configuration coil that does not completely encircle the pipe could be used.
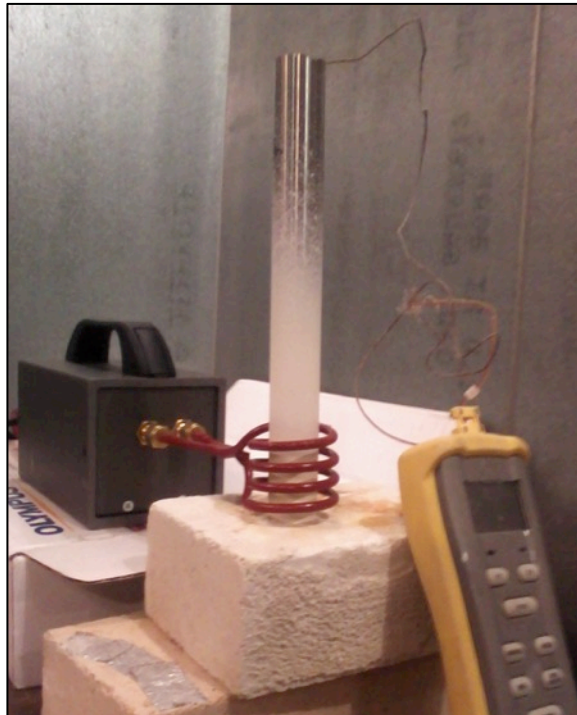
Figure 2.3. *Induction heating coils and thermocouple display to control consolidation of a PZT/BT transducer deposited on a stainless steel pipe.*

After the piezoceramic coating was densified the electrodes were applied. Initially, a layer of gold was painted on the coating and then silver electrodes were painted. These electrodes were used in transducers that transmitted and received bulk waves. However, since silver electrodes limit the service temperature we also evaluated nickel paste and platinum paint. Platinum has been extensively researched for use as an electrode in traditionally fabricated ceramics and has been chosen for its elevated temperature capability and inert effects to the ceramic. A platinum electrode was painted on but two issues arose; the paint ingressed the porous microstructure of the piezoceramic coating resulting in a resistive connection between the electrodes, and in some cases the platinum particles in the paint agglomerated leaving some portions of the electrode nonconductive. Agglomeration can be minimized by appropriate use of thinner and mixing. Figure 2.4 shows a painted silver electrode on a stainless steel pipe. We verified that the transducer was poled by ultrasound signals received in pulse-echo mode. As noted in subsection 2.1 painted silver electrodes function adequately at room temperature, but exposure to elevated temperature causes migration of electrode material into the porous

piezoceramic, where an undesirable reaction occurs that nullifies the piezoelectric effect. Thus, various methods to electrode the transducer were investigated, none of which were totally satisfactory.

Figure 2.4. *PZT/BT transducer with painted silver electrode.*

A nickel paste was procured to be used as the high temperature electrode. This paste was successfully painted onto the BT/LN transducer that had been sintered. This was the first trial with this nickel paste and initial proof testing was successful.

The next step was to pattern the electrodes such that we have a comb transducer that enables preferential actuation of a preselected guided wave mode; here the L(0,4) mode. Laser ablation had good potential to make such a transducer and a laser was readily available. After building a rotary stage and practicing the ablation process in order to remove the right width and depth of material, a three-element comb transducer was produced. To enable use of a single lead wire for all three elements, material was not ablated 360° around the circumference, but there was a small region where the elements remained interconnected. Figure 2.5 is a photograph of the ablated electrodes.

Figure 2.5. *25.4 mm outer diameter stainless steel pipe with BT/LN spray-on transducer with nickel electrode that was laser ablated.*

The lead wire was then connected to the patterned electrode such that the BT/LN could be polarized. Unfortunately, the electric field broke down and the transducer could not be poled. Nickel was abandoned as a choice for an electrode once we learned that at elevated temperatures ~100°C the nickel draws oxygen from the porous ceramic microstructure removing the ferroelectric property from the ceramic.

A multi-element comb transducer was created by laser ablating the silver electrode into four 1.6 mm wide rings as shown in Figure 2.6. The material removed between each ring was also 1.6 mm wide, thus the pitch of the transducer is 3.2 mm. At this point processing of the transducer is complete; a lead wire is connected to the electrode and the pipe itself is connected to ground.
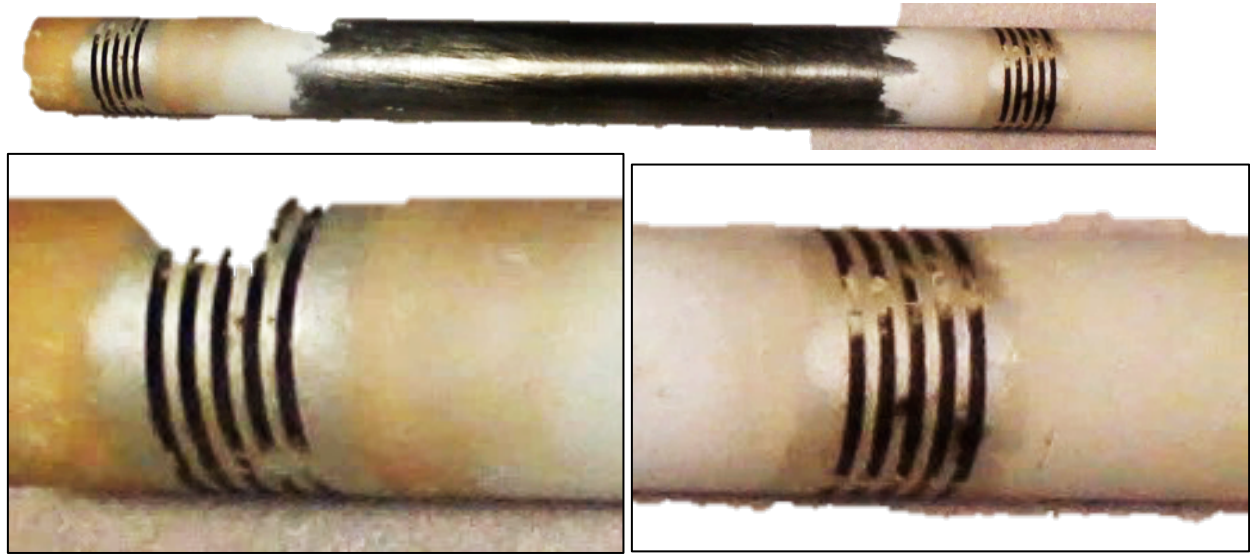
Figure 2.6. *Four-element laser ablated PZT/BT comb transducers on a 25 mm diameter stainless steel pipe. The black stripes are where the laser has ablated away the silver electrode and oxidized the top of the PZT/BT coating. A ligament of silver remains between the electrodes to preserve continuity between them, so that only one lead wire is necessary to activate each element.*

Other methods of patterning electrodes included simply painting stripes with the help of a mask. The results are shown in Figure 2.7, and it is apparent that the mask smeared the paint boundaries making mode control more difficult. A significant advantage of this method is that it is field deployable.
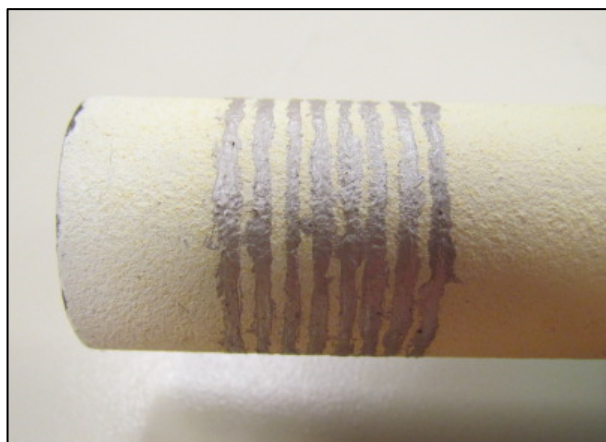
Figure 2.7. *Pipe #2, a five-spray, eight-element PZT-BiTi transducer situated 25mm and 200mm from the two ends of the steel tubing. The silver electrode on this sample was painted over a metal foil mask, making a less controllable but more field-deployable comb transducer than the laser-ablation method.*

A third trial patterning method was to laser ablate a mask to use in a sputter chamber or an evaporation chamber. The pipe is too large for a sputter chamber, so a patterned aluminum electrode that was deposited through the mask by evaporation, with the result shown in Figure 2.8. The transducer shown in Figure 2.8 is only a portion of a ring, but a ring could be formed by rotating the pipe during deposition inside the evaporation chamber. Aluminum was used as an inexpensive demonstration of the deposition methodology.
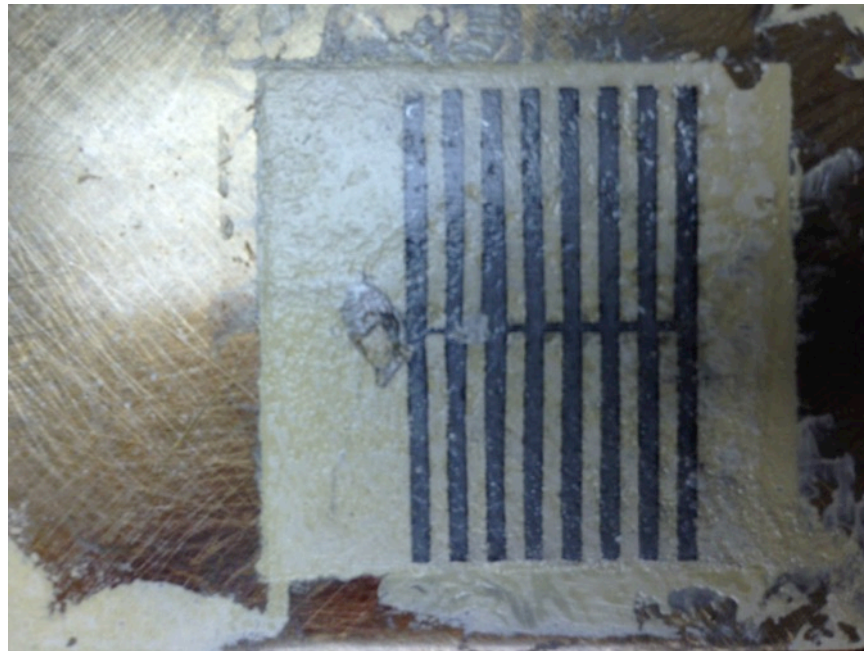
Figure 2.8. *PZT/BT transducer with an evaporation deposited aluminum electrode that was patterned using a mask.*

2.2.2 Experimental Results

Three type 304 stainless steel pipe samples were instrumented with working PZT/BT comb transducers. Pipe #1 has two laser-ablated transducers, while Pipe #3 has just one. The eight-element electrode on Pipe #2 was painted with the help of a mask in order to assess a more field-deployable electrode installation methodology. The Ritec SNAP RAM 5000, with a high-power gated amplifier, was used to activate these comb transducers in order to generate axisymmetric longitudinal guided wave modes L(0,n). Waveforms have been received by the same transducer (using pulse-echo) as well as by another transducer (using through-transmission). A photograph of Pipe #1 having comb transducers near each end of the pipe is shown in Figure 2.9. Each laser ablated comb transducer consists of 4 ring-shaped elements that are 1.6 mm wide and separated by a 1.6 mm gap and was processed by painting silver onto the PZT/BT and then using a laser to ablate the gaps between the ring elements. The photograph of Pipe #2 in Figure 2.7 shows that the mask caused the paint to bleed, resulting in

ring elements with very nonuniform widths. However, the resulting functionality is still reasonably good (as described subsequently).

Figure 2.9. *Pipe #1: four-element PZT/BT comb transducers on a 25mm diameter type 304 stainless steel pipe.*

The experimental setup for Pipe #1 is shown in the three photographs that comprise Figure 2.10. Pipe #1 was tested in through-transmission mode, while Pipe #3 was tested via pulse-echo, and in both cases waveforms with multiple wave packets were received as shown in Figure 2.11. Despite the nonuniformity of the electrode elements on Pipe #2, the transducer is capable of generating and receiving longitudinal guided waves as shown in Figure 2.12.

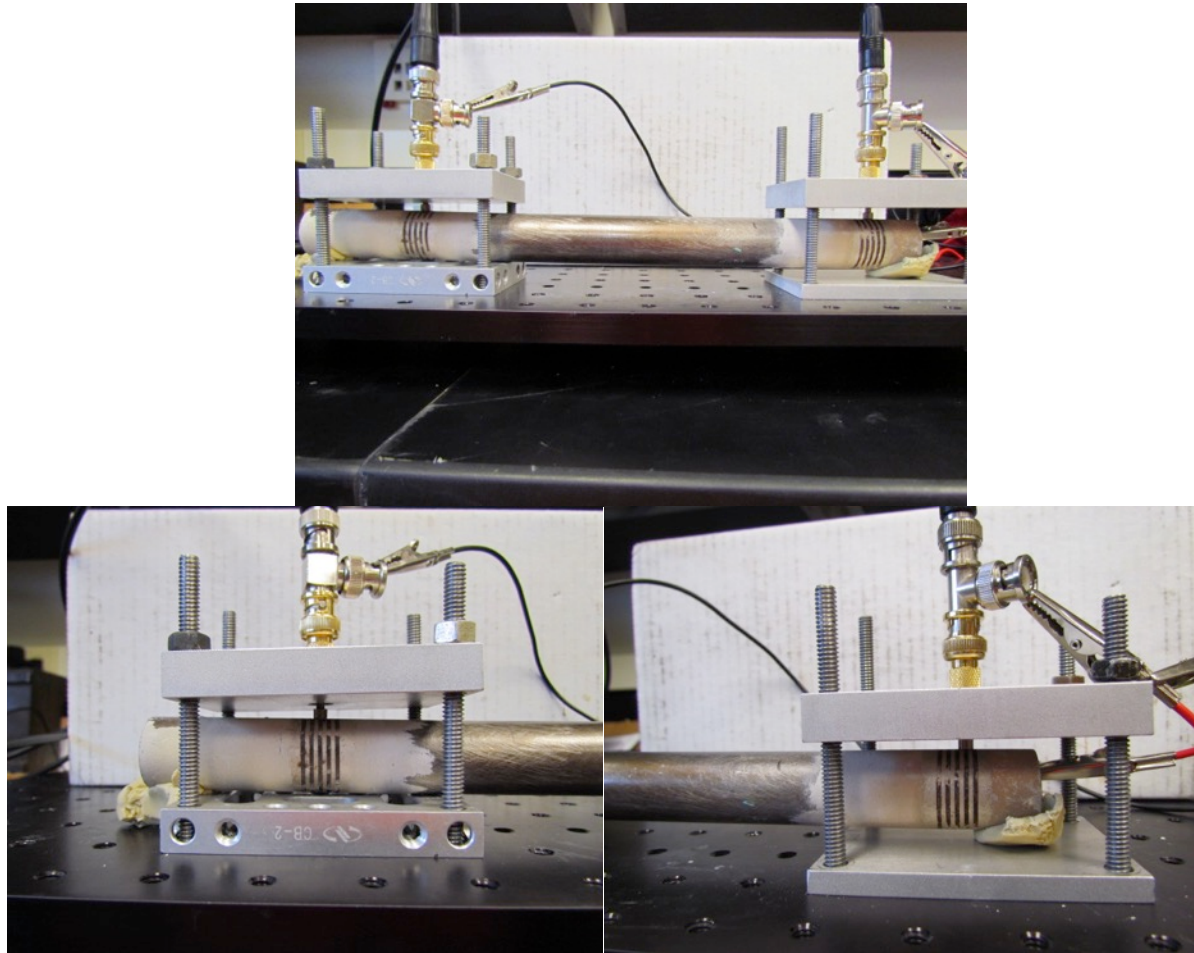**Figure 2.10.** *Experimental setup for Pipe #1.*
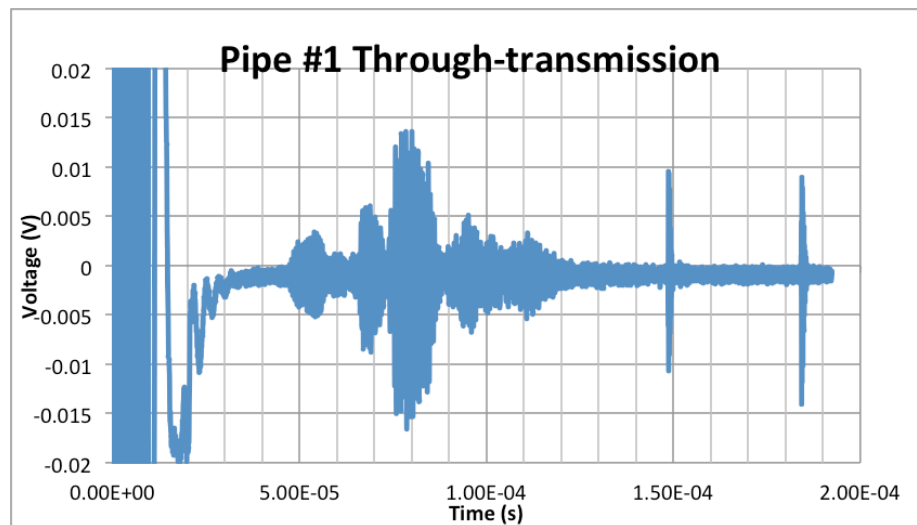
Figure 2.11. *Through-transmission received waveform from PZT/BT comb transducer on pipe #1. Many wave packets from end wall reflections and different L(0,n) modes are present. Receiver gain is 66 dB.*
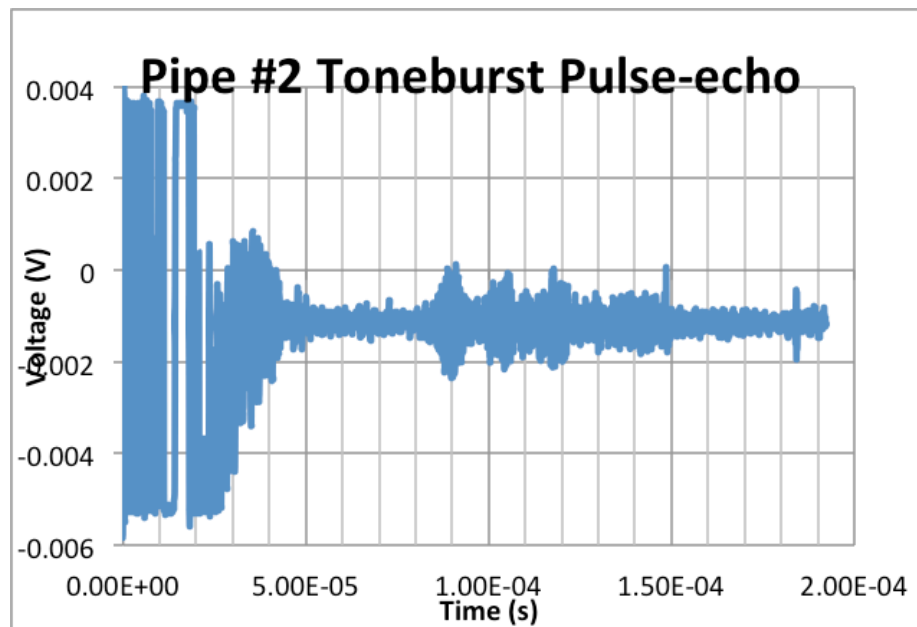
Figure 2.12. *Room temperature pulse-echo signals from pipe #2. The first wave packet corresponds to the L(0,4) mode.*

The A-scan shown in Figure 2.11 is from a toneburst excitation with a central frequency of 1.83 MHz. As indicated by the group velocity dispersion curves in Figure 2.1 there are four longitudinal modes that exist for this frequency, L(0,1) – L(0,4), which have group velocities that range from 2.4 – 4.5 mm/μs. Comb transducers also produce side bands that can be significant, but these have not been analyzed here. Based on the distance between transmitter and receiver being 213 mm, the expected arrival times of the L(0,4) and L(0,2) modes are 47 and 89 μs, respectively, which correspond to the first and fourth wave packets received in Figure 2.11. In addition to the multiple modes there are end wall reflections in the A-scan of Figure 2.11, which are probably responsible for the second and third wave packets that have higher amplitudes from the positive interference associated with the left-propagating and right-propagating reflected waves arriving simultaneously. We are primarily interested in the L(0,4) mode so we analyze that wave packet further. The FFT of the first arriving wave packet in Figure 2.11 is provided in Figure 2.13 and shows that the frequency is 1.83 MHz and that use of a low pass filter would be helpful. Calculated group velocities for L(0,4) and L(0,2) are 213 mm/48 μs = 4.4 mm/μs and 213 mm/89 μs = 2.4 mm/μs, which agree well with the values from the dispersion curves.

The A-scan from Pipe #2 shown in Figure 2.12 for a 1.83 MHz center excitation frequency does not appear to exhibit a L(0,2) mode, perhaps because the larger number of ring elements (8 for Pipe #2 relative to 4 for Pipes #1 and #3) reduces the side bands. For Pipe #2 the propagation distance is 400 mm (to far end wall and back), thus the group velocity of the first arriving wave

packet is 400 mm/89 µs = 4.5 mm/µs. This agrees with the L(0,4) mode. The second and third wave packets are either other modes or endwall reflections.
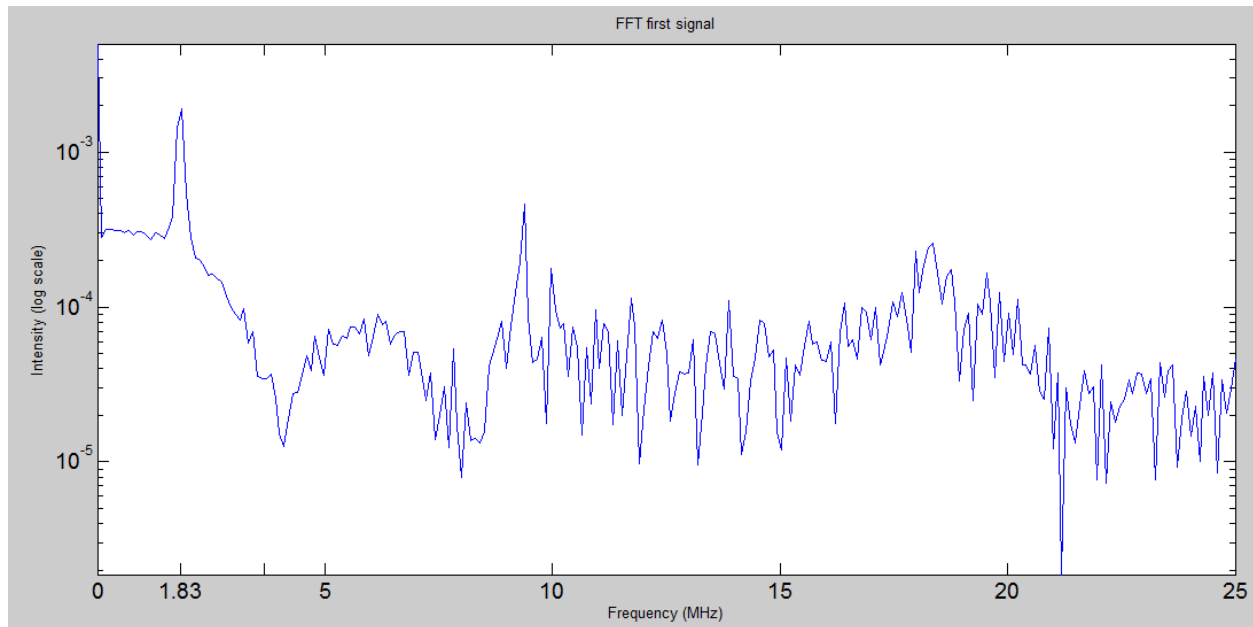
Figure 2.13. *FFT of the first arriving wave packet from Pipe #1, confirming the central excitation frequency is 1.83 MHz.*

In summary, multi-element PZT/BT transducers have been shown to actuate ultrasonic guided wave modes in a stainless steel pipe. The transducers are formed from air-sprayed sol-gel PZT-BT composite and have patterned ring electrodes to excite axisymmetric longitudinal guided wave modes.

2.3 Microstructural Evaluation

This subsection merely summarizes the achievements for this milestone (#4), the details of which are published in proceedings, journals, and a patent application as listed at the end of the document. Research began by extending our previous work on nonlinear guided wave propagation in plates to hollow cylinders (e.g., pipes). Formulating the equations in a curvilinear coordinate system made this possible and we were able to identify primary wave modes that generate cumulative second harmonics. By assessing the power flux from the primary mode to the secondary mode it was possible to select the modes with the best potential for characterizing microstructural evolution indicative of early stages of damage. Example results taken from Liu et al, 2013, *J. Acoustic Soc. Am*. 133(5):2541-2553 for steel having the properties given in Table II are shown in Figure 3.1 and Table III.
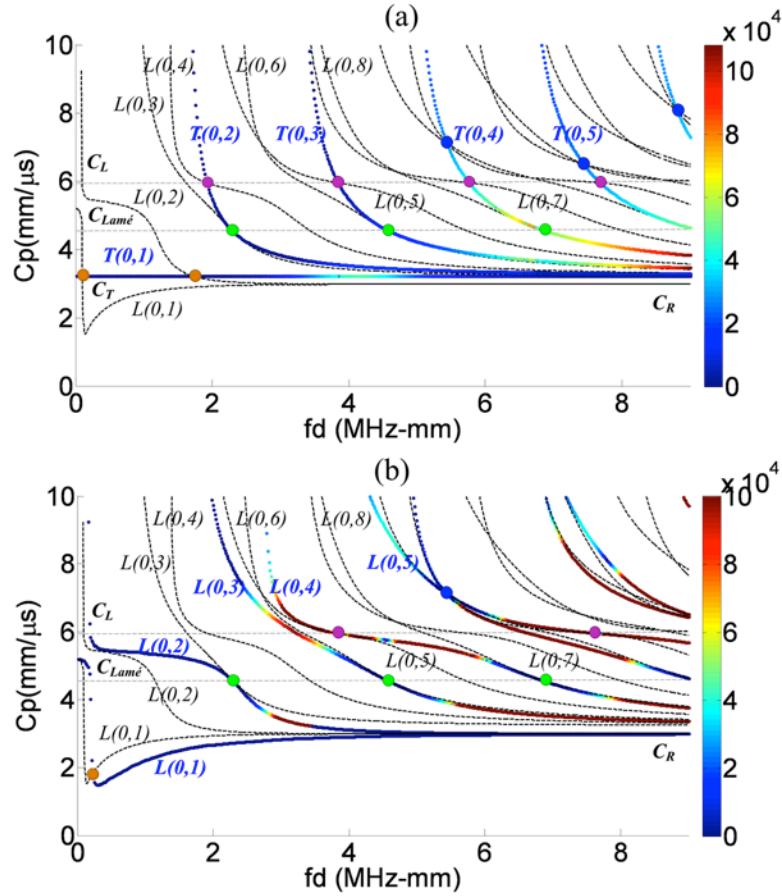
Figure 3.1. *Internal resonance plots: (a) Fundamental axisymmetric torsional modes to secondary L(0,5) mode, and (b) fundamental axisymmetric longitudinal modes to secondary L(0,5) mode. Color scaled lines represent the fundamental modes superimposed with normalized power flux intensity to the secondary L(0,5) mode. The black dashed lines are the possible cumulative secondary modes and the small circles indicate the synchronism points.*

TABLE II. Input parameters for the finite element models.

Dimensions		Material properties[a]					
R_i (mm)	R_o (mm)	ρ (kg/m^3)	λ (GPa)	μ (GPa)	A (GPa)	B (GPa)	C (GPa)
9	10.5	7932	116.2	82.7	-325	-310	-800

[a]A, B, and C are obtained from Rushchitsky (Ref. 25). A conversion between Landau and Lifshitz third order elastic constants and Murnaghan constants can be found in Norris (Ref. 26).

TABLE III. Normalized power flux intensity for some synchronism mode pairs for steel pipe dimensions and material properties given in Table II.

Synchronism fundamental mode types			Secondary wave field	fd value (MHz-mm)	Normalized power flux intensity
Torsional modes		$T(0,1)$	$L(0,1)$	0.06	1.62×10^{-6}
	C_T	$T(0,1)$	$L(0,2)$	1.72	1.29×10^{2}
	$C_{\text{Lamé}}$	$T(0,2)$	$L(0,3)$	2.28	1.23×10^{1}
		$T(0,3)$	$L(0,6)$	4.56	2.36×10^{2}
	C_L	$T(0,2)$	$L(0,4)$	1.92	4.10×10^{3}
		$T(0,3)$	$L(0,5)$	3.85	1.27×10^{4}
		$T(0,4)$	$L(0,7)$	5.78	5.47×10^{4}
Longitudinal modes		$L(0,1)$	$L(0,1)$	0.15	2.68×10^{-6}
	$C_{\text{Lamé}}$	$L(0,2)$	$L(0,3)$	2.28	1.35×10^{-3}
		$L(0,3)$	$L(0,6)$	4.56	2.18×10^{-2}
		$L(0,4)$	$L(0,8)$	6.84	3.63×10^{2}
	C_L	$L(0,4)$	$L(0,5)$	3.85	2.81×10^{4}
		$L(0,5)$	$L(0,9)$	7.70	1.36×10^{5}

We were the first researchers to simulate higher harmonic generation with finite element analysis. The Comsol multiphysics software has a hyperelastic material model that enables simulation of both material and geometric nonlinearities. This computational modeling is a valuable tool for verifying assumptions implicit to the theoretical modeling. The other valuable aspect is that simulation results contain only the nonlinearities input to the analysis, whereas experimental results have inherent measurement system nonlinearities.

Since the number of potential primary modes that generate strong second harmonics is somewhat limited we studied third harmonics and found the Lamb and shear horizontal (SH) modes that generate cumulative third harmonics. It turns out that any SH mode at any frequency will generate a cumulative third harmonic and the nondispersive fundamental SH0 mode has some very attractive features for third harmonic generation. Furthermore, in related research we found that guided wave modes in plates provide the asymptotic limits for guided wave modes in pipes. Therefore, our findings in plates can be extended to pipes.

The next major accomplishment was to develop an understanding of nonlinear flexural wave propagation in pipes. Making use of this understanding requires a new interpretation of flexural wave modes as waves that propagate along a helical path on the pipe at a tilt angle that can be determined based on the mode. This interpretation made it possible to perform finite element simulations that verified the theoretical model.

Finally, we have analyzed nonlinear mixing of guided wave modes to enable condition monitoring of early degradation that is localized. The system and method uses spectroscopy and has a patent pending. There are also other important benefits; i.e., the wave mixing can be

controlled in such a way that measurements are made away from system nonlinearities, and it is possible to do condition monitoring for localized degradation without using a historical baseline (a spatial baseline is sufficient).

Higher harmonic generation experiments on pipes were planned. The axisymmetric L(0,4) mode has been selected as the primary mode, and it generates a second harmonic of the L(0,5) mode. Internal resonance occurs for a frequency-thickness product, fd = 3.85 MHz-mm and has high power flux transferred to the second harmonic. Transducers were designed to preferentially excite the L(0,4) mode over the multitude of other modes that exist at 3.85 MHz-mm and to preferentially receive the second harmonic L(0,5) mode at 7.70 MHz-mm. The transducers are multi-element comb transducers having an element spacing matched to the wavelength. The comb transducers have 5 equally spaced ring elements and are designed for a 25.4 mm diameter schedule 40 stainless steel pipe. The element widths are 1.62 and 0.81 mm for the transmitter and receiver respectively. The transducers are processed as follows:

- Air-spray multiple coats of PZT/BT sol-gel around the circumference of the pipe

- Consolidate the piezoceramic coatings using an induction heating system

- Paint a silver electrode over the footprint of the transducer

- Laser ablate the electrode to form the spaces between the ring electrodes

- Attach lead wires to the ring electrodes

- Pole the piezoceramic with the ring electrodes.

In order to measure second harmonics (i.e., the L(0,5) mode here) the signal to noise ratio needs to be as high as possible so a high power gated amplifier is used to send a Hanning windowed tone burst to the transmitter. The transducer that we fabricated failed to actuate a finite amplitude wave because arcing between the narrow ring electrodes occurred. The two most likely causes of this problem are: (1) the laser ablation went too deep into the piezoceramic coating and exposed the substrate and (2) the arcing occurred through the air from one electrode to an adjacent one. Both problems should be correctable by (1) improvement of the laser ablation process and (2) application of a protective insulator (e.g., sauereisen) on top of the electrodes. Unfortunately, problems with the electrodes earlier in the project (for milestones 1 and 2) cost time and we are unable to successfully show that the temperature resistant piezoceramics PZT/BT and BT/LN are capable of generating higher harmonics before the project end date. However, we plan to continue this work.

In closure, the published work cited below indicates that excellent progress was made on the use of higher harmonic generation for microstructural evaluation and prognostics.

Patents:

1. Y. Liu, C.J. Lissenden, G. Choi, X. Yao, J.L. Rose, 2014, "System and method for characterization of materials using nonlinear acoustic guided wave spectroscopy," U.S. Patent Office serial number 62/066,650.

Published in Journals (these are included as the Appendix for completeness):

2. C.J. Lissenden, Y. Liu, J.L. Rose, 2015, "Use of nonlinear ultrasonic guided waves for early damage detection," *Insight* Vol. 57(4), in-press.
3. Y. Liu, C.J. Lissenden, J.L. Rose, 2014, "Higher order interaction of elastic waves in weakly nonlinear circular cylinders. I. analytical foundation," *J. Appl. Phys*. Vol. 115:214901.
4. Y. Liu, E. Khajeh, C.J. Lissenden, J.L. Rose, 2014, "Higher order interaction of elastic waves in weakly nonlinear circular cylinders. II. physical interpretation and numerical simulation," *J. Appl. Phys*. Vol. 115:214902.
5. Y. Liu, V.K. Chillara, C.J. Lissenden, J.L. Rose, 2013, "Cubic nonlinear shear horizontal and Rayleigh Lamb waves in weakly nonlinear plates," *J. Appl. Phys*. Vol. 114:114908.
6. Y. Liu, E. Khajeh, C.J. Lissenden, J.L. Rose, 2013, "Interaction of torsional and longitudinal guided waves in weakly nonlinear circular cylinders," *J. Acoustic Soc. Am*. Vol. 133(5):2541-2553.

Published in Proceedings:

7. C.J. Lissenden, Y. Liu, J.L. Rose, 2014, "Use of nonlinear ultrasonic guided waves for early damage detection," Proceedings of the NDT 2014 Conference, British Institute of Non-Destructive Testing.
8. C.J. Lissenden, Y. Liu, V.K. Chillara, G. Choi and X. Yao, 2014, "Nonlinear guided waves for continuous material microstructure state awareness," Proceedings of the ASME 2014 International Mechanical Congress and Exhibition, ASME International, Paper IMECE2014-39699 (8 pages).
9. Y. Liu, C. Lissenden, J. Rose, 2014, "Nonlinear ultrasonic guided waves for microstructure characterization of hollow cylinders," 13th International Symposium on Nondestructive Characterization of Materials (NDCM-XIII), B. Djorjevic, Ed., May 2013, www.NDT.net?ID=15519.
10. Y. Liu, C.J. Lissenden, J.L. Rose, 2014, "Microstructural characterization in plates using guided wave third harmonic generation," In: *Review of Progress in Quantitative Nondestructive Evaluation*, Vol. 33, D.E. Chimenti, L.J. Bond, D.O. Thompson, Eds., American Institute of Physics Proc. 1581, pp. 639-645.

11. Y. Liu, C.J. Lissenden, J.L. Rose, 2013, "Higher harmonic generation of guided waves in plate: power flux density and synchronism co-analysis for mode selection," In: *Review of Progress in Quantitative Nondestructive Evaluation*, Vol. 32, D.O. Thompson and D.E. Chimenti, Eds., American Institute of Physics Proc. 1511, pp. 151-158.

2.4 Field Implementation on Mockup Structure

The ability to process spray-on piezoceramic transducers for high temperature applications is a relatively new development. As such, transducer processing has been performed in the laboratory using laboratory techniques and equipment. However, with online condition monitoring applications in mind, the vision for these transducers is that they could be applied both (i) on new components in the factory and (ii) in the field on existing structural components. The latter requires innovative adaption of laboratory procedures to in-the-field settings and is the subject of this investigation.

The spray deposition and densification of temperature resistant piezoceramic coatings, the installation of electrodes, and the polarization method are described in detail in subsection 2.1. Two composite piezoceramics were investigated, lead zirconate/bismuth titanate (PZT/BT) for applications up to 400°C and bismuth titanate/lithium niobate (BT/LN) for applications up to 950°C. The reader is referred to this milestone report for details not provided herein. Only field application of PZT/BT transducers are demonstrated, but the field application of BT/LN transducers will follow the same methods (although different processing parameters like densification temperature are likely to be different).

While the transducer processing is physically done in the laboratory, care has been taken to only use equipment and procedures that could be directly taken to the field for transducer deposition and processing on an existing component in a nuclear power plant. For instance, typical laboratory samples are cylinders 25 mm in diameter by 25 mm long. For these samples a hot plate can be used for pyrolization, a 50 mm diameter tube furnace can be used for consolidation, a 150 mm diameter vacuum chamber can be used for sputter coating electrodes, and a fully contained oil bath apparatus can be used for poling. Translating this fabrication process to practical, full scale structures requires substantial changes to the process design.

The objective is to demonstrate that spray-on transducers can be applied to a realistic structure using in-situ appropriate techniques. For this purpose a steel mockup structure was selected. As shown in Figure 4.1 the primary structure is a portion of a cylindrical shell and there is an outlet port welded in place. There are geometric similarities to a reactor pressure vessel. The structure is 1.35 m long by 1.22 m wide, has a 1 m radius, and is 6.4 mm thick steel. The outlet

port is 100 mm diameter. The structure was fabricated for an unrelated project and has piezoelectric transducers bonded to it. This test case will especially challenge our spray, densification, and poling technologies. Analysis was performed to design the transducers.

Figure 4.1. *Steel mockup structure to be instrumented with spray-on transducers*

The goal of this investigation was to deposit comb transducers to generate and receive ultrasonic guided waves in the steel structure. The guided waves would enable damage detection in the structure. The S1 symmetric Lamb mode was selected from the dispersion curves for a plate because when excited with a phase velocity equal to the longitudinal wave speed (at a frequency-thickness product of 3.85 MHz-mm) the out of plane displacement component on the surface of the plate is zero. Therefore, if there is fluid inside the vessel no energy will leak into the fluid, as would be the case for other modes. The excitation frequency should be f = 3.85 MHz-mm/6.4 mm = 0.60 MHz. The activation line for a comb transducer is $c_p = \lambda f$ (where c_p is the phase velocity, λ is the wavelength, and f is the frequency), because the pitch, p, (element spacing) of the transducer dictates the wavelength $p = \lambda$. Given a phase velocity of 6 mm/μs, the transducer pitch is computed to be p = (6 mm/μs)/(0.60 MHz) = 10 mm. Therefore, using an element width of p/2, the electrode width needs to be 5 mm. In this case the PZT/BT coating is continuous and the discrete electrodes define the individual elements in the comb transducer as shown in Figure 4.2. The comb transducer has four elements that are electrically connected together. Two comb transducers were deposited on the convex side of the steel structure with the intent of one transmitting a wave packet that is received by the other.
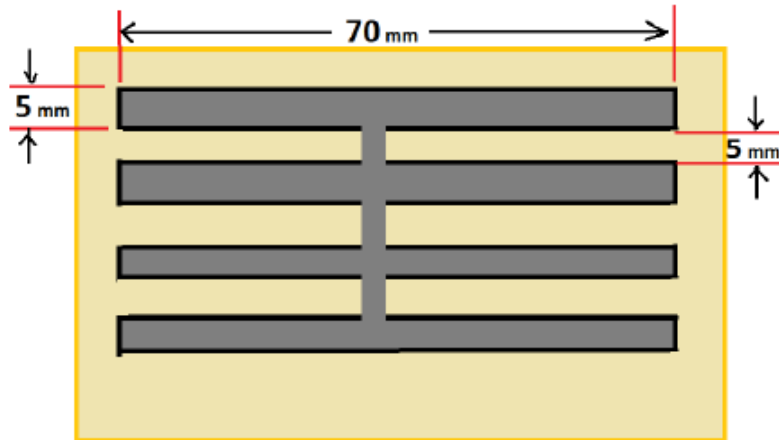
Figure 4.2. *Comb transducer schematic for steel mockup structure, to excite S1 Lamb mode at the longitudinal wave speed. The PZT/BT is shown in tan, and the electrode is gray. Silver strip connecting four comb elements was applied after poling.*

2.4.1 Plan for Field Deployment

A field deployable methodology to process transducers on the steel mockup structure was developed and then tested in our laboratory. The important aspect of this methodology is that it could be followed in the field as opposed to the laboratory. An outline of the procedure is given below.

1. Place the mockup structure on its side (as shown in the right side of Figure 4.1) inside a fume hood. Use a standard paint spray gun to spray multiple coats of PZT/BT sol-gel onto the convex outer surface. Two transducers will be sprayed to enable use of the through-transition mode. The transducers will be located approximately 0.5 m apart. The transducer footprint is approximately 35 mm by 70 mm. The use of the hood is appropriate in the laboratory, however in the field where no hood is available the personnel doing the spraying will need to wear protective clothing and masks. A portable air compressor is needed in the field.

2. The piezoceramic coating will be densified by induction heating with a pancake coil, which enables heating of a flat surface or a surface with a large radius of curvature.

3. Silver electrode stripes will be painted using a stencil. The stripes will make each transducer a comb transducer so that the mode to be generated can be controlled.

The four stripes will be 5 mm wide by 70 mm long and spaced 5 mm apart so that we can excite the S1 Lamb mode at the longitudinal wave speed.

4. The transducers will be poled through the thickness by using a peanut oil bath contained within a putty dam to prevent the high voltage from ionizing the air around the electrodes.

5. Lead wires will be connected to the electrodes for both transmitter and receiver.

6. Toneburst voltage will be supplied to the transmitter. A signal will be acquired from the receiver.

2.4.2 Processing Equipment[*]

Laboratory fabrication takes place inside a chemical hood, to isolate paint toxins from the broader environment. The spray-gun is powered by a compressed gas line. Samples may be pyrolized on a hot plate, densified in a tube furnace, electroded in a vacuum sputtering chamber, and poled in an oil bath. This equipment is ideal for small samples, but not for large structural components. Thus, in-field deposition requires alternatives to this equipment.

An air compressor replaces the laboratory compressed air line used previously. An Ambrell induction heater with a pancake coil (see Figure 4.3) pyrolizes and densifies the PZT/BT coating. A small Ortec 3kV high electrical power supply box replaces the laboratory oil bath poling unit.

This equipment is inexpensive by the standards of industrial processing. The induction heater and the high power supply cost roughly $10K and $3K respectively. Furthermore, this portable equipment requires only electricity inputs. The system can function with one six-plug power strip.

---

[*] Sections marked with an * are based largely on the Honors Thesis of Nathan Malarich entitled, "Spray-On Comb Transducers For Health Monitoring Of High-Temperature Structures," in Engineering Science at Penn State, May, 2015.
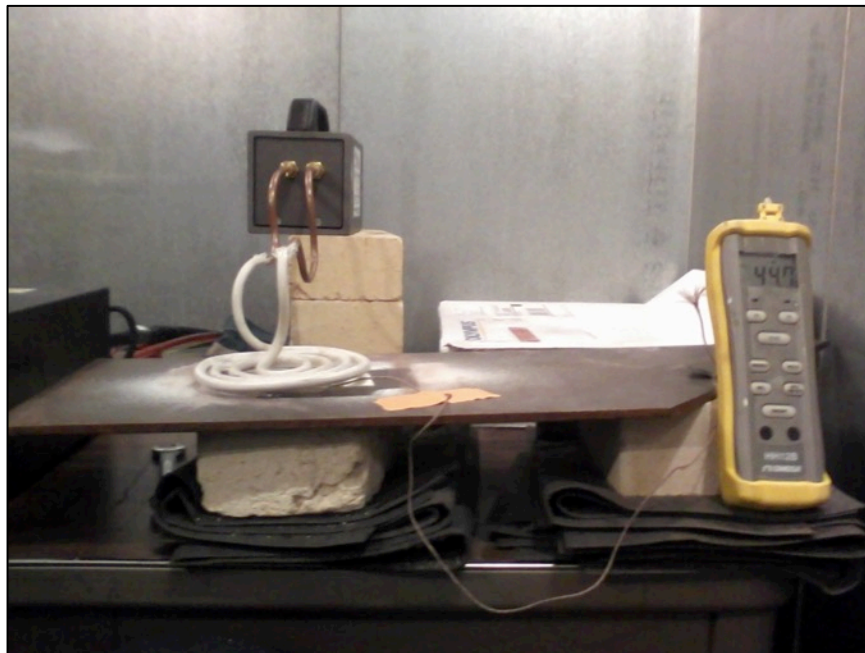
Figure 4.3*. Pancake induction heating coil for in-situ thermal processing of piezoceramic transducers on plates or large radius shell structures.*

2.4.3 Deposition and Processing*

Transducers were sprayed with three coats of PZT/BT, using the sol-gel/powder slurry prepared in the chemical hood. Figure 4.4 illustrates the spraying process. The spray-gun was powered with the air compressor shown in Figure 4.5.

Figure 4.4. *(left to right) Steel surface is roughened and degreased before spraying; the field spray operation is constrained; the first spray coat.*

Figure 4.5. *Side view of the structure during processing. Left arrow points to the induction heater coil positioned on opposite side of the structure from the PZT/BT coating. Right arrow points to the air compressor used to power the spray gun.*

Because the steel mockup structure has a large radius and is relatively thin, the induction heater coil was positioned on the side opposite the PZT/BT coating for pyrolization and densification as shown in Figure 4.5. This arrangement allowed easy inspection of the ceramic during heating, and ready use of a laser infrared thermometer to record surface temperatures. The induction heater pyrolized each spray at 100-150°C using 40A and 110W, and densified the final three-coat PZT/BT at 240-300°C with 65A and 300W. The current and power measurements are from the induction heater display panel, and the temperature measurements are from the infrared thermometer. The actual emissivity is unknown, but because the transducer is not an ideal blackbody, actual temperatures exceeded these recorded values. Temperatures varied across the PZT/BT, because the small pancake coil unevenly heated the steel underneath the ceramic. Improved coil design would provide a more uniform temperature distribution. It's worth noting that induction heating provides much more uniform heating than does the blow torch heating that was used earlier in the project.
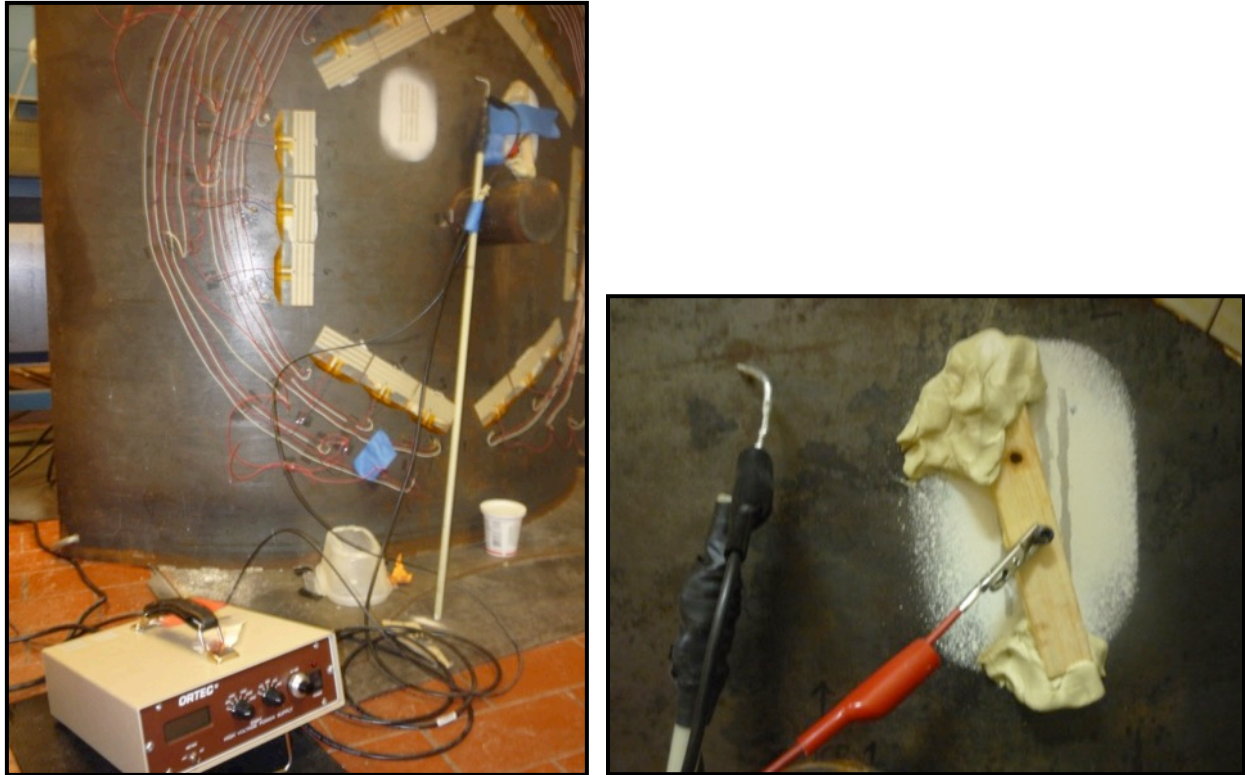
Figure 4.6. *PZT/BT poling setup. Left, high-voltage supply on the ground in front of the structure. Note that the hexagonal array of sensors and their wiring are left over from an unrelated previous project. Right, close-up of a PZT/BT coating, with red high-voltage clip connecting to silver electrode via a screw. Plumbers' putty, masking tape and balsa wood support the high-voltage connection.*

Silver paint was brush applied through a steel foil mask to form the electrodes for the comb transducers. Unfortunately, many of the electrode strips were short-circuited to the steel structure. These undesired electrical connections likely occurred where silver was painted over pores in the ceramic. A magnifying glass revealed several such pores in the 3000 mm^2 surface area of the ceramic sprays. Applying additional sprays of ceramic would likely cover these pores. Thus, the first lesson learned is that 3 spray coats are too few, 5-6 would have yielded a much better result.

The two comb elements with no measurable conductivity were poled as shown in Figure 4.6. The 3kV power supply, shown on the bottom left of Figure 4.6, provided 300-370 V across the three PZT/BT sprays (~60μm thick, for an electric field > 50kv/cm). The induction heater raised the PZT/BT temperature to approximately 100°C during poling. Prior experience dictated that the minimum electric field and temperature to provide a strong piezoelectric-coupling PZT/BT coating are 40kV/cm and 25°C.

These transducers, shown in Figure 4.7, were the first to be poled without an oil bath. This technique is not recommended for future work, as many sparks in the air dealt the electrodes both visual and functional damage. The dark splotch on strip 6 (numbered from the left) formed underneath the high-voltage screw and actually disconnected the electrode into two parts.
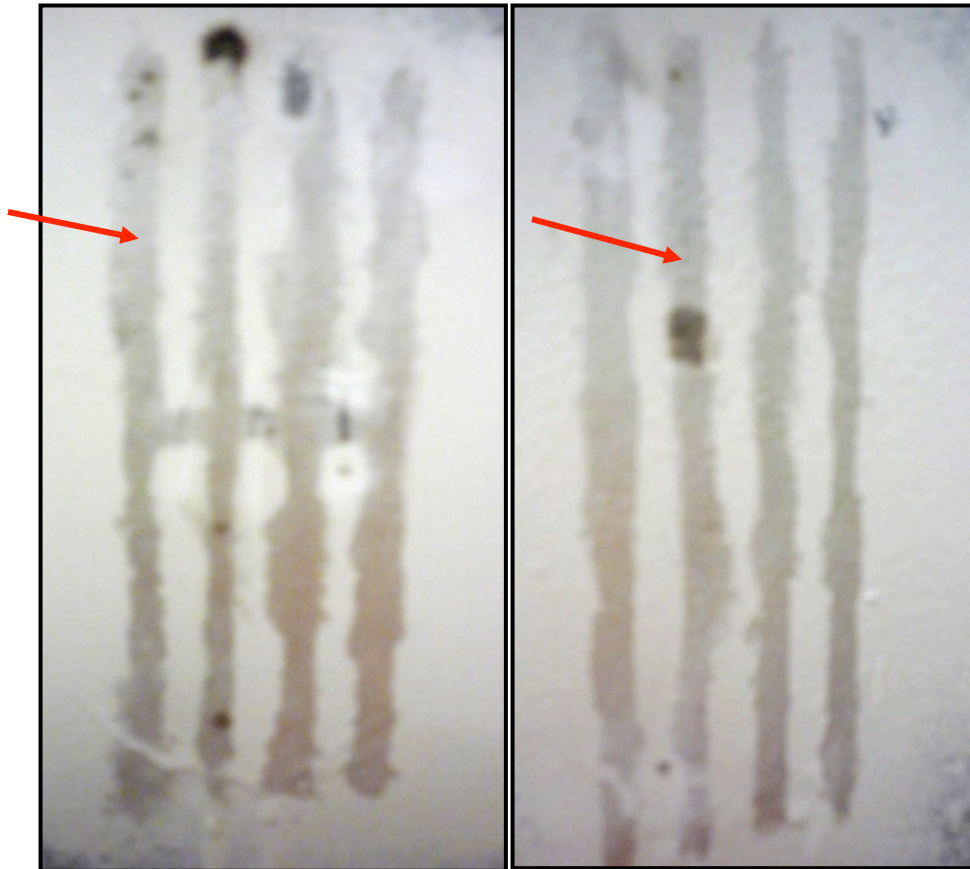
Figure 4.7. *Photos of PZT/BT comb transducers after poling was attempted. Two arrows point to the two locations where the transducers were poled. Dark splotches on the silver paint are burn marks where sparking either ablated or changed the silver to a nonconductive chemistry.*

2.4.4 Ultrasonic Testing*

The two poled portions of the transducers were tested in pulse-echo mode. Figures 4.8 and 4.9 show many strong through-thickness echoes, using 50μJ pulses with 40dB gain. The echoes are spaced at 2.08 μs. This time of flight corresponds to the ultrasonic velocity of 6.1 mm/μs in a 6.4 mm thick shell, which is roughly the longitudinal wave speed in steel. Since only a small

portion of the comb transducers were poled, the propagation of Lamb waves was not attempted.
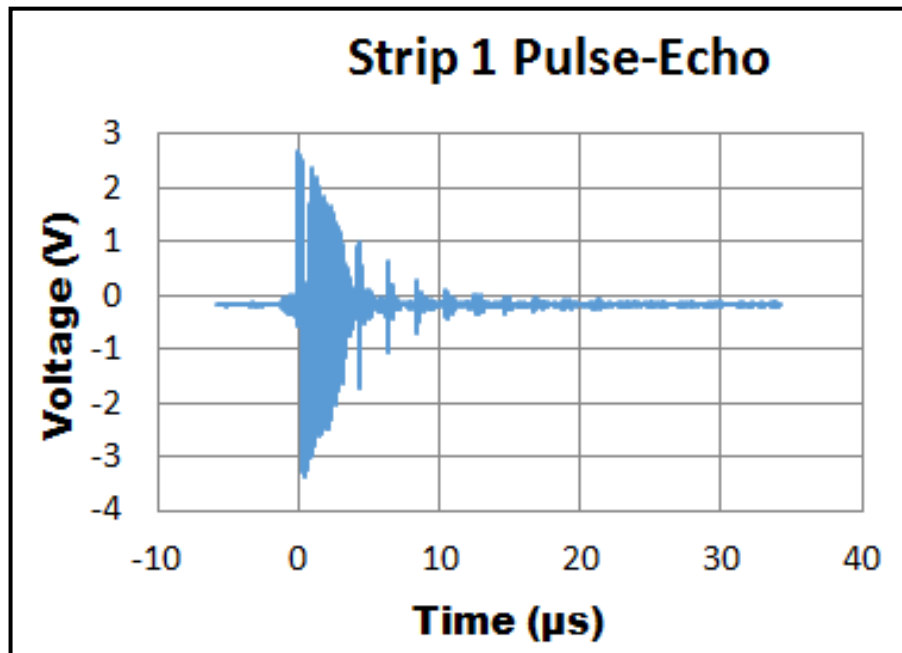
Figure 4.8. *Pulse-echo A-scan from first poled portion of PZT/BT transducer; through the 6.4 mm thickness of the steel structure.*
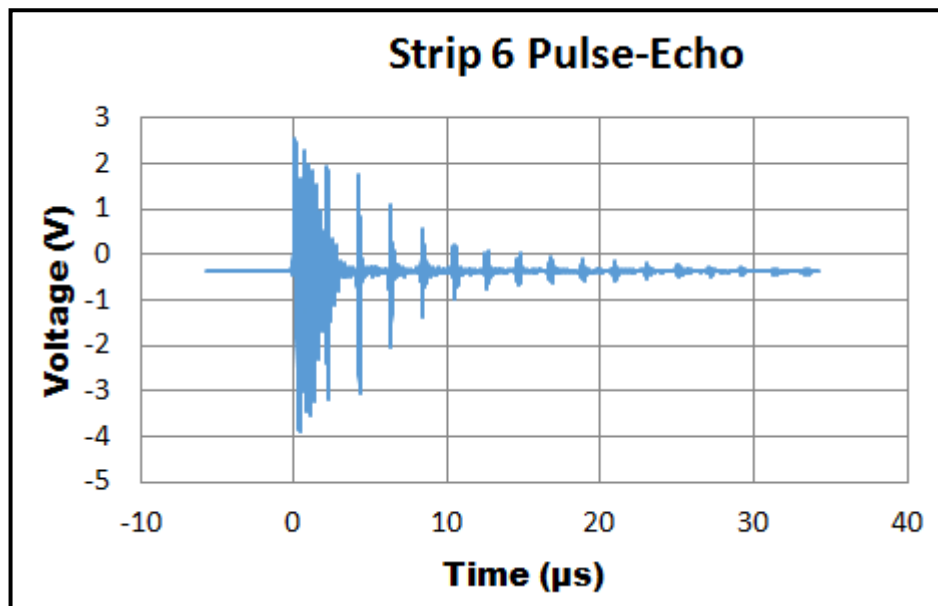
Figure 4.9. *Pulse-echo A-scan from second poled portion of PZT/BT transducer; through the 6.4 mm thickness of the steel structure.*

The second lesson learned from this experiment is to use an oil bath to prevent arcing during the poling process. This could be done by laying the steel structure upside down and building a dam around the transducer with putty or sealant as shown in Figure 4.10. The fragile connection between the screw and electrode also likely caused some sparking during poling. A higher-quality portable poling unit will improve future experiments on large structures. Perhaps a small fiberglass open-roof box with a spring-loaded high-voltage line could surround the transducer. Putty and tape could seal the box to the structure, and electrically insulating mineral oil could fill the box.

2.4.5 Conclusion

A methodology has been developed to deposit and process temperature resistant piezoceramic transducers on large structural components in the field. PZT/BT transducers installed on a steel structure were able to generate ultrasonic signals. However, because an insufficient number of PZT/BT layers were deposited the transducers had open porosity through the thickness of the PZT/BT coating making it not possible to pole a significant portion of the comb transducers intended to launch and receive the S1 Lamb mode. The solution is simply to deposit more layers, 5-6 should suffice, to ensure that there is not significant open porosity. Given the proper equipment, which is inexpensive, in-situ application of sol-gel based piezoceramic ultrasonic transducers is reasonably straightforward.

Figure 4.10. *Poling of a PZT/BT comb transducer on a steel mockup structure: high voltage source, connection screw mounted on balsa wood, putty dam for oil bath.*

2.5 Transducer Applicability to Compact IHX

2.5.1 Compact Intermediate Heat Exchanger

The very high temperature reactor is one of several types of next generation nuclear plants that could be constructed. The very high temperature (900-950°C) over a long duration service life (60 years) requires robust components as well as condition monitoring. Intermediate heat exchangers (IHXs) transfer the thermal output of the reactor to a power conversion unit or a hydrogen production plant as depicted in Figure 5.1. The heat exchangers use helium as the heat transfer medium. Few alloys are resistant to these very high temperatures, with the leading candidate being Alloy 617 [Mizia, 2008]. There are concerns about the feasibility and practicality of conventional tube and shell style heat exchangers given the size necessary and the availability of materials. Thus, a compact IHX based on a plate style heat exchanger is in the development phase. One such design known as a printed circuit heat exchanger (PCHE) has been investigated at Ohio State University [Mylavarapu, 2008] and could be manufactured by a company like Heatric, which specializes in compact heat exchangers.

The compact IHX is a plate structure built up by diffusion bonding many foils together. Each foil has machined or etched channels to facilitate heat exchange. Integrity of the diffusion bonds and unimpeded open flow channels are vital to reliable operation of the compact IHX. The economic benefit of the compact IHX cannot be attained without condition monitoring to ensure separation of the heat transfer media. The inaccessibility of the internal channels renders conventional inspection methods inapplicable. However, condition monitoring with sprayed-on transducers has the potential to solve the problem.
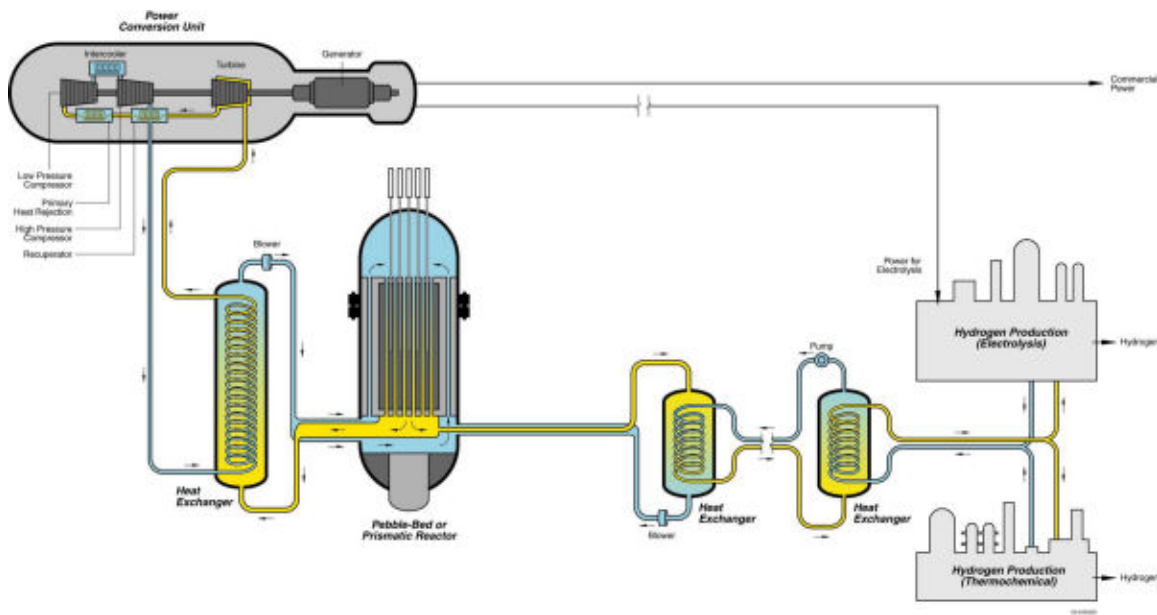
Figure 5.1. *Very High-Temperature Reactor [www.inl.gov].*

The potential for bismuth titanate/lithium niobate (BT/LN) sprayed-on transducers, which have been described in detail in the report for Milestones 1 & 2, for condition monitoring of a compact IHX has been investigated. The BT/LN spray-on transducers have been shown to function up to 1000°C, as shown in Figure 5.2.
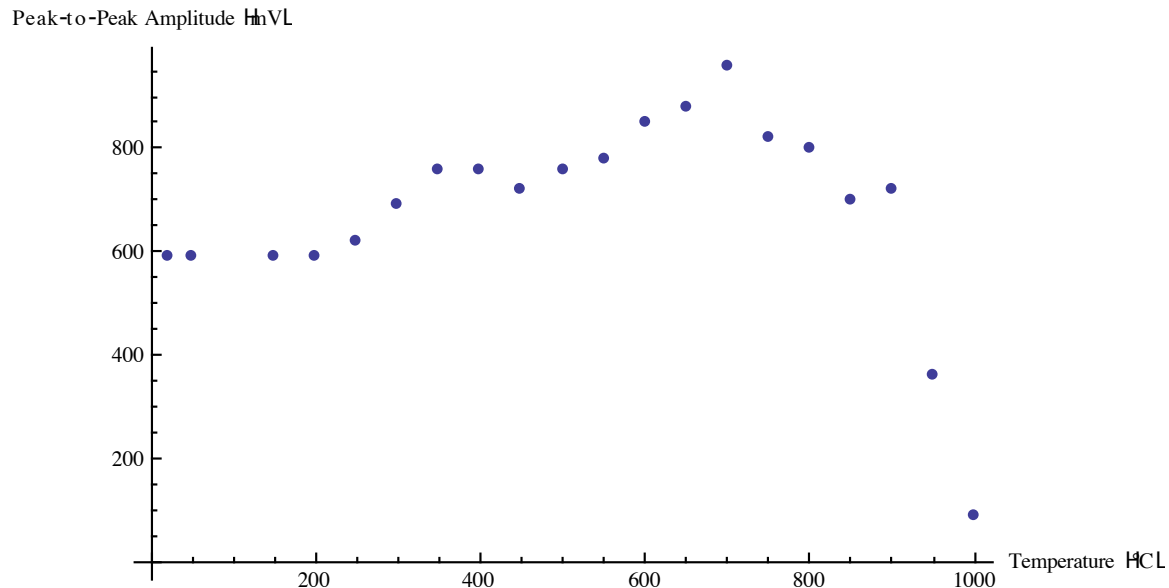
Figure 5.2. *Peak-to-peak amplitude (in mV) as a function of temperature (°C) for BT/LN transducer on Alloy 617 substrate.*

The specifics of the compact IHX that we analyzed were taken from Mylavarapu [2008], which is a PCHE design. Alloy 617 foils 1.63 mm thick have 12 channels photoetched into one surface, these channels have a semielliptical cross-section 2 mm wide by 1 mm deep and are shown in Figure 5.3. The channel spacing (or pitch) is 2.5 mm. Adjacent foils have hot fluid and cold fluid inputs that flow in different directions. Fluid flowing in each direction needs an input and an output as shown in Figure 5.4 [Mylavarapu, 2008]. The PCHE core has 20 foils sandwiched between two 19 mm thick plates. The foils and plates are diffusion bonded as shown in Figure 5.5. Kazakov [1985] defines diffusion bonding of materials in solid state as "a process for making a monolithic joint through the formation of bonds at the atomic level, as a result of the closure of the mating surfaces due to local plastic deformation at elevated temperature which aids interdiffusion at the surface layers of the materials being joined." Properly formed, diffusion bonds are of high quality. That said, the compact IHX must function in a very harsh environment and there is concern about clogged channels and disbonds that lead to mixing of the heat transfer media (helium in this case).
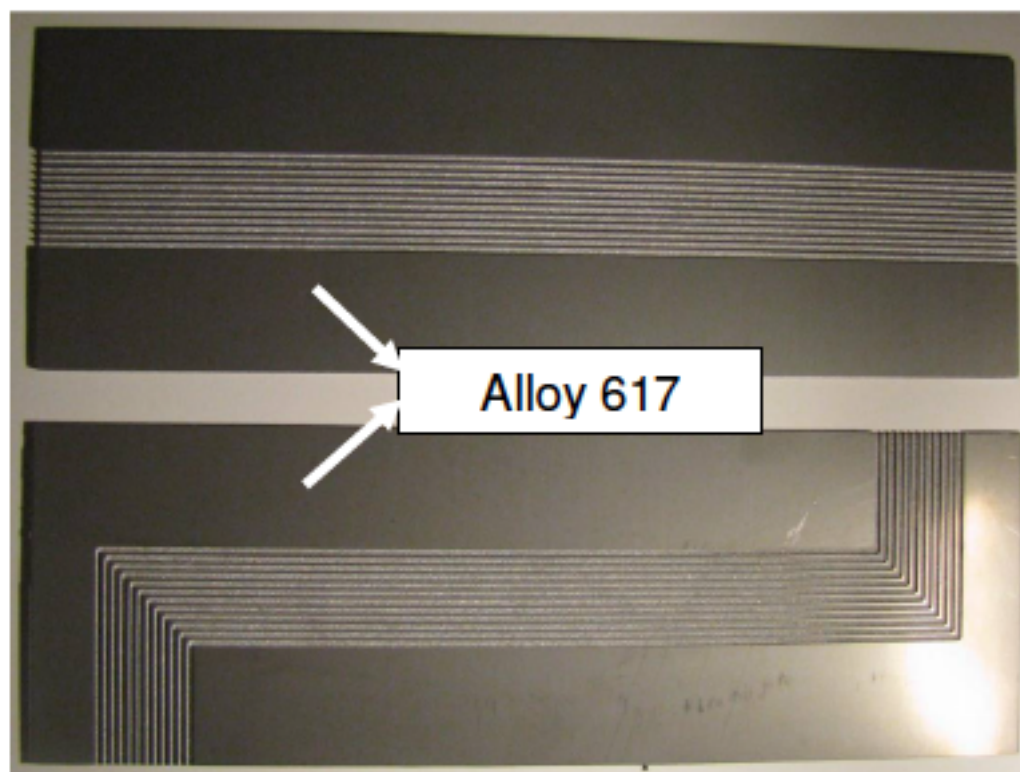
Figure 5.3. *Photoetched channels in Alloy 617 foils, after Mylavarapu [2008].*

diffusion bonded heat exchanger core   machined heat exchanger core

one of four headers   PCHE assembly with welded headers
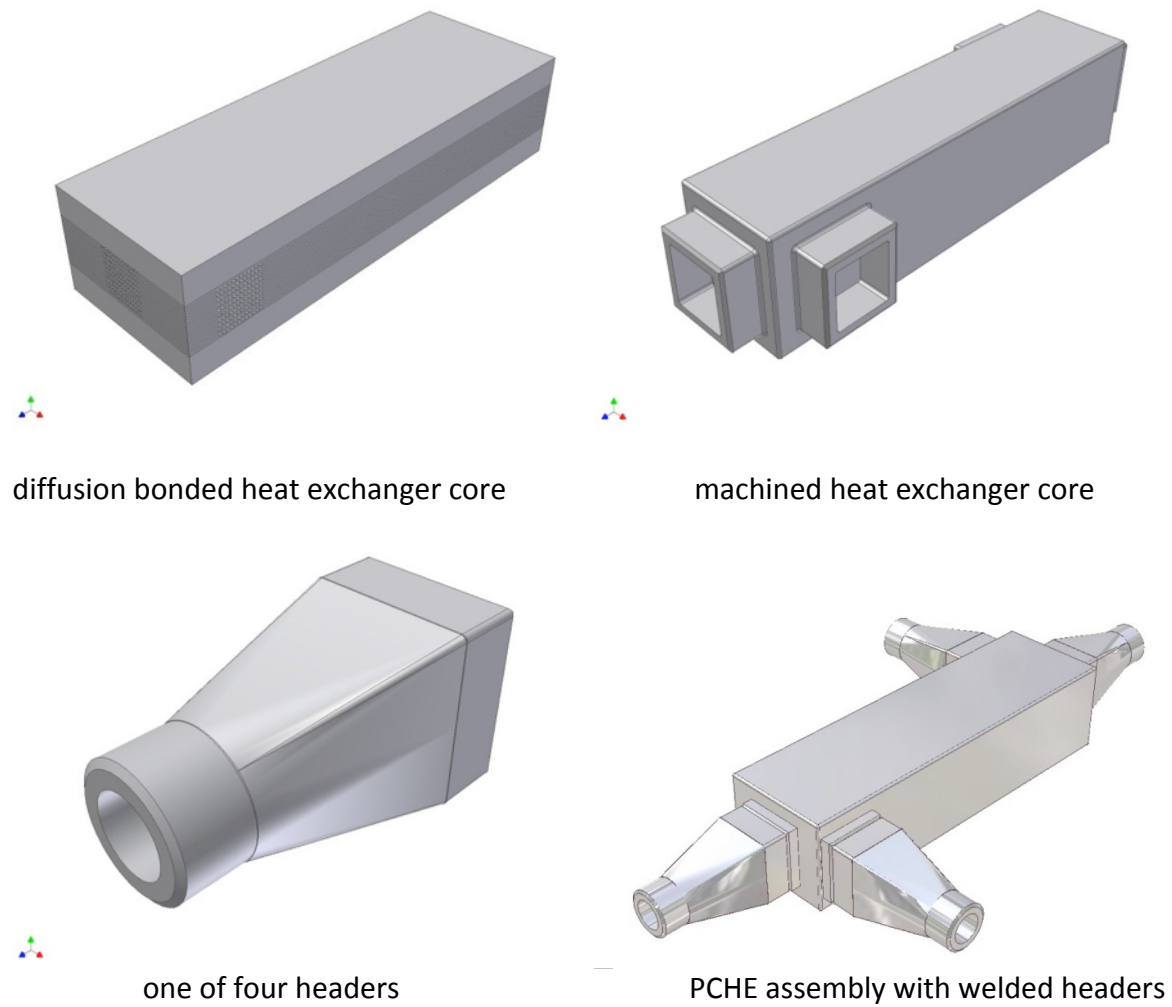
Figure 5.4. *Printed circuit heat exchanger, after Mylavarapu [2008].*
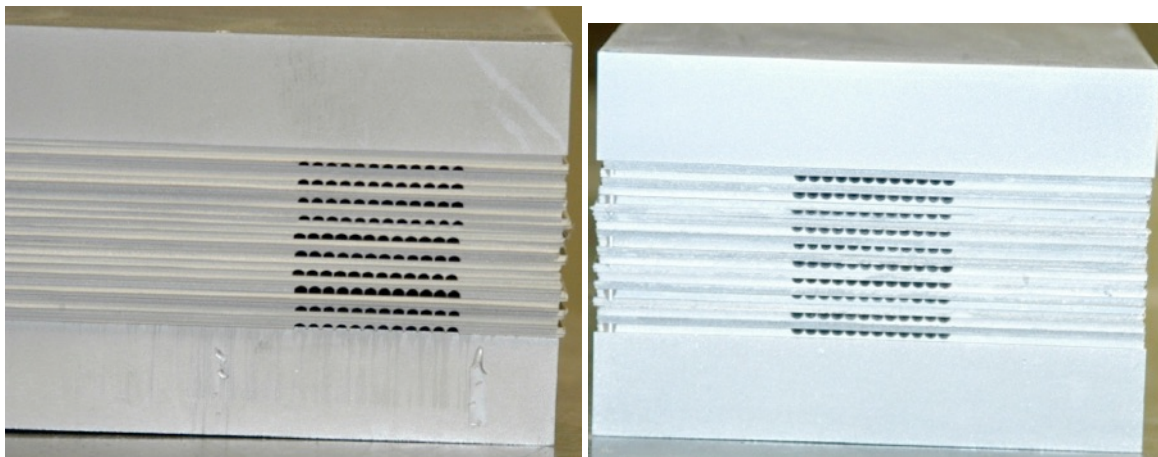
Figure 5.5. *Heat exchange channels in core side (left) and end (right), after Mylavarapu [2008].*

2.5.2 Condition Monitoring Plan

Before we had a concrete picture of the compact IHX geometry we planned to use ultrasonic interface waves to monitor the IHX condition. This plan was based on the compact IHX being comprised of etched foils diffusion bonded together. Generating interface waves along each diffusion bond would be challenging from a transduction standpoint. Based on Figure 5.4 there appears to be a much simpler solution, which is to put a piston-like normal beam transducer on the top surface and propagate a bulk wave through the thickness of the diffusion bonded IHX core. The majority of the ultrasonic wave energy will be transmitted across high quality diffusion bonds, with only a small portion of the energy being reflected. But poor quality or degraded bonds will reflect a much larger portion of the energy, reducing the energy transmitted across the bond.

The geometry of the PCHE assembly is quite amenable to depositing transducers on the top and bottom surfaces as shown in Figure 5.6. An array of transducers can be deposited to achieve full coverage of the PCHE.
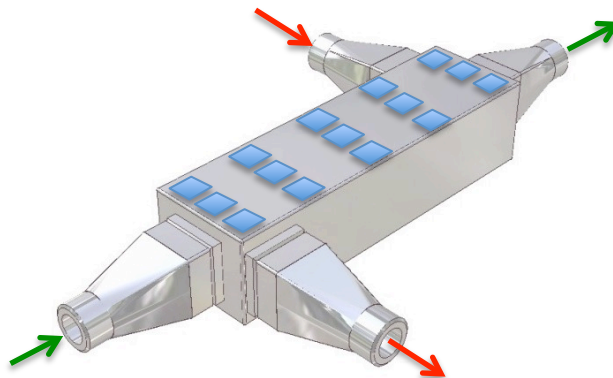
Figure 5.6. *Array of transducers deposited on the PCHE to monitor the condition of diffusion bonds and flow channels. PCHE after Mylavarapu [2008].*

2.5.3 Feasibility Study

To demonstrate the feasibility of the compact IHX condition monitoring plan a simple experiment was devised. The premise is that spray-on transducers using longitudinal waves and pulse-echo mode can detect poor quality diffusion bonds or degraded bonds by the reflections that they create. Good diffusion bonds will cause relatively little reflection, but poor quality or degraded bonds will create a significant reflection. Thus, a stack of 4" by 4" steel plates is used

as a surrogate PCHE. Echoes from interfaces in the stack represent poor diffusion bonds, while high quality diffusion bonds would not cause echoes.

Measurements are made on three different plate stacks:

A. One ¾" thick plate;

B. Two ¾" thick plates; and

C. Three plates – ¾" top, ¼" middle, ¾" bottom.

The plates are coupled together with ultrasonic gel and held together with two clamps. A bismuth titanate (BT) coating (5 sprays, each approximately 20 μm thick) was deposited on the top surface of the top ¾" thick plate. A 4x4 array of silver electrodes was painted onto the BT coating as shown in Figure 5.7 and used to pole the BT coating directly under the individual electrodes. The array of electrodes enables us to assess the condition of the diffusion bond over an area of reasonably large size, but here results are only provided for one electrode. A two cycle toneburst was sent by a Matec pulser/receiver. High pass and low pass filters were set to 1 and 5 MHz, respectively, after a frequency sweep revealed a sweet spot at 3.7 MHz, which was used to excite the BT transducer. The gain was set to 60 dB and 500 signal averages were used. A conventional piston-type transducer with central frequency of 2.25 MHz was used to benchmark the results for the BT transducer. Two sinusoidal cycles with a central frequency of 2.25 MHz were sent to the transducer using the same filters. However, the gain was set to 20 dB and 100 signal averages were used.
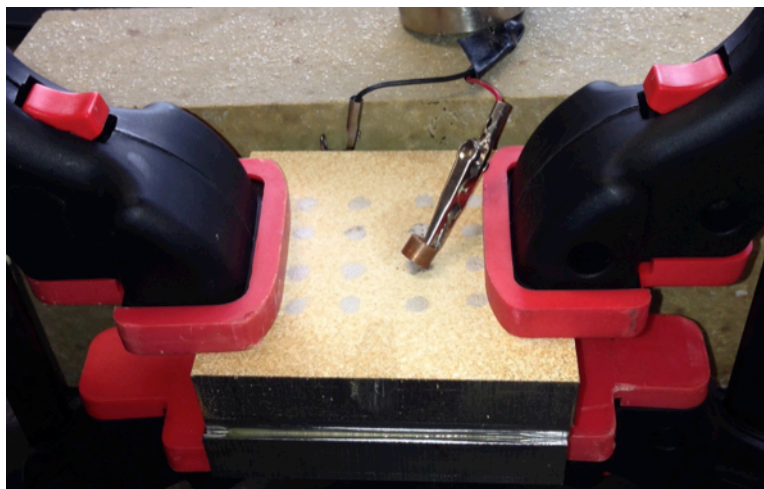
Figure 5.7. Steel plate stack with bismuth titanate coating deposited on top surface. A 4x4 array of electrodes enable interrogation of interfaces below.

The received signals (A-scans) for stack A (a single plate) are shown in Figure 5.8 for the spray deposited BT transducer and conventional UT transducer. The wave speed was measured to be 5.9 mm/µs, thus echoes should appear every 6.46 µs. For discussion purposes, lets define TOF = 6.46 µs. The BT transducer receives 10 echoes before they drop below the noise floor, which is shown in Figure 5.9. Thus, the signal should be able to propagate approximately 10*2*0.75" = 15". As expected the amplitudes of the echoes from the BT transducer are lower than those from the conventional transducer (Figure 5.8) because the piezoelectric coupling of bismuth titanate is much lower than that of PZT at room temperature. However, its Curie temperature is much higher so BT transducers can operate at much higher temperatures than PZT. Temperature capabilities are not demonstrated in this feasibility experiment.

Figure 5.8. *A-scan comparison for plate stack A (single plate): Left − spray-deposited BT transducer with 60 dB gain, Right − conventional transducer with 20 dB gain. X-axis is time in seconds and Y-axis is amplitude in arbitrary units.*
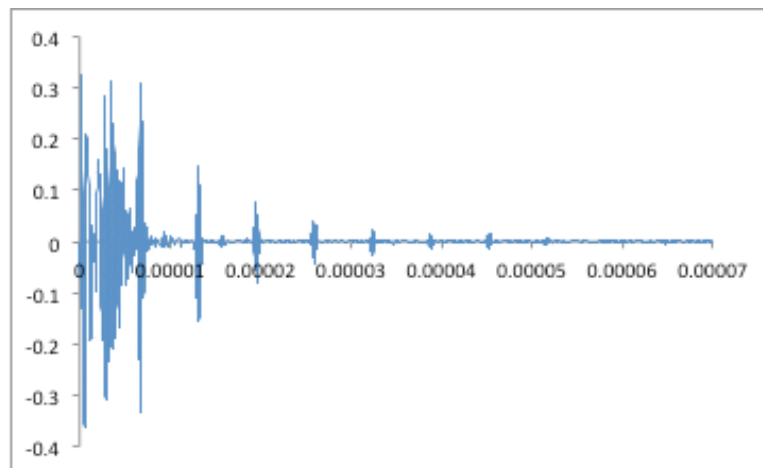
Figure 5.9. *A-scan for plate stack A − spray-deposited BT transducer with 60 dB gain, X-axis is time in seconds and Y-axis is amplitude in arbitrary units.*

The received signals (A-scans) for stack B (two plates) are shown in Figure 5.10 for the spray deposited BT transducer and conventional UT transducer. Because the two plates are the same thickness the echo patterns are similar to those for a single plate (Figure 5.8). In hindsight, it would have been more instructive to use two plates of different thicknesses in order to distinguish the interface reflection from the back wall echo. Therefore, an experiment on stack C was conducted.
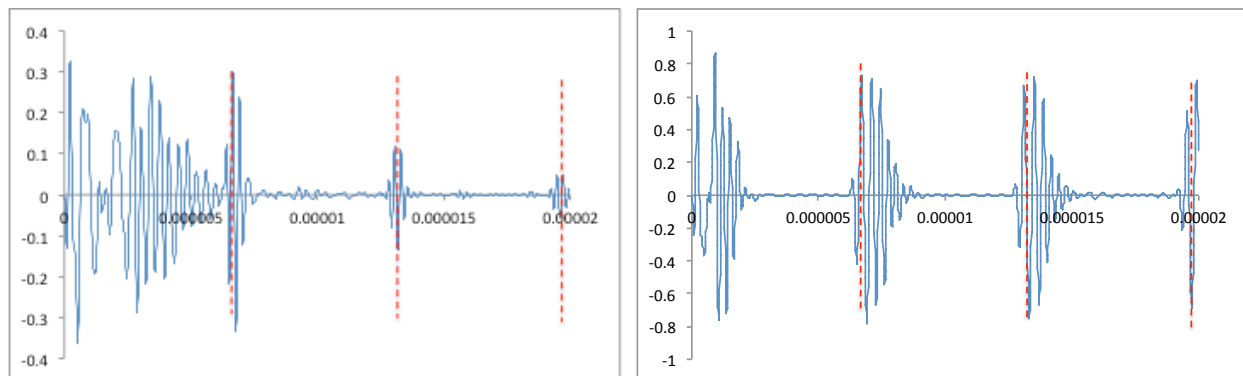
Figure 5.10. A-scan comparison for plate stack B (two plates): Left – spray-deposited BT transducer with 60 dB gain, Right – conventional transducer with 20 dB gain. X-axis is time in seconds and Y-axis is amplitude in arbitrary units.

The received signals (A-scans) for stack C (three plates) are shown in Figure 5.11 for the spray deposited BT transducer and conventional UT transducer. The thickness of the middle plate is one third that of the top and bottom plates, which generates echoes at intervals of TOF/3 = 2.15 μs after the occurrence of the echo from the first interface at TOF. The echoes at 7/3*TOF and 8/3*TOF are noticeably larger than at 4/3*TOF and 5/3*TOF due to the constructive interference of internal reflections (reverberations occur in each plate). This result suggests that it would be possible to detect multiple poor diffusion bonds at the same location by constructive interference. The key result of this feasibility experiment is that the echoes from internal interfaces, which represent poor diffusion bonds, are reasonably evident in Figure 5.11 for the BT transducers. Thus, it is reasonable to expect that BT transducers and this pulse-echo methodology could be developed to detect poor quality or damaged diffusion bonds in the proposed PCHE.

In closing, it is worth mentioning that it might also be possible to detect clogged cooling paths with this arrangement of spray-on transducers. Unclogged cooling paths will be filled with helium gas, while cooling paths containing corrosion products or impurities will have a much different acoustic impedance, which will result in significantly different wave scattering fields. Further analysis would need to be conducted based on the actual geometry of the PCHE, such as that given in Figures 5.4 and 5.5.
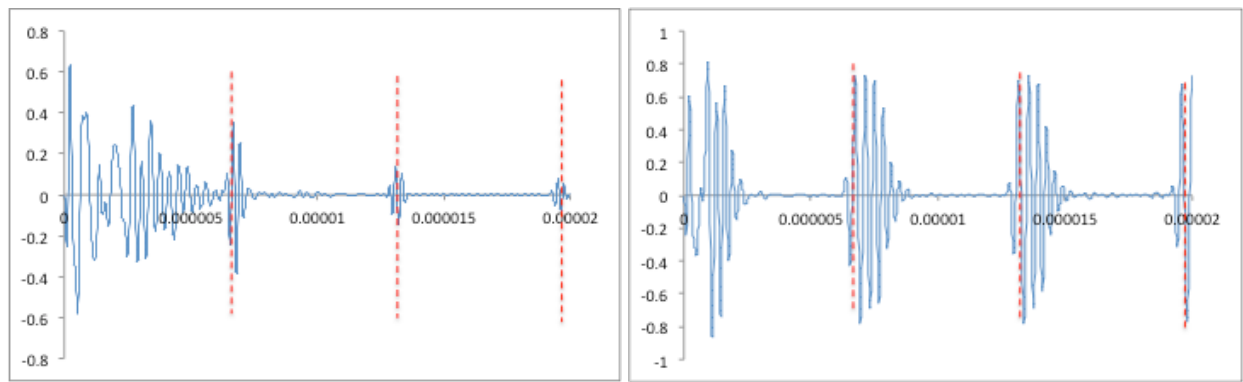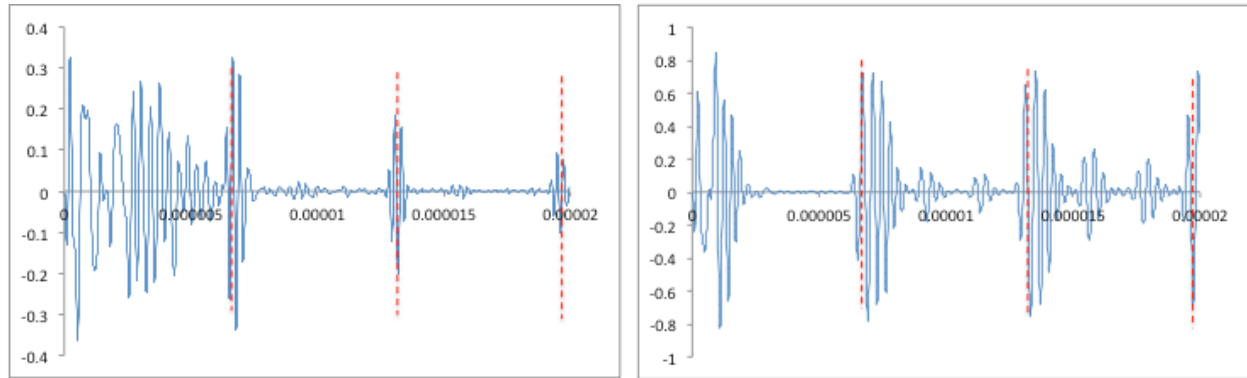
Figure 5.11. *A-scan comparison for plate stack C (three plates): Left – spray-deposited BT transducer with 60 dB gain, Right – conventional transducer with 20 dB gain. X-axis is time in seconds and Y-axis is amplitude in arbitrary units.*

2.5.4 References

Kazakov, N.F., 1985, Diffusion Bonding of Materials, Pergamon Press, New York (in English).

Mizia, R.E., 2008, Next generation nuclear plant intermediate heat exchanger acquisition strategy, INL/EXT-08-14054, Idaho National Laboratory, Idaho Falls, ID.

Mylavarapu, S.K., 2008, Development of compact heat exchangers for very high-temperature gas-cooled reactors, M.S. Thesis, Ohio State University, Columbus, OH.

2.6 Technology Gap Analysis

Safe and cost effective operation of current and future nuclear power plants is a national priority to meet the demands for sustainable electric power. Online monitoring of structural elements is critical for detecting damage and initiating an informed decision-making process regarding maintenance and operations. It is typical of macroscale damage to progress quite rapidly to failure, necessitating characterization of microstructure evolution that precedes macroscale damage in order to enable accurate useful life prediction at a smaller fraction of the life. In many cases the online monitoring must be done in high temperature service environments. The capabilities of ultrasonic transducers for high temperature service are discussed in this report. A critical technology gap exists relative to online condition monitoring (CM) of advanced nuclear plant components for damage accumulation; there are not capable

sensors and infrastructure available for the high temperature environment. This subsection reports on the current technology gap.

2.6.1 Need for Online Condition Monitoring

Looking forward, the nuclear energy industry has two general needs: (1) life extension of existing light water reactor plants and (2) maturation of the next generation nuclear power plant. The former is reliant upon online condition monitoring technologies because some of the relevant material degradation modes progress quite rapidly to failure once they have been initiated (e.g., stress corrosion cracking). Thus, inspections during planned outages are insufficient. In addition, new degradation modes having unknown growth rates are expected to be discovered as plant operations continue beyond 60 years. Since active components are closely monitored now and are replaceable, it is the passive components like reactor vessels and piping that are of the utmost concern, because their wholesale replacement is not economically feasible. There are numerous considerations involved with the paradigm shift from periodic inspections to online condition monitoring, which are discussed in the PNNL report by Meyer et al. [2011]. This subsection focuses on only two of these issues, both of which are equally applicable for life extension of existing plants and the next generation nuclear power plant. First, online condition monitoring must be conducted in harsh operating environments in terms of elevated temperature and in some cases radiation. Thus transducers that can operate reliably at elevated temperature for long durations are critical. Second, nondestructive methodologies sensitive to the earliest possible indicators of degradation are highly desirable to provide the earliest warning and allow time to schedule maintenance, which is greatly facilitated by remaining useful life prediction modeling (i.e., prognostics). Life predictions, from all types of models, are reliant upon an accurate description of the current state. The better the monitoring methodology can describe the entire hierarchy of damage progression from detection $\rightarrow$ location $\rightarrow$ classification $\rightarrow$ extent, the more accurate the life prediction.

While perfect materials would not be susceptible to damage, we know that in reality degradation is inevitable and maintenance needs to be planned accordingly. In summary, nondestructive methods that can be applied as online condition monitoring and are capable of fully describing the current damage state are sought. In addition, the online monitoring should be sensitive to the earliest indication of degradation. And on top of that, the online monitoring must be done at elevated temperature.

It appears that monitoring acoustic emissions is the only method currently certified for online monitoring in nuclear power plants. However, as this method is passive it is sometimes difficult to distinguish damage events from background operational noise. It is even harder to accurately characterize the damage, and sensitivity to precursors of damage is low at best.

2.6.2 Precursor Detection State of the Art

The PNNL report by Ramuhalli et al. [2012] assesses nondestructive characterization methods for precursors to degradation. The PNNL report by Meyer et al. [2011] discusses nonlinear acoustics, acousto-ultrasonics, magnetic Barkhausen emission, magnetic loop parameters, and other technologies to monitor precursors. In recent research supported by the Nuclear Energy University Programs (10-915 – Monitoring microstructural evolution of Alloy 617 with nonlinear acoustics for remaining useful life prediction; multiaxial creep-fatigue and creep-ratcheting), we investigated the use of nonlinear ultrasonic guided waves to nondestructively characterize microstructure evolution in Alloy 617 relative to service in an intermediate heat exchanger of a very high temperature reactor. This investigation, in and of itself, serves as a precursor to the NEUP sponsored project for which this report is being written (11-3046 – High temperature transducers for online monitoring of microstructure evolution). Because guided waves are multimodal the excitation frequency and transducer design are key considerations in a viable methodology. It is imperative to have a theory on which to base transducer design and excitation input parameters. Building on the important contributions of [Bermes et al., 2007; Deng, 1998 & 1999; de Lima and Hamilton, 2003 & 2005; Matlack et al., 2011; Matsuda and Biwa, 2011; Müller et al., 2010; Pruell et al., 2009; Srivastava and Lanza di Scalea, 2009 & 2010; Srivastava et al., 2010] we have progressed from nonlinear ultrasonic guided waves in plates to pipe applications [Chillara and Lissenden, 2012a, 2012b, 2013; Liu et al., 2013a, 2013b, 2013c] with theory, numerical simulations, and experiments. The remainder of this subsection focuses on ultrasonic transducers for high temperature applications.

2.6.3 High Temperature Ultrasonic Transducers

Ultrasonic transduction, i.e., conversion of an electric signal into a mechanical disturbance having a frequency higher than humans can hear (or vice versa), can be accomplished in a variety of ways such as piezoelectric materials, magnetostrictive materials, electromagnetic acoustic transducers, and lasers. Piezoelectric materials are the most commonly used, but their serviceable temperature range is limited by the Curie temperature, above which the piezoelectric coupling breaks down. Piezoelectric transducers for high temperature environments must have a high Curie temperature in addition to effective piezoelectric coupling. Also, an electric field must be applied to the piezoelectric material through lead wires and electrodes that are temperature resistant for transduction to occur, and the piezoelectric material must be effectively coupled to the substrate material to be interrogated. Conventional gels do not function at elevated temperature, and ceramic compounds can be difficult to work with and expensive. Direct coupling of a piezoelectric material to the substrate is an effective solution. One technique for direct deposition of a piezoceramic to a substrate is sol gel processing, which both eliminates the need for couplant and can be applied in the field.

The historical development of sol gel processing of spray-on ultrasonic transducers is reviewed in the Ph.D. thesis by Searfass [2012], with emphasis on the ferroelectric material bismuth titanate for service at elevated temperatures. Section 1.5 of the thesis is repeated here.

Bismuth titanate ($Bi_4Ti_3O_{12}$) is a ferroelectric material and is a member of the family of bismuth layer structure ferroelectrics (BLSF) and was first discovered by Aurivilius in 1949 [Aurivillius, 1949]. The BLSF family of materials is composed of bismuth oxide layers, $(Bi_2O_2)^{2+}$ interleaved in between layers of perovskite units which are infinite in two dimensions. Materials with an odd number of perovskite layers tend to have a single first order phase transition, whereas many with even number perovskite layers show two phase transitions with the high temperature transition considered to be the Curie point [Newnham et al., 1971]. Chemically, this family of materials can be represented by $Bi_2M_{n-1}R_nO_{3n+3}$, where n =1, 2, 3, 4, 5, and n represents the number of perovskite groups separated by the bismuth oxide layer. Following the typical convention used to describe ABO_3 perovskites, the A site can accept Bi, Ba, Sr, K, Ca, Na, and Pb ions and the B site can accept T, Nb, Ta, Fe, W, Mo, Gr, and Cr ions. There exist over 70 compounds of these groups, 50 of which are known to be ferroelectric, and another 50 more may exist [Newnham et al., 1971; Subbarao, 1962]. Recently, industrial interest in high temperature piezoelectrics has generated a renewed interest in members of the BLSF family since many of the bismuth based members of this group have high Curie points. Several materials are compared in Table V. The high Curie temperatures and modest piezoelectricity make this family of materials appealing for high temperature ultrasonic nondestructive evaluation (UNDE). However, their low resistivity, often combined with high coercive fields, coupled with a large T_c, can make them difficult to pole.

Table V. Comparison of some members of the bismuth layer structure family.

Material	T_c (°C)	Resitivity ($\Omega \cdot m$)	d_{33}	Source
$Bi_4Ti_3O_{12}$*	675	10^9	25	[Seth and Schulze, 1989]
$Na_{0.5}Bi_{4.5}Ti_4O_{15}$	660	10^{12}	~17	[Takenaka and Sakata, 1984]
Bi_3TiNbO_9	~920	10^{12}	5	[Moure et al., 2001]
$CaBi_4Ti_4NbO_{15}$	790	10^{11}	8	[Shulman, 1997]

Of the BLSF family, bismuth titanate is the most well-researched material. Bismuth titanate has 3 perovskite units (A=Bi, B=Ti) between the bismuth oxide layers. Since there are an odd number of perovskite units, bismuth titanate has only one phase transition at its Curie point at 685 °C. There have been some reports of dielectric anomalies in single

crystal and ceramic samples at temperatures below the Curie point, that have been attributed to several mechanisms including a phase transition. However, more recent research of the material seems to indicate that observed peaks are due to space charge or ion jump mechanisms and not a phase transition [Ehara et al., 1981; Ehara et al., 1986; Seth and Schulze, 1989; Shulman et al., 1996; Shulman, 1997). In grain oriented ceramics, d_{33} values as high as 26 pC/N have been reported (with pulse poling) [Seth and Schulze, 1989].

One of the primary issues with bismuth titanate is that it has a large coercive field (~100 kV/cm) combined with high conductivity [Cumins and Cross, 1968]. Originally, there was a discrepancy in the electronic nature of bismuth titanate, but Shulman et al. [1996] showed bismuth titanate is electronic p-type. Through donor doping with Nb, it was demonstrated that the conductivity can be decreased by as much as three orders of magnitude. By decreasing the conductivity, larger field strengths could be used during poling and the value of d_{33} was increased from 3.5 pC/N to 20 pC/N. There are a few bismuth titanate based piezoelectrics available commercially, such as Piezo Technologies K-12 and K-15 products, which are reported to have a T_c of 820 ^{o}C and 600 ^{o}C, respectively [Custom Piezoelectrics, 2010]. It has also been shown that bismuth titanate is capable of operating as an ultrasonic transducer in pulse-echo mode up to 670 ^{o}C, at least for short time periods and has also been shown that it can be used as an ultrasonic drill at 500 ^{o}C [Searfass et al., 2010a and 2010b; Bao et al., 2010].

Fabrication of bismuth titanate is well established in both bulk and thin film form. In mixed oxide methods a solid-state reaction between oxide powders occurs. This method is frequently used to make ceramics since it is inexpensive and reproducible. For bismuth titanate, mixed oxide precursors are Bi_2O_3 and TiO_2. Sol gel routes have also been formulated. A typical route for sol gel processing involves dissolving bismuth nitrate pentahydrate ($Bi(NO_3)_3 \cdot 5H_2O$) in acetic acid. Titanium isopropoxide is then added to the solution followed by addition of water [Fuierer and Li, 2002]. Bismuth titanate has also been fabricated by various other techniques such as co-precipitation, molten salt synthesis for bulk materials, and there are also PVD and CVD techniques for thin film deposition. A good review of all these techniques has been presented by Lazarevic et al. [2005].

A rather novel approach for developing high temperature ultrasonic transducers was developed by Kobayashi et al. [2000]. In this approach, a sol gel based method is used to spray piezoelectric transducers, via an air gun, onto metallic substrates. This is particularly advantageous for high temperature UNDE since it can potentially eliminate the difficulties of finding a means of coupling and making contact with structures at elevated

temperatures. There is also potential for in-field deposition with this technique. This technique was adapted from the work of Barrow et al. [1995, 1997] for making PZT 0-3 ceramic/ceramic composites. In this method, 0-3 composites are made by adding ceramic powders to sol gel solution and the films can be prepared via spin or spray coating, dipping, or screen printing. Sol gel films adhere well to oxide surfaces of the substrate as well as to those found on the crystallites dispersed in the solution, thus strong bonds form between sol gel, the powders and the substrate. A good analogy given is that "the sol gel makes up the mortar and the ceramic particles make up the bricks in a wall" [Barrow et al., 1995]. This method has the advantages of sol gel fabrication such as cost effectiveness and ease of fabrication, but now thicker films can be achieved due to the addition of the ceramic powders. In many applications, such as wireless surface acoustic wave devices, the thickness of thin films is enough. However, for typical industrial UNDE (i.e., non-medical) where frequencies of 500 kHz-20 MHz are commonly desired, standard sol gel deposition is not adequate as thick enough films are not easily achieved.

In the work by Barrow's group, films were made by spin coating. This technique was later adapted by the same group to spin coat several types of diphasic composite piezoelectrics. The first was a lithium niobate/lithium niobate composite, where lithium niobate powders were dispersed into a lithium niobate sol gel solution which was spin coated onto stainless steel substrates. The objective here was being able to fabricate high temperature ultrasonic transducers [Zou et al., 1997]. These transducers' thicknesses were 170 μm and had center frequencies around 10 MHz. Later, $LiTaO_3$-PZT composites were fabricated by dispersing $LiTaO_3$ powders into a PZT sol gel solution followed by spin coating onto stainless steel substrates. The objective of this work was once again to be able to obtain a high temperature ultrasonic transducer [Chen et al., 1999]. These films were 56 μm thick with center frequencies of 12 MHz. This transducer showed reasonable piezoelectric strength, with a k_t that was determined to be 0.17. The parameters were determined by curve fitting the impedance spectrum using a method developed by Lukacs et al. [1999]. Since these materials are on a substrate, the guidelines laid out by the IEEE standards for determining piezoelectric properties cannot be used due to the mechanical boundary conditions imposed by the substrate. It was determined that the maximum operating temperature of the fabricated $LiTaO_3$-PZT composites was 368 °C. No x-ray diffraction patterns were reported, so the desired phases were assumed to have formed.

The first spray-on transducers fabricated were composed of $LiTaO_3$/PZT and PZT/Al_2O_3 composites [Kobayashi et al., 2000]. These composites were fabricated with PZT and $LiTaO_3$ powders dispersed in Al_2O_3 and PZT sol gels, respectively, and were deposited onto stainless steel and aluminum substrates by using a spray gun similar to what one might

find in an arts and crafts store. Fabricated transducers had center frequencies between 4 and 15 MHz. Here, the high temperature LiTaO$_3$/PZT transducers were capable of operating to temperatures of 250 ^{o}C. It is difficult to tell the efficiency of these transducers since characterization of the piezoelectric properties was not performed and ultrasonic signal strengths were reported in arbitrary amplitudes. Again, no x-ray diffraction data were given, so phase formation must have been assumed or not reported. It should also be noted that the composites are reported with a connectivity of (0-3), however, due to deposition process, the films are inherently quite porous. Thus, it is likely that the pores introduce a third inactive phase into the composite and, following the convention laid out by Pilgrim et al., 1987], the connectivity of the material is likely to be more accurately classified with a connectivity of {3(0-3)-0}.

This spray-on technique was then utilized to deposit bismuth titanate/PZT composites and bismuth titanate/bismuth titanate composite transducers for high temperature applications [Kobayashi and Jen, 2004; Kobayashi et al., 2004]. The bismuth titanate/PZT samples were fabricated by dispersing bismuth titanate powders into a PZT sol gel with a volume ratio of powder to solution being about 3:1. These transducers were deposited onto flat and curved stainless steel substrates and corona poling was used to pole the samples. X-ray diffraction was performed on the samples and only the bismuth titanate phase was detected and the authors speculate as to whether the PZT was able to crystallize at the annealing temperature of 650 ^{o}C. For the samples deposited onto planar substrates, films were 200 µm thick with center frequencies of 4 MHz. These transducers were able to operate up to 440 ^{o}C with only a 2 dB loss in signal strength. In a later study it was shown that these transducers are not suitable for temperatures above 450 ^{o}C [Kobayashi et al., 2007a]. The bismuth titanate/bismuth titanate transducers were fabricated by dispersing bismuth titanate powders into a sol gel of bismuth titanate. The bismuth titanate slurry was then sprayed onto flat and curved steel substrates. Deposited films were 40 µm thick and had center frequencies of 10 MHz. The transducers ultrasonic wave velocity was determined to be 2.2 mm/µs. This is half the wave velocity of bulk bismuth titanate and this difference in wave velocities is attributed to the porosity in the films. The transducers were capable of operation to 200 ^{o}C. It was reported that the bismuth titanate/bismuth titanate composites were about 20 dB weaker than the bismuth titanate/PZT transducers. However, the substrates between the two papers through which the comparisons were claimed to have been made were of different thicknesses and the operating frequencies at which the transducers operated at were also different. This of course will skew the comparison between the two materials' performance as ultrasonic transducers since the operating frequency and distance the ultrasonic signal traveled will greatly affect the detected signal amplitude (unless of course identical substrates and center frequencies are used, but this was not conveyed to

be the case). Furthermore, for both the bismuth titanate/bismuth titanate and bismuth titanate/PZT transducers characterization of the piezoelectric properties was not performed (which is not a trivial procedure, especially for low *k*, highly damped materials). The ultrasonic signals were also reported with arbitrary units so no real conclusion can be made about the strength of the transducers nor can any real comparison be made between the two different materials. All that can be concluded is that the transducers are, to some degree, functional, given some unknown excitation source. Of course, one could argue that a trained ultrasonic technician could guess at the signal amplitude by judging the number of backwall echos seen in the reported wave trains; however this is by no means a way to make a good quantitative comparison. Additionally, the fabrication process described is rather vague, in particular, the firing and annealing times and environments in which they are performed are not reported, although this is most likely for proprietary reasons. Nonetheless, transducers fabricated in this manner have been used successfully in industrial applications such as polymer injection molding [Kobayashi et al., 2006].

More piezoelectric composites were later reported using the same technique. These include manganese sodium doped bismuth titanate (NBT+Mn)/PZT and lithium niobate/PZT [Kobayashi et al., 2007b]. It was determined that NBT+Mn/PZT composites were not suitable for temperatures above 450 ^{o}C while the lithium niobate/PZT transducers showed good stability to 700 ^{o}C. Again, no x-ray diffraction studies were performed so the phases formed during fabrication are assumed as reported and all measured signals were provided in arbitrary units. Despite the arbitrary quantitative results, it seems that this method of fabricating ultrasonic transducers by mixing and matching multiple materials for specific applications is possible and is worthy of further investigation.

Utilization of a spray-on deposition technique of ferroelectric bismuth titanate ($Bi_4Ti_3O_{12}$) was investigated by Searfass [2012]. Since initial results with conventional sintering methods were unsuccessful, microwave sintering was pursued and is capable of producing films with superior quality. Industrial partners showed strong interest for on-site deposition transducers. However, with on-site deposition, microwave sintering may not be a viable option. As a result, a crude, but very successful, method of sintering with a blow torch was developed and transducers fabricated in this fashion showed equivalent electromechanical strength.

Moreover, the entire temperature range which bismuth titanate fabricated with the spray-on technique had yet to be explored. In this work it was shown that spray-deposited bismuth titanate transducers are capable of generating ultrasonic signals with strengths equivalent to room temperature signals up to 650 ^{o}C for short periods of time. Above this temperature,

thermal depoling of the sample occurs rapidly as temperature increases and signal strength diminishes. Furthermore, little has been done to date to characterize material properties of bismuth titanate films deposited with the spray-on technique. Initial results indicated that higher electromechanical coupling could be achieved with films deposited in this fashion when compared to their bulk counterparts due to the fact that larger field strengths can be employed during poling without breakdown. Typically, the electromechanical properties of substrate supported films are determined via curve fitting methods since the standards outlined by the Institute of Electrical and Electronic Engineers are not valid for the boundary conditions inherent to substrate supported films. However, as it is demonstrated in this work with the Mason model, due to the loading on the transducer from the substrate and the porosity of the films, these techniques cannot be employed as no electromechanical resonance is observed in the impedance spectrum of the transducer. Values for the d_{33} of the films were approximated by using a commercial d_{33} meter and suggested d_{33} values within the range of 13-16 pC/N are being achieved. Extrapolation of field strengths applied to the films fabricated herein during poling to numbers reported for bulk bismuth titanate imply that these values for the d_{33} are fairly accurate. Conductivity measurements were made of the bismuth titanate films and were found to be equivalent to bulk bismuth titanate, thus eliminating lower conductivity as a possible reason as to why larger field strengths are attainable. It is well known that if thermal breakdown is the mechanism responsible for breakdown within a material, larger field strengths can be achieved in samples as thickness decreases due to the fact that localized heating can be dissipated more quickly in thinner materials. Therefore, thermal breakdown is posited here as the breakdown mechanism in bismuth titanate and it has been calculated that breakdown strength of the material increases inversely proportional roughly to the cube root of the thickness of the samples.

Ultrasonic techniques have been widely applied for non-destructive evaluation (NDE) of material properties and structural integrity [Schulz, et al., 2003]. The ability to apply typical ultrasonic techniques in high temperature environments is desired for the monitoring of process variables, such as viscosity of melts and the evaluation of structural/material integrity in harsh environments, e.g., turbine blades, combustion engines and nuclear reactors [Alig, et al., 2010; Holbert, et al., 2005; Scruby and Wadley, 1982; Takeda et al., 1997].

High temperature piezoelectric materials have been surveyed previously. For example, the commercial piezoelectric material PZT possesses a Curie temperature of about 350°C but has a maximum recommended operation temperature of 150-250° C [Kažys, et al., 2008; Zhang and Yu, 2011]. As a result, buffer rods/ultrasonic guided waves have been utilized to keep the piezoelectric materials out of the high temperature region for extended periods of time [Frederic, 2011; Hara et al., 2005]. However, the limitations of a guided wave system include, depending on the required waveguide geometry the following limitations:

- Dispersion characteristics limiting bandwidth

- Sensor aperture size

- Cumulative attenuation losses over the waveguide propagation length

- Losses due to material discontinuities along the ultrasonic propagation path.

The limitations imposed by this methodology have been one of many driving forces that are leading to the development of new piezoelectric materials with operational temperatures exceeding 350 ^{o}C. The relatively new high temperature capable materials include high Curie temperature ferroelectric materials and non-ferroelectric single crystals. Additionally, depending on the intended operating frequency, electrical resistivity becomes problematic for high temperatures and low frequency operation conditions [Turner et al., 1994; Zhang and Yu, 2011].

Previous reports have shown numerous piezoelectric materials to be capable of operating as ultrasonic transducers up to 1000 ^{o}C. However, the longevity of these materials under such conditions has been questioned. The group III-V material Aluminum Nitride (AlN) belongs to the Wurtzite structure and point group 6mm and is not ferroelectric. No phase transitions exist aside from the melting point at 2800 ^{o}C and the resistivity of high quality crystalline samples is on the order of 10 MΩ cm at 200 ^{o}C [Berger, 1997; Bickermann et al., 2004]. The dielectric constant has been measured at 8.5 and the piezoelectric strain constant has been estimated from thin films to be roughly 5 pC/N [Bu et al., 2006; Lueng et al, 2000]. Oriented thin films of AlN have been utilized for high temperature transducers up to 1000 °C with satisfactory results on at least two separate occasions and in a high nuclear radiation environment [Kazys et al., 2005; Patel and Nicholson, 1990; Stubbs and Dutton, 2005]. Bulk single crystal materials have received less attention because of the difficulty of growing high quality single crystal wafers; nonetheless bulk single crystal AlN has been used for ultrasonic transducers up to 1000 ^{o}C and in an operating nuclear reactor core [Parks et al., 2010; Parks and Tittmann, 2011]. However, AlN bulk single crystal material shows a very wide range of crystal quality, with electrical resistivity being strongly correlated with a crystal's ability to operate as a pulse echo transducer at elevated temperatures. The AlN sample reported in this work was selected from a collection based on its measured resistivity in excess of 10 MΩ at 400° C and measured coupling coefficient of 0.2.

Lithium niobate has also been extensively studied for high temperature transducer applications and is a ferroelectric material with a Curie temperature in excess of 1000 °C depending on the stoichiometry [Wong, 2002]. Lithium niobate displays the 3m crystal symmetry with the corundum structure [Zhang and Yu, 2011]. The 36° rotated Y- cut is quite sensitive in the

longitudinal mode of vibration with a coupling coefficient of 0.48. However, lithium niobate is known to lose oxygen at elevated temperatures, particularly at low oxygen partial pressure [Jorgensen, and Bartlett, 1969; Schulz, et al., 2003]. Given that hermetic packaging is commonly employed in high temperature electronics this may be particularly problematic. Further, lithium niobate has been shown to decompose at 600 °C even in oxygen at atmospheric pressure [Svaasand et al., 1974]. However, the oxygen loss is an activated process and as such is not likely to have a discernible effect for short periods of time as shown, for example by Svaasand, who treated his samples for 170 hours before observing their decomposition [Svaasand et al., 1974].

Oxyborate crystals with general formula $ReCa_4O(BO_3)_3$ (Re = rare earth element, abbreviated as ReCOB) have been extensively studied for nonlinear optic applications, such as second and third harmonic generation [Zhang et al., 1999]. The crystals can be readily grown from the melt using the Czochralski (CZ) pulling or Bridgman technique at around 1500°C. Analogous to AlN crystals, no phase transitions occur prior to their melting points, being on the order of 1400-1500 °C, thus expanding the potential temperature usage range. Recently, oxyborate crystals have attracted attention for piezoelectric applications, due to their ultrahigh electrical resistivity at elevated temperatures. For example, $YCa_4O(BO_3)_3$ (YCOB) possesses a resistivity of 2×10^8 Ωcm at 800 °C [Zhang et al., 2008a]. The dielectric permittivity, piezoelectric strain coefficient, and electromechanical coupling factor of the (XYlw -15° /45°) cut were found to be on the order of 11, 6.5 pC/N, and 12.5%, respectively, with little variation in the range of room temperature to 950° C [Zhang et al., 2008b].

The three above mentioned high temperature piezoelectric single crystals were studied for use in ultrasonic transducers and their behavior was studied under exposure to high temperatures [Parks et al., 2013]. $LiNbO_3$, AlN and a new material $YCa_4O(BO_3)_3$ were studied for use in ultrasonic transducers under continuous operation for 55 hours at 550 °C. Additionally, "thermal ratcheting" tests were performed on the transducers by subjecting the crystals to heat treatments followed by ultrasonic performance testing at room temperature and 500 °C, respectively. The changes due to the heat treatments where less than the statistical spread obtained in repeated experiments and thus considered negligible. Finally, in-situ measurements up to 950 °C, of the pulse echo response of $YCa_4O(BO_3)_3$ were performed for the first time, showing stable characteristics up to these high temperature.

At atmospheric oxygen partial pressures, 48 hours of exposure to 950 °C or 24 hours exposure to 1000 °C had no significant effect on the efficiency of ultrasonic transduction of $LiNbO_3$, $YCa_4O(BO_3)_3$ and AlN. But longer-term operation of $LiNbO_3$ was limited to about 500 °C due to the oxygen loss and the presence of ionic conductivity, especially at low oxygen partial

pressure, such as that encountered in high temperature hermetic packaging, whereas $YCa_4O(BO_3)_3$ and AlN showed no deleterious effects.

The oxidation of AlN, known to occur at these temperatures, had no significant effect on the ultrasonic transduction efficiency, but the difficulty to achieve high quality AlN single crystals limit their applications greatly. YCOB was found to be capable of efficient ultrasonic transduction to about 1000 °C.

2.6.4 Remaining Challenges for Materials Investigated

In the current project sol-gel spray-on PZT/BT (lead zirconate titanate/bismuth titanate) and BT/LN (bismuth titanate/lithium niobate) were investigated for temperatures ranging up to 400 °C and 950 °C respectively. The deposition and consolidation processes, which were described in detail in subsection 2.1, result is a porous microstructure. Thus, the deposition method of the top electrode can make a large difference in the functionality of the transducer. Sputtered platinum electrodes work well but require a vacuum chamber. Painted electrodes of various metals were found to not function after a short exposure to elevated temperature because there is an undesirable chemical reaction with the transducer material that nullifies the piezoelectric behavior. In order to have transducers applied in the field, which is highly desirable for condition monitoring, an application methodology for the electrodes other than sputtering is required. One solution is to work out the chemistry of the electrode so that it is temperature resistant and does not react with the piezoceramic. Another possible solution is cold spray deposition of the electrode onto the piezoceramic. This unidirectional deposition process could seal the surface porosity as does sputter deposition. However, it is unknown whether the piezoceramic coating, which is generally fragile, will be able to endure the high velocity impacts of powder particles during cold spraying.

Another challenge is associated with the patterning of electrodes in order to control the activation of ultrasonic guided waves in pipes. Multi-element transducers are able to preferentially activate a guided wave mode based on matching the element spacing to the wavelength of the preferred mode. A good process for applying these transducers is: air-spray the piezoelectric coating, consolidate it, apply the electrode material, and then pattern the electrodes using laser ablation to remove unwanted material (resulting in a linear array of ring electrodes), connect lead wires, and then pole. Again, the details of this process were described in subsection 2.1. The laser used to ablate patterns in the electrodes can create sub-millimeter sized features, but is not field deployable. Thus, another tool to place thin ring electrodes onto a wrap-around transducer on a pipe in the field is necessary.

We are confident that both of these challenges can be met in future research.

2.6.5 Technology Gap References

Alig, I., Steinhoff, B., and Lellinger, D., 2010, "Monitoring of polymer melt processing," *Meas. Sci. Technol.* 21:062001 (19pp).

Aurivillius, B. 1949, "Mixed bismuth oxides with layer lattices, II. $Bi_4Ti_3O_{12}$," *Arki. Kemi*, 1:499-512.

Bao, X., Scott, J., Boudreu, K., Bar-Cohen, Y., Sherrit, S., Badescu, M., Shout, T, Zhang, S., 2010, "Ultrasonic/sonic drill for high temperature applications," *Sensors and Smart Technologies for Civil, Mechanical, and Aerospace Systems*, SPIE Proceedings.

Barrow, D.A., Petroff, T.E., Sayer, M., 1995, "Thick ceramic coatings using a sol gel based ceramic-ceramic 0-3 composite," *Surf. Coat. Technol.* 76-77:113-118.

Barrow, D.A., Petroff, T.E., Tandon, R.P., Sayer, M., 1997, "Characterization of thick lead zirconate titanate films fabricated using a new sol gel based process," *J. Appl. Phys.* 81(2): 876-881.

Berger, L, 1997, *Semiconductor Materials*. CRC Press.

Bermes, C., Kim, J.Y., Qu, J., Jacobs, L.J., 2007, "Experimental characterization of material nonlinearity using Lamb waves," *Appl. Phys. Lett.* 90:021901.

Bickermann, M., Epelbaum, B.M., and Winnacker, A., 2004, "Characterization of bulk AlN with low oxygen content," *Journal of Crystal Growth*, 269:432-442.

Bu, G., Ciplys, D., Shur, M., Schowalter, L.J., Schulman, S., and Gaska, R., 2006, "Surface acoustic wave velocity in single-crystal AlN substrates," *IEEE Trans. Ultra., Ferro., Frequency Control* 53(1):251-254.

Chen, Y., Sayer, M., Zou, L., Jen, C.K. 1999, "Lithium tantalate/lead zirconate titanate composite ultrasonic transducers," *Appl. Phys. Lett.*, 74:2552-2554.

Chillara, V.K., Lissenden, C.J., 2012a, "Interaction of guided wave modes in isotropic nonlinear elastic plates: higher harmonic generation," *J. Appl. Phys.*, Vol. 111(12) 124909 (7 pages).

Chillara, V.K., Lissenden, C.J., 2012b, "Analysis of second harmonic guided waves in pipes using a large radius asymptotic approximation for axis-symmetric longitudinal modes," *Ultrasonics*. DOI: 10.1016/j.ultras.2012.12.007.

Chillara, V.K., Lissenden, C.J., 2013, "Higher harmonic guided waves in isotropic weakly non-linear elastic plates," In: *Review of Progress in Quantitative Nondestructive Evaluation* 31 (D.O. Thompson and D.E. Chimenti, Ed.) in-press.

Cummins, S.E., Cross, L.E., 1968, "Electrical and optical properties of ferroelectric Bi4Ti3O12 single crystals," *J. Appl. Phys*. 39(5):2268-2274.

Custom Piezoelectrics*,* 2010, http://www.piezotechnologies.com/piezoelectrics.htm#bismuth-titanate (accessed 11/11/2011).

de Lima, W.J.N., Hamilton, M.F., 2003, "Finite-amplitude waves in isotropic elastic plates*," J. Sound Vib.* 265:819-839.

de Lima, W.J.N., Hamilton, M.F., 2005, "Finite-amplitude waves in isotropic elastic waveguides with arbitrary constant cross-sectional area," *Wave Motion* 41:1-11.

Deng, M., 1998, "Cumulative second-harmonic generation accompanying nonlinear shear horizontal mode propagation in a solid plate," *J. Appl. Phys.* 84:3500-3505.

Deng, M., 1999, "Cumulative second-harmonic generation of Lamb-mode propagation in a solid plate," *J. Appl. Phys.* 85:3051-3058.

Ehara, S., Muramatsu, K., Shimazu, M., Tanaka, J., Tsukioka, M., Mori, Y., Hattori, T., Tamura, H., 1981, "Dielectric properties of Bi4Ti3O12 below the Curie temperature," *Jap. J. of Appl. Phys.*, 20:877-881.

Ehara, S., Hattori, T., Tanaka, J., Tsukioka, M., Muramatsu, K., Shimazu, M., 1986, "Raman spectroscopy and dielectric anomaly in Bi4Ti3O12," *Jap. J. Appl. Phys.*, 25:1749-1750.

Frederic, B., 2011, "Monitoring using dry-coupled ultrasonic waveguide transducers," *IEEE Trans. Ultra., Ferro., Frequency Control*, 58(1):156-167.

Fuierer, P., Li, B., 2002, "Nonepitaxial orientation in sol-gel bismuth titanate films," *J. Am. Ceram. Soc.* 85:299-304.

Hara, I.I., Urhan, D.B., and Eda, Y.S., 2005, "In situ monitoring of solid-liquid interface of aluminum alloy using high-temperature ultrasonic sensor tapered clad Ti buffer rod," *Japanese Journal of Applied Physics*, 44(6):4370-4373.

Holbert, K.E., Sankaranarayanan, S., and McCready, S.S., 2005, "Response of lead metaniobate acoustic emission sensors to gamma irradiation," *IEEE Trans. Nuc. Sci*. 52(6):2583-2590.

Jorgensen, P.J., Bartlett, R.W., 1969, "High temperature transport processes in lithium niobate," *J. Phys. Chem. Solids*, 30:2639-2648.

Kažys, R., Voleišis, A., and Voleišienė, B., 2008, "High temperature ultrasonic transducers: review," *Ultrasound*, 63(2):7-17.

Kazys, R., Voleisis, A., Sliteris, R., Mazeika, L., Van Nieuwenhaove, R., Kupschus, P., Abderrahim, H.A., 2005, "High Temperature Ultrasonic Transducers for Imaging and Measurements in a Liquid Pb/Bi Eutectic Alloy," *IEEE Trans. Ultra., Ferro., Frequency Control* 52(4):525-537.

Kobayashi, M., Olding, T.R., Zou, L., Sayer, M., Jen, C.K., Rehmen, A.U., 2000, "Piezoelectric thick film ultrasonic transducers fabricated by a spray technique," 2000 *IEEE Ultrasonics Symp. Proc.*, 985-989.

Kobayashi, M., Jen, C.-K., 2004, "Piezoelectric thick bismuth titanate/lead zirconate titanate composite film transducers for smart NDE of metals." *Smart Mat. Struct.* 13(4):951-956.

Kobayashi, M., Ono, Y., Jen, C.K., Cheng, C.C., 2006, "High-temperature piezoelectric film ultrasonic transducers by a sol-gel spray technique and their application to process monitoring of polymer injection molding." *IEEE Sensors* 6(1):55-62.

Kobayashi, M., Jen, C.K., Moisan, J.F., Mrad, N., Nguyen, S.B., 2007a, "Integrated ultrasonic transducers made by the sol-gel spray technique for structural health monitoring," *Smart Mater. Struct*. 16:317-322.

Kobayashi, M., Jen, C.K., Nagata, H., Hiruma, Y., Tokutsu, T., Takenaka, T., 2007b, "Integrated ultrasonic transducers above 500°C," 2007 *IEEE Ultrasonics Symp. Proc.*, 953-956.

Lazarević, Z., Stojanović, B.D., Varela, J.A., 2005, "An approach to analyzing synthesis, structure, and properties of bismuth titanate ceramics," *Sci. of Sintering* , 37:199-216.

Lueng, C., Chan, H., Surya, C., and Choy, C., 2000, "Piezoelectric coefficient of aluminum nitride and gallium nitride," *J. Appl. Phys.* 88(9):5360-5363.

Liu, Y., Chillara, V.K., Lissenden, C.J., 2013a, "On selection of primary modes for generation of strong internally resonant second harmonics in plate" submitted for publication.

Liu, Y., Khajeh, E., Lissenden, C.J., Rose, J.L., 2013b, "Higher harmonic generation of guided waves in hyperelastic cylinders: interaction of axisymmetric torsional and longitudinal modes," submitted for publication.

Liu, Y., Lissenden, C.J., Rose, J.L., 2013c, "Strongly cumulative second harmonic generation in hyperelastic plates: finite element simulation," In: *Review of Progress in Quantitative Nondestructive Evaluation* 31 (D.O. Thompson and D.E. Chimenti, Ed.) in-press.

Liu, Y., Lissenden, C.J., Rose, J.L., 2013d, "Interaction of elastic waves in weakly nonlinear circular cylinders: I. analytical foundation," in preparation.

Liu, Y., Khajeh, E., Lissenden, C.J., Rose, J.L., 2013e, "Interaction of elastic waves in weakly nonlinear circular cylinders: II. numerical simulation," in preparation.

Lukacs, M., Olding, T., Sayer, M., Tasker, R., Sherrit, S., 1999, "Thickness mode material constants of a supported piezoelectric film," *J. Appl. Phys.* 85:2835-2843.

Matlack, K.H., Kim, J.Y., Jacobs, L.J., Qu, J., 2011, "Experimental characterization of efficient second harmonic generation of Lamb waves in a nonlinear elastic isotropic plate," *J. Appl. Phys.* 109:014905.

Matsuda, N., Biwa, S., 2011, "Phase and group velocity matching for cumulative harmonic generation in Lamb waves," *J. Appl. Phys.* 109:094903.

Meyer, R.M., P. Ramuhalli, J.B. Coble, L.J. Bond, 2011, "Advanced instrumentation, information, and control system technologies: nondestructive examination technologies – FY11 report," PNNL-20671, Pacific Northwest National Laboratory, Richland, Washington.

Moure, A., Pardo, L., Alemany, C., Millan, P., Castro, A., 2001, "Piezoelectric ceramics based on Bi_3TiNbO_9 from mechanochemically activated precursors," *J. Eur. Ceram. Soc.* 21:1399-1402

Müller, M.F., Kim, J.Y., Qu, J., Jacobs, L.J., 2010, "Characteristics of second harmonic generation of Lamb waves in nonlinear elastic plates," *J. Acoust. Soc. Am.* 127:2141-2152.

Newnham, R.E., Wolfe, R.W., Dorrian, J.F., 1971, "Structural basis of ferroelectricity in bismuth titanate family," *Mat. Res. Bul.* 6:1029-1040.

Parks, D.A., Tittmann, B.R., Kropf, M.M., 2010, "Aluminum nitride as a high temperature transducer," In: *Review of Progress in Quantitative Nondestructive Evaluation* 29 (D.O. Thompson and D.E. Chimenti, Ed.) pp. 1029-1034.

Parks, D.A., Tittmann, B.R., 2011, "Ultrasonic NDE in a reactor core," 2011 *IEEE Sensors*, pp. 618-622.

Parks, D.A., Zhang, S., Tittmann, B.R., 2013, "High temperature (>500 ^{o}C) ultrasonic transducers: an experimental comparison among three candidate piezoelectric materials", IEEE-UFFC Transactions, in-press.

Patel, N.D., Nicholson, P.S., 1990, "High frequency , high temperature ultrasonic transducers," *NDT Inter.* 23(5):262-266.

Pilgrim, S.M., Newnham, R.E., Rohlfing, L.L., 1987, "An extension of the composite nomenclature scheme," *Mat. Res. Bull.* 22:677-684.

Pruell, C., Kim, J.Y., Qu, J., Jacobs, L.J., 2009, "A nonlinear-guided wave technique for evaluating plasticity-driven material damage in a metal plate," *NDT&E Int.* 42:199-203.

Ramuhalli, P., J.W. Griffin, R.M. Meyer, S.G. Pitman, J.M. Fricke, M.E. Dahl, M.S. Prowant, T.A. Kafentzis, J.B. Coble, T.J. Roosendaal, 2012, "Detection and characterization of degradation precursors," PNNL-21692, Pacific Northwest National Laboratory, Richland, Washington.

Searfass, C.T., 2012, Characterization of bismuth titanate thick films fabricated using a spray-on technique for high temperature ultrasonic non-destructive evaluation, Ph.D. Thesis, The Pennsylvania State University, University Park.

Searfass, C.T., Baba, A., Tittmann, B.R., Agrawal, D.K., 2010, "Fabrication and testing of microwave sintered sol-gel spray-on bismuth titanate-lithium niobate based piezoelectric composite for use as a high temperature (>500 °C) ultrasonic transducer," In: *Review of Progress in Quantitative Nondestructive Evaluation* 29 (D.O. Thompson and D.E. Chimenti, Ed.) pp. 1035-1042.

Searfass, C.T., Tittmann, B.R., Agrawal, D.K., 2009, "Sol-gel deposited thick film bismuth titanate based transducer achieves operation over 600 C," In: *Review of Progress in Quantitative Nondestructive Evaluation* 28 (D.O. Thompson and D.E. Chimenti, Ed.) pp. 1751-1758.

Seth, V.K., Schulze, W.E., 1989, "Grain oriented fabrication of bismuth titanate ceramics and its electrical properties." *IEEE Trans. Ultrason. Ferroelectr. Freq. Control* 36(1):41-49.

Schulz, M.J., Sundaresan, M.J., Mcmichael, J., Clayton, D., Sadler, R., and Nagel, B., 2003, "Piezoelectric materials at elevated temperature," *J. Intell. Mat. Sys. Struct.* 14:693-705.

Scruby, C.B., Wadley, H.N.G., 1982, "An assessment of acoustic emission for nuclear pressure vessel monitoring," *Progress in Nuclear Energy*, 11(3):275-297.

Shulman, H.S., Testorf M., Damjanovic, D., Setter, N., 1996, "Microstructure, electrical conductivity, and piezoelectric properties of bismuth titanate," *J. Am. Ceram. Sci*. 79(12):3124-3128.

Shulman, H.S., 1997, *Piezoelectric Bismuth Titanate Ceramics.* Lausanne, Switzerland: Thesis, EPFL.

Srivastava, A., Lanza di Scalea, F., 2009, "On the existence of antisymmetric or symmetric Lamb waves at nonlinear higher harmonics," *J. Sound Vib.* 323:932-943.

Srivastava, A., Lanza di Scalea, F., 2010, "On the existence of longitudinal or flexural waves in rods at nonlinear higher harmonics," *J. Sound. Vib*. 329:1499-1506.

Srivastava, A., Bartoli, I., Salvatore, S., Lanza di Scalea, F., 2010, "Higher harmonic generation in nonlinear waveguides of arbitrary cross-section," *J. Acoust. Soc. Am*. 127, 2790-2796.

Stubbs, D. A., and Dutton, R.E., 2005, "High-temperature ultrasonic sensor for in situ monitoring of hot isostatic processing," *SPIE*, 2948:165-172.

Subbarao, E.C., 1962, "A family of ferroelectric bismuth compounds," *J. Phys. Chem. Solids* 23:665-676.

Svaasand, L., Eriksrud, M., Nakken, G., Grande, A.P., 1974, "Solid-solution range of LiNbO3," *J. Crystal Growth* 22(1):230-232.

Takeda, T., Kunitomi, K., Horie, T., and Iwata, K., 1997, "Feasibility study on the applicability of a diffusion-welded compact intermediate heat exchanger to next-generation high temperature gas-cooled reactor," *Nuclear Engineering and Design*, 168:11-21.

Takenaka, T., Sakata, K., 1984, "Piezoelectric properties of grain oriented $Na_{0.5}Bi_{4.5}Ti_4O_{15}$," *Trans. Insititute of Electronics and Communicaton Engineers of Japan*, 1984: 172-173.

Turner, R.C., Fuierer, P.A., Newnham, R.E., and Shrout, T.R., 1994, "Materials for high temperature acoustic and vibration sensors: a review," *Applied Acoustics* 41:299-324.

Wong, K. K., 2002, *Properties of Lithium Niobate*. INSPEC/Institution of Electrical Engineers.

Zhang, S., Cheng, Z., Lv, J., Li, G., Lu, R., Shao, Z., Chen, H., 1999, *J. Crystal Growth,* 205:453-456.

Zhang, S., Fei, Y., Chai, B.H.T., Frantz, E., Snyder, D., Jiang, X., Shrout, T., 2008a, "Characterization of piezoelectric single crystal $YCa_4O(BO_3)_3$ for high temperature applications," *Appl. Phys. Lett.*, 92:202905.

Zhang, S., Fei, Y., Frantz, E., Snyder, D., Chai, H., Shrout, T., 2008b, "High-temperature piezoelectric single crystal $ReCa_4O(BO_3)_3$ for sensor applications," *IEEE Trans. Ultrason. Ferroelectr. Freq. Control* 55(12):2703-2708.

Zhang, S. and Yu, F., 2011, "Piezoelectric materials for high temperature sensors," *J. Am. Ceram. Soc.*, 94(10):3153-3170.

Zou, L., Sayer, M., Jen, C.-K., 1997, "Sol-gel fabricated thick piezoelectric ultrasonic transducers for potential applications in industrial material process." 1997 *IEEE Ultrasonics Symposium*, 1007-1011.

2.7 Technology Roadmap

2.7.1 Piezoelectric Materials and Processing

Piezoelectric composites were investigated in this project, lead zirconate titanate/bismuth titanate (PZT/BT) for applications up to 400°C and bismuth titanate/lithium niobate (BT/LN) for applications up to 950°C. A detailed description of these composites and sol-gel processing of spray-on transducers is provided in subsection 2.1. Processing and deposition of piezoelectric materials in this way has a number of advantages:

- The transducer is chemically bonded to the substrate, which provides a significantly more efficient coupling for ultrasound than does gel couplant. Furthermore, gel couplant has temperature limitations, produces coupling conditions that are difficult to repeat due mainly to thickness variations, and is not suitable for stay-in-place transducers intended for long term condition monitoring.

- Transducers can be easily air-spray deposited onto both flat and curved substrates, making them applicable to many types of structures including plates, pipes, and cylindrical or spherical vessels.

- The composition of the composite can be tailored to fit the needs of a specific application (e.g., temperature resistance and piezoelectric coupling coefficients) by selection of the constituents and their weight fractions. Piezoelectric composites can be designed by using micromechanical modeling.

The disadvantage of direct spray deposition of a piezoelectric transducer onto a metal substrate is that the mismatch in thermoelastic properties of the piezoceramic coating and the metal substrate lead to residual stresses that could damage or fracture the coating. Thus, deposition and processing of the transducer needs to take residual stresses into account.

In order to fully develop the potential of spray-on piezoceramic composite transducers for ultrasonic wave generation and reception modeling of the full transducer processing procedure should be conducted. This modeling effort has two objectives:

1. Prediction of the piezoelectric properties of the as-processed transducer as a function of temperature,

2. Prediction of the mechanical integrity of the as-processed transducer.

The need for these modeling capabilities is clarified and accentuated by a brief summary of the transducer processing methodology. A piezoceramic is suspended in an organic solution to form a sol-gel, which is then combined and mixed with a piezeceramic powder to form a slurry that can be air-spray deposited onto a substrate. The coating is then pyrolized to burn off the organics. As a spray deposited layer is roughly 20 μm thick, typically multiple layers are deposited to achieve the desired transducer thickness. Each layer is pyrolized before the subsequent layer is deposited because there is a significant volume reduction associated with removing the organics. After all the layers have been deposited and pyrolized the transducer is densified by another thermal treatment. Note that thick transducers can be densified in steps of 5 or 6 layers. All components of the process to this point affect the microstructure on which the piezoelectric efficiency and mechanical integrity are based (e.g., selection of constituents, grain size of powder, pyrolysis and densification temperatures and durations). Major tradeoffs between porosity and residual stress exist based on the maximum temperatures and durations of both pyrolysis and densification processes. Of course both porosity and residual stress affect the mechanical integrity of the coating.

The piezoelectric functionality and efficiency also depends strongly on the porosity (and microstructure) in both obvious ways (e.g., dipole eccentricity and dipole alignment in polycrystals) and less obvious ways (e.g., (i) electrode material filling voids in the piezoceramic and causing localized short circuits, (ii) chemical reaction of electrode materials with the piezoceramic at elevated temperature causes loss of piezoelectricity). Thus, selection of the electrode material and its deposition method is of critical importance for effective spray-on piezoceramic transducers due to the inherent porosity. A firm grasp on the interaction between the piezoceramic and the electrode at the atomic level is needed for material selection, but so is a thorough understanding of the effect of electrode deposition methods. In this project we found a significant difference in sputter deposited and brushed-on electrodes of the same material; the difference being sputter deposited electrodes functioned and brush painted electrodes did not. These less-obvious issues with electrodes were unexpected and demanded much attention during this project, which limited the depth of effort available for other tasks.

This project started to address long-term durability and functionality issues with operation of spray-deposited transducers in high temperature applications. However, additional research is necessary in this area to ensure that the transducers can both survive and function in harsh environments for extended periods of time as is required for CM.

2.7.2 Condition Monitoring (CM)

The spray-on transducers could be used for condition monitoring (CM) in many ways. Wall thinning in pipes or vessels could be monitored with longitudinal bulk waves in pulse-echo mode. This could be done at key points where corrosion or erosion is expected to be worst, or it could be done with an array of transducers. Likewise, ultrasonic guided waves could be employed to monitor a length of pipe or a region of a vessel with dimensions of meters. Because multiple guided wave modes exist at any given frequency it is beneficial to control which mode gets preferentially generated. Multi-element transducers enable control over mode generation. Spray-on transducers with multiple elements can be processed by patterning the electrodes. For example, a comb transducer for a pipe has an array of equally spaced ring elements to control which axisymmetric longitudinal modes L(0,m) are generated. Such patterned electrodes could be deposited through a mask template, or a continuous electrode could be deposited first and then patterned using selective material removal. Both methods were successfully performed in this project. Patterned deposition of elements having widths larger than about 1 mm were brush painted with a stencil. Smaller features were created using selective laser ablation to pattern electrode rings on a pipe. However, the laser that we used is confined to the laboratory so another method to create patterned electrodes for transducers in-situ needs to be researched and developed. Potential methods include: delivery of laser pulses through an optical fiber that is rastered in the desired pattern, selective chemical etching, and affixing a pre-patterned electrode onto the transducer surface.

CM with ultrasonic guided waves using features of the linear wave propagation does not require small element sizes and is known to be sensitive to macroscale damage such as corrosion-induced material loss and fatigue cracks. However, in many cases (e.g., fatigue) once a crack grows to measurable size the remaining life is relatively short and there is insufficient time to plan maintenance actions. Thus, it is extremely desirable to have the ability to detect precursors to macroscale damage and enable remaining useful life prediction based on the current condition at an early stage of the degradation process. There are a number of methods that have potential to identify precursors to macroscale damage that are being evaluated and developed. We think that nonlinear ultrasonic guided waves have strong potential for detection of microstructural evolution that precedes macroscale damage through the generation of higher harmonics. The literature shows that harmonic generation from bulk waves or guided waves is associated with many different types of microstructure evolution: plastic deformation, fatigue, precipitates, and radiation embrittlement. A monochromatic wave propagating in a nonlinear media is distorted, which causes higher harmonic generation at integer multiples of the excitation frequency. Furthermore, the mutual interaction of two or more waves generates harmonics at linear combinations of the excitation frequencies. There are three main benefits of using nonlinear wave mixing to detect precursors: (1) combinational harmonics can be

selected to occur at frequencies away from instrumentation nonlinearities, (2) the wave interaction point can be adjusted to enable detection of localized microstructure evolution, and (3) localized microstructural evolution is detectable without using a temporal baseline since a spatial baseline can be used. However, in addition to understanding the nonlinear harmonic generation and being able to characterize it, we must also be able to relate it to the features of the microstructural evolution.

Analysis of nonlinear ultrasonic guided waves depends on having a very high signal to noise ratio because the interrogation signal is at a frequency other than the excitation signal, and most importantly because its amplitude is orders of magnitude lower than that of the excitation signal. Thus, it is common to use a high power amplifier that provides the cleanest possible signal to the transducer. Many researchers opt to use lithium niobate transducers for nonlinear ultrasonics experiments because despite having a significantly lower piezoelectric coupling than PZT they have much lower nonlinearity. Because we had to devote so much time and attention to functioning electrodes in this project we were unable to demonstrate that PZT/BT and BT/LN comb transducers can generate higher harmonic guided waves. We did process comb transducers to send the L(0,4) guided wave mode and receive the L(0,5) second harmonic on a stainless steel pipe. These transducers were able to generate the L(0,4) wave mode and receive it, but when we increased the voltage sent to the transducer it created sparks. We were unable to determine whether the arcing occurred between the closely spaced ring-shaped electrodes or whether the laser ablation processing of the ring electrodes had gone to deep into the piezoceramic and caused short circuit. Thus, it remains to be determined that the spray-on transducers are able to activate a guided wave mode that generates measurable higher harmonics.

2.7.3 Prognostics

The value of the diagnostic CM information provided by the sprayed-on transducers would be dramatically increased by using it to predict remaining useful life. Knowing the current condition and the remaining useful life, which of course depends on expected operating conditions, enables condition-based maintenance. The logistics for effective management of the life cycle of nuclear power plant structures depends on whether the estimated remaining life is sufficiently long. Detection of damage near the end of life enables shut down to avoid failure, but does not provide sufficient warning to have replacement parts ready and plan the outage. Fatigue crack growth is a good example (see Figure 7.1). A macroscale crack is generally not detectable until 80% or more of the life has been expended. However, the microstructure evolves prior to macroscale crack initiation. A method to characterize microstructure evolution,

such as formation of persistent slip bands (PSBs) would enable tracking the progression of degradation from a significantly early point in the service life of the structure.
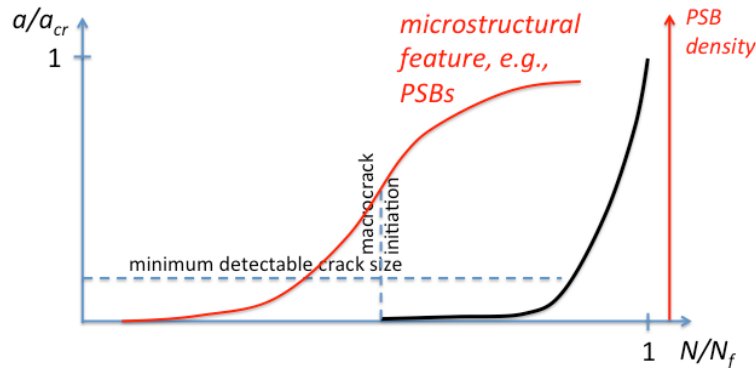
Figure 7.1. *Schematic and microscopic and macroscopic damage evolution during fatigue.*

There are a number of methods to nondestructively characterize microstructure evolution currently being researched (e.g., higher harmonic generation from elastic (ultrasonic) waves, Barkhausen noise, resonant ultrasonic spectroscopy (RUS), acoustic emissions (AE), electromechanical impedance (EMI), surface texture, temperature). We believe that nonlinear ultrasonics is the leading candidate. Spray-on transducers could be used to measure higher harmonic generation or for nonlinear wave mixing as described earlier, or perhaps for RUS. If nonlinear ultrasonics is used then further research is necessary to relate the measured nonlinear wave signals to the microstructure changes. As described in subsection 2.3, other researchers have investigated the correlation of bulk wave second harmonic generation with dislocation substructures and precipitates. In another project our research group is investigating this issue for guided waves using a 3D mesoscale model framework based on an energy measure instead of the 1D nonlinearity parameter. This framework accepts homogenized input from a micromechanical model representative of the actual microstructure.

2.7.4 Spray-on High Temperature Transducer Technology Development Roadmap

A list of tasks for the technology development roadmap of spray-on high temperature transducers for online condition monitoring is provided in this section.

1. Identify electrode materials and in-situ deposition techniques for electrodes compatible with porous piezoceramic coatings in high temperature environments. Electrodes for PZT/BT, BT/LN, and possibly other piezoceramic composite coatings should be investigated.

2. Develop a micromechanical modeling capability to predict the thermopiezoelectric response of composite transducers (actuation and reception of ultrasonic waves as a function of temperature) in terms of the constituent properties, porosity, and weight fractions.

3. Perform thermoelastic modeling of transducer processing to assess mechanical integrity as a function of processing parameters, especially pyrolization temperature and duration and densification temperature and duration based on realistic temperature distributions.

4. Assess the long-term durability (i.e., mechanical integrity) and functionality (i.e., piezoelectric coupling) of transducers in realistic service environments.

5. Research a method to create in-situ patterned electrodes having sub-millimeter feature size to enable CM based on higher harmonic generation.

6. Demonstrate that spray-on transducers can send guided wave modes, which generate higher harmonics or combinational harmonics measureable with the spray-on transducers in through-transmission.

7. Correlate higher harmonic and/or combinational harmonic generation with the evolving microstructural features that cause it.

3. ACCOMPLISHMENTS

This project reduced the critical technology gap that exists between online condition monitoring (CM) of nuclear plant components for damage accumulation and sensors available for high temperature environments. As such, it supports the DOE mission to develop a fundamental understanding of advanced sensors and methods to improve physical measurement accuracy and reduce uncertainty. Spray deposition and processing methods for the temperature resistance piezoceramic materials bismuth titanate (BT) and lithium niobate (LN) were developed. Specifically, we combined a sol-gel with powders to form a slurry that can be air-spray deposited onto a substrate to form the basis for a composite piezoceramic transducer. The research focused on PZT/BT and BT/LN, where the first material is in the sol-gel and the second is a powder. These composites are designed to have better properties than their constituents alone. The spray deposition involves forming a sol-gel, combining and mixing in the powder, and then air-spraying onto a substrate. Subsequent processing includes pyrolization, densification, electrode application, lead wire connections, and poling. The deposition and processing result in a piezoceramic microstructure with porosity, which is both beneficial because it provides strain-tolerance and challenging because it limits both electrode material selection and the deposition method. In fact, many deposition and processing challenges were identified throughout the course of the research, most of these were solved but some remain for future work as indicated in the technology development roadmap.

The transducers are intended to send and receive ultrasonic guided waves that can provide condition monitoring coverage over a relatively large domain. Due to the multimodal nature of guided waves it is beneficial to control the modes generated by the transducer. One way to control guided wave generation is with multi-element transducers; e.g., a comb transducer composed of ring elements on a pipe. We created comb transducers by spraying a continuous piezoceramic coating on a substrate and then patterning the electrodes. Patterned electrodes can be created by painting stripes or by painting a continuous domain and removing unwanted electrode material via laser ablation. Comb transducers deposited and processed on a stainless steel pipe (using laser ablation) successfully generated and received guided wave modes. Electrode patterning techniques are chosen according to the feature size required for the transducer.

A condition monitoring plan for compact intermediate heat exchangers in the NGNP was proposed and a feasibility demonstration performed. Compact intermediate heat exchangers are comprised of many relatively thin plates (with machined cooling paths) that are diffusion bonded together. Poor quality or degraded diffusion bonds will generate significantly larger reflections from ultrasonic waves than will good diffusion bonds, therefore an array of spray-

deposited transducers could provide online CM capabilities. Results show that interface reflections are detectable and suggest that the transducers have sufficient penetration power.

Linear ultrasonic methods work well for characterization of macroscale defects, but nonlinear methods have far better potential to characterize the evolution of material microstructure that precedes macroscale damage. However, much analysis was necessary to make nonlinear guided waves practical for microstructure evolution characterization through higher harmonic generation. We performed analysis to show which axisymmetric primary modes generate strong cumulative higher harmonics in pipes by using the internal resonance criteria; i.e., primary and secondary wave modes must be synchronized (phase matched) and have non-zero power flux. However, the number of usable primary modes that generate cumulative second harmonics is quite limited so we expanded the analysis to third harmonics. Our analysis of third harmonic generation was conducted on plates in order to use a Cartesian coordinate system instead of a curvilinear one. Previous research in our group has shown that in the context of higher harmonic generation, axisymmetric waves in pipes approach Lamb waves in a plate in the asymptotic limit. So analysis of Lamb waves is also useful for pipe applications. Furthermore, we analyzed higher harmonic generation of flexural modes in a pipe. In this analysis, nonlinear wave interaction from two sources was considered in addition to single source excitation. The modeling research was verified by finite element simulations of nonlinear wave interaction. This analysis and associated numerical simulations led to a system and method for characterization of materials using nonlinear acoustic guided wave spectroscopy, which was submitted as a provisional patent. Using higher harmonic generation to signal changes in the microstructure (such as dislocation substructures, precipitate growth, and void nucleation) requires a correlation of nonlinear ultrasonics to microstructural features, for which we have provided some valuable insight.

Online condition monitoring applies to large structural components, but initial transducer deposition and processing was performed in a laboratory on small scale coupons. We have now demonstrated that the deposition and processing methods can be adapted to field installation on large structures. The most significant changes necessary to go from the laboratory to the field are: a portable sprayer, pyrolizing and densifying with an induction heater, electrode patterning, and application of high voltage for poling.

Our reports on a technology gap analysis and a technology development roadmap indicate that spray-on transducer benefits include: elimination of the need for couplant, better acoustic impedance matching than couplant, conformability to curved surfaces, and design tailorability to match requirements. The key items on the roadmap are:

1. Identify electrode materials and in-situ deposition techniques for electrodes compatible with porous piezoceramic coatings in high temperature environments. Electrodes for

PZT/BT, BT/LN, and possibly other piezoceramic composite coatings should be investigated.

2. Develop a micromechanical modeling capability to predict the thermopiezoelectric response of composite transducers (actuation and reception of ultrasonic waves as a function of temperature) in terms of the constituent properties, porosity, and weight fractions.

3. Perform thermoelastic modeling of transducer processing to assess mechanical integrity as a function of processing parameters, especially pyrolization temperature and duration and densification temperature and duration based on realistic temperature distributions.

4. Assess the long-term durability (i.e., mechanical integrity) and functionality (i.e., piezoelectric coupling) of transducers in realistic service environments.

5. Research a method to create in-situ patterned electrodes having sub-millimeter feature size to enable CM based on higher harmonic generation.

6. Demonstrate that spray-on transducers can send guided wave modes, which generate higher harmonics or combinational harmonics measureable with the spray-on transducers in through-transmission.

7. Correlate higher harmonic and/or combinational harmonic generation with the evolving microstructural features that cause it.

Over the course of the project 6 graduate students and 2 undergraduates have been supported and 5 theses have been completed (1 Ph.D., 2 M.S., and 2 honors). Two more Ph.D. degrees are in progress. The project benefited tremendously from their efforts, and in return they were rewarded with invaluable experience.

The results of the project were widely disseminated in journals and at conferences. In total, 14 articles were published. Five of those are in top archival journals [*J. Appl. Phys*. (3), *J. Acoustic Society of America, Insight*.]. We count a total of 21 presentations given at the following forums:

- *ASME International Mechanical Engineering Congress and Exposition*, Montreal, Canada, November 14-20, 2014

- *Workshop on Current and Future of Nonlinear Ultrasonic Techniques for NDE*, Seoul, Korea, October 21-24, 2014

- *NDT 2014 53rd Annual Conference of the British Institute of Non-Destructive Testing*, Manchester, England, September 9-11, 2014

- *Review of Progress in Quantitative Nondestructive Evaluation*, Boise, Idaho, July 20-25, 2014

- *Idaho National Laboratory*, Idaho Falls, Idaho, July 17, 2014

- *Joint IEEE Int. Symposium on the Applications of Ferroelectrics*, University Park, PA, May 12-16, 2014

- *Future of Advanced Nuclear Technologies National Academies Keck Futures Initiative*, Irvine, CA, August 8, 2013

- *Review of Progress in Quantitative Nondestructive Evaluation*, Baltimore, Maryland, July 21-26, 2013

- *13th International Symposium on Nondestructive Characterization of Materials*, Le Mans, France, May 20-25, 2013

- *International Workshop on Acoustic Transduction Materials and Devices*, University Park, Pennsylvania, May 6-9, 2013

- *Center for Acoustics and Vibration Spring Workshop*, Penn State University, University Park, PA, April 29-30, 2013

- *ASNT 22nd Research Symposium*, Memphis, Tennessee, March 18-21, 2013

- *Review of Progress in Quantitative Nondestructive Evaluation*, Denver, Colorado, July 15-20, 2012

PART III. LIST OF PUBLICATIONS

1. PATENTS
Y. Liu, C.J. Lissenden, G. Choi, X. Yao, J.L. Rose, 2014, "System and method for characterization of materials using nonlinear acoustic guided wave spectroscopy," U.S. Patent Office serial number 62/066,650.

2. JOURNALS AND PROCEEDINGS
C.J. Lissenden, Y. Liu, J.L. Rose, 2015, "Use of nonlinear ultrasonic guided waves for early damage detection," *Insight* Vol. 57(4), in-press.

Y. Liu, C.J. Lissenden, J.L. Rose, 2014, "Higher order interaction of elastic waves in weakly nonlinear circular cylinders. I. analytical foundation," *J. Appl. Phys*. Vol. 115:214901.

Y. Liu, E. Khajeh, C.J. Lissenden, J.L. Rose, 2014, "Higher order interaction of elastic waves in weakly nonlinear circular cylinders. II. physical interpretation and numerical simulation," *J. Appl. Phys*. Vol. 115:214902.

Y. Liu, V.K. Chillara, C.J. Lissenden, J.L. Rose, 2013, "Cubic nonlinear shear horizontal and Rayleigh Lamb waves in weakly nonlinear plates," *J. Appl. Phys*. Vol. 114:114908.

Y. Liu, E. Khajeh, C.J. Lissenden, J.L. Rose, 2013, "Interaction of torsional and longitudinal guided waves in weakly nonlinear circular cylinders," *J. Acoustic Soc. Am*. Vol. 133(5):2541-2553.

C.J. Lissenden, Y. Liu, V.K. Chillara, G. Choi, and X. Yao, 2014, "Nonlinear guided waves for continuous material microstructure state awareness," *Proceedings of the ASME 2014 International Mechanical Congress and Exhibition*, ASME International, Paper IMECE2014-39699 (8 pages).

C.J. Lissenden, Y. Liu, J.L. Rose, 2014, "Use of nonlinear ultrasonic guided waves for early damage detection," *Proceedings of the NDT 2014 Conference*, British Institute of Non-Destructive Testing.

K. Sinding, A. Orr, B. Reinhardt, L. Tien, N. Malarich and B. Tittmann, 2014, "Spray-on Ferroelectrics for Fabrication of Custom Tailored Composite Transducers for NDE and SHM," *Proceedings of the Joint IEEE Int. Symposium on the Applications of Ferroelectrics*, IEEE.

Y. Liu, C.J. Lissenden, J.L. Rose, 2014, "Microstructural characterization in plates using guided wave third harmonic generation," In: *Review of Progress in Quantitative Nondestructive Evaluation*, Vol. 33, D.E. Chimenti, L.J. Bond, D.O. Thompson, Eds., American Institute of Physics Proc. 1581, pp. 639-645.

K. Sinding, C. Searfass, N. Malarich, B. Reinhardt, B.R. Tittmann, 2014, "High temperature ultrasonic transducers for generation of guided waves for non-destructive evaluation of pipes," In: *Review of Progress in Quantitative Nondestructive Evaluation*, Vol. 33, D.E. Chimenti, L.J. Bond, D.O. Thompson, Eds., American Institute of Physics Proc. 1581, pp. 302-307.

Y. Liu, C. Lissenden, J. Rose, 2014, "Nonlinear ultrasonic guided waves for microstructure characterization of hollow cylinders," 13th International Symposium on Nondestructive Characterization of Materials (NDCM-XIII), B. Djorjevic, Ed., May 2013, www.NDT.net?ID=15519.

B. Tittmann, D. Parks, and S. Zhang, 2014, "High temperature piezoelectrics – a comparison," 13th International Symposium on Nondestructive Characterization of Materials (NDCM-XIII), B. Djorjevic, Ed., May 2013, www.NDT.net?ID=15537.

B. Reinhardt, C. Searfass, R. Cyphers, K. Sinding, C. Pheil, B. Tittmann, 2013, "Fabrication and modeling of bismuth titanate-PZT ceramic transducers for high temperature applications," In: *Review of Progress*

in Quantitative Nondestructive Evaluation, Vol. 32, D.O. Thompson and D.E. Chimenti, Eds., American Institute of Physics Proc. 1511, pp. 1685-1692.

Y. Liu, C. Lissenden, J. Rose, 2013, "Strongly cumulative second harmonic generation in hyperelastic plates: finite element simulation," Vol. 32, D.O. Thompson and D.E. Chimenti, Eds., American Institute of Physics Proc. 1511, pp. 151-158.

3. THESES

N. Malarich, "Spray-on comb transducers for health monitoring of high-temperature structures," Honors thesis in Engineering Science, The Pennsylvania State University, University Park, PA, May 2015 (expected).

A. Orr, "A bond stiffness study of sol-gel spray-on transducers," Master of Science thesis in Acoustics, The Pennsylvania State University, University Park, PA, May 2015.

Y. Liu, "Characterization of global and localized material degradation in plates and cylinders via nonlinear interaction of ultrasonic guided waves," Ph.D. in Engineering Science and Mechanics, The Pennsylvania State University, University Park, PA, August 2014.

K. Sinding, "The effect of weight percent on the properties of ultrasonic transducers fabricated though a sol-gel deposition process," Honors thesis in Engineering Science, The Pennsylvania State University, University Park, PA, May 2014.

R.L. Cyphers, "Research on low frequency composite transducers fabricated using a sol-gel spray-on method," Master of Science thesis in Engineering Science, The Pennsylvania State University, University Park, PA, December 2012.

4. PRESENTATIONS

C.J. Lissenden, Y. Liu, V.K. Chillara, G. Choi, X. Yao, "Nonlinear guided waves for continuous material microstructure state awareness," *ASME International Mechanical Engineering Congress and Exposition*, Montreal, Canada, November 14-20, 2014.

C.J. Lissenden, "Early damage detection with nonlinear ultrasonic guided waves," *Workshop on Current and Future of Nonlinear Ultrasonic Techniques for NDE*, Seoul, Korea, October 21-24, 2014.

C.J. Lissenden, Y. Liu*, J.L. Rose, "Use of nonlinear ultrasonic guided waves for early damage detection," *NDT 2014 53rd Annual Conference of the British Institute of Non-Destructive Testing,* Manchester, England, September 9-11, 2014.

Y. Liu, C.J. Lissenden, J.L. Rose, "NDE and SHM of pipes with acoustic guided wave: from macro to micro scale damages," *Review of Progress in Quantitative Nondestructive Evaluation*, Boise, Idaho, July 20-25, 2014.

Y. Liu, C.J. Lissenden, J.L. Rose, "NDE and SHM of pipes with acoustic guided wave: from macro to micro scale damages," *Idaho National Laboratory*, Idaho Falls, Idaho, July 17, 2014.

B.R. Tittmann, "Ultrasonic Sensors for Harsh Environments," GE Conference: NDE - A Strategic and Competitive Advantage for GE, Lewistown, Pennsylvania, July 15-16, 2014.

K. Sinding, A. Orr, L., Breon and B. R. Tittmann, "Sol-Gel Spray Sensor Technology," *Electric Power and Research Institute - NDE Issues Conference*, Charlotte, North Carolina, June 16-19, 2014.

K. Sinding, A. Orr, B. Reinhardt, L. Tien, N. Malarich and B. Tittmann, "Spray-on Ferroelectrics for Fabrication of Custom Tailored Composite Transducers for NDE and SHM," *Joint IEEE Int. Symposium on the Applications of Ferroelectrics*, University Park, PA, May 12-16, 2014.

B.R. Tittmann, "Ultrasonic sensor enablement for in-core testing," *Future of Advanced Nuclear Technologies National Academies Keck Futures Initiative*, Irvine, CA, August 8, 2013.

Y. Liu, C.J. Lissenden, J.L. Rose, "Characterization of microstructure evolution in plates using guided wave third harmonics," *Review of Progress in Quantitative Nondestructive Evaluation*, Baltimore, Maryland, July 21-26, 2013.

K. Sinding, C. Searfass, N. Malarich, B. Reinhardt, B.R. Tittmann, "High temperature ultrasonic transducers for generation of guided waves for non-destructive evaluation of pipes," *Review of Progress in Quantitative Nondestructive Evaluation*, Baltimore, Maryland, July 21-26, 2013.

Y. Liu, C.J. Lissenden, J.L. Rose, "Nonlinear ultrasonic guided waves for microstructure characterization of hollow cylinders," *13th International Symposium on Nondestructive Characterization of Materials*, Le Mans, France, May 20-25, 2013.

B. Tittmann, D. Parks, and S. Zhang, "High Temperature (>500° C) Ultrasonic Transducers: An Experimental Comparison among Three Candidate Piezoelectric Materials," *13th International Symposium on Nondestructive Characterization of Materials*, Le Mans, France, May 20-25, 2013.

Y. Liu, C.J. Lissenden, J.L. Rose, "Characterization of material microstructural evolution by nonlinear elastic waves," *International Workshop on Acoustic Transduction Materials and Devices*, University Park, Pennsylvania, May 6-9, 2013.

B.R. Tittmann, "Acoustic characterization of materials – toward ultrasonic sensors for harsh environments," *International Workshop on Acoustic Transduction Materials and Devices*, University Park, Pennsylvania, May 6-9, 2013.

B.R. Tittmann, "The purpose, experimental design and expected impact of the ATR-NSUF ultrasonic transducer irradiation project," *International Workshop on Acoustic Transduction Materials and Devices*, University Park, Pennsylvania, May 6-9, 2013.

A. Orr, R. Cyphers, B. Reinhardt, B.R. Tittmann, "Spray-on PZT/Bismuth Titanate Thick Films For High Temperature Ultrasonic NDE," *International Workshop on Acoustic Transduction Materials and Devices*, University Park, Pennsylvania, May 6-9, 2013.

K. Sinding, C. Searfass, B.R. Tittmann, "High Temperature Ultrasonic Transducers for Generation of Guided Waves for Non-Destructive Evaluation of Pipes," *International Workshop on Acoustic Transduction Materials and Devices*, State College, Pennsylvania, May 6-9, 2013.

K. Sinding, C. Searfass and B.R. Tittmann, "High Temperature Ultrasonic Transducers for Generation of Guided Waves for Non-Destructive Evaluation of Pipes," *Center for Acoustics and Vibration Spring Workshop*, Penn State University, University Park, PA, April 29-30, 2013.

Orr, A., B. Cyphers, and B. Tittmann, "Fabrication and Characterization of PZT/Bismuth Titanate Thick Films Fabricated Using a Spray-on Deposition Technique For High Temperature Ultrasonic Non-Destructive Evaluation," *International Workshop on Acoustic Transduction Materials and Devices*, State College, Pennsylvania, May 6-9, 2013.

B. Reinhardt and B.R. Tittmann, "Damage characterization using finite amplitude wave propagation for in-core measurements of nuclear reactors," *Center for Acoustics and Vibration Spring Workshop*, Penn State University, University Park, PA, April 29-30, 2013.

A. Orr, R. Cyphers and B. Tittmann, "Fabrication and Characterization of PZT/Bismuth Titanate Thick Films Fabricated using a Spray-on Deposition Technique for High Temperature Ultrasonic Non-Destructive Evaluation," *Center for Acoustics and Vibration Spring Workshop*, Penn State University, University Park, PA, April 29-30, 2013.

Y. Liu, C.J. Lissenden, and J.L. Rose, "Conditions for cumulative second harmonic generation in plates and pipes," *ASNT 22nd Research Symposium*, Memphis, Tennessee, March 18-21, 2013.

Tittmann, B. R., "Ultrasonic Transducers for Harsh Environments," presented at *64th ICAT/JTTAS Joint International Smart Actuator Symposium*, State College, Pennsylvania, October 2-3, 2012,.

B. Reinhardt, C. Searfass, R. Cyphers, K. Sinding, C. Pheil, B. Tittmann, "Fabrication and modeling of bismuth titanate-PZT ceramic transducers for high temperature applications," *Review of Progress in Quantitative Nondestructive Evaluation*, Denver, Colorado, July 15-20, 2012.

Y. Liu, C. Lissenden, J. Rose, "Strongly cumulative second harmonic generation in hyperelastic plates: finite element simulation," *Review of Progress in Quantitative Nondestructive Evaluation*, Denver, Colorado, July 15-20, 2012.

PART IV. FINAL QUADCHART & NEET ASI SUMMARY

High Temperature Transducers for Online Monitoring of Microstructure Evolution

OVERVIEW

Purpose: Develop ultrasonic transducers and methods for online condition monitoring of LWR (up to 400°C) and NGNP (up to 950°C) components. Online monitoring of structural damage and precursors to damage will improve safety and operations of nuclear plants.

Objectives: The sensory system, monitoring methodology, data acquisition, and damage characterization algorithm that comprise a condition monitoring system will be researched. The objectives of this research are to: (1) assess the concept viability of spray-on piezoelectric coatings to generate ultrasonic guided waves that are sensitive to microstructure evolution, (2) provide a detailed technology gap analysis, and (3) create a comprehensive technology development roadmap.

IMPACT

Logical Path: is shown in the flowchart below

Technology Gap Assessment

Sensor Materials

T<400C (LWR)   T<950C (NGNP)

Durability

Ancillary Components

Monitoring Methodology

Microstructure Evaluation

Prognostics

Technology Development Roadmap

Outcomes: The much-desired ability to perform online condition monitoring in high temperature environments will be achieved through research and development of high temperature piezoelectric transducers and ultrasonic guided waves. The technology gap will be assessed and a roadmap developed.

DETAILS

Principal Investigator: Cliff Lissenden

Institution: Penn State

Collaborators: Bernhard Tittmann, Penn State
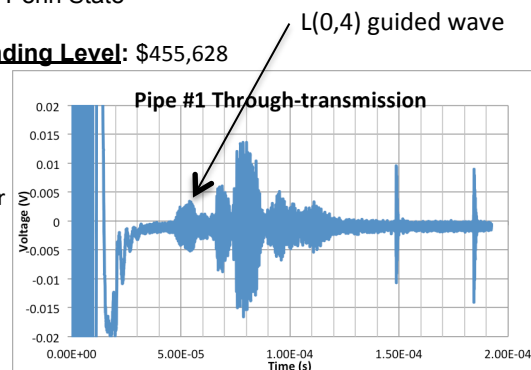
Duration: 3 years   **Total Funding Level:** $455,628

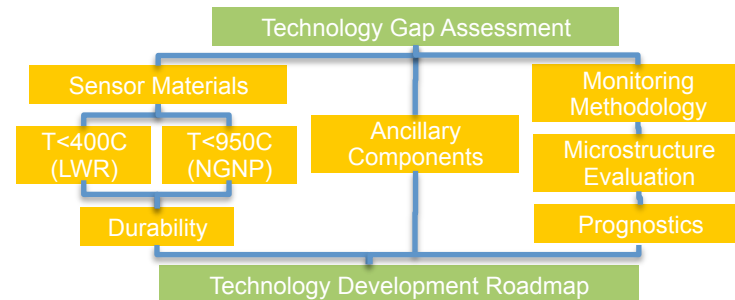**TPOC:** Pradeep Ramuhalli

Federal Manager: Suibel Schuppner

Workscope: NEET

PICSNE Workpackage #:
NEUP Project number 120237

PZT/BiTi

L(0,4) guided wave

Pipe #1 Through-transmission

(Voltage (V) vs Time (s), axis from 0.00E+00 to 2.00E-04)

RESULTS

Results: PZT/bismuth titanate and bismuth titanate/lithium niobate transducers were spray-deposited using sol-gels and powders. Electrodes were patterned using laser ablation to create comb transducers for preferential excitation of axisymmetric guided wave modes in pipes. Procedures were developed to deposit and process these transducers in the field on large structural components. Nonlinear guided waves for characterization of microstructure evolution associated with incipient material degradation were analyzed. Primary wave modes that generate strong higher harmonics were identified and a nonlinear guided wave spectroscopy method based on mixing waves to generate nonlinear interactions was developed. Journal articles include:
- C.J. Lissenden, Y. Liu, J.L. Rose, 2015, "Use of nonlinear ultrasonic guided waves for early damage detection," *Insight*, in-press.
- Y. Liu, C.J. Lissenden, J.L. Rose, 2014, *J. Appl. Phys*. Vol. 115:214901.
- Y. Liu, E. Khajeh, C.J. Lissenden, J.L. Rose, 2014, *J. Appl. Phys*. Vol. 115:214902.
- Y. Liu, V.K. Chillara, C.J. Lissenden, J.L. Rose, 2013, *J. Appl. Phys*. Vol. 114:114908.
- Y. Liu, E. Khajeh, C.J. Lissenden, J.L. Rose, 2013, *J. Acoustic Soc. Am*. Vol. 133(5): 2541-2553.

Accomplishments: Guided wave signals have been demonstrated for spray-on PZT/BiTi transducers on stainless steel pipe. A provisional patent application has been submitted for nonlinear acoustic guided wave spectroscopy.

High Temperature Transducers for Online Monitoring of Microstructure Evolution

Cliff Lissenden and Bernhard Tittmann, Penn State

Description of project: The objectives of this project were to: (1) assess the concept viability of spray-on piezoelectric coatings to generate ultrasonic guided waves that are sensitive to microstructure evolution, (2) provide a detailed technology gap analysis, and (3) create a comprehensive technology development roadmap. Progress toward the much-desired ability to perform online condition monitoring in high temperature environments was achieved through development of sol-gel processing of PZT and bismuth titanate in combination with bismuth titanate and lithium niobate powders and then air-sprayed directly onto a substrate. In addition, the sensitivity of nonlinear ultrasonic guided waves to microstructure evolution that precedes macroscale damage was investigated.

Recent results and highlights: Sol-gel processing of PZT/bismuth titanate and bismuth titanate/ lithium niobate provided transducers that can function up to 400°C and 950°C respectively. A method to process transducers in-situ was developed that includes: air-spray, pyrolyzation, densi-fication, electrode deposition, poling, and installation of lead wires. Further, methods to create patterned elect-rodes enabled pre-ferential generation and reception of guided wave modes. Analysis was per-formed to identify axisymmetric long-itudinal wave modes in a pipe that generate strong second harmonics, which are sensitive to microstructure evolution. Gener-

Stainless steel pipe (25 mm diameter) with two PZT/Bismuth Titanate spray-on comb transducers (with 4-1.6 mm wide elements) generates axisymmetric L(0,n) modes when excited at 1.83 MHz.

ation of higher harmonic flexural modes and nonlinear mutual interactions between multiple guided wave modes were also analyzed to improve sensitivity to microscale degradation.

Impact and value to nuclear applications: Ultrasonic transducers can be sprayed onto curved surfaces in the field, and used for online condition monitoring of components in LWRs (up to ~400°C) and the NGNP (up to ~950°C). Online monitoring of structural damage and precursors to damage will improve safety and operations of nuclear plants.
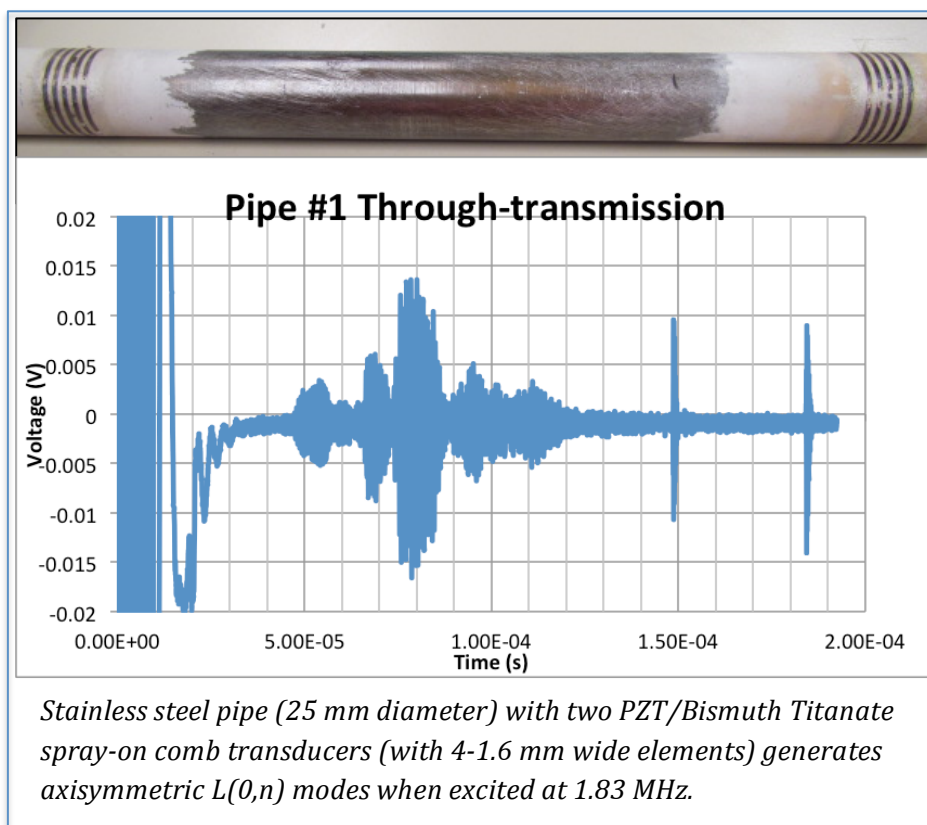
PART V. OTHER RELEVANT INFORMATION

(Students supported and degrees earned)

The project supported a number of Penn State students, whom are listed below along with the degrees that were earned.

Brian Reinhardt, PSU, ESM, USA, PhD in-progress
Gloria Choi, PSU, ESM, USA, PhD in-progress
Yang Liu, PSU, ESM, China, PhD August 2014
Cliff Searfass, PSU, ESM USA, PhD May 2012
Alison Orr, PSU, Acoustics, USA, MS Acoustics May 2015
Robert Cyphers, PSU, ESM, USA, MS Engineering Science December 2012
Kyle Sinding, PSU Engineering Science, USA, BS Engineering Science May 2014
Nathan Malarich, PSU Engineering Science, BS Engineering Science expected May 2015

APPENDIX. <u>JOURNAL ARTICLES</u>

1. C.J. Lissenden, Y. Liu, J.L. Rose, 2015, "Use of nonlinear ultrasonic guided waves for early damage detection," *Insight* Vol. 57(4), in-press.

2. Y. Liu, C.J. Lissenden, J.L. Rose, 2014, "Higher order interaction of elastic waves in weakly nonlinear circular cylinders. I. analytical foundation," *J. Appl. Phys*. Vol. 115:214901.

3. Y. Liu, E. Khajeh, C.J. Lissenden, J.L. Rose, 2014, "Higher order interaction of elastic waves in weakly nonlinear circular cylinders. II. physical interpretation and numerical simulation," *J. Appl. Phys*. Vol. 115:214902.

4. Y. Liu, V.K. Chillara, C.J. Lissenden, J.L. Rose, 2013, "Cubic nonlinear shear horizontal and Rayleigh Lamb waves in weakly nonlinear plates," *J. Appl. Phys*. Vol. 114:114908.

5. Y. Liu, E. Khajeh, C.J. Lissenden, J.L. Rose, 2013, "Interaction of torsional and longitudinal guided waves in weakly nonlinear circular cylinders," *J. Acoustic Soc. Am*. Vol. 133(5):2541-2553.

Higher order interaction of elastic waves in weakly nonlinear hollow circular cylinders. I. Analytical foundation

Yang Liu, Cliff J. Lissenden, and Joseph L. Rose

Articles you may be interested in

Higher order interaction of elastic waves in weakly nonlinear hollow circular cylinders. II. Physical interpretation and numerical results
J. Appl. Phys. **115**, 214902 (2014); 10.1063/1.4879460

Third harmonic shear horizontal and Rayleigh Lamb waves in weakly nonlinear plates
J. Appl. Phys. **114**, 114908 (2013); 10.1063/1.4821252

Interaction of torsional and longitudinal guided waves in weakly nonlinear circular cylinders
J. Acoust. Soc. Am. **133**, 2541 (2013); 10.1121/1.4795806

Interaction of guided wave modes in isotropic weakly nonlinear elastic plates: Higher harmonic generation
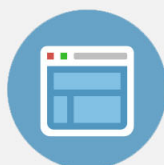J. Appl. Phys. **111**, 124909 (2012); 10.1063/1.4729554

Guided circumferential shear horizontal waves in an isotropic hollow cylinder
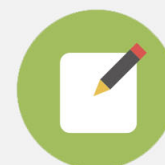J. Acoust. Soc. Am. **115**, 1912 (2004); 10.1121/1.1691037

Higher order interaction of elastic waves in weakly nonlinear hollow circular cylinders. I. Analytical foundation

Yang Liu, Cliff J. Lissenden,[a)] and Joseph L. Rose
Department of Engineering Science and Mechanics, The Pennsylvania State University, University Park, Pennsylvania 16802, USA

A mathematical framework to analyze the cumulative behavior of higher order harmonic generation due to the interaction of two collimated waves in a weakly nonlinear hollow circular cylinder is formulated in this article. A total number of $(N+1)(N+2)/2 - 3$ nonlinear boundary problems are formulated due to the Nth order mode interactions in a cylinder with Kth order nonlinearity ($N \leq K$). The cumulative criteria for the second order harmonics (second harmonics, sum and difference harmonics) due to the quadratic interactions of two waves are examined based on the nonlinear forcing terms in curvilinear coordinates. These criteria are formulated by a synchronism condition, the circumferential orders of the primary modes, as well as the nature of the primary and the secondary wave fields, i.e., torsional or longitudinal. A generalized analysis that provides insight into the cumulative nature of the Nth order harmonics by Nth order interaction of two collimated waves is conducted by considering a cylinder with strain energy function written as Murnaghan's power series. The nature of the cumulative Nth order harmonics can be determined by the parity of the number of times the primary waves interact, and their circumferential orders. © 2014 AIP Publishing LLC. [http://dx.doi.org/10.1063/1.4879459]

I. INTRODUCTION

Nonlinear ultrasonics has the potential to provide sensitivity to the changes in microstructural features such as dislocation density,[1–5] persistent slip bands,[6] irradiation,[7] and second phase precipitates[8] that precede the initiation of macro scale defects. Anharmonicity of ultrasonics is produced by the scattering of the monochromatic waves due to the nonlinearity involving anomalies in lattice structures and the associated higher order lattice potential. The second order harmonic generation due to the quadratic interactions of bulk longitudinal and transverse waves was investigated by Gol'dberg,[9] Jones and Kobett,[10] Childress and Hambrick,[11] and Bender et al.,[12] based on Landau's qualitative formulation of anharmonic vibration.[13] Deng,[14,15] de Lima and Hamilton,[16,17] Srivastava and Lanza di Scalea,[18,19] Müller et al.,[20] Liu et al.,[21–23] and Chillara and Lissenden[24] extend the study of higher order harmonic generation to waveguides: i.e., plates, rods, and rails, which combines the sensitivity of nonlinear ultrasonics with the large inspection range of guided waves.

The elastic guided waves in hollow circular cylinders have drawn research efforts for many years due to the many uses for hollow circular cylinders and the unique defect characterization potential and energy focusing capability of guided waves.[25] However, there has been limited understanding of nonlinear generation of elastic waves in cylindrical waveguides. De Lima and Hamilton[17] solved the nonlinear wave equation in quadratic nonlinear waveguides with arbitrary cross-sections. They presented a criterion for cumulative second order harmonics in cylindrical rods and shells due to the quadratic interactions of longitudinal modes. Srivastava

and Lanza di Scalea[19] studied the higher harmonic generation due to a single longitudinal mode in rods, and found that the nature of the primary generating modes restricts the mode circumferential orders that can be generated as higher harmonics. Liu et al.[22] formulated the problem of nonlinear interaction of axisymmetric torsional and longitudinal modes in a general curvilinear coordinate system. Their analysis indicated that both torsional and longitudinal second order harmonics can be internally resonant with a specific type of primary wave interaction. Nonlinear finite element results corroborated their theoretical predications.

In this article, a generalized approach is presented to analze the cumulative nature of higher order harmonics due to the scattering of two collimated interacting wave modes a and b in an isotropic weakly nonlinear elastic hollow circular cylinder. The nonlinear stress and the nonlinear body force are formulated in curvilinear coordinates, which enables us to analyze the cumulative behavior of the second order harmonics due to the different natures of wave interactions, i.e., torsional-torsional (*TF-TF*), longitudinal-longitudinal (*LF-LF*), and torsional-longitudinal (*TF-LF*). Waves with either torsional or longitudinal nature are considered as secondary wave fields. The analysis is further generalized to the Nth order higher harmonic generation due to the interactions of two waves in a cylinder with Kth order nonlinearity.

Before proceeding with the formulation of this general nonlinear wave problem, it is helpful to clarify nomenclature used herein.

- Kth order nonlinearity: the elastic stress-strain relation is of order K.
- Second harmonic generation (SHG): harmonics generated due to self interaction at twice the excitation frequency.

a)Author to whom correspondence should be addressed. Electronic mail: lissenden@psu.edu

- Second order harmonics (SOH): sum and difference harmonics in addition to second harmonics.
- Nth harmonic generation (NHG): harmonics generated at N times the excitation frequency due to mode self interaction.
- Nth order harmonics (NOH): including two Nth harmonics and $2(N-1)$ higher harmonics due to the mutual interactions ($N \leq K$).
- Waves with torsional nature (TF): typically denoted T_μ^M, where M is circumferential order and μ is the family order, this includes axisymmetric ($M=0$) modes and flexural ($M \neq 0$) modes.
- Waves with longitudinal nature (LF): typically denoted L_μ^M, this also includes axisymmetric and flexural modes.

II. NONLINEAR MODE INTERACTIONS-PROBLEM FORMULATION

Consider a weakly nonlinear, isotropic, elastic medium that is homogeneous with strain energy density given by Murnaghan's power series[26]

$$S_E = \phi_2 + \phi_3 + \cdots + \phi_{K+1}, \quad (1)$$

where ϕ_2 consists of the second order strain terms that provide linear elasticity, and ϕ_3 consists of third order strain terms that correspond to the quadratic nonlinearity. Similarly, the Kth order nonlinearity is associated with ϕ_{K+1}, which consists of $(K+1)$th order strain terms.

In finite strain theory, the Lagrangian strain tensor $\boldsymbol{E}$ is given by

$$E_{ij} = \frac{1}{2}\left(u_{i;j} + u_{j;i} + u^k_{;i}u_{k;j}\right), \quad (2)$$

where $u_i = u_i(Y^1, Y^2, Y^3, t)$ is the particle displacement in the curvilinear reference configuration. The term $u_{i;j}$ is the gradient of particle displacement, which is given by the co-variant derivative of u_i with respect to Y^j.

The second Piola-Kirchhoff stress T_{ij}^{RR} is a referential measure of stress that is paired with the Lagrangian strain tensor through the strain energy function

$$T_{ij}^{RR} = \frac{\partial S_E}{\partial E^{ij}}. \quad (3)$$

The first Piola-Kirchhoff stress T_{ij}^R is related to the second Piola-Kirchhoff stress T_{ij}^{RR} by

$$T_{ij}^R = T_{ij}^{RR} + u_{i;k}(T^{RR})^k_{;j}, \quad (4)$$

which can be decomposed into linear and nonlinear parts

$$T_{ij}^R = T_{ij}^{R-L} + \bar{T}_{ij}, \quad (5)$$

where T_{ij}^{R-L} is the linear part that corresponds to a monochromatic elastic wave. $\bar{T}_{ij}$ collects all the anharmonic particle displacement terms, which are associated with distortion of the elastic waves and result in the generation of higher harmonics.

The main methodology for investigating elastic waves in cylinders is in terms of normal modes,[27] which categorizes these waves by mode type, i.e., axisymmetric longitudinal, axisymmetric torsional, and flexural waves when the wave vector is in the axial direction; circumferential waves for propagation around the annulus. In this work, we focus on the analysis of the higher order harmonic generation of waves having a wavevector that coincides with the Z axis of a cylinder as shown in Fig. 1. The phase velocity dispersion curves that demonstrate these normal modes are shown in Fig. 2 for a steel pipe of inner radius R_i and outer radius R_o. The black solid lines and blue dashed lines represent for modes with torsional and longitudinal nature, respectively. Axisymmetric waves and flexural waves with circumferential order up to 8 are shown in Fig. 2.

Consider two collimated guided wave modes $\mathbf{u}^{(a)}$ and $\mathbf{u}^{(b)}$ propagating in the cylinder shown in Fig. 1. The two wave modes propagate in the same direction or opposite directions, for both cases they interact in a region Ω. Both TF and LF nature modes are considered for $\mathbf{u}^{(a)}$ and $\mathbf{u}^{(b)}$ using a cylindrical coordinate system. The particle displacement for the waves with torsional nature is[27]

$$\mathbf{u}_\mu^M = \left\{ U_{\mu R}^M(R)\sin(M\Theta)\mathbf{e}_R + U_{\mu\Theta}^M(R)\cos(M\Theta)\mathbf{e}_\Theta \right.$$
$$\left. + U_{\mu Z}^M(R)\sin(M\Theta)\mathbf{e}_Z \right\}e^{\pm i\left(k_\mu^M Z - \omega_\mu^M t\right)}, \quad (6)$$

while for longitudinal guided waves it is[27]

$$\mathbf{u}_\mu^M = \left\{ U_{\mu R}^M(R)\cos(M\Theta)\mathbf{e}_R + U_{\mu\Theta}^M(R)\sin(M\Theta)\mathbf{e}_\Theta \right.$$
$$\left. + U_{\mu Z}^M(R)\cos(M\Theta)\mathbf{e}_Z \right\}e^{\pm i\left(k_\mu^M Z - \omega_\mu^M t\right)}, \quad (7)$$

where k_μ^M and ω_μ^M are the wavenumber and circular frequency of the μth family order of the Mth circumferential order, respectively. The indices "+" and "−" denote the phase changing pattern of the waves.

The total displacement field in the interacting region Ω of the two guided wave modes $\mathbf{u}^{(a)}$ and $\mathbf{u}^{(b)}$ can be decomposed into fundamental and secondary wave fields with a perturbation assumption (up to Nth order mode interaction)

$$\mathbf{u} = \mathbf{u}^{(a)} + \mathbf{u}^{(b)} + \mathbf{u}^{(a,b,2,0)} + \mathbf{u}^{(a,b,0,2)} + \mathbf{u}^{(a,b,1,1)}$$
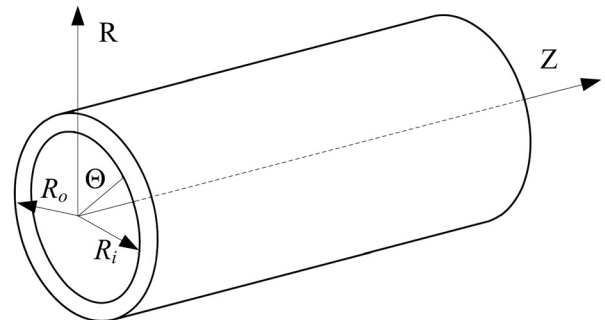$$+ \cdots + \mathbf{u}^{(a,b,N_1,N_2)}, \quad (8)$$

FIG. 1. Geometry and the reference coordinate system of the hollow circular cylinder.
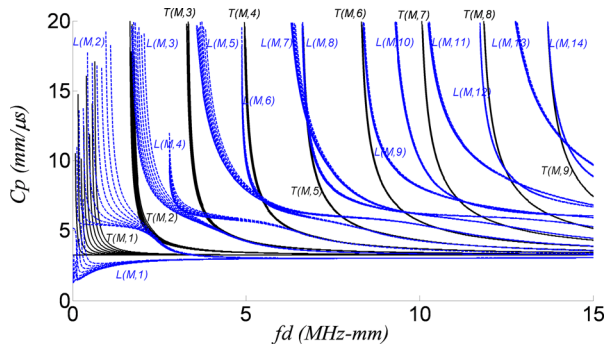
FIG. 2. Phase velocity dispersion curves for a steel pipe. $T(M,\mu)$ and $L(M,\mu)$ represent torsional flexural and longitudinal flexural modes in family μ having circumferential order M, respectively. $c_L = 5.96\,\text{mm}/\mu s$, $c_T = 3.23\,\text{mm}/\mu s$, $R_i = 9\,\text{mm}$, $R_o = 10.5\,\text{mm}$, and $d = R_o - R_i$.

where $\mathbf{u}^{(a,b,2,0)}$ and $\mathbf{u}^{(a,b,0,2)}$ are the particle displacements of the SHG due to the quadratic self interaction of mode a and mode b, respectively. $\mathbf{u}^{(a,b,1,1)}$ is the displacement field due to the quadratic mutual interaction of the two modes. We shall use $\mathbf{u}^{(aa)}$, $\mathbf{u}^{(bb)}$, and $\mathbf{u}^{(ab)}$ to represent the SOHs in the following text for conciseness. The term $\mathbf{u}^{(a,b,N_1,N_2)}$ represents the NOHs due to mutual interaction, where mode a participates N_1 times $(N_1 = 0, 1, 2\ldots N)$ and mode b interacts N_2 times $(N_2 = 0, 1, 2,\ldots N)$, with $N_1 + N_2 = N$. A $2N$ number of NOHs exist at Nth order mode interaction; e.g., SOHs exist at frequencies $2\omega_a$, $2\omega_b$, $\omega_a + \omega_b$, $\omega_a - \omega_b$ for $N = 2$. It is assumed that the secondary displacements are very small compared with the fundamental displacement, that is

$$|\mathbf{u}^{(aa)}|, |\mathbf{u}^{(bb)}|, |\mathbf{u}^{(ab)}|, \cdots, |\mathbf{u}^{(a,b,N_1,N_2)}| \leq\leq |\mathbf{u}^{(a)}|, |\mathbf{u}^{(b)}|. \quad (9)$$

Substituting Eqs. (8) and (9) into the first Piola-Kirchhoff stress Eq. (5)

$$
\begin{aligned}
T_{ij}^R = &\, T_{ij}^{R-L}\big(\mathbf{u}^{(a)}\big) + T_{ij}^{R-L}\big(\mathbf{u}^{(b)}\big) + T_{ij}^{R-L}\big(\mathbf{u}^{(aa)}\big) + T_{ij}^{R-L}\big(\mathbf{u}^{(bb)}\big) \\
&+ T_{ij}^{R-L}\big(\mathbf{u}^{(ab)}\big) + \cdots + T_{ij}^{R-L}\big(\mathbf{u}^{(a,b,N_1,N_2)}\big) \\
&+ \bar{T}_{ij}\big(\mathbf{u}^{(a)}, \mathbf{u}^{(b)}, 2, 0\big) + \bar{T}_{ij}\big(\mathbf{u}^{(a)}, \mathbf{u}^{(b)}, 0, 2\big) \\
&+ \bar{T}_{ij}\big(\mathbf{u}^{(a)}, \mathbf{u}^{(b)}, 1, 1\big), \\
&+\ldots + \bar{T}_{ij}\big(\mathbf{u}^{(a)}, \mathbf{u}^{(b)}, N, 0\big) + \bar{T}_{ij}\big(\mathbf{u}^{(a)}, \mathbf{u}^{(b)}, 0, N\big) \\
&+\ldots + \bar{T}_{ij}\big(\mathbf{u}^{(a)}, \mathbf{u}^{(b)}, N_1, N_2\big), \quad (10)
\end{aligned}
$$

where $T_{ij}^{R-L}\big(\mathbf{u}^{(a)}\big)$ and $T_{ij}^{R-L}\big(\mathbf{u}^{(b)}\big)$; $T_{ij}^{R-L}\big(\mathbf{u}^{(aa)}\big)$, $T_{ij}^{R-L}\big(\mathbf{u}^{(bb)}\big)$, $T_{ij}^{R-L}\big(\mathbf{u}^{(ab)}\big)$; and $T_{ij}^{R-L}\big(\mathbf{u}^{(a,b,N_1,N_2)}\big)$ are the first, second, and Nth order approximations of the linear part of the first Piola-Kirchhoff stress. The notation $\bar{T}_{ij}\big(\mathbf{u}^{(a)}, \mathbf{u}^{(b)}, N_1, N_2\big)$ represent the nonlinear terms of order N in the displacement gradient of the first Piola-Kirchhoff stress due to the interactions between modes a and b. Both self interactions and mutual interactions are considered. All other terms containing nonlinear stress are quadratic or higher order powers of secondary displacements and therefore are disregarded according to the perturbation assumption of Eq. (9).

Equation (10) suggests that the nonlinear stress terms require the following exponential terms:

$$e^{\pm i\big\{\big(k_{\mu_a}^{M_a} \pm k_{\mu_b}^{M_b}\big)Z - \big(\omega_{\mu_a}^{M_a} \pm \omega_{\mu_b}^{M_b}\big)t\big\}}, \cdots,$$

$$e^{\pm i\big\{\big(N_1 k_{\mu_a}^{M_a} \pm N_2 k_{\mu_b}^{M_b}\big)Z - \big(N_1\omega_{\mu_a}^{M_a} \pm N_2\omega_{\mu_b}^{M_b}\big)t\big\}}, \quad (11)$$

which correspond to the secondary waves at frequency-wavenumber pairs $(\omega_{\mu_a}^{M_a} \pm \omega_{\mu_b}^{M_b}, k_{\mu_a}^{M_a} \pm k_{\mu_b}^{M_b}), \cdots, (N_1 k_{\mu_a}^{M_a} \pm N_2 k_{\mu_b}^{M_b}, N_1\omega_{\mu_a}^{M_a} \pm N_2\omega_{\mu_b}^{M_b})$ due to the Nth order mode self interactions and mutual interactions. The sum harmonics (at $\omega_{\mu_a}^{M_a} + \omega_{\mu_b}^{M_b}\cdots, N_1\omega_{\mu_a}^{M_a} + N_2\omega_{\mu_b}^{M_b}$) are produced when the two guided waves $\mathbf{u}^{(a)}$ and $\mathbf{u}^{(b)}$ are of the same phase changing pattern, while the difference harmonics (at $\omega_{\mu_a}^{M_a} - \omega_{\mu_b}^{M_b}\cdots, N_1\omega_{\mu_a}^{M_a} - N_2\omega_{\mu_b}^{M_b}$) are generated provided $\mathbf{u}^{(a)}$ and $\mathbf{u}^{(b)}$ have opposite phase changing patterns.

The balance of linear momentum in the reference configuration and satisfying the traction free boundary conditions provide the primary and secondary boundary value problems (BVPs) with the help of the perturbation analysis. The primary BVP for modes a and b is

$$
\begin{aligned}
T_{ij;j}^{R-L} &= \rho_0 \ddot{u}_i, \\
T_{ij}^{R-L} n^j &= 0. \quad (12)
\end{aligned}
$$

There are a total of $(N+1)(N+2)/2 - 3$ secondary BVPs to be formulated due to the Nth order mode interactions. These secondary BVPs include mode a self interaction at quadratic nonlinearity

$$
\begin{aligned}
T_{ij;j}^{R-Lj}\big(\mathbf{u}^{(aa)}\big) - \rho_0 \ddot{u}_i^{(aa)} &= -\bar{T}_{ij;j}^j\big(\mathbf{u}^{(a)}, \mathbf{u}^{(b)}, 2, 0\big) \\
(T_{ij}^{R-L}\big(\mathbf{u}^{(aa)}\big))n^j &= -\bar{T}_{ij}\big(\mathbf{u}^{(a)}, \mathbf{u}^{(b)}, 2, 0\big)n^j, \quad (13)
\end{aligned}
$$

mode b self interaction at quadratic nonlinearity

$$
\begin{aligned}
T_{ij;j}^{R-Lj}\big(\mathbf{u}^{(bb)}\big) - \rho_0 \ddot{u}_i^{(bb)} &= -\bar{T}_{ij;j}^j\big(\mathbf{u}^{(a)}, \mathbf{u}^{(b)}, 0, 2\big) \\
(T_{ij}^{R-L}\big(\mathbf{u}^{(bb)}\big))n^j &= -\bar{T}_{ij}\big(\mathbf{u}^{(a)}, \mathbf{u}^{(b)}, 0, 2\big)n^j, \quad (14)
\end{aligned}
$$

mode a and b mutual interaction at quadratic nonlinearity

$$
\begin{aligned}
T_{ij;j}^{R-Lj}\big(\mathbf{u}^{(ab)}\big) - \rho_0 \ddot{u}_i^{(ab)} &= -\bar{T}_{ij;j}^j\big(\mathbf{u}^{(a)}, \mathbf{u}^{(b)}, 1, 1\big) \\
(T_{ij}^{R-L}\big(\mathbf{u}^{(ab)}\big))n^j &= -\bar{T}_{ij}\big(\mathbf{u}^{(a)}, \mathbf{u}^{(b)}, 1, 1\big)n^j, \quad (15)
\end{aligned}
$$

and N_1th power mode a and N_2th power mode b mutual interactions, which gives Nth mode interactions

$$
\begin{aligned}
T_{ij;j}^{R-Lj}\big(\mathbf{u}^{(a,b,N_1,N_2)}\big) - \rho_0 \ddot{u}_i^{(a,b,N_1,N_2)} &= -\bar{T}_{ij;j}^j\big(\mathbf{u}^{(a)}, \mathbf{u}^{(b)}, N_1, N_2\big) \\
(T_{ij}^{R-L}\big(\mathbf{u}^{(a,b,N_1,N_2)}\big))n^j &= -\bar{T}_{ij}\big(\mathbf{u}^{(a)}, \mathbf{u}^{(b)}, N_1, N_2\big)n^j. \quad (16)
\end{aligned}
$$

As an example, for cubic interactions[23] $(N = 3)$, the $(N+1)(N+2)/2 - 3 = 7$ secondary BVPs entail the mode interactions: aa, bb, ab, aaa, bbb, aab, abb.

Following the method of de Lima and Hamilton,[16] the secondary problem due to the mode interactions can be solved using the normal mode expansion technique along with the complex reciprocity relation given by Auld.[28] Let solution '1' be an arbitrary secondary mode with

circumferential and family orders $\bar{M}$ and $\bar{\mu}$, respectively. The modal expansion of the reciprocal solution '2' is

$$u_i^{(2)} = \sum_{M=0}^{\infty} \sum_{\mu} A_\mu^M(Z) u_{\mu\ i}^M(R,\Theta) e^{i\left(N_1 \omega_{\mu_a}^{M_a} \pm N_2 \omega_{\mu_b}^{M_b}\right)t}, \quad (17)$$

where $u_i^{(2)}$ is the secondary displacement field, which could be $\mathbf{u}^{(aa)}$, $\mathbf{u}^{(bb)}$, $\mathbf{u}^{(ab)} \ldots \mathbf{u}^{(a,b,N_1,N_2)}$. The term $u_{\mu\ i}^M(R,\Theta)$ is the displacement component of an arbitrary guided wave mode with the Mth circumferential order and the μth family order at frequency $N_1 \omega_{\mu_a}^{M_a} \pm N_2 \omega_{\mu_b}^{M_b}$. $A_\mu^M(Z)$ is the modal amplitude of the secondary wave field. Further, the modal displacement profile enables us to write

$$v_i^{(2)} = \frac{\partial u_i^{(2)}}{\partial t}, \quad (18)$$

$$T_{ij}^{R-L(2)} = \lambda u_{l;}^{(2)l} g_{ij} + \mu(u_{i;j}^{(2)} + u_{j;i}^{(2)}). \quad (19)$$

The modal amplitudes, $A_\mu^M(Z)$, are determined for each mode from the ordinary differential equation

$$4 P_{\bar{\mu}\ \mu}^{\bar{M}\ M}\left(\frac{\partial A_\mu^M(Z)}{\partial Z} + i k_{\bar{\mu}}^{\bar{M}^*} A_\mu^M(Z)\right) = p_{\bar{\mu}}^{\bar{M}} e^{-i k_{\bar{\mu}}^{\bar{M}^*} Z}, \quad (20)$$

where

$$P_{\bar{\mu}\ \mu}^{\bar{M}\ M} = -\frac{1}{16}\int_0^{2\pi}\int_{R_i}^{R_o}(\mathbf{v}_{\bar{\mu}}^{\bar{M}^*} \cdot \mathbf{T}_\mu^M + \mathbf{v}_\mu^M \cdot \mathbf{T}_{\bar{\mu}}^{\bar{M}^*}) \cdot \mathbf{n}_Z R dR d\Theta, \quad (21)$$

$$p_{\bar{\mu}}^{\bar{M}} = p_{\bar{\mu}}^{\bar{M}-surf} + p_{\bar{\mu}}^{\bar{M}-vol}, \quad (22)$$

$$p_{\bar{\mu}}^{\bar{M}-surf} = \frac{R_o}{2}\int_0^{2\pi}\mathbf{v}_{\bar{\mu}}^{\bar{M}^*}(R_o,\Theta) \cdot \bar{\mathbf{T}}_{\bar{\mu}}^{\bar{M}}(R_o,\Theta) \cdot \mathbf{n} d\Theta$$
$$- \frac{R_i}{2}\int_0^{2\pi}\mathbf{v}_{\bar{\mu}}^{\bar{M}^*}(R_i,\Theta) \cdot \bar{\mathbf{T}}_{\bar{\mu}}^{\bar{M}}(R_i,\Theta) \cdot \mathbf{n} d\Theta, \quad (23)$$

$$p_{\bar{\mu}}^{\bar{M}-vol} = \frac{1}{2}\int_0^{2\pi}\int_{R_i}^{R_o} Div(\bar{\mathbf{T}}_{\bar{\mu}}^{\bar{M}}) \mathbf{v}_{\bar{\mu}}^{\bar{M}^*} R dR d\Theta. \quad (24)$$

The solution to Eq. (20) is

$$A_\mu^M(Z) = \frac{i p_{\bar{\mu}}^{\bar{M}}}{4 P_{\bar{\mu}\ \mu}^{\bar{M}\ M}[k_{\bar{\mu}}^{\bar{M}^*} - (N_1 k_{\mu_a}^{M_a} \pm N_2 k_{\mu_b}^{M_b})]}$$
$$\times \left(e^{i\left(N_1 k_{\mu_a}^{M_a} \pm N_2 k_{\mu_b}^{M_b}\right)Z} - e^{i k_{\bar{\mu}}^{\bar{M}^*} Z}\right)$$
$$\text{if } k_{\bar{\mu}}^{\bar{M}^*} \neq (N_1 k_{\mu_a}^{M_a} \pm N_2 k_{\mu_b}^{M_b}), \quad (25)$$

$$A_\mu^M(Z) = \frac{p_{\bar{\mu}}^{\bar{M}} Z}{4 P_{\bar{\mu}\ \mu}^{\bar{M}\ M}} e^{i\left(N_1 k_{\mu_a}^{N_a} \pm N_2 k_{\mu_b}^{N_b}\right)Z},$$
$$\text{if } k_{\bar{\mu}}^{\bar{M}^*} = (N_1 k_{\mu_a}^{N_a} \pm N_2 k_{\mu_b}^{N_b}), \quad (26)$$

where $P_{\bar{\mu}\ \mu}^{\bar{M}\ M}$ is the complex power flux in the propagation direction, $k_{\bar{\mu}}^{\bar{M}^*}$ is the wavenumber of the unique mode such

that $P_{\bar{\mu}\ \mu}^{\bar{M}\ M} \neq 0$, $p_{\bar{\mu}}^{\bar{M}-surf}$, and $p_{\bar{\mu}}^{\bar{M}-vol}$ are interpreted as power flux through the surface and through the volume, respectively, due to the fundamental mode interactions.

A cumulative higher order harmonic mode, having linearly increasing amplitude with propagation distance, therefore requires that: (i) $k_{\bar{\mu}}^{\bar{M}^*} = (N_1 k_{\mu_a}^{M_a} \pm N_2 k_{\mu_b}^{M_b})$, i.e., generalized phase matching, (ii) $p_{\bar{\mu}}^{\bar{M}} \neq 0$, i.e., non-zero power flux. These two conditions are driven by Eqs. (25) and (26) and taken together represent the requirement for internal resonance. In Secs. III and IV, we will comment on which modes, if any, show cumulative nature due to the interactions of mode a and b.

III. MODE INTERACTIONS AT QUADRATIC NONLINEARITY

Consider a material with quadratic nonlinearity, i.e., $K = 2$. Truncating the strain energy function in Eq. (1) at third order and writing it in terms of strain components as given by Landau and Lifshitz[13,22]

$$S_E = \frac{1}{2}\lambda\left(E_k^{\ k}\right)^2 + \mu E_{ij} E^{ji} + \frac{1}{3}C\left(E_k^{\ k}\right)^3$$
$$+ B E_k^{\ k} E_{ij} E^{ji} + \frac{1}{3}A E_{ij} E^j_{\ k} E^{ki}, \quad (27)$$

where λ and μ are Lamé's constants and A, B, and C are Landau third order elastic constants.

Substitute Eq. (27) into Eq. (3) and keep all terms up to second order in the displacement gradient $u_{i;j}$. The linear and nonlinear parts of the first Piola-Kirchhoff stress are given by[22]

$$T_{ij}^{R-L} = \lambda u_{l;}^{\ l} g_{ij} + \mu(u_{i;j} + u_{j;i}), \quad (28)$$

$$\bar{T}_{ij} = \frac{\lambda}{2} u_{k;l} u^{k;l} g_{ij} + (\lambda + B) u_{l;}^{\ l} u_{i;j} + C\left(u_{l;}^{\ l}\right)^2 g_{ij}$$
$$+ \frac{B}{2}\left(u_{l;k} u^{k;l} + u_{k;l} u^{k;l}\right) g_{ij} + B u_{l;}^{\ l} u_{j;i} + \frac{A}{4} u_{k;i} u_{j;}^{\ k}$$
$$+ \left(\mu + \frac{A}{4}\right)\left(u_{i;k} u^k_{\ ;j} + u_{k;i} u^k_{\ ;j} + u_{i;k} u_{j;}^{\ k}\right) + O\left((u_{i;j})^3\right), \quad (29)$$

respectively. Furthermore, the divergence of the nonlinear stress, $\bar{f}_i$, which is often referred to as the nonlinear body force, is

$$\bar{f}_i = (\lambda + B)\left(u_{k;}^{\ kj} u_{i;j} + u_{k;}^{\ k} u_{i;j}^{\ j} + u_{k;ji} u^{k;j}\right)$$
$$+ (B + 2C) u_{j;}^{\ j} u_{k;\ i}^{\ k} + \left(\frac{A}{4} + B\right)\left(u_{k;}^{\ kj} u_{j;i} + u_{j;ki} u^{k;j}\right)$$
$$+ \left(\mu + \frac{A}{4}\right)\left(u_{i;k}^{\ j} u^k_{\ ;j} + u_{i;k} u^k_{\ ;j}^{\ j} + u_{k;i}^{\ j} u^k_{\ ;j}\right.$$
$$\left. + u_{k;i} u^k_{\ ;j}^{\ j} + u_{i;k} u_{j;}^{\ k} + u_{i;k} u_{j;}^{\ kj}\right) + O\left((u_{i;j})^3\right). \quad (30)$$

Equations (29) and (30) extend Gol'dberg's[9] expression of quadratic nonlinear forcing terms from Cartesian coordinates to a general curvilinear coordinate system. Equations (29) and (30) can be adapted for a specific curvilinear coordinate system, such as cylindrical coordinates by using the metric tensor g_{ij} and Christoffel symbols Γ_{ij}^k in the corresponding coordinates. The expressions for the nonlinear

stress components in cylindrical coordinates for flexural guided waves are provided in the Appendix.

The secondary problem of quadratic interactions between modes a and b can be classified into three general cases: (i) both modes a and b are of torsional nature (TF-TF), (ii) both modes a and b are of longitudinal nature (LF-LF), or (iii) modes a and b are of different nature - one torsional and one longitudinal (TF-LF). The quadratic nonlinear stress and the nonlinear body force are given by

$$\bar{T}_{ij}^M = \bar{T}_{ij}\big(\mathbf{u}^{(a)}, \mathbf{u}^{(b)}, 2, 0\big) + \bar{T}_{ij}\big(\mathbf{u}^{(a)}, \mathbf{u}^{(b)}, 0, 2\big)$$
$$+ \bar{T}_{ij}\big(\mathbf{u}^{(a)}, \mathbf{u}^{(b)}, 1, 1\big), \tag{31}$$

$$\bar{f}_i^M = \bar{f}_i\big(\mathbf{u}^{(a)}, \mathbf{u}^{(b)}, 2, 0\big) + \bar{f}_i\big(\mathbf{u}^{(a)}, \mathbf{u}^{(b)}, 0, 2\big)$$
$$+ \bar{f}_i\big(\mathbf{u}^{(a)}, \mathbf{u}^{(b)}, 1, 1\big). \tag{32}$$

The nonzero power flux condition can be assessed by substituting Eqs. (6) and (7) into Eqs. (31) and (32) and examining the trigonometric properties of the nonlinear stress and the nonlinear body force with respect to the circumferential direction. The cases of non-zero power flux $p_{\bar{\mu}}^{\bar{M}}$

can be identified by inspecting Eq. (22). De Lima and Hamilton[21] did this for longitudinal modes, but here all longitudinal and torsional modes (axisymmetric and flexural) are considered. De Lima and Hamilton[21] were unable to distinguish between the types of modes present, i.e., longitudinal or torsional, because they did not have the expressions of the nonlinear forcing terms for flexural waves. Within our framework, Eqs. (29), (30), and (A1)–(A9) enable us to analyze cumulative behavior of second order harmonic generation due to quadratic interactions of waves having different nature.

A. Mode *a* and mode *b* are of the same nature (*LF-LF* or *TF-TF*)

Consider both mode a and mode b to have the same nature, either longitudinal or torsional, and let modes a and b have circumferential orders P and Q, respectively. The circumferential dependence of the nonlinear stress $\bar{\mathbf{T}}$ and the nonlinear body force $\bar{\mathbf{f}}$ can be obtained by assessing the nonlinear stress components given in the appendix Eqs. (A1)–(A9) along with Eqs. (6) and (7). The superscript S denotes that modes a and b are of the same nature. In matrix form we have

$$\bar{\mathbf{T}}^S = \begin{bmatrix} \bar{T}_{RR}^{(1)}\cos 2P\Theta + \bar{T}_{RR}^{(2)}\cos 2Q\Theta & \bar{T}_{R\Theta}^{(1)}\sin 2P\Theta + \bar{T}_{R\Theta}^{(2)}\sin 2Q\Theta & \bar{T}_{RZ}^{(1)}\cos 2P\Theta + \bar{T}_{RZ}^{(2)}\cos 2Q\Theta \\ +\bar{T}_{RR}^{(3)}\cos(P\pm Q)\Theta & +\bar{T}_{R\Theta}^{(3)}\sin(P\pm Q)\Theta & +\bar{T}_{RZ}^{(3)}\cos(P\pm Q)\Theta \\ \bar{T}_{\Theta R}^{(1)}\sin 2P\Theta + \bar{T}_{\Theta R}^{(2)}\sin 2Q\Theta & \bar{T}_{\Theta\Theta}^{(1)}\cos 2P\Theta + \bar{T}_{\Theta\Theta}^{(2)}\cos 2Q\Theta & \bar{T}_{\Theta Z}^{(1)}\sin 2P\Theta + \bar{T}_{\Theta Z}^{(2)}\sin 2Q\Theta \\ +\bar{T}_{\Theta R}^{(3)}\sin(P\pm Q)\Theta & +\bar{T}_{\Theta\Theta}^{(3)}\cos(P\pm Q)\Theta & +\bar{T}_{\Theta Z}^{(3)}\sin(P\pm Q)\Theta \\ \bar{T}_{ZR}^{(1)}\cos 2P\Theta + \bar{T}_{ZR}^{(2)}\cos 2Q\Theta & \bar{T}_{Z\Theta}^{(1)}\sin 2P\Theta + \bar{T}_{Z\Theta}^{(2)}\sin 2Q\Theta & \bar{T}_{ZZ}^{(1)}\cos 2P\Theta + \bar{T}_{ZZ}^{(2)}\cos 2Q\Theta \\ +\bar{T}_{ZR}^{(3)}\cos(P\pm Q)\Theta & +\bar{T}_{Z\Theta}^{(3)}\sin(P\pm Q)\Theta & +\bar{T}_{ZZ}^{(3)}\cos(P\pm Q)\Theta \end{bmatrix}, \tag{33}$$

$$\bar{\mathbf{f}}^S = \begin{Bmatrix} \bar{f}_R^{(1)}\cos 2P\Theta + \bar{f}_R^{(2)}\cos 2Q\Theta + \bar{f}_R^{(3)}\cos(P\pm Q)\Theta \\ \bar{f}_\Theta^{(1)}\sin 2P\Theta + \bar{f}_\Theta^{(2)}\sin 2Q\Theta + \bar{f}_\Theta^{(3)}\sin(P\pm Q)\Theta \\ \bar{f}_Z^{(1)}\cos 2P\Theta + \bar{f}_Z^{(2)}\cos 2Q\Theta + \bar{f}_Z^{(3)}\cos(P\pm Q)\Theta \end{Bmatrix}. \tag{34}$$

The superscripts (1), (2), and (3) on the nonlinear stress and body force components represent lengthy terms of self and mutual interactions that do not depend on Θ. The actual elements contained within these theta-independent terms (e.g., $T_{RR}^{(1)}, \bar{f}_R^{(3)}$) are not important for this analysis.

Consider an arbitrary SOH wave field with circumferential order M, which has either torsional or longitudinal nature.

- If the SOH wave field is of torsional nature (denoted by superscript *ST*), then the total power flux from Eq. (22) is

$$p_{\bar{\mu}}^{ST} = \int\limits_0^{2\pi} F^{ST}\begin{pmatrix} \sin M\Theta\cos 2P\Theta, \sin M\Theta\cos 2Q\Theta, \ \sin M\Theta\cos(P\pm Q)\Theta, \\ \cos M\Theta\sin 2P\Theta, \cos M\Theta\sin 2Q\Theta, \cos M\Theta\sin(P\pm Q)\Theta \end{pmatrix}d\Theta = 0, \tag{35}$$

where the types of Θ-dependent terms are shown within the parenthesis for F^{ST}. The integral evaluates to be zero due to the orthogonality relations of sine and cosine.

- If the SOH wave field is of longitudinal nature (denoted by superscript *SL*), then the total power flux is

$$p_{\bar{\mu}}^{SL} = \int_0^{2\pi} F^{SL} \begin{pmatrix} \cos M\Theta \cos 2P\Theta, \ \cos M\Theta \cos 2Q\Theta, \ \cos M\Theta \cos(P\pm Q)\Theta, \\ \sin M\Theta \sin 2P\Theta, \ \sin M\Theta \sin 2Q\Theta, \ \sin M\Theta \sin(P\pm Q)\Theta \end{pmatrix} d\Theta$$

$$\Rightarrow \begin{cases} \neq 0 \ \ if \ \ M = 2P \ \ or \ \ M = 2Q \ \ or \ \ M = P\pm Q, \\ = 0 \ \ for \ \ other \ \ cases. \end{cases} \tag{36}$$

where the types of Θ-dependent terms are shown within the parenthesis for F^{SL}. Notice that SHG is just a special case of mode self interactions. Observations on the behavior of the SOH wave fields due to the second order interaction of two guided wave modes of the same nature can now be made.

(i) Only longitudinal type SOH wave fields can be cumulative by wave interaction of the same nature, and synchronism must occur for this to happen. Torsional type SOH wave fields cannot be in resonance with either type of primary wave field (*TF-TF* or *LF-LF*); they will exhibit a beat effect within the propagation distance, as no power flux occurs from the primary modes to torsional nature secondary fields.

(ii) The non-zero power flux condition is determined by the relationship between the circumferential orders of the primary and the SOH modes. The power flux will be non-zero if and only if $M = 2P$ or $M = 2Q$ or $M = P\pm Q$ for longitudinal nature SOH modes. For example, if the first and second order longitudinal (or torsional) flexural modes are generated as the funda-

mental wave field ($P = 2$, $Q = 1$), the cumulative SOH wave fields will be of the fourth order ($M = 2P$ at $\omega = 2\omega_a$), the second order ($M = 2Q$ at $\omega = 2\omega_b$), the first order ($M = P - Q$), or the third longitudinal modes ($M = P + Q$).

(iii) No cumulative flexural modes can be generated provided the two interacting modes a and b are axisymmetric waves ($P = Q = 0$) of the same nature. However, two interacting flexural modes of the same nature with identical circumferential orders have the potential to generate a cumulative axisymmetric longitudinal secondary wave.

B. Mode *a* and *b* are of the opposite nature (*TF-LF*)

Consider mode a and mode b to be of opposite nature. The circumferential dependence of the nonlinear stress $\bar{\mathbf{T}}$ and the nonlinear body force $\bar{\mathbf{f}}$ can be obtained by assessing the nonlinear stress components given in the appendix Eqs. (A1)–(A9) along with Eqs. (6) and (7). The superscript O denotes that modes a and b are of opposite nature. In matrix form we have

$$\bar{\mathbf{T}}^O = \begin{bmatrix} \bar{T}_{RR}^{(1)}\cos 2P\Theta + \bar{T}_{RR}^{(2)}\cos 2Q\Theta & \bar{T}_{R\Theta}^{(1)}\sin 2P\Theta + \bar{T}_{R\Theta}^{(2)}\sin 2Q\Theta & \bar{T}_{RZ}^{(1)}\cos 2P\Theta + \bar{T}_{RZ}^{(2)}\cos 2Q\Theta \\ +\bar{T}_{RR}^{(3)}\sin(P\pm Q)\Theta & +\bar{T}_{R\Theta}^{(3)}\cos(P\pm Q)\Theta & +\bar{T}_{RZ}^{(3)}\sin(P\pm Q)\Theta \\ \bar{T}_{\Theta R}^{(1)}\sin 2P\Theta + \bar{T}_{\Theta R}^{(2)}\sin 2Q\Theta & \bar{T}_{\Theta\Theta}^{(1)}\cos 2P\Theta + \bar{T}_{\Theta\Theta}^{(2)}\cos 2Q\Theta & \bar{T}_{\Theta Z}^{(1)}\sin 2P\Theta + \bar{T}_{\Theta Z}^{(2)}\sin 2Q\Theta \\ +\bar{T}_{\Theta R}^{(3)}\cos(P\pm Q)\Theta & +\bar{T}_{\Theta\Theta}^{(3)}\sin(P\pm Q)\Theta & +\bar{T}_{\Theta Z}^{(3)}\cos(P\pm Q)\Theta \\ \bar{T}_{ZR}^{(1)}\cos 2P\Theta + \bar{T}_{ZR}^{(2)}\cos 2Q\Theta & \bar{T}_{Z\Theta}^{(1)}\sin 2P\Theta + \bar{T}_{Z\Theta}^{(2)}\sin 2Q\Theta & \bar{T}_{ZZ}^{(1)}\cos 2P\Theta + \bar{T}_{ZZ}^{(2)}\cos 2Q\Theta \\ +\bar{T}_{ZR}^{(3)}\sin(P\pm Q)\Theta & +\bar{T}_{Z\Theta}^{(3)}\cos(P\pm Q)\Theta & +\bar{T}_{ZZ}^{(3)}\sin(P\pm Q)\Theta \end{bmatrix}, \tag{37}$$

$$\bar{\mathbf{f}}^O = \begin{Bmatrix} \bar{f}_R^{(1)}\cos 2P\Theta + \bar{f}_R^{(2)}\cos 2Q\Theta + \bar{f}_R^{(3)}\sin(P\pm Q)\Theta \\ \bar{f}_\Theta^{(1)}\sin 2P\Theta + \bar{f}_\Theta^{(2)}\sin 2Q\Theta + \bar{f}_\Theta^{(3)}\cos(P\pm Q)\Theta \\ \bar{f}_Z^{(1)}\cos 2P\Theta + \bar{f}_Z^{(2)}\cos 2Q\Theta + \bar{f}_Z^{(3)}\sin(P\pm Q)\Theta \end{Bmatrix}. \tag{38}$$

• If the secondary wave field is of torsional nature (denoted by superscript *OT*), the total power flux is

$$p_{\bar{\mu}}^{OT} = \int_0^{2\pi} F^{OT} \begin{pmatrix} \sin M\Theta \cos 2P\Theta, \ \sin M\Theta \cos 2Q\Theta, \ \sin M\Theta \sin(P\pm Q)\Theta, \\ \cos M\Theta \sin 2P\Theta, \ \cos M\Theta \sin 2Q\Theta, \ \cos M\Theta \cos(P\pm Q)\Theta \end{pmatrix} d\Theta \Rightarrow \begin{cases} \neq 0 \ \ if \ \ M = P\pm Q \\ = 0 \ \ if \ \ M \neq P\pm Q. \end{cases} \tag{39}$$

where the Θ dependence of F^{OT} is shown in the parenthesis.

• If the secondary wave field is of longitudinal nature (denoted by superscript *OL*), the total power flux is

$$p_{\bar{\mu}}^{OL} = \int_0^{2\pi} F^{OL} \begin{pmatrix} \cos M\Theta \cos 2P\Theta, \ \cos M\Theta \cos 2Q\Theta, \ \cos M\Theta \sin(P\pm Q)\Theta, \\ \sin M\Theta \sin 2P\Theta, \ \sin M\Theta \sin 2Q\Theta, \ \sin M\Theta \cos(P\pm Q)\Theta \end{pmatrix} d\Theta \Rightarrow \begin{cases} \neq 0 \ \ if \ \ M = 2P \ \ or \ \ M = 2Q \\ = 0 \ \ for \ \ other \ \ cases. \end{cases} \tag{40}$$

where the Θ dependence of F^{OL} is shown in the parenthesis.

Some remarks are given on the quadratic interactions for when modes a and b are of the opposite nature.

(i)   SOH wave fields with either torsional or longitudinal nature have the potential to be cumulative along the propagation distance. The cumulative SOH torsional waves will occur at sum or difference frequencies ($\omega = \omega_a \pm \omega_b$), while the cumulative second harmonic longitudinal waves are present at double frequencies ($\omega = 2\omega_a \; or \; \omega = 2\omega_b$).

(ii)   The power flux from *LF-TF* interaction to the torsional SOH wave field is non-zero if and only if $M = P \pm Q$. For instance, if the first order longitudinal flexural mode (or torsional flexural mode) and second order torsional flexural mode (or longitudinal flexural mode) are generated as the primary wave field, the torsional type of internal resonance secondary wave field will be of first order ($M = P - Q$) or third order ($M = P + Q$).

(iii)   The power flux from *LF-TF* interaction to the longitudinal second harmonic wave field is non-zero if and only if $M = 2P \; or \; M = 2Q$. For example, if the first order longitudinal flexural mode (or torsional flexural mode) and second order torsional flexural mode (or longitudinal flexural mode) are generated as the primary wave field, the longitudinal nature of the internally resonant second harmonic wave field is second order ($M = 2P$) or fourth order ($M = 2Q$).

(iv)   No cumulative flexural waves can be generated if the two interacting modes a and b are axisymmetric waves ($P = Q = 0$) of the opposite nature. However, the two opposite nature interacting flexural modes with identical circumferential order have the potential to generate a cumulative axisymmetric torsional secondary wave.

IV. MODE INTERACTIONS AT HIGHER ORDER NONLINEARITY

Srivastava and Lanza di Scalea[19] addressed the power flux of a rod with higher nonlinearity by considering the functional forms of the nonlinear forcing terms. However, their work is limited to higher harmonic generation from a single longitudinal primary mode. In this section, we will analyze the nature of the higher harmonics due to two intersecting waves (longitudinal or torsional) in a cylinder with Kth order nonlinearity. A higher order harmonic with wavenumber-frequency pair $(N_1 k_{\mu_a}^{M_a} \pm N_2 k_{\mu_b}^{M_b}, N_1 \omega_{\mu_a}^{M_a} \pm N_2 \omega_{\mu_b}^{M_b})$ could be generated due to interactions where mode a participates N_1 times and mode b interacts N_2 times, where the total number of interactions is N ($N_1 + N_2 = N$). Without selecting a specific value for N, a specific analysis as in Sec. III is not possible. However, a more generalized approach can be taken to assess flexural mode interactions. Let modes a and b have either torsional or longitudinal nature and consider the angular dependence of the Nth order nonlinear stress $\bar{\mathbf{T}}$ and its divergence (nonlinear body force $\bar{\mathbf{f}}$). The angular dependence of these terms is rooted in the displacement field [Eqs. (6) and (7)] and is limited to sines and cosines. Thus, the nonlinear stress and nonlinear body force have the following trigonometric form with respect to Θ:

$$\mathbf{T} = \mathbf{T}(R)(\sin P\Theta)^{\alpha}(\cos P\Theta)^{\beta}(\sin Q\Theta)^{\gamma}(\cos Q\Theta)^{\zeta}, \quad (41)$$

$$\mathbf{f} = \mathbf{f}(R)(\sin P\Theta)^{\alpha}(\cos P\Theta)^{\beta}(\sin Q\Theta)^{\gamma}(\cos Q\Theta)^{\zeta}, \quad (42)$$

where α, β, γ, and ζ are non-negative integers that depend on the order of the secondary field, $\alpha + \beta = N_1$, $\gamma + \zeta = N_2$, and $N_1 + N_2 = N$. Define

$$\Pi_{\Theta} = \sin^{\alpha}P\Theta \cos^{\beta}P\Theta \sin^{\gamma}Q\Theta \cos^{\zeta}Q\Theta. \quad (43)$$

Thus, the power flux to a prescribed secondary wave field of circumferential order M (torsional or longitudinal nature) due to the Nth order mode interactions can be written as

$$p_{\bar{\mu}}^{\bar{M}} = p(R)\int_0^{2\pi} \Pi_{\Theta}(\sin M\Theta + \cos M\Theta)d\Theta. \quad (44)$$

To analyze the power flux to the higher order harmonics consider the N_1 and N_2 interactions between modes a and b through the circumferential orders, which involves the exponents of the sine and cosine functions. An example of the various exponents is given in Table I for third order harmonics ($N = 3$) at cubic material nonlinearity ($K = 3$). The special cases of self interaction are included in the table. While a particular mode interaction can be specified through the values of N_1 and N_2, the values of the exponents α, β, γ, and ζ are determined solely by the nonlinear wave interactions.

There are four general cases to consider based on the parity of N: (I) N is even, while N_1 and N_2 are odd, (II) N is even, while N_1 and N_2 are even, (III) N is odd, with N_1 odd and N_2 even, and (IV) N is odd, with N_1 even and N_2 odd. The trigonometric power reduction formula facilitates analysis of power flux because Π_{Θ} can be rewritten based on the parity of the integer exponents α, β, γ, and ζ as shown in Tables II and III. Both tables show the parity of each exponent, the expression for Π_{Θ}, and the circumferential orders M of the secondary modes that have nonzero power flux

TABLE I. Complete set of combinations of exponents for $N = 3$.

N_1	N_2	α	β	γ	ζ
0	3	0	0	0	3
0	3	0	0	1	2
0	3	0	0	2	1
0	3	0	0	3	0
1	2	0	1	0	2
1	2	0	1	1	1
1	2	0	1	2	0
1	2	1	0	0	2
1	2	1	0	1	1
1	2	1	0	2	0
2	1	0	2	0	1
2	1	0	2	1	1
2	1	1	1	0	1
2	1	1	1	1	0
2	1	2	0	0	1
2	1	2	0	1	0
3	0	0	3	0	0
3	0	1	2	0	0
3	0	2	1	0	0
3	0	3	0	0	0

from the fundamental modes. Importantly, the power flux is zero to all secondary modes having circumferential orders not equal to M shown in the tables.

Tables II and III clearly show that there is always a secondary mode to which nonzero power flux occurs. The circumferential orders of these important secondary modes are linear combinations of the circumferential orders of the fundamental flexural modes, $M = l_1 P \pm l_2 Q$, where l_1 and l_2 are non-negative integers (zero, odd, or even depending on the case). From the subset of secondary modes with non-zero power flux, points that satisfy $k_{\bar{\mu}}^M = N_1 k_{\mu_a}^{M_a} \pm N_2 k_{\mu_b}^{M_b}$ are sought to identify the internal resonance condition.

Some observations can be compiled on higher order mode interactions for Nth order nonlinearity.

(i)   A $2N$ number of NOHs can be generated due to the two interacting waves a and b at Nth order interactions, including two Nth order harmonics by self interaction of a and b ($\mathbf{u}^{(a,b,N,0)}$ at $\omega = N\omega_a$ and $\mathbf{u}^{(a,b,0,N)}$ at $\omega = N\omega_b$), and $2N - 2$ number of Nth order sum and difference harmonics by a and b mutual interactions. The circumferential order of a NOH $\mathbf{u}^{(a,b,N_1,N_2)}$ (mode a participate N_1 times and mode b interacts N_2

times) is determined by the parity of N_1 and N_2, and the circumferential orders of primary mode a and b.

(ii)   NOH with either torsional or longitudinal nature have the potential to be cumulative along the propagation distance in a cylinder with Kth order nonlinearity. However, the detailed cumulative behavior of the higher harmonics with torsional or longitudinal nature can be observed only with the exact solution of nonlinear forcing terms in the corresponding Nth order mode interaction.

(iii) NHG with either torsional or longitudinal nature are generated as special cases of Nth order self interactions ($N_1 = 0$ or $N_2 = 0$). The cumulative conditions of NHG obtained within our framework essentially agree with the results of Srivastava and Lanza di Scalea.[19] We explain the cumulative behavior of NHG as follows: self interaction, an odd number of times (N is odd) results in a cumulative odd NHG with circumferential orders that are odd multiples (up to N) of the primary mode; self interaction, an even number of times (N is even) results in a cumulative even NHG with circumferential orders that are even multiples (up to N) of the primary mode.

TABLE II. Secondary modes having non-zero power flux when the interaction times N is even (Note: $O = $ odd, $E = $ even; A_{k_i} and B_{k_i} are coefficients that are independent of Θ).

α	β	γ	ζ	Circumferential dependence of the nonlinear stresses, Π_Θ	M yielding $p_{\bar{\mu}}^{\bar{M}} \neq 0$
				N_1 and N_2 are both odd	
O	E	O	E	$A_{k_0} \sum\limits_{l_1=1,3,5...}^{N_1} \sum\limits_{l_2=1,3,5...}^{N_2} (\cos((l_1P - l_2Q)\Theta) - \cos((l_1P + l_2Q)\Theta))$	
O	E	E	O	$A_{k_1} \sum\limits_{l_1=1,3,5...}^{N_1} \sum\limits_{l_2=1,3,5...}^{N_2} (\sin((l_1P + l_2Q)\Theta) + \sin((l_1P - l_2Q)\Theta))$	$l_1P \pm l_2Q$
E	O	O	E	$A_{k_2} \sum\limits_{l_1=1,3,5...}^{N_1} \sum\limits_{l_2=1,3,5...}^{N_2} (\sin((l_1P + l_2Q)\Theta) - \sin((l_1P - l_2Q)\Theta))$	
E	O	E	O	$A_{k_3} \sum\limits_{l_1=1,3,5...}^{N_1} \sum\limits_{l_2=1,3,5...}^{N_2} (\cos((l_1P - l_2Q)\Theta) + \cos((l_1P + l_2Q)\Theta))$	
				N_1 and N_2 are both even	
O	O	O	O	$B_{k_0} \sum\limits_{l_1=0,2,4...}^{N_1} \sum\limits_{l_2=0,2,4...}^{N_2} (\cos((l_1P - l_2Q)\Theta) - \cos((l_1P + l_2Q)\Theta))$	$l_1P \pm l_2Q$
O	O	E	E	$B_{k_1} \sum\limits_{l_2=0,2,4...}^{N_1} \sin(l_1P\Theta)$ $+ B_{k_2} \sum\limits_{l_1=0,2,4...}^{N_1} \sum\limits_{l_2=0,2,4...}^{N_2} (\sin((l_1P + l_2Q)\Theta) + \sin((l_1P - l_2Q)\Theta))$	l_1P or $l_1P \pm l_2Q$
E	E	O	O	$B_{k_3} \sum\limits_{l_2=0,2,4...}^{N_2} \sin(l_2Q\Theta)$ $+ B_{k_4} \sum\limits_{l_1=0,2,4...}^{N_1} \sum\limits_{l_2=0,2,4...}^{N_2} (\sin((l_1P + l_2Q)\Theta) - \sin((l_1P - l_2Q)\Theta))$	l_2Q or $l_1P \pm l_2Q$
E	E	E	E	$B_{k_5} + B_{k_6} \sum\limits_{l_1=0,2,4...}^{N_1} \cos(l_1P\Theta) + B_{k_7} \sum\limits_{l_2=0,2,4...}^{N_2} \cos(l_2Q\Theta)$ $+ B_{k_8} \sum\limits_{l_1=0,2,4...}^{N_1} \sum\limits_{l_2=0,2,4...}^{N_2} (\cos((l_1P - l_2Q)\Theta) - \cos((l_1P + l_2Q)\Theta))$	l_1P, l_2Q or $l_1P \pm l_2Q$

TABLE III. Secondary modes having non-zero power flux when the interaction times N is odd (Note: O = odd, E = even; C_{k_i} and D_{k_i} are coefficients that are independent of Θ).

α	β	γ	ζ	Circumferential dependence of the nonlinear stresses, Π_Θ	M yielding $p_{\bar\mu}^{\bar M} \neq 0$
				N_1 is odd and N_2 is even	
O	E	O	O	$C_{k_0} \sum\limits_{l_1=1,3,5...}^{N_1} \sum\limits_{l_2=0,2,4...}^{N_2} (\cos((l_1 P - l_2 Q)\Theta) - \cos((l_1 P + l_2 Q)\Theta))$	$l_1 P \pm l_2 Q$
O	E	E	E	$C_{k_1} \sum\limits_{l_1=1,3,5...}^{N_1} \sin(l_1 P\Theta)$ $+ C_{k_2} \sum\limits_{l_1=1,3,5...}^{N_1} \sum\limits_{l_2=0,2,4...}^{N_2} (\sin((l_1 P + l_2 Q)\Theta) + \sin((l_1 P - l_2 Q)\Theta))$	$l_1 P$ or $l_1 P \pm l_2 Q$
E	O	O	O	$C_{k_3} \sum\limits_{l_1=1,3,5...}^{N_1} \sum\limits_{l_2=0,2,4...}^{N_2} (\sin((l_1 P + l_2 Q)\Theta) - \sin((l_1 P - l_2 Q)\Theta))$	$l_1 P \pm l_2 Q$
E	O	E	E	$C_{k_4} \sum\limits_{l_1=1,3,5...}^{N_1} \cos(l_1 P\Theta)$ $+ C_{k_5} \sum\limits_{l_1=1,3,5...}^{N_1} \sum\limits_{l_2=0,2,4...}^{N_2} (\cos((l_1 P - l_2 Q)\Theta) + \cos((l_1 P + l_2 Q)\Theta))$	$l_1 P$ or $l_1 P \pm l_2 Q$
				N_1 is even and N_2 is odd	
O	O	O	E	$D_{k_0} \sum\limits_{l_1=0,2,4...}^{N_1} \sum\limits_{l_2=1,3,5...}^{N_2} (\cos((l_1 P - l_2 Q)\Theta) - \cos((l_1 P + l_2 Q)\Theta))$	$l_1 P \pm l_2 Q$
O	O	E	O	$D_{k_1} \sum\limits_{l_1=0,2,4...}^{N_1} \sum\limits_{l_2=1,3,5...}^{N_2} (\sin((l_1 P - l_2 Q)\Theta) + \sin((l_1 P + l_2 Q)\Theta))$	
E	E	O	E	$D_{k_2} \sum\limits_{l_2=1,3,5...}^{N_2} \sin(l_2 Q\Theta)$ $+ D_{k_3} \sum\limits_{l_1=0,2,4...}^{N_1} \sum\limits_{l_2=1,3,5...}^{N_2} (\sin((l_1 P + l_2 Q)\Theta) - \sin((l_1 P - l_2 Q)\Theta))$	$l_2 Q$ or $l_1 P \pm l_2 Q$
E	E	E	O	$D_{k_4} \sum\limits_{l_2=1,3,5...}^{N_2} \cos(l_2 Q\Theta)$ $+ D_{k_5} \sum\limits_{l_1=0,2,4...}^{N_1} \sum\limits_{l_2=1,3,5...}^{N_2} (\cos((l_1 P + l_2 Q)\Theta) + \cos((l_1 P - l_2 Q)\Theta))$	

V. SUMMARY

A generalized method is presented to analyze the cumulative nature of higher order harmonics due to the scattering of two collimated interacting waves a and b in isotropic weakly nonlinear hollow circular cylinders. The waves with both torsional and longitudinal natures are considered as primary or secondary wave fields. The quadratic nonlinear interaction of two propagating waves is analyzed by considering a material with the Landau strain energy function. The nonlinear forcing terms in curvilinear coordinates are manipulated to analyze the power flux with a given pattern of mode interactions. The SOH wave fields of torsional nature are found to be cumulative at sum or difference frequencies ($\omega = \omega_a \pm \omega_b$) provided the two interacting waves a and b are of the opposite nature, while the cumulative longitudinal type SOH wave fields can be generated at $\omega = 2\omega_a$, $\omega = 2\omega_b$, or $\omega = \omega_a \pm \omega_a$ if the two interacting waves a and b are of the identical nature, or at twice frequencies ($\omega = 2\omega_a$, $\omega = 2\omega_b$) when the two interacting waves a and b are of the opposite nature. A methodology for assessing cumulative higher harmonics due to Nth order interaction of two propagating waves is formulated in a material with strain energy density given by a Murnaghan's power series. A $2N$ number of NOHs can be generated at wavenumber-frequency pairs $(N_1 k_{\mu_a}^{N_a} \pm N_2 k_{\mu_b}^{N_b},\ N_1 \omega_{\mu_a}^{N_a} \pm N_2 \omega_{\mu_b}^{N_b})$ due to the two interacting waves a and b at Nth order interaction. The circumferential order of the cumulative higher harmonics can be determined by the parity properties of N_1 and N_2, and the circumferential orders of primary modes. The results render physical insights into the cumulative behaviors of higher order harmonics due to the interaction of two collimated waves, and provide a theoretical guidance for experimentally generating strong cumulative higher harmonics. We note that the framework presented in this article is also valid for solid rods as the inner radius tends to zero. A physical interpretation and a numerical evaluation of higher order harmonic generation in weakly nonlinear hollow circular cylinders will be given in Paper II[29] of this paper series.

ACKNOWLEDGMENTS

APPENDIX: QUADRATIC NONLINEAR STRESS COMPONENTS

The components of the quadratic nonlinear stress can be obtained through Eq. (29) by considering cylindrical coordinates

$$\bar{T}_{RR} = \left(\frac{3\lambda}{2} + 3\mu + A + 3B + C\right)\frac{\partial u_R}{\partial R}\frac{\partial u_R}{\partial R} + B\frac{1}{R}\frac{\partial u_\Theta}{\partial Z}\frac{\partial u_Z}{\partial \Theta} + 2C\frac{1}{R}\frac{\partial u_\Theta}{\partial \Theta}\frac{\partial u_Z}{\partial Z} + 2C\frac{u_R}{R}\frac{\partial u_Z}{\partial Z}$$

$$+ \left(\frac{\lambda}{2} + B + C\right)\left(\frac{u_R}{R}\frac{u_R}{R} + 2\frac{\partial u_R}{\partial R}\frac{u_R}{R} + \frac{1}{R^2}\frac{\partial u_\Theta}{\partial \Theta}\frac{\partial u_\Theta}{\partial \Theta} + 2\frac{1}{R^2}\frac{\partial u_\Theta}{\partial \Theta}u_R + 2\frac{1}{R}\frac{\partial u_R}{\partial R}\frac{\partial u_\Theta}{\partial \Theta} + 2\frac{\partial u_R}{\partial R}\frac{\partial u_Z}{\partial Z} + \frac{\partial u_Z}{\partial Z}\frac{\partial u_Z}{\partial Z}\right)$$

$$+ \left(\frac{\lambda}{2} + \mu + \frac{A}{4} + \frac{B}{2}\right)\left(\frac{1}{R^2}\frac{\partial u_R}{\partial \Theta}\frac{\partial u_R}{\partial \Theta} - 2\frac{1}{R^2}\frac{\partial u_R}{\partial \Theta}u_\Theta + \frac{\partial u_R}{\partial Z}\frac{\partial u_R}{\partial Z} + \frac{u_\Theta}{R}\frac{u_\Theta}{R} + \frac{\partial u_\Theta}{\partial R}\frac{\partial u_\Theta}{\partial R} + \frac{\partial u_Z}{\partial R}\frac{\partial u_Z}{\partial R}\right)$$

$$+ \left(\mu + \frac{A}{2} + B\right)\left(\frac{1}{R}\frac{\partial u_R}{\partial \Theta}\frac{\partial u_\Theta}{\partial R} - \frac{\partial u_\Theta}{\partial R}\frac{u_\Theta}{R} + \frac{\partial u_R}{\partial Z}\frac{\partial u_Z}{\partial R}\right) + \left(\frac{\lambda}{2} + \frac{B}{2}\right)\left(\frac{\partial u_\Theta}{\partial Z}\frac{\partial u_\Theta}{\partial Z} + \frac{1}{R^2}\frac{\partial u_Z}{\partial \Theta}\frac{\partial u_Z}{\partial \Theta}\right), \tag{A1}$$

$$\bar{T}_{R\Theta} = \left(\mu + \frac{A}{2} + B\right)\left(\frac{1}{R^2}\frac{\partial u_R}{\partial \Theta}\frac{\partial u_\Theta}{\partial \Theta} + \frac{1}{R}\frac{\partial u_R}{\partial \Theta}\frac{u_R}{R} + \frac{1}{R}\frac{\partial u_R}{\partial R}\frac{\partial u_R}{\partial \Theta} - \frac{\partial u_R}{\partial R}\frac{u_\Theta}{R} - \frac{u_R}{R}\frac{u_\Theta}{R} - \frac{1}{R}\frac{\partial u_\Theta}{\partial \Theta}\frac{u_\Theta}{R}\right)$$

$$+ \left(\mu + \frac{A}{4}\right)\left(\frac{\partial u_R}{\partial Z}\frac{\partial u_\Theta}{\partial Z} + \frac{\partial u_\Theta}{\partial Z}\frac{\partial u_Z}{\partial R} + \frac{1}{R}\frac{\partial u_Z}{\partial R}\frac{\partial u_Z}{\partial \Theta}\right) + (\lambda + B)\frac{\partial u_\Theta}{\partial R}\frac{\partial u_Z}{\partial Z} + \frac{B}{R}\frac{\partial u_R}{\partial \Theta}\frac{\partial u_Z}{\partial Z}$$

$$+ \left(\lambda + 2\mu + \frac{A}{2} + B\right)\left(\frac{1}{R}\frac{\partial u_\Theta}{\partial \Theta}\frac{\partial u_\Theta}{\partial R} + \frac{\partial u_R}{\partial R}\frac{\partial u_\Theta}{\partial R} + \frac{\partial u_\Theta}{\partial R}\frac{u_R}{R}\right) + \frac{1}{R}\frac{A}{4}\frac{\partial u_R}{\partial Z}\frac{\partial u_Z}{\partial \Theta} - B\frac{u_\Theta}{R}\frac{\partial u_Z}{\partial Z}, \tag{A2}$$

$$\bar{T}_{RZ} = \left(\lambda + 2\mu + \frac{A}{2} + B\right)\left(\frac{\partial u_R}{\partial R}\frac{\partial u_Z}{\partial R} + \frac{\partial u_Z}{\partial R}\frac{\partial u_Z}{\partial Z}\right) + \left(\mu + \frac{A}{2} + B\right)\left(\frac{\partial u_R}{\partial R}\frac{\partial u_R}{\partial Z} + \frac{\partial u_R}{\partial Z}\frac{\partial u_Z}{\partial Z}\right)$$

$$+ (\lambda + B)\left(\frac{1}{R}\frac{\partial u_\Theta}{\partial \Theta}\frac{\partial u_Z}{\partial R} + \frac{\partial u_Z}{\partial R}\frac{u_R}{R}\right) + \frac{A}{4}\left(\frac{\partial u_R}{\partial \Theta}\frac{\partial u_\Theta}{\partial Z} - \frac{\partial u_\Theta}{\partial Z}\frac{u_\Theta}{R}\right) + B\left(\frac{\partial u_R}{\partial Z}\frac{u_R}{R} + \frac{1}{R}\frac{\partial u_R}{\partial Z}\frac{\partial u_\Theta}{\partial \Theta}\right)$$

$$+ \left(\mu + \frac{A}{4}\right)\left(\frac{1}{R^2}\frac{\partial u_R}{\partial \Theta}\frac{\partial u_Z}{\partial \Theta} + \frac{\partial u_\Theta}{\partial R}\frac{\partial u_\Theta}{\partial Z} + \frac{\partial u_\Theta}{\partial R}\frac{\partial u_Z}{\partial \Theta} - \frac{1}{R}\frac{\partial u_Z}{\partial \Theta}\frac{u_\Theta}{R}\right), \tag{A3}$$

$$\bar{T}_{\Theta R} = \left(\lambda + 2\mu + \frac{A}{2} + B\right)\left(\frac{1}{R}\frac{\partial u_R}{\partial R}\frac{\partial u_R}{\partial \Theta} - \frac{\partial u_R}{\partial R}\frac{u_\Theta}{R} - \frac{u_R}{R}\frac{u_\Theta}{R} - \frac{1}{R}\frac{\partial u_\Theta}{\partial \Theta}\frac{u_\Theta}{R} + \frac{1}{R^2}\frac{\partial u_R}{\partial \Theta}\frac{\partial u_\Theta}{\partial \Theta} + \frac{1}{R}\frac{\partial u_R}{\partial \Theta}\frac{u_R}{R}\right)$$

$$+ \left(\mu + \frac{A}{2} + B\right)\left(\frac{\partial u_R}{\partial R}\frac{\partial u_\Theta}{\partial R} + \frac{1}{R}\frac{\partial u_\Theta}{\partial R}\frac{\partial u_\Theta}{\partial \Theta} + \frac{\partial u_\Theta}{\partial R}\frac{u_R}{R}\right) + (\lambda + B)\left(\frac{1}{R}\frac{\partial u_R}{\partial \Theta}\frac{\partial u_Z}{\partial Z} - \frac{\partial u_Z}{\partial Z}\frac{u_\Theta}{R}\right)$$

$$+ \left(\mu + \frac{A}{4}\right)\left(\frac{\partial u_R}{\partial Z}\frac{\partial u_\Theta}{\partial Z} + \frac{1}{R}\frac{\partial u_R}{\partial Z}\frac{\partial u_Z}{\partial \Theta} + \frac{1}{R}\frac{\partial u_Z}{\partial R}\frac{\partial u_Z}{\partial \Theta}\right) + B\frac{\partial u_Z}{\partial Z}\frac{\partial u_\Theta}{\partial R} + \frac{A}{4}\frac{\partial u_\Theta}{\partial Z}\frac{\partial u_Z}{\partial R}, \tag{A4}$$

$$\bar{T}_{\Theta\Theta} = \left(\frac{3\lambda}{2} + 3\mu + A + 3B + C\right)\left(\frac{u_R}{R}\frac{u_R}{R} + \frac{1}{R^2}\frac{\partial u_\Theta}{\partial \Theta}\frac{\partial u_\Theta}{\partial \Theta} + \frac{2}{R}\frac{\partial u_\Theta}{\partial \Theta}\frac{u_R}{R}\right) + 2C\frac{\partial u_R}{\partial R}\frac{\partial u_Z}{\partial Z} + B\frac{\partial u_R}{\partial Z}\frac{\partial u_Z}{\partial R}$$

$$+ \left(\frac{\lambda}{2} + \mu + \frac{A}{4} + \frac{B}{2}\right)\left(\frac{1}{R^2}\frac{\partial u_R}{\partial \Theta}\frac{\partial u_R}{\partial \Theta} + \frac{u_\Theta}{R}\frac{u_\Theta}{R} + \frac{\partial u_\Theta}{\partial R}\frac{\partial u_\Theta}{\partial R} + \frac{\partial u_\Theta}{\partial Z}\frac{\partial u_\Theta}{\partial Z} - \frac{2}{R}\frac{\partial u_R}{\partial \Theta}\frac{u_\Theta}{R} + \frac{1}{R^2}\frac{\partial u_Z}{\partial \Theta}\frac{\partial u_Z}{\partial \Theta}\right)$$

$$+ \left(\frac{\lambda}{2} + B + C\right)\left(\frac{\partial u_R}{\partial R}\frac{\partial u_R}{\partial R} + 2\frac{\partial u_R}{\partial R}\frac{u_R}{R} + \frac{2}{R}\frac{\partial u_R}{\partial R}\frac{\partial u_\Theta}{\partial \Theta} + \frac{2}{R}\frac{\partial u_\Theta}{\partial \Theta}\frac{\partial u_Z}{\partial Z} + 2\frac{\partial u_Z}{\partial Z}\frac{u_R}{R} + \frac{\partial u_Z}{\partial Z}\frac{\partial u_Z}{\partial Z}\right)$$

$$+ \left(\mu + \frac{A}{2} + B\right)\left(\frac{1}{R}\frac{\partial u_R}{\partial \Theta}\frac{\partial u_\Theta}{\partial R} - \frac{\partial u_\Theta}{\partial R}\frac{u_\Theta}{R} + \frac{\partial u_\Theta}{\partial Z}\frac{\partial u_Z}{\partial \Theta}\right) + \left(\frac{\lambda}{2} + \frac{B}{2}\right)\left(\frac{\partial u_R}{\partial Z}\frac{\partial u_R}{\partial Z} + \frac{\partial u_Z}{\partial R}\frac{\partial u_Z}{\partial R}\right), \tag{A5}$$

$$\bar{T}_{\Theta Z} = \left(\lambda + 2\mu + \frac{A}{2} + B\right)\left(\frac{1}{R}\frac{\partial u_Z}{\partial \Theta}\frac{u_R}{R} + \frac{1}{R^2}\frac{\partial u_\Theta}{\partial \Theta}\frac{\partial u_Z}{\partial \Theta} + \frac{1}{R}\frac{\partial u_Z}{\partial \Theta}\frac{\partial u_Z}{\partial Z}\right) + \frac{A}{4}\frac{\partial u_R}{\partial Z}\frac{\partial u_\Theta}{\partial R} + B\frac{\partial u_R}{\partial R}\frac{\partial u_\Theta}{\partial Z}$$

$$+ \left(\mu + \frac{A}{2} + B\right)\left(\frac{\partial u_R}{\partial R}\frac{\partial u_\Theta}{\partial Z} + \frac{1}{R}\frac{\partial u_\Theta}{\partial \Theta}\frac{\partial u_\Theta}{\partial Z} + \frac{\partial u_\Theta}{\partial Z}\frac{u_R}{R}\right) + (\lambda + B)\frac{1}{R}\frac{\partial u_R}{\partial R}\frac{\partial u_Z}{\partial \Theta}$$

$$+ \left(\mu + \frac{A}{4}\right)\left(\frac{1}{R}\frac{\partial u_R}{\partial \Theta}\frac{\partial u_R}{\partial Z} + \frac{1}{R}\frac{\partial u_R}{\partial \Theta}\frac{\partial u_Z}{\partial R} - \frac{\partial u_R}{\partial Z}\frac{u_\Theta}{R} + \frac{\partial u_\Theta}{\partial R}\frac{\partial u_Z}{\partial R} - \frac{\partial u_Z}{\partial R}\frac{u_\Theta}{R}\right), \tag{A6}$$

$$\bar{T}_{ZR} = \left(\mu + \frac{A}{4}\right)\left(\frac{1}{R}\frac{\partial u_R}{\partial \Theta}\frac{\partial u_\Theta}{\partial Z} + \frac{1}{R^2}\frac{\partial u_R}{\partial \Theta}\frac{\partial u_Z}{\partial \Theta} + \frac{\partial u_\Theta}{\partial Z}\frac{\partial u_\Theta}{\partial R} - \frac{\partial u_\Theta}{\partial Z}\frac{u_\Theta}{R} - \frac{\partial u_Z}{\partial \Theta}\frac{u_\Theta}{R}\right)$$

$$+ \left(\lambda + 2\mu + \frac{A}{2} + B\right)\left(\frac{\partial u_R}{\partial Z}\frac{\partial u_R}{\partial R} + \frac{\partial u_R}{\partial Z}\frac{\partial u_Z}{\partial Z}\right) + \left(\mu + \frac{A}{2} + B\right)\left(\frac{\partial u_R}{\partial R}\frac{\partial u_Z}{\partial R} + \frac{\partial u_Z}{\partial R}\frac{\partial u_Z}{\partial Z}\right)$$

$$+ (\lambda + B)\left(\frac{\partial u_R}{\partial Z}\frac{u_R}{R} + \frac{1}{R}\frac{\partial u_R}{\partial Z}\frac{\partial u_\Theta}{\partial \Theta}\right) + \frac{1}{R}B\frac{\partial u_\Theta}{\partial \Theta}\frac{\partial u_Z}{\partial R} + B\frac{\partial u_Z}{\partial R}\frac{u_R}{R} + \frac{1}{R}\frac{A}{4}\frac{\partial u_\Theta}{\partial R}\frac{\partial u_Z}{\partial \Theta}, \tag{A7}$$

$$\bar{T}_{Z\Theta} = \left(\lambda + 2\mu + \frac{A}{2} + B\right)\left(\frac{1}{R}\frac{\partial u_\Theta}{\partial \Theta}\frac{\partial u_\Theta}{\partial Z} + \frac{\partial u_\Theta}{\partial Z}\frac{\partial u_Z}{\partial Z} + \frac{\partial u_\Theta}{\partial Z}\frac{u_R}{R}\right) + (\lambda + B)\frac{\partial u_R}{\partial R}\frac{\partial u_\Theta}{\partial Z}$$

$$+ \left(\mu + \frac{A}{2} + B\right)\left(\frac{1}{R^2}\frac{\partial u_\Theta}{\partial \Theta}\frac{\partial u_Z}{\partial \Theta} + \frac{1}{R}\frac{\partial u_Z}{\partial \Theta}\frac{u_R}{R} + \frac{1}{R}\frac{\partial u_Z}{\partial \Theta}\frac{\partial u_Z}{\partial Z}\right) + \frac{A}{4}\left(\frac{1}{R}\frac{\partial u_R}{\partial \Theta}\frac{\partial u_Z}{\partial R} - \frac{\partial u_Z}{\partial R}\frac{u_\Theta}{R}\right)$$

$$+ \left(\mu + \frac{A}{4}\right)\left(\frac{1}{R}\frac{\partial u_R}{\partial \Theta}\frac{\partial u_R}{\partial Z} + \frac{\partial u_R}{\partial Z}\frac{\partial u_\Theta}{\partial R} - \frac{\partial u_R}{\partial Z}\frac{u_\Theta}{R} + \frac{\partial u_\Theta}{\partial R}\frac{\partial u_Z}{\partial R}\right) + B\frac{1}{R}\frac{\partial u_R}{\partial R}\frac{\partial u_Z}{\partial \Theta}, \tag{A8}$$

$$\bar{T}_{ZZ} = \left(\frac{3\lambda}{2} + 3\mu + A + 3B + C\right)\frac{\partial u_Z}{\partial Z}\frac{\partial u_Z}{\partial Z} + \left(\frac{\lambda}{2} + \mu + \frac{A}{4} + \frac{B}{2}\right)\left(\frac{\partial u_R}{\partial Z}\frac{\partial u_R}{\partial Z} + \frac{\partial u_Z}{\partial R}\frac{\partial u_Z}{\partial R}\right)$$

$$+ \left(\frac{\lambda}{2} + B + C\right)\left(\frac{\partial u_R}{\partial R}\frac{\partial u_R}{\partial R} + \frac{u_R}{R}\frac{u_R}{R} + \frac{1}{R^2}\frac{\partial u_\Theta}{\partial \Theta}\frac{\partial u_\Theta}{\partial \Theta} + \frac{2}{R}\frac{\partial u_\Theta}{\partial \Theta}\frac{u_R}{R} + \frac{2}{R}\frac{\partial u_\Theta}{\partial \Theta}\frac{\partial u_Z}{\partial Z} + 2\frac{\partial u_Z}{\partial Z}\frac{u_R}{R} + 2\frac{\partial u_R}{\partial R}\frac{\partial u_Z}{\partial Z}\right)$$

$$+ \left(\mu + \frac{A}{2} + B\right)\left(\frac{1}{R}\frac{\partial u_\Theta}{\partial Z}\frac{\partial u_Z}{\partial \Theta} + \frac{\partial u_R}{\partial Z}\frac{\partial u_Z}{\partial R}\right) + \left(\mu + \frac{A}{4}\right)\left(\frac{1}{R^2}\frac{\partial u_Z}{\partial \Theta}\frac{\partial u_Z}{\partial \Theta} + \frac{\partial u_\Theta}{\partial Z}\frac{\partial u_\Theta}{\partial Z}\right)$$

$$+ \left(\frac{\lambda}{2} + \frac{B}{2}\right)\left(\frac{1}{R^2}\frac{\partial u_R}{\partial \Theta}\frac{\partial u_R}{\partial \Theta} + \frac{1}{R^2}\frac{\partial u_Z}{\partial \Theta}\frac{\partial u_Z}{\partial \Theta} + \frac{u_\Theta}{R}\frac{u_\Theta}{R} + \frac{\partial u_\Theta}{\partial R}\frac{\partial u_\Theta}{\partial R} + \frac{\partial u_\Theta}{\partial Z}\frac{\partial u_\Theta}{\partial Z} - \frac{2}{R}\frac{\partial u_R}{\partial \Theta}\frac{u_\Theta}{R}\right)$$

$$+ B\left(\frac{1}{R}\frac{\partial u_R}{\partial \Theta}\frac{\partial u_\Theta}{\partial R} - \frac{\partial u_R}{\partial R}\frac{u_\Theta}{R}\right) + 2C\left(\frac{\partial u_R}{\partial R}\frac{u_R}{R} + \frac{1}{R}\frac{\partial u_R}{\partial R}\frac{\partial u_\Theta}{\partial \Theta}\right). \tag{A9}$$

[1] A. Hikata, B. B. Chick, and C. Elbaum, Appl. Phys. Lett. **3**, 195 (1963).
[2] A. Hikata and C. Elbaum, Phys. Rev. **144**, 469 (1966).
[3] A. Hikata and C. Elbaum, Phys. Rev. **151**, 442 (1966).
[4] J. H. Cantrell, J. Appl. Phys. **105**, 043520 (2009).
[5] W. D. Cash and W. Cai, J. Appl. Phys. **109**, 014915 (2011).
[6] J. H. Cantrell, Proc. R. Soc. London, Ser. A **460**, 757 (2004).
[7] K. H. Matlack, J. J. Wall, J. Y. Kim, J. Qu, L. J. Jacobs, and H. W. Viehrig, J. Appl. Phys. **111**, 054911 (2012).
[8] J. H. Cantrell and W. T. Yost, Appl. Phys. Lett. **77**, 1952 (2000).
[9] Z. A. Gol'dberg, Sov. Phys. Acoust. **6**, 306 (1961).
[10] G. L. Jones and D. R. Kobett, J. Acoust. Soc. Am. **35**, 5 (1963).
[11] J. D. Childress and C. G. Hambrick, Phys. Rev. **136**, A411 (1964).
[12] F. A. Bender, J. Y. Kim, L. J. Jacobs, and J. Qu, Wave Motion **50**, 146 (2013).
[13] L. D. Landau and E. M. Lifshitz, *Theory of Elasticity* (Pergamon, New York, 1986).
[14] M. Deng, J. Appl. Phys. **84**, 3500 (1998).
[15] M. Deng, J. Appl. Phys. **85**, 3051 (1999).
[16] W. J. N. de Lima and M. F. Hamilton, J. Sound Vib. **265**, 819 (2003).
[17] W. J. N. de Lima and M. F. Hamilton, Wave Motion **41**, 1 (2005).
[18] A. Srivastava and F. Lanza di Scalea, J. Sound Vib. **323**, 932 (2009).

[19] A. Srivastava and F. Lanza di Scalea, J. Sound Vib. **329**, 1499 (2010).
[20] M. F. Müller, J. Y. Kim, J. Qu, and L. J. Jacobs, J. Acoust. Soc. Am. **127**, 2141 (2010).
[21] Y. Liu, V. Chillara, and C. J. Lissenden, J. Sound Vib. **332**, 4517 (2013).
[22] Y. Liu, E. Khajeh, C. J. Lissenden, and J. L. Rose, J. Acoust. Soc. Am. **133**, 2541 (2013).
[23] Y. Liu, V. Chillara, C. J. Lissenden, and J. L. Rose, J. Appl. Phys. **114**, 114908 (2013).
[24] V. Chillara and C. J. Lissenden, J. Appl. Phys. **111**, 124909 (2012).
[25] J. Li and J. L. Rose, IEEE Trans. Ultrason., Ferroelectr., Freq. Control **49**, 1720 (2002).
[26] F. D. Murnaghan, *Finite Deformation of an Elastic Solid* (John Wiley and Sons, Inc., New York, 1951).
[27] J. L. Rose, *Ultrasonic Waves in Solid Media* (Cambridge University Press, Cambridge, 1999).
[28] B. A. Auld, *Acoustic Fields and Waves in Solids* (Robert E. Krieger Publishing Company, Malabar, Florida, 1990), Vol. II.
[29] Y. Liu, C. J. Lissenden, and J. L. Rose, "Higher order interaction of elastic waves in weakly nonlinear hollow circular cylinders. II. Numerical results," J. Appl. Phys. **115**, 214902 (2014).

Yang Liu, Ehsan Khajeh, Cliff J. Lissenden, and Joseph L. Rose

Articles you may be interested in
Higher order interaction of elastic waves in weakly nonlinear hollow circular cylinders. I. Analytical foundation
J. Appl. Phys. 115, 214901 (2014); 10.1063/1.4879459

Wave propagation in assemblies of cemented spheres
AIP Conf. Proc. 1542, 233 (2013); 10.1063/1.4811910

Interaction of torsional and longitudinal guided waves in weakly nonlinear circular cylinders
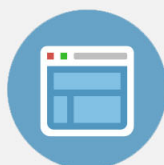J. Acoust. Soc. Am. 133, 2541 (2013); 10.1121/1.4795806

Two-dimensional wave propagation in an elastic half-space with quadratic nonlinearity: A numerical study
J. Acoust. Soc. Am. 125, 1293 (2009); 10.1121/1.3075597

Guided circumferential shear horizontal waves in an isotropic hollow cylinder
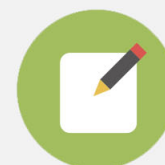J. Acoust. Soc. Am. 115, 1912 (2004); 10.1121/1.1691037

Higher order interaction of elastic waves in weakly nonlinear hollow circular cylinders. II. Physical interpretation and numerical results

Yang Liu, Ehsan Khajeh, Cliff J. Lissenden,[a)] and Joseph L. Rose
Department of Engineering Science and Mechanics, The Pennsylvania State University, University Park, Pennsylvania 16802, USA

A plate ray perspective for elastic wave propagation in hollow circular cylinders is presented in order to excite a predominant flexural mode, which in turn generates higher order harmonics due to nonlinear material behavior. The scattering angles are determined for the internally resonant higher order harmonics due to the interactions of two collimated waves. Primary waves that can generate strongly cumulative higher order harmonics are identified for mode self interactions and mutual interactions. A helical inter-digital transducer has been designed for the excitation of a single dominant flexural mode. Numerical evaluations that demonstrate cumulative second harmonic generation are undertaken for both torsional and longitudinal flexural waves. Quadratic sum and difference harmonic generation is observed for the mutual interaction between two primary torsional flexural wave modes. © 2014 AIP Publishing LLC. [http://dx.doi.org/10.1063/1.4879460]

I. INTRODUCTION

A mathematical framework has been proposed to analyze the cumulative behavior of the higher order harmonics due to the scattering of two collimated interacting waves in isotropic weakly nonlinear elastic hollow circular cylinders in Part I of this work.[1] The approach of this analysis considers the wave scattering resulting from quadratic and higher order interactions of the two collimated waves. The criteria for different orders of internally resonant higher harmonics were formulated, which include the following: a synchronism condition, a circumferential order relation between primary and secondary waves, and the natures of primary waves, i.e., torsional or longitudinal. This work (Part I) agrees with the early work of de Lima Hamilton,[2] Srivastava and di Scalea[3] and Liu *et al.*[4] and extends the scope to the harmonic generation of flexural waves due to higher order mode interactions.

The primary methodology for investigating elastic waves propagating in hollow circular cylinders uses normal modes. Gazis[5,6] presented the first exact solution for both axisymmetric and non-axisymmetric modes in an infinitely long, isotropic, hollow circular cylinder. He showed that there exists a doubly infinite number of wave modes in a hollow cylinder. These wave modes include an infinite number of axisymmetric longitudinal wave modes, an infinite number of axisymmetric torsional wave modes, and a doubly infinite number of flexural modes that are of longitudinal or torsional nature. Ditri and Rose[7,8] proved that the double infinite number of guided wave modes in a hollow circular cylinder are all normal modes, and then determined the modal amplitude of each normal mode by applying source loading conditions.

To solve some complicated acoustic problems, structural acousticians try to use various asymptotic expansions, among which the ray concepts from geometrical optics provide many physical insights. The work of Smith,[9] Steele,[10] Feit,[11] and Germogenova[12] are examples of geometric acoustic solutions to shell equations. Pierce *et al.*[13,14] and Norris *et al.*[15,16] used rays to interpret acoustic radiation and scattering from fluid-loaded elastic shells. Likewise, a plate wave approximation of guided waves in hollow circular cylinders has been investigated by a number of authors.[17–20] By comparing the dispersion characteristics of plates and pipes, their works demonstrated that a plate approximation of circular cylinders is acceptable when the mean radius is significantly larger than the wall thickness. Both modal and geometric approaches are used in linear ultrasonics, but neither one, alone, provides sufficient understanding to implement the analysis of Part I.

State of the art transducers generate axisymmetric modes or a family of flexural modes as shown in Fig. 1; there is no way to generate a single predominant flexural mode. The energy is distributed among the many circumferential orders. However, the analysis in Part I relies on this ability due to the role circumferential order plays in the relation between primary and secondary waves. Thus, in order to make use of the higher order interaction of elastic waves a new technique to generate a single predominant flexural mode is prerequisite.

The purpose of this article is to bridge the gap between theory and practical usage of nonlinear guided waves in hollow cylinders. A plate ray perspective of the elastic waves in hollow circular cylinders is presented in Sec. II. This approach is a hybrid analytical, geometrical, and numerical analysis that provides new insight into elastic waves in hollow circular cylinders. The new understanding leads to the design of a new type of transducer that is capable of generating the intended single predominant flexural mode. Physical interpretation for the circumferential order relations of the higher order harmonics is given in Sec. III, which are associated with their scattering angles. Accordingly, the preferred primary modes that are capable of generating strongly

---

[a)]Author to whom correspondence should be addressed. Electronic mail: lissenden@psu.edu
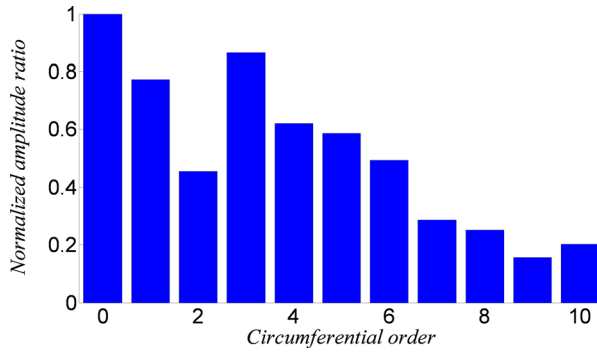
FIG. 1. Normalized modal amplitude factors for the $L(M,2)$ family excited at 1 MHz by partial loading with an angle beam transducer on a steel pipe.

cumulative higher order harmonics due to mode self interactions and mutual interactions are identified in Sec. IV. In Sec. V, we present numerical examples to demonstrate the potential of the cumulative second harmonic generation by torsional flexural and longitudinal flexural waves. A numerical evaluation of a higher order sum and difference harmonic generation is also presented for mutual interaction of torsional flexural modes. Finally, conclusions are drawn in Sec. VI. Note that this paper uses the definitions and nomenclature described in Part I.[1]

II. PLATE RAY PERSPECTIVE OF FLEXURAL WAVES

Consider a wave field in an isotropic homogeneous hollow circular cylinder due to an omni-directional harmonic source. According to the geometric ray concept,[13–16] the emission of wave energy follows the trajectories of an infinite number of helical rays from the source, which are given by the surface geodesic equation of the cylinder,

$$\frac{d^2 u^{\alpha_1}}{ds^2} + \Gamma^{\alpha_1}_{\beta_1 \gamma_1} \frac{du^{\beta_1}}{ds} \frac{du^{\gamma_1}}{ds} = 0, \quad (1)$$

where u^ξ ($\xi = \alpha_1, \beta_1, \gamma_1 = 1, 2$) are the contravariant components of the unit wave normal, s is referred as the affine parameter in general relativity, which is specified as the arc length of the geodesic rays in this study. $\Gamma^{\alpha_1}_{\beta_1 \gamma_1}$ are Christoffel symbols of the second kind. Using the plate approximation, the elastic waves in hollow circular cylinders can be regarded as plate waves propagating via cylindrical contours in the form of numerous plate wave rays, which we simply denote as plate rays. Interpret a flexural mode as a plate ray propagating at tilt angle ϕ with respect to the cylinder axis of symmetry, which physically forms the helical wave. With this interpretation, the axisymmetric modes are special cases of flexural waves that are formed by an infinite number of meridional plate rays (with tilt angle $\phi = 0$).

The wave energy carried by each plate ray mode depends on the source conditions, the underlying geometries, and the propagation paths. The intensity of the wave field at an arbitrary point is given by a superposition of all plate rays passing the point at the time t,

$$u(R, s, t) = \sum u_i(R, s, t)$$
$$u_i(R, s, t) = U_i(R)e^{\pm i(k_i s - \omega_i t)}, \quad (2)$$

where U_i is the amplitude factor carried by each plate ray mode, k_i is the plate ray wavenumber, ω_i is the corresponding frequency.

The wavenumber of an arbitrary plate ray mode with tilt angle ϕ can be decomposed into a circumferential (Θ) component and an axial (Z) component

$$k_i = k_i \sin \phi \mathbf{e}_\Theta + k_i \cos \phi \mathbf{e}_Z. \quad (3)$$

Combining Eqs. (2) and (3), the displacement field for a plate ray mode can be recast as

$$u_i(R, \Theta, Z, \phi) = U_i(R)e^{i(k_i \cos(\phi)Z + k_i \sin(\phi)R_m \Theta - \omega_i t)}, \quad (4)$$

where R_m is the radius of the undeformed middle surface of the cylinder. In the normal mode analysis of elastic wave propagation in hollow circular cylinders, the displacement field for a flexural mode (denoted by a subscript f), either of torsional or longitudinal nature, can be given by[21]

$$u_f(R, \Theta, Z) = U_f(R)e^{iM\Theta}e^{i(k_f Z - \omega_f t)}, \quad (5)$$

where $U_f(R)$ is the flexural mode amplitude factor, while k_f and ω_f are the corresponding wavenumber and frequency. $M = \pm 1, \pm 2, \pm 3 \ldots$ is the circumferential order of a flexural mode, where the "$\pm$" indicates the right-handed or left handed helical waves. Right handed helical waves are taken to be positive, making left handed helical waves negative.

Equations (4) and (5) should be identical when the plate rays form specific flexural modes, which leads to a relation between the circumferential order M and the plate ray tilt angle ϕ,

$$k_i \sin(\phi) R_m = M. \quad (6)$$

The phase velocity of a flexural wave $C_p^{(f)}$ relates to the phase velocity of the corresponding axisymmetric wave $C_p^{(0)}$ (at the identical frequency) of the same family by

$$C_p^{(f)} = \frac{\omega}{k_i \cos \phi} = \frac{1}{\cos \phi} C_p^{(0)}. \quad (7)$$

As a result, Eqs. (6) and (7) lead to

$$\sin \phi = \frac{MC_p^{(0)}}{\omega R_m} = \frac{M\lambda^{(0)}}{2\pi R_m}, \quad M = \pm 1, \pm 2, \pm 3 \ldots, \quad (8)$$

where $\lambda^{(0)}$ is the wavelength of the axisymmetric mode in the corresponding family. Equation (8) is subject to the assumptions of the asymptotic approximation, which are that the mean radius to thickness ratio is large and the elastic wavelengths are much greater than the thickness but far smaller than the mean radius of the hollow cylinder.

III. NONLINEAR WAVE SCATTERING DIRECTIONS

In Part I of this article series, the circumferential orders of the possible internal resonant higher order harmonics have been determined mathematically through analysis of non-zero power flux from the primary wave field to the

corresponding order of secondary wave fields. The plate ray perspective provides a physical interpretation for the circumferential orders of the higher order harmonics, which is associated with their scattering angles with respect to the Z-axis. In any other direction, the higher order harmonics will not have internal resonance with the primary modes and only bounded oscillation will occur.

A. Scattering direction of Nth harmonic generation (NHG)

The NHGs (second harmonics, third harmonics, etc.) are generated by N^{th} order mode self interactions within a material of Kth order nonlinearity $(N \leq K)$.[1] Odd NHGs are generated due to the odd number of times the waves self interact. Possible circumferential order numbers span over all odd integers from 1 to the number of interacting times N. Likewise, even NHGs are generated due to wave self interaction an even number of times, and they will have circumferential orders spanning all even numbers from 0 to the interacting times N. Consider a mode $\mathbf{u}^{(a)}$ with circumferential order M self interacting N times, a NHG with circumferential order lM will occur at $N\omega_a$. The synchronism condition leads to the NHG having a wavenumber Nk_a, thus the phase velocity of the NHG will be

$$C_p^{(f)} = \frac{N\omega_a}{Nk_a} = \frac{\omega_a}{k_a}, \qquad (9)$$

while the phase velocity of the axisymmetric wave in the same family of the NHG will be

$$C_p^{(0)} = C_p^{(f)} \cos \psi = \frac{\omega_a}{k_a} \cos \psi, \qquad (10)$$

where ψ is the scattering angle of the NHG. Substituting Eq. (10) into Eq. (8) leads to

$$\tan \psi = \frac{lM}{Nk_aR_m} \begin{cases} l = 1, 3, 5, ..., N, & \text{if } N \text{ is an odd number} \\ l = 0, 2, 4, ..., N, & \text{if } N \text{ is an even number.} \end{cases} \qquad (11)$$

Equation (11) gives the scattering direction of the NHG. As an example, consider the scattering of second harmonic generation (SHG) due to the quadratic self interaction of mode $\mathbf{u}^{(a)}$, which can be of either torsional or longitudinal nature. The internally resonant SHG will be of longitudinal nature with circumferential order $2M$.[1] The scattering angle of the second harmonic has the relation

$$\tan \psi = \frac{M}{k_aR_m}. \qquad (12)$$

The wavenumber of $\mathbf{u}^{(a)}$ is related with the wavenumber of the corresponding axisymmetric mode by

$$k_a = k^{(0)} \cos \psi. \qquad (13)$$

Substituting Eq. (13) into Eq. (12) and making use the relation between wavenumber and phase velocity $C_p = \omega/k$, we have

$$\sin \psi = \frac{MC_p^{(0)}}{\omega R_m}. \qquad (14)$$

Equation (14) indicates that the scattering of SHG has the same direction as the primary wave given in Eq. (8).

B. N^{th} order sum and difference harmonics

Sum harmonics are generated when the two interacting waves $\mathbf{u}^{(a)}$ and $\mathbf{u}^{(b)}$ are of the same phase changing pattern, while difference harmonics are generated when the two interacting waves $\mathbf{u}^{(a)}$ and $\mathbf{u}^{(b)}$ are of the opposite phase changing pattern.[1] Requirements for the generation of these sum and difference harmonics will be elaborated upon in Sec. IV. N^{th} order sum and difference harmonics are generated due to the Nth order mutual interaction of two interacting waves in a material with K^{th} order nonlinearity $(N \leq K)$.[1] The circumferential order of the Nth order sum or difference harmonics is determined by the parity of the number of times the participating waves interact, and the circumferential orders of the primary waves. Consider the two intersecting waves $\mathbf{u}^{(a)}$ and $\mathbf{u}^{(b)}$ with circumferential orders P and Q, respectively. Following the same methodology as for the scattering analysis of NHG, the scattering direction for N^{th} order sum and difference harmonics are given by

$$\tan \psi = \frac{l_1P \pm l_2Q}{(N_1k_a \pm N_2k_b)R_m}, \qquad (15)$$

where l_1 and l_2 can be zero or span over all odd (even) numbers up to N depending on the parity of the number of times the waves participate in the interaction.

Take the quadratic interaction of two collimated flexural waves for example, three cases of mutual interaction must be considered: (1) both waves have torsional nature, (2) both waves have longitudinal nature, and (3) one wave is torsional and one is longitudinal. For brevity, we shall just consider when the two waves have torsional nature. The second order harmonics of circumferential order $P \pm Q$ will occur at sum and difference frequencies $\omega_a \pm \omega_b$. Substituting these results into Eq. (15) leads to

$$\tan \psi = \frac{P \pm Q}{(k_a \pm k_b)R_m}. \qquad (16)$$

Equation (16) gives the scattering angles of the second order harmonics. The analysis of higher order harmonic scattering provides physical interpretation of the cumulative behavior of the higher order harmonics, and indicates that internally resonant higher order harmonics only propagate at special tilt angles. This analysis provides guidance for experimentalists in designing measurement setups. Details of the behavior of higher order harmonics, including the wave type, the resonant frequency, the circumferential orders, and the scattering angles, are summarized in Table I.

IV. IDENTIFICATION OF PREFERRED PRIMARY EXCITATIONS

While higher order harmonics can and do exist without internal resonance, the focus in this section is placed solely

TABLE I. Interaction cases that produce scattering higher order harmonics ("L" represents for waves of longitudinal nature and 'T' means torsional nature waves. "Y" means the secondary mode is potentially cumulative, 'N' indicates that the secondary field is not cumulative.).

Primary waves			Secondary waves T	Secondary waves L	Resonant frequency T	Resonant frequency L	Circumferential order T	Circumferential order L	Scattering angle $\tan\psi$ T	Scattering angle $\tan\psi$ L
Self interactions	Quadratic	L	N̸	Y	...	$2\omega_a$ or $2\omega_b$	...	$2P$ or $2Q$	...	$\dfrac{P}{k_a R}$ or $\dfrac{Q}{k_b R}$
		T	N̸	Y	...	$2\omega_a$ or $2\omega_b$	...	$2P$ or $2Q$	...	$\dfrac{P}{k_a R}$ or $\dfrac{Q}{k_b R}$
	N^{th} order interaction	...		...		$N\omega_a$		lP	$\dfrac{lP}{Nk_a R}$	$\begin{cases} l=1,3,...,N, & \text{if N is an odd number} \\ l=0,2,...,N, & \text{if N is an even number} \end{cases}$
Mutual interactions	Quadratic	T-T	N̸	Y	...	$2\omega_a, 2\omega_b$ or $\omega_a\pm\omega_b$	...	$2P, 2Q$ or $P\pm Q$	...	$\dfrac{P}{k_a R}$ or $\dfrac{Q}{k_b R}$ $\dfrac{P\pm Q}{(k_a\pm k_b)R}$
		L-L								
		L-T	Y	Y	$\omega_a\pm\omega_b$	$2\omega_a$ or $2\omega_b$	$P\pm Q$	$2P$ or $2Q$	$\dfrac{P\pm Q}{(k_a\pm k_b)R}$	$\dfrac{P}{k_a R}$ or $\dfrac{Q}{k_b R}$
	N^{th} order interaction	...		...		$N_1\omega_a\pm N_2\omega_b$		$l_1 P\pm l_2 Q$		$\dfrac{l_1 P\pm l_2 Q}{(N_1 k_a\pm N_2 k_b)R}$

on primary waves that satisfy the internal resonance criteria since the cumulative nature of these internally resonant higher order harmonics is advantageous in experimental measurements. The dimensions and the material properties of the steel pipe used here for illustrative purpose are given in Table II. For the NHG (self interaction), the synchronism condition is given by $k_N = Nk_0$ at $N\omega_0$, which results in a phase velocity matching condition. Seeking non-zero power flux leads to a relationship between the circumferential order of the primary mode (P) and that of NHG (M): $M = NP$. Thus the internal resonance conditions of the NHGs could be displayed in a plot that contains the phase velocity dispersion curve of primary waves, and secondary phase velocity dispersion curves plotted on a scale of fd/N which represents the potential cumulative NHGs. The synchronism points are the intersections of the primary and the secondary phase velocity dispersion curves, while the internal resonances occur for those points satisfying $M = NP$ at the synchronism points.

Consider the SHG in a quadratic nonlinear hollow circular cylinder for example, as shown in Figure 2. Phase velocity dispersion curves for primary waves with torsional and longitudinal nature are plotted with black solid lines and blue dashed lines in Fig. 2(a), respectively. The phase velocity dispersion curves of potential cumulative SHGs (already proven to have longitudinal nature) are plotted on a scale of $fd/2$ with red dotted lines. In this way, the intersections between the primary and the secondary dispersion curves

display the synchronized SHGs. Only a finite number of primary modes satisfy the SHG synchronism conditions, which are distributed in special zones on the dispersion curves. They are in: (i) vicinities of special phase velocities (longitudinal wave speed C_L, shear wave speed C_T, Lamé wave speed $C_{Lamé}$, or Rayleigh wave speed C_R); (ii) vicinities of primary wave intersections; and (iii) the low frequency range for the three fundamental mode families L(M,1), L(M,2), and T(M,1). Comparing with the synchronism points for the SHG in plates,[22–24] a number of extra synchronism points are available for hollow circular cylinders due to the existence of non-axisymmetric modes in each family. Figures 2(b) and 2(c) show magnified views of one synchronism vicinity marked in Fig. 2(a); the circles in the figure denote the synchronism points with the circumferential order relations $M = 2P$, which indicate the internal resonance points for SHGs.

For the NOHs (mutual interaction), the synchronism condition is given by $k_N = N_1 k_a \pm N_2 k_b$ at the frequencies $N_1\omega_a \pm N_2\omega_b$. The non-zero power flux results in a relationship between the circumferential order of primary (P and Q) and secondary (M) waves: $M = l_1 P \pm l_2 Q$. The variables l_1 and l_2 can be odd or even numbers spanning the range of N, which are determined by the parity of the number of interacting times N_1 and N_2. Figure 3 gives a diagram in the wave-number-frequency-thickness plane, which illustrates the existence of internally resonant higher order scattering waves due to the interaction of two guided wave modes in a hollow cylinder. Examples of some internally resonant higher harmonics (up to third order nonlinearity) due to mode interactions are provided in Table III. Mode pairs 1, 2, and 6 are selected for finite element simulation in Sec. V.

TABLE II. Material and input parameters for the finite element models.

Dimensions		Material properties[a]					
R_i (mm)	R_o (mm)	ρ (kg/m^3)	λ (GPa)	μ (GPa)	A (GPa)	B (GPa)	C (GPa)
9	10.5	7932	116.2	82.7	-325	-310	-800

[a]A, B, and C are from the Ref. 27. A conversion between Landau and Lifshitz third order elastic constants and Murnaghan constants can be found in Norris.[28]

V. NUMERICAL RESULTS

Numerical evaluation of the characteristics of higher order harmonics due to the nonlinear wave interactions is performed using 3D nonlinear finite element analysis and the results presented. Aside from the selection of which primary
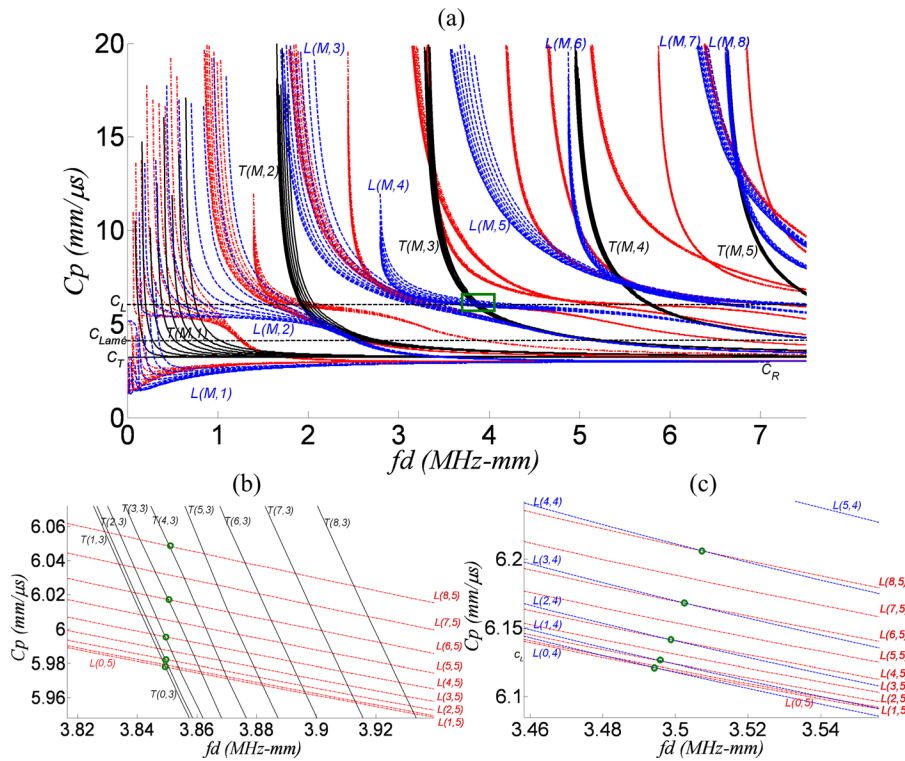
FIG. 2. Phase velocity-frequency thickness plots illustrate the phase matching of SHGs in a hollow circular cylinder. In (a), the black solid line and blue dashed lines are dispersion curves for primary modes with torsional and longitudinal nature, respectively. The potential cumulative SHG dispersion curves are plotted with red dotted lines. Intersections between primary waves and second harmonics indicate the synchronism points. (b) and (c) are magnifications showing internal resonance points for torsional and longitudinal primary waves respectively.

modes to generate these results are independent of the modeling conducted in Part I and are presented to demonstrate that modeling[1] can correctly identify primary modes that generate cumulative higher harmonics. A steel pipe with the parameters given in Table II is considered for this study. Based on the plate ray perspective of flexural waves, devices such as inter-digital transducers (IDTs) can be designed to generate a predominant flexural mode. A traditional IDT provides mode control based on the element width D being equal to a half wavelength of the generated mode, that is, $D = \lambda_f/2$. Substituting this relation into Eq. (8), the excitation angle for a flexural mode of circumferential order M by a helical inter-digital transducer (HIDT) can be obtained from

$$\sin \phi_\mu^M = \frac{MD}{\pi R_m}, \quad M = \pm 1, \pm 2, \pm 3..., \quad (17)$$

where the central frequency for the corresponding flexural mode excitation is

$$f = \frac{2 C_{P_\mu}^{(0)}}{D}, \quad (18)$$

where $C_{P_\mu}^{(0)}$ is the phase velocity of the axisymmetric mode in the μth family.

Equations (17) and (18) give the transducer loading parameters to excite a single predominant flexural mode based on the plate ray interpretation. Our particular interest is in the pipe geometry and parameters given in Table II, which is unusual in that the radius is quite small. The mean radius to thickness ratio is $R_m/t = 6.5$, whereas most pipes of usual interest have much larger ratios. According to Khajeh,[25] the asymptotic analysis is valid for $R_m/t > 16$, while Chillara and Lissenden[18] consider both R_m and frequency. Due to the small R_m/t ratio used here, Eq. (17) provides only an estimate of the tilt angle. While the estimate is reasonably good, it is insufficient to demonstrate the circumferential order-power flux relation. The inexact nature of the estimate is apparent from unequal energy in circumferential orders adjacent to the primary mode order. Thus, a tilt angle tuning procedure is implemented.

Tuning the tilt angle is performed by a finite element based feedback adjustment procedure (FEFAP). First, the tilt angle is calculated from Eq. (17) and then a transient dynamics finite element analysis of wave propagation is run. Then
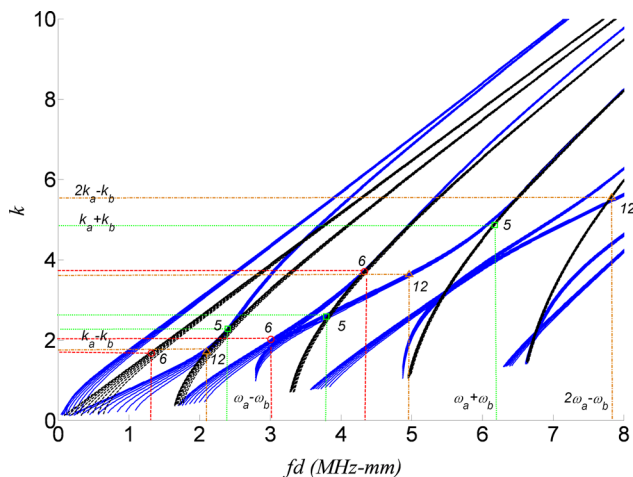

FIG. 3. The wave number-frequency thickness plot shows the existence of phase matched scattering waves due to the mutual interaction of two guided wave modes in a hollow circular cylinder. Examples show sum (mode pair 5) and difference (mode pair 6) frequency phase matching points at quadratic interactions, and a difference frequency phase matching pair at third order interactions (mode pair 12). The detailed information for the interaction mode pairs is provided in Table III.

TABLE III. Examples of candidate mode pairs for internally resonant higher order harmonic generation (notice that ω_a and ω_b are not specific frequency values, they indicate different order of wave interactions. "*P*" and "*S*" represent for primary and secondary waves, respectively).

Order of interaction		Mode pair NO.	Mode types		f-k pair		Circum order		Scattering angle (°)
			P	S	P	S	P	S	
2	$2\omega_a$	1	$T(2,3)$	$L(4,5)$	(2.56,2.67)	(5.12,5.34)	2	4	4.36
	$2\omega_b$	2	$L(4,4)$	$L(8,5)$	(2.33,2.36)	(4.66,4.72)	4	8	9.83
	$\omega_a + \omega_b$	3	$T(3,2)/T(0,4)$	$L(4,5)$	(1.20,0.92)/(4.00,4.54)	(5.20,5.46)	3/0	4	4.29
		4	$L(1,3)/L(5,6)$	$L(6,8)$	(1.60,1.34)/(3.51,2.82)	(5.11,4.16)	1/5	6	17.73
		5	$T(2,2)/L(5,4)$	$T(7,4)$	(1.60,2.28)/(2.52,2.59)	(4.12,4.87)	2/5	7	6.13
	$\omega_a - \omega_b$	6	$T(3,1)/T(4,3)$	$L(1,3)$	(0.88,1.68)/(2.89,3.70)	(2.01,2.02)	3/4	1	2.90
		7	$L(2,3)/L(4,4)$	$L(2,2)$	(2.3,2.52)/ (3.4,3.78)	(1.1,1.26)	2/4	2	8.39
		8	$T(3,1)/L(0,5)$	$T(3,4)$	(0.80,1.53)/ (4.37,4.39)	(3.57,2.86)	3/0	3	8.34
3	$3\omega_a$	9	$T(0,1)$	$T(0,1)$	…	…	0	0	0
	$3\omega_b$	10	$L(2,2)$	$L(6,3)$	(0.86,1.00)	(2.58,3.00)	2	6	11.88
	$2\omega_a + \omega_b$	11	$T(2,1)/L(0,3)$	$L(4,3)$	(0.60,1.15)/ (1.74,1.58)	(2.94,3.88)	2/0	4	6.06
	$2\omega_a - \omega_b$	12	$L(4,5)/T(2,2)$	$T(6,5)$	(3.31,3.64)/ (1.40,1.72)	(5.22,5.56)	4/2	6	6.29
	$\omega_a + 2\omega_b$	13	$L(0,1)/T(4,2)$	$L(8,3)$	(0.51,1.46)/ (1.60,2.24)	(3.71,5.94)	0/4	8	7.85
	$\omega_a - 2\omega_b$	14	$L(6,6)/L(3,2)$	$L(0,4)$	(4.95,5.50)/ (0.90,1.02)	(3.15,3.45)	6/3	0	0

a circumferential Fourier transform is applied and the displacement components of the circumferential orders adjacent to the one targeted for excitation are analyzed. If one adjacent order is significantly larger than the other, the tilt angle is adjusted and the finite element analysis re-run. This process is iterated until the displacements in the adjacent circumferential orders have nearly equal values that are low.

A. Mode self interaction of a torsional flexural wave—mode pair 1

We first present the numerical results for the study of cumulative behavior of the SHGs due to a primary torsional flexural wave self interaction. According to the analysis in Sec. III, a 4-element HIDT that wraps around the circumference of the pipe is simulated for the excitation of the $T(2,3)$ mode, which is an internal resonance case as shown in Table III. A 15-cycle tone burst traction with a central frequency $f = 2.56$ MHz has been applied in the circumferential direction to generate the primary $T(2,3)$ mode. The HIDT element spacing matches the half wavelength and the element width is half of the spacing. The wavelength for $T(2,3)$ at $f = 2.56$ MHz is $\lambda = 2.36$ mm. Knowing the circumferential order, the element spacing and the mean radius of the cylinder, the tilt angle for the primary $T(2,3)$ mode is calculated to be 4.36° from Eq. (17). Tuning via FEFAP resulted in a tilt angle of 3.80°.

Figure 4 shows the circumferential (u_Θ) and axial (u_Z) displacement components of the time domain signals received at the outer surface of the cylinder for a propagation distance of 25λ. Components u_Θ and u_Z are analyzed because the primary $T(2,3)$ mode has a dominant circumferential displacement component, as shown in the wavestructure plot in Fig. 5(a), while the predicted SHG $L(4,5)$ has a prevailing axial component and an almost zero circumferential component on the outer surface as shown in Fig. 5(b). Figure 6 shows the frequency spectra for the windowed first received wave packets of u_Θ and u_Z. It should be pointed out that all

the simulation data are analyzed with the same window type and a fixed window size for each data set.[2] It is observed in Fig. 6 that both u_Θ and u_Z are present at the primary and third harmonics, while u_Z has an additional second harmonic component. This is explained by Eq. (37) in Part I of this article series, which indicates that no torsional waves can be generated as SHGs for a mode self interaction at quadratic nonlinearity.[1] The second harmonic component of u_Z should be the $L(4,5)$ mode. The observation of third harmonics of torsional waves in pipes is reasonable since this is analogous with the holo-internal-resonant third harmonic shear horizontal waves in plate.[26] Figure 7 shows the circumferential order for u_Θ at the primary frequency ($f = 2.56$ MHz) and u_Z at the second harmonic frequency ($f = 5.12$ MHz), respectively. Observation of the circumferential orders indicates that the primary wave is of order 2 ($T(2,3)$), while the SHG has circumferential order 4 ($L(4,5)$). Results for the tilt angle computed from Eq. (17) and the tuned FEFAP are shown. In this case there is very little difference between tilt angles of
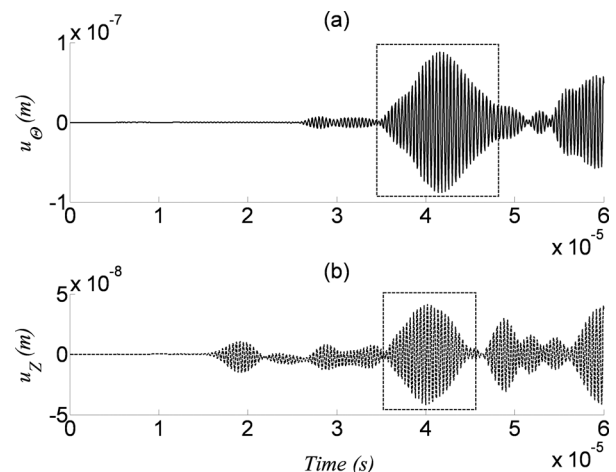

FIG. 4. Time domain signals from $T(2,3)$ primary excitation at a propagation distance of 25λ; (a) u_Θ and (b) u_Z displacement components. The dashed rectangles indicate time domain windows used for a Fourier transform.
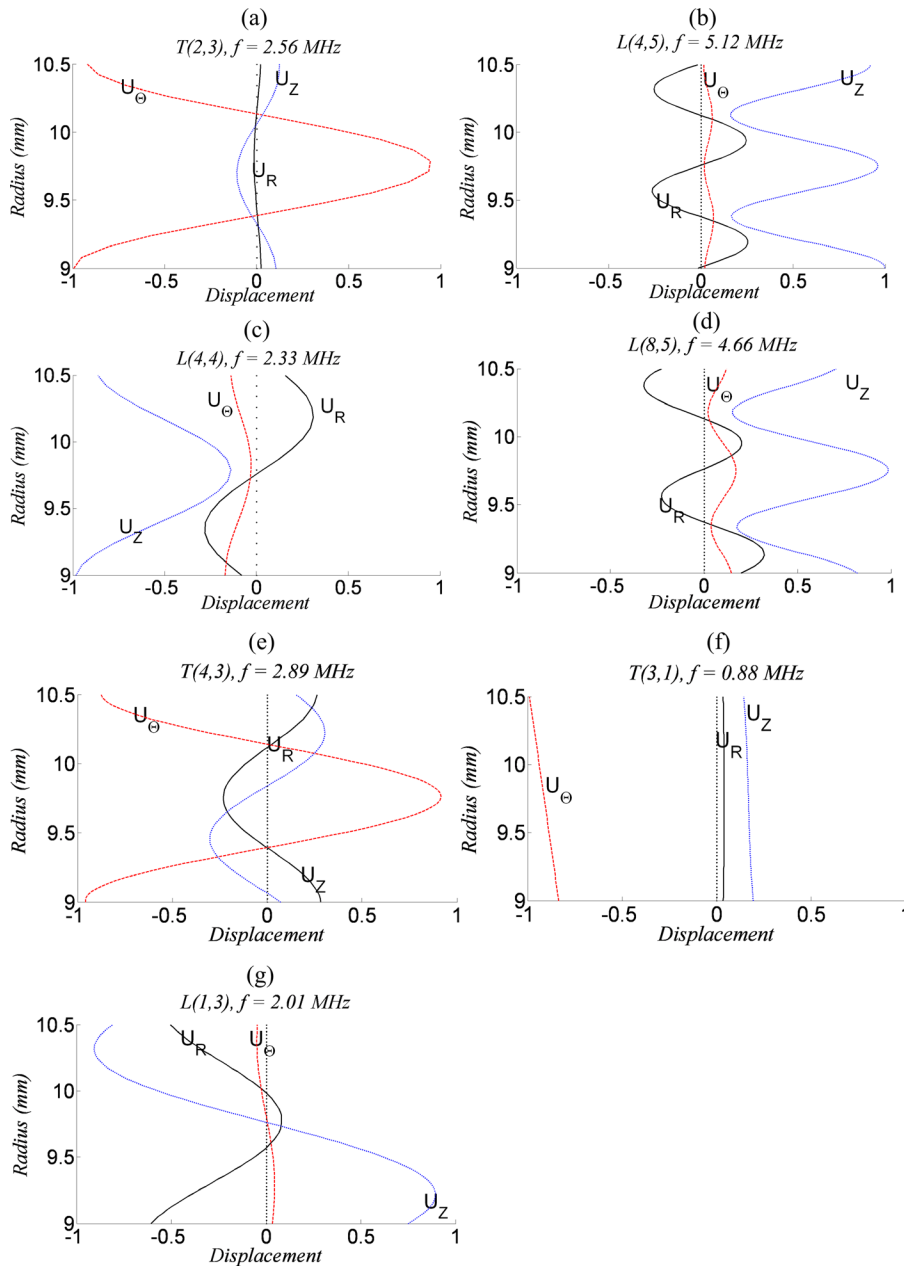
FIG. 5. Wavestructures for the mode pairs 1, 2, and 6 used in the numerical evaluation.

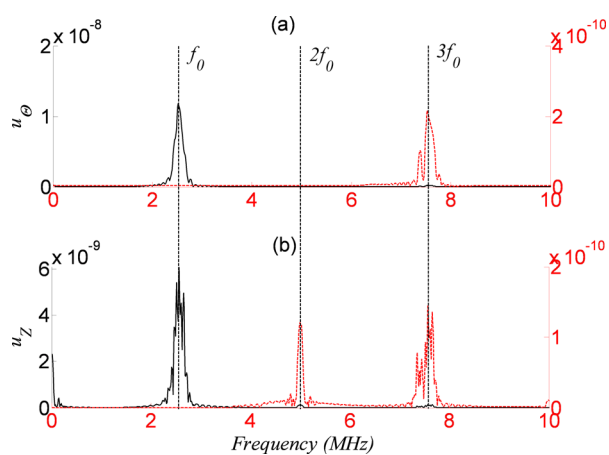FIG. 6. Frequency spectra from $T(2,3)$ primary excitation for (a) u_Θ and (b) u_Z displacement components. The SHG component is absent for u_Θ, while it is evident for u_Z.
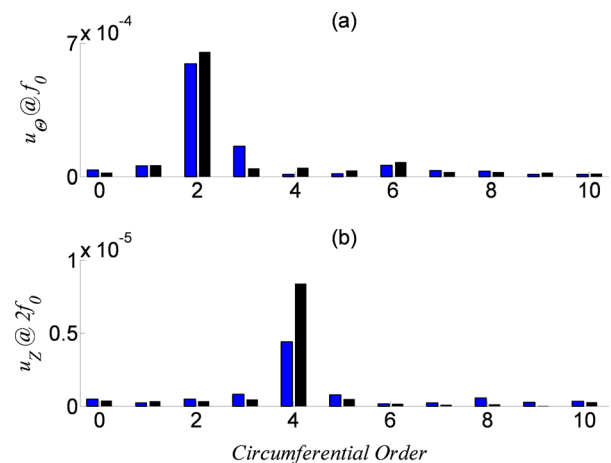

FIG. 7. Histograms for mode pair 1 $T(2,3)/L(4,5)$; (a) u_θ at 2.56 MHz, (b) u_z at 5.12 MHz. Blue and black bars represent tilt angles of 4.36° and 3.8°, from Eq. (17) and FEFAP, respectively.

4.36 and 3.8°. The normalized modal amplitude ratio, $A_2/A_1{}^2$, where A_1 and A_2 are the amplitudes of u_Θ at f_0 and u_Z at $2f_0$, respectively, is plotted as a function of propagation distance in Fig. 8. All of the amplitude ratios are normalized with respect to the value of $A_2/A_1{}^2$ at the propagation distance 5λ. A regression line shows that the SHG $L(4,5)$ is cumulative as per Eq. (26) in Part I.[1]

B. Mode self interaction of a longitudinal flexural wave—mode pair 2

The second numerical example focuses on the SHGs due to the self interaction of a longitudinal flexural wave. The primary $L(4,4)$ mode at $f = 2.33$ MHz (mode pair 2 shown in Table III) is generated by a 4-element HIDT transducer through axial tone burst traction components applied at half-wavelength spacing. The wavelength for the mode is 2.65 mm, while the tilt angle calculated by Eq. (17) is 9.83, which is tuned by FEFAP to 9.2°. The receivers are placed at nodes located at 5λ, 10λ, 15λ, 20λ, and 25λ from the transducer. The axial displacement component is analyzed as both the primary $L(4,4)$ and the predicted SHG $L(8,5)$ modes have a dominant u_Z component at the outer surface of the circular cylinder, as indicated in Figs. 5(c) and 5(d). Figure 9(a) shows the time domain signal of the axial displacement component received at a propagation distance of 25λ. A Tukey window was applied to the first-received wave packet and the corresponding frequency spectrum is shown in Fig. 9(b), where a SHG component is obvious. A 2D Fourier transformation of the axial displacements taken in time and around the circumference enabled identification of circumferential orders for both primary and secondary frequencies. Both tilt angles, 9.83 from Eq. (17) and 9.2° as tuned by FEFAP, are shown in Fig. 10. Even though the primary mode circumferential order of 4 is well excited by both tilt angles, the angle computed by Eq. (17) resulted in significantly more energy in order 5 than 3 indicating that Eq. (17) was inexact. The result of the error in the tilt angle is evident in Fig. 10(b), where the energy is distributed to many circumferential orders. Energy tends to remain in the circumferential order of the primary mode. However, the tuned tilt angle not only concentrates more energy in the circumferential order for the
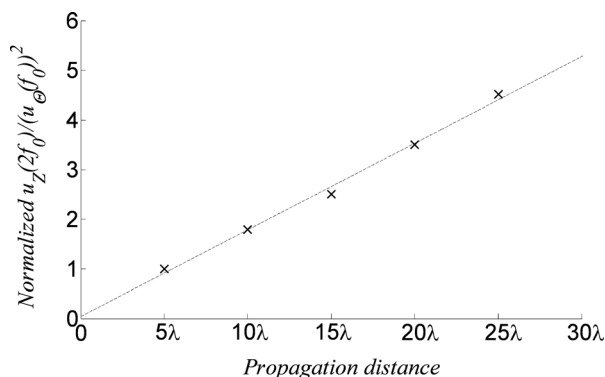

FIG. 9. Signal received from primary $L(4,4)$ excitation at a propagation distance of 25λ. (a) Received time domain signals of u_Z component, and (b) the corresponding frequency spectrum for the windowed wave packet.

primary excitation, but it also permits most of the energy at the secondary frequency to exist at the circumferential order 8 associated with mode $L(8,5)$.

The normalized modal amplitude ratio $A_2/A_1{}^2$, where A_1 is the amplitude of the primary $L(4,4)$ mode at f_0 and A_2 is the SHG $L(8,5)$ mode at $2f_0$, is plotted as a function of propagation distance in Fig. 11. A linear increase of the normalized $A_2/A_1{}^2$ is observed, which indicates that $L(4,4)$ at $f = 2.33$ MHz is in internal resonance with the SHG $L(8,5)$ at $f = 4.66$ MHz.

C. Mode mutual interaction—mode pair 6

The third numerical example investigates the sum and difference harmonic generation due to the quadratic mutual interaction of two collimated waves with torsional nature. The primary modes $T(3,1)$ and $T(4,3)$, having wavestructures shown in Figs. 5(e) and 5(f), are generated by two independent HIDTs, which are located near the right-end and left-end of the circular cylinder respectively. The HIDT for the primary $T(3,1)$ mode has an element spacing of 1.86 mm and tilt angle of 10.3°, while the HIDT for the primary $T(4,3)$ has element spacing 0.85 mm and an tilt angle of 5.8°. These tilt

FIG. 8. The normalized modal amplitude ratio $A_2/A_1{}^2$ for $T(2,3)$ mode excitation as a function of propagation distance. A_1 is the modal amplitude of u_Θ at the primary frequency, while A_2 is the amplitude of u_Z at double harmonic frequency. A best fit line of the data points is included.

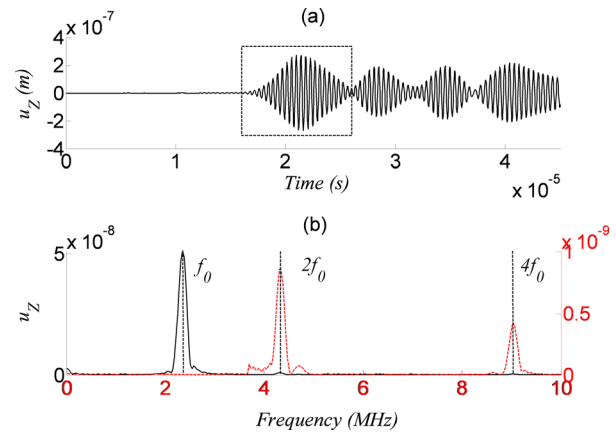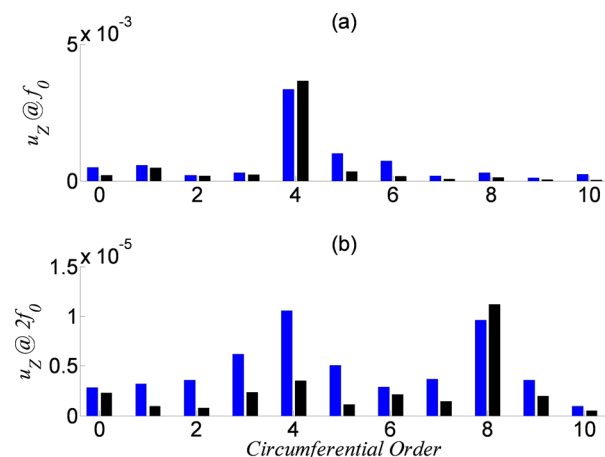FIG. 10. Histograms for mode pair 2 $L(4,4)/L(8,5)$; (a) u_Z at 2.33 MHz, (b) u_z at 4.66 MHz. Blue and black bars represent tilt angles of 9.83° and 9.2°, from Eq. (17) and FEFAP respectively.
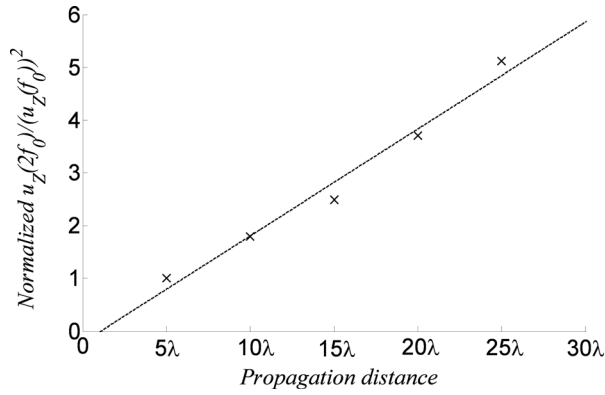
FIG. 11. The normalized modal amplitude ratio A_2/A_1^2 for $L(4,4)$ mode excitation as a function of propagation distance. A_1 is the modal amplitude of u_Z at the primary frequency, while A_2 is the amplitude of u_Z at the double frequency. The line represents regression to the data points.

angles were tuned using FEFAP (the tilt angles computed from Eq. (17) are 10.5° and 6.3° for modes $T(3,1)$ and $T(4,3)$, respectively). The interaction between the counter propagating $T(3,1)$ (at $f_2 = 0.88$ MHz) and $T(4,3)$ (at $f_1 = 2.89$ MHz) generate the difference harmonics $L(1,3)$ (at $f = f_1 - f_2 = 2.01$ MHz) (mode pair 6 in Table III). Time delays can be conveniently applied to each HIDT to enable a full length scan of the localized acoustic nonlinearity by the mode mutual interactions. Axial displacement component u_Z is analyzed, since the predicted difference harmonic $L(1,3)$ (at $f = 2.01$ MHz) has a dominant u_Z displacement on the outer surface of the circular cylinder as shown in Fig. 5(g). Figure 12(a) shows the time domain signals of the u_Z component on the outer surface for the propagation distance where the two primary waves interact. A Fourier transformation of the interacting wave packets (indicated by the dotted window) shows the generation of the two primary waves at f_1 and f_2, and the difference harmonics at $f_1 - f_2 = 2.01$ MHz [Fig. 12(b)]. The generation of SHG from the primary $T(3,1)$ mode (at $2f_2 = 1.72$ MHz) and sum harmonics (at $f_1 + f_2 = 3.77$ MHz) are also observed in Fig. 11(b), which is reasonable as higher order harmonics can exist without
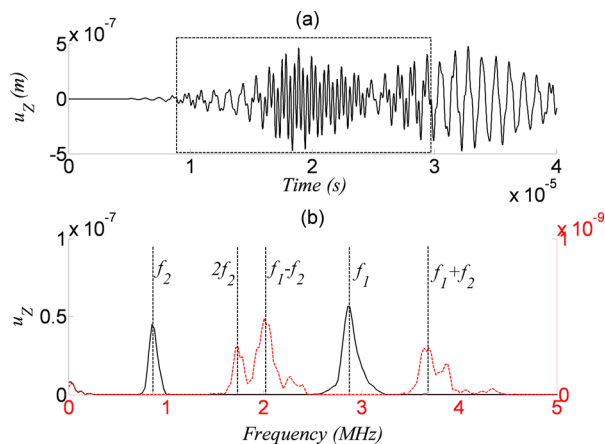

FIG. 12. Signals received from primary $T(3,1)/T(4,3)$ mutual interaction. (a) Received time domain signals of u_Z component in the wave interaction zone, (b) the corresponding frequency spectrum for the windowed wave packet.
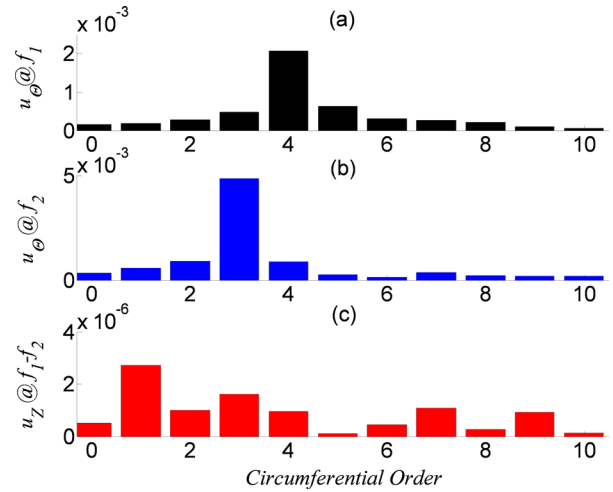

FIG. 13. Histograms for mode pair 6 $T(3,1)/T(4,3)$ mutual interaction. (a) u_Θ component at frequency f_1 has a circumferential order 4 ($T(4,3)$), (b) u_Θ at frequency f_2 shows the excitation of $T(3,1)$, and (c) u_Z component at frequency $f_1 - f_2$ shows a high circumferential order 1 that indicates the excitation of $L(1,3)$.

internal resonance.[2] It is observed that a wave with circumferential order 4 ($T(4,3)$) has been generated at f_1 as shown in Fig. 13(a). In addition, a wave with order 3 ($T(3,1)$) has been excited at f_2 as shown in Fig. 13(b). Their interaction results in the difference harmonic being of circumference order 1 ($L(1,3)$) as shown in Fig. 13(c).

VI. CONCLUSION

A new perspective of elastic wave propagation in hollow circular cylinders has been described in this article, which considers the wave energy carried by numerous plate rays. The wave intensity for an arbitrary point in the cylinder is given by a superposition of the plate rays passing through the point. The axisymmetric waves can be treated as a wave that formed by meridional plate rays that propagate along the axis of the hollow circular cylinders, while a flexural mode is formed by a group of plate rays that propagate at a tilt angle with respect to the axis. Based on this new understanding of flexural waves, the scattering direction of the higher harmonics due to wave interactions are determined. The scattering angles are of practical importance for experimentalists to determine the position of the receiver for the best reception of a specific the higher harmonics. Interpreting flexural modes as helically propagating waves makes it possible to implement the analysis of higher order interactions between elastic waves in hollow cylinders. A helical interdigital transducer has been proposed for the excitation of a single dominant flexural mode. Finite element modeling has been utilized to simulate second harmonic generation by $T(2,3)$ and $L(4,4)$ modes. A linear increase of the normalized amplitude ratio A_2/A_1^2 has been observed for both cases, which indicates mode $L(4,5)$ and $L(8,5)$ are effectively generated as cumulative second harmonics, respectively. A numerical example for the excitation of difference harmonics has been presented by the counter propagation of the $T(3,1)$ and $T(4,3)$ modes. The results show that $L(1,3)$ has been

generated efficiently as a difference harmonic in the zone where the two primary waves interact.

ACKNOWLEDGMENTS

[1]Y. Liu, C. J. Lissenden, and J. L. Rose, "Higher order interaction of elastic waves in weakly nonlinear hollow circular cylinders. I. theoretical foundation," J. Appl. Phys. **115**, 214901 (2014).

[2]W. J. N. de Lima and M. F. Hamilton, Wave Motion **41**, 1 (2005).

[3]A. Srivastava and F. Lanza di Scalea, J. Sound. Vib. **329**, 1499 (2010).

[4]Y. Liu, E. Khajeh, C. J. Lissenden, and J. L. Rose, J. Acoust. Soc. Am. **133**, 2541 (2013).

[5]D. C. Gazis, J. Acoust. Soc. Am. **31**, 568 (1959).

[6]D. C. Gazis, J. Acoust. Soc. Am. **31**, 573 (1959).

[7]J. J. Ditri and J. L. Rose, J. Appl. Phys. **72**, 2589 (1992).

[8]J. J. Ditri, J. Acoust. Soc. Am. **96**, 3769 (1994).

[9]P. W. Smith, Jr., J. Acoust. Soc. Am. **27**, 1065 (1955).

[10]C. R. Steele, Int. J. Eng. Sci. **9**, 681 (1971).

[11]D. Feit, J. Acoust. Soc. Am. **49**, 1499 (1971).

[12]O. A. Germogenova, J. Acoust. Soc. Am. **53**, 535 (1973).

[13]A. D. Pierce and H. G. Kil, ASME J. Vib. Acoust. **112**, 399 (1990).

[14]A. D. Pierce, ASME J. Vib. Acoust. **115**, 384 (1993).

[15]A. N. Norris and D. A. Rebinsky, ASME J. Vib. Acoust. **116**, 457 (1994).

[16]A. N. Norris and D. A. Rebinsky, Wave Motion **21**, 127 (1995).

[17]J. Li and J. L. Rose, Ultrasonics **44**, 35–45 (2006).

[18]W. Luo, X. Zhao, and J. L. Rose, J. Pressure Vessel Technol. **127**, 345 (2005).

[19]A. Velichko and P. D. Wilcox, J. Acoust. Soc. Am. **125**, 3623 (2009).

[20]V. K. Chillara and C. J. Lissenden, Ultrasonics **53**, 862 (2013).

[21]J. L. Rose, *Ultrasonic Waves in Solid Media* (Cambridge University Press, Cambridge, 1999).

[22]M. F. Müller, J. Y. Kim, J. Qu, and L. J. Jacobs, J. Acoust. Soc. Am. **127**, 2141 (2010).

[23]N. Matsuda and S. Biwa, J. Appl. Phys. **109**, 094903 (2011).

[24]Y. Liu, V. Chillara, and C. J. Lissenden, J. Sound. Vib. **332**, 4517 (2013).

[25]E. Khajeh, "Guided wave propagation in complex curved waveguides: flexural guided waves and their application for defect classification in pipes," Ph.D. thesis (The Pennsylvania State University, University Park, 2013).

[26]Y. Liu, V. Chillara, C. J. Lissenden, and J. L. Rose, J. Appl. Phys. **114**, 114908 (2013).

[27]J. J. Rushchitsky, Int. Appl. Mech. **41**, 770 (2005).

[28]A. N. Norris, "Finite amplitude waves in solids," in *Nonlinear Acoustics*, edited by M. F. Hamilton, D. T. Blackstock (Academic Press, San Diego, 1998).

Third harmonic shear horizontal and Rayleigh Lamb waves in weakly nonlinear plates

Yang Liu, Vamshi K. Chillara, Cliff J. Lissenden, and Joseph L. Rose

Additional information on J. Appl. Phys.

Third harmonic shear horizontal and Rayleigh Lamb waves in weakly nonlinear plates

Yang Liu, Vamshi K. Chillara, Cliff J. Lissenden,[a] and Joseph L. Rose
Department of Engineering Science and Mechanics, The Pennsylvania State University, University Park, Pennsylvania 16802, USA

The third order harmonic generation (third harmonics as well as cubic sum and difference harmonics) due to the cubic interaction of two collimated elastic waves in a homogeneous, isotropic, weakly nonlinear plate is investigated by using a fourth order expansion of strain energy density to formulate the nonlinear boundary problems. Waves with both shear horizontal (SH) and Rayleigh Lamb (RL) nature are considered as primary or tertiary wave fields. The non-zero power flux condition is evaluated using characteristic parity matrices of the cubic nonlinear forcing terms and third order harmonic mode shapes. Results indicate that waves with either SH or RL nature receive power flux from a specific pattern of primary mode interaction. Further analytical evaluation of the synchronism condition enables identification of primary SH and RL modes that are able to generate cumulative third harmonics. The primary SH modes are shown to be holo-internal-resonant with third harmonic SH fields. This simply means that all points on the primary dispersion curves are internally resonant with third harmonics, which is not the case for second harmonics. Such flexibility will be advantageous for laboratory and field measurements. © *2013 AIP Publishing LLC*. [http://dx.doi.org/10.1063/1.4821252]

I. INTRODUCTION

Interest is growing in higher harmonic generation of ultrasonic waves associated with the scattering of monochromatic waves due to the nonlinearity from anomalies in lattice structures and nonlinear lattice potential. The work of Hikata et al.,[1] Cantrell and Yost,[2–5] and Kim et al.[6] are examples that show that nonlinear generation of higher harmonics from bulk ultrasonic waves correlate to the changes in microstructural features such as dislocation density and persistent slip bands as precursors to macroscopic cracks[1–3,6] and precipitates and coarsening due to thermal aging.[4,5] Higher harmonic generation of plate waves—both shear-horizontal (SH) and Rayleigh-Lamb (RL) modes—combines the penetration power of guided waves with the sensitivity of nonlinear techniques and is an attractive option for monitoring and characterizing material degradation. The higher harmonic generation in a weakly nonlinear elastic plate has been investigated by Deng,[7,8] de Lima and Hamilton,[9] Strivastava and Lanza di Scalea,[10] Müller et al.,[11] Liu et al.,[12] and Chillara and Lissenden.[13] These works demonstrate that the primary modes with phase matching and large power flux to secondary modes will generate cumulative higher harmonics that are advantageous in experimental measurements. Müller et al.[11] and Matsuda and Biwa[14] manipulated the dispersion relation of RL waves and identified primary modes that are capable of generating cumulative second harmonics. Liu et al.[12] extended the analysis to the interaction of primary SH and RL modes. Additional primary SH modes are identified in their work to generate cumulative second harmonics

with symmetric RL nature. Experimental results confirmed the theoretical predictions and demonstrated the sensitivity of second harmonics to material degradation associated with fatigue[15–18] and creep.[19]

Despite all the aforementioned success in using second harmonics of plate waves to characterize material microstructural changes, one major challenge is the difficulty in exciting these primary modes with the current state of transducer technology. While much research effort has been placed on the second harmonic generation from a single primary mode excitation, the understanding of higher order harmonic generation due to guided wave mode interactions is quite limited. Strivastava and Lanza di Scalea studied the higher harmonic generation of RL waves in plates[10] and rods[20] from a single primary excitation. However, their results are limited in qualitatively determining the nature of higher harmonics that are possible to be generated and thus cannot be used as a theoretical guideline for experiments. Chillara and Lissenden[13] investigated the interaction of two RL waves at quadratic nonlinearity; they concluded that RL primary guided waves of the same nature can generate symmetric modes at the sum and difference frequencies, while the interactions between primary modes of opposite nature result in antisymmetric second harmonic modes. They also investigated higher harmonic generation from a mode interaction standpoint. Liu et al.[21] presented an analysis of the interaction of torsional and longitudinal guided waves in quadratic nonlinear circular cylinders, then provided an internal resonance plot to select the preferred primary modes that are able to generate strongly cumulative second harmonics. Finite element simulation results corroborated their theoretical model for primary excitations with longitudinal or torsional nature.

---

[a]Author to whom correspondence should be addressed. Electronic mail: Lissenden@psu.edu

Hikata and Elbaum modeled the generation of second and third harmonics due to mobile dislocations in a solid.[22] By comparing the expressions for the second and third harmonics, they concluded that dislocation dynamics is studied more easily through third harmonics. Further experimental results[23] confirmed the sensitivity of third harmonics to dislocation density and loop length. Third harmonic generation of guided waves are also observed numerically and experimentally in the previous works.[10,12,21] However, a literature survey indicates that no mathematical model is available for nonlinear guided wave generation at cubic nonlinearity. Thus, the discrepancy between understanding the physics and the observed phenomena precludes practical application for structural health monitoring.

The objective of this work is to provide a mathematical approach to predict the cumulative behavior of the third order harmonics due to the interaction of two collimated waves in an isotropic elastic plate with cubic nonlinearity. In Sec. II, we formulate and solve the cubic nonlinear boundary problems based on a fourth order expansion of the strain energy density. The cubic nonlinear forcing terms due to primary SH and RL wave interactions are derived in Sec. III. The characteristic parity matrix of these nonlinear forcing terms facilitate analysis of the power flux condition for a given third order harmonic field due to an arbitrary primary interaction. In Sec. IV, we present an analytical examination of phase matching for third harmonic generation. A list of primary excitations (including both SH and RL modes) that are able to generate cumulative third harmonics is provided. Compared with second harmonics, additional phase matching points with good mode excitability are available, which is a big advantage for experiments. Finally, conclusions are drawn in Sec. V.

II. CUBIC NONLINEAR BOUNDARY VALUE PROBLEM

The analysis of the cubic nonlinear problem in a traction free plate is undertaken in the reference configuration using a Cartesian coordinate system, which is shown in Figure 1. Assume both RL and SH waves have wavevectors that coincide with the $X1$ axis, thus, the RL waves polarize in $X1$ and $X3$, while the SH modes have particle displacement in the $X2$ direction. In finite strain theory, the Lagrangian strain tensor $\mathbf{E}$ is given by
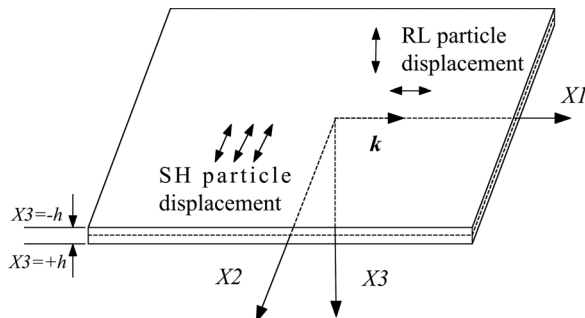

FIG. 1. Stress free plate in a Cartesian coordinate system. $X(X_1, X_2, X_3)$ indicates a reference configuration.

$$\mathbf{E} = \frac{1}{2}(\mathbf{H} + \mathbf{H}^T + \mathbf{H}^T\mathbf{H}), \tag{1}$$

where $\mathbf{H} = \nabla\mathbf{u}$ is the gradient of particle displacement.

Murnaghan[24] used a power series to represent the strain energy density of an isotropic, elastic, weakly nonlinear medium in the three strain invariants. Likewise, Landau and Lifshitz[25] proposed a third order expansion for the elastic energy density. An appropriate extension to the fourth order is given by[26]

$$
\begin{aligned}
S_E = {}& \frac{1}{2}\lambda\big(tr(\mathbf{E})\big)^2 + \mu\, tr(\mathbf{E}^2) \\
& + \frac{1}{3}\bar{A}\,tr(\mathbf{E}^3) + \bar{B}\,tr(\mathbf{E})tr(\mathbf{E}^2) + \frac{1}{3}\bar{C}\big(tr(\mathbf{E})\big)^3 \\
& + \bar{E}\,tr(\mathbf{E})tr(\mathbf{E}^3) + \bar{F}\big(tr(\mathbf{E})\big)^2 tr(\mathbf{E}^2) \\
& + \bar{G}\big(tr(\mathbf{E}^2)\big)^2 + \bar{H}\big(tr(\mathbf{E})\big)^4 + O(\mathbf{E}^5),
\end{aligned} \tag{2}
$$

where λ and μ are Lamé's constants and $\bar{A}$, $\bar{B}$, and $\bar{C}$ are Landau and Lifshitz third order elastic constants, $\bar{E}, \bar{F}, \bar{G}$ are fourth order elastic constants, and $tr()$ represents the trace.

The second Piola-Kirchhoff stress $\mathbf{T}_{RR}$ can be obtained from

$$\mathbf{T}_{RR} = \frac{\partial S_{\mathbf{E}}}{\partial \mathbf{E}}, \tag{3}$$

which gives

$$
\begin{aligned}
\mathbf{T}_{RR} = {}& \lambda\, tr(\mathbf{E})\mathbf{I} + 2\mu\mathbf{E} \\
& + \bar{A}\mathbf{E}^2 + \bar{B}\,tr(\mathbf{E}^2)\mathbf{I} + 2\bar{B}\,tr(\mathbf{E})\mathbf{E} + \bar{C}\big(tr(\mathbf{E})\big)^2\mathbf{I} \\
& + \bar{E}\,tr(\mathbf{E}^3)\mathbf{I} + 3\bar{E}\,tr(\mathbf{E})\mathbf{E}^2 + 2\bar{F}\,tr(\mathbf{E})tr(\mathbf{E}^2)\mathbf{I} + 2\bar{F}\big(tr(\mathbf{E})\big)^2\mathbf{E} \\
& + 4\bar{G}\big(tr(\mathbf{E}^2)\big)\mathbf{E} + 4\bar{H}\big(tr(\mathbf{E})\big)^3\mathbf{I} + O\big((\mathbf{E})^4\big),
\end{aligned} \tag{4}
$$

where $\mathbf{I}$ is the identity tensor. The second Piola-Kirchoff stress $\mathbf{T}_{RR}$ can be decomposed into linear, quadratic, cubic and higher order parts, that is

$$\mathbf{T}_{RR} = \mathbf{T}_{RR}^L + \mathbf{T}_{RR}^Q + \mathbf{T}_{RR}^C + O\big((\mathbf{E})^4\big). \tag{5}$$

The first Piola-Kirchhoff stress $\mathbf{T}_R$ is related to $\mathbf{T}_{RR}$ through

$$\mathbf{T}_R = (\mathbf{I} + \mathbf{H})\mathbf{T}_{RR}. \tag{6}$$

Substituting Eq. (5) into Eq. (6), we can obtain the linear, quadratic and cubic terms of $\mathbf{T}_R$

$$
\begin{aligned}
\mathbf{T}_R^L &= \mathbf{T}_{RR}^L, \\
\mathbf{T}_R^Q &= \mathbf{T}_{RR}^Q + \mathbf{H}\mathbf{T}_{RR}^L, \\
\mathbf{T}_R^C &= \mathbf{T}_{RR}^C + \mathbf{H}\mathbf{T}_{RR}^Q,
\end{aligned} \tag{7}
$$

where $\mathbf{T}_R^L$ is the linear stress due to the linear Hooke's Law, $\mathbf{T}_R^Q$ is the quadratic nonlinear stress that accounts for quadratic nonlinearity, and $\mathbf{T}_R^C$ is the cubic nonlinear stress that drives the generation of third order harmonics. Substituting Eqs. (1) and (3) into Eq. (7), the linear, quadratic, and cubic parts of the first Piola-Kirchhoff stress $\mathbf{T}_R$ can be written explicitly in terms of the displacement gradient $\mathbf{H}$, respectively,

$$\mathbf{T}_R^L = \frac{\lambda}{2} tr(\mathbf{H}+\mathbf{H}^T)\mathbf{I} + \mu(\mathbf{H}+\mathbf{H}^T), \tag{8}$$

$$\begin{aligned}
\mathbf{T}_R^Q &= \frac{\lambda}{2} tr(\mathbf{H}+\mathbf{H}^T)\mathbf{H} + \frac{\lambda}{2} tr(\mathbf{H}^T\mathbf{H})\mathbf{I} \\
&+ \mu(\mathbf{H}\mathbf{H}+\mathbf{H}\mathbf{H}^T+\mathbf{H}^T\mathbf{H}) \\
&+ \frac{1}{4}\bar{A}(\mathbf{H}\mathbf{H}+\mathbf{H}\mathbf{H}^T+\mathbf{H}^T\mathbf{H}+\mathbf{H}^T\mathbf{H}^T) \\
&+ \frac{\bar{B}}{4} tr(\mathbf{H}\mathbf{H}+\mathbf{H}\mathbf{H}^T+\mathbf{H}^T\mathbf{H}+\mathbf{H}^T\mathbf{H}^T)\mathbf{I} \\
&+ \bar{B}\, tr(\mathbf{H})(\mathbf{H}+\mathbf{H}^T)+\mathrm{C}\big(tr(\mathbf{H})\big)^2\mathbf{I}, \tag{9}
\end{aligned}$$

$$\begin{aligned}
\mathbf{T}_R^C &= \frac{\lambda}{2} tr(\mathbf{H}^T\mathbf{H})\mathbf{H} + \mu\mathbf{H}\mathbf{H}^T\mathbf{H} + \frac{1}{4}\bar{A}\left(\begin{array}{c} \mathbf{H}\mathbf{H}\mathbf{H}+\mathbf{H}\mathbf{H}\mathbf{H}^T+\mathbf{H}\mathbf{H}^T\mathbf{H}^T+2\mathbf{H}\mathbf{H}^T\mathbf{H} \\ +\mathbf{H}^T\mathbf{H}^T\mathbf{H}+\mathbf{H}^T\mathbf{H}\mathbf{H}+\mathbf{H}^T\mathbf{H}\mathbf{H}^T \end{array}\right) \\
&+ \frac{\bar{B}}{4} tr(\mathbf{H}\mathbf{H}^T\mathbf{H}+\mathbf{H}^T\mathbf{H}^T\mathbf{H}+\mathbf{H}^T\mathbf{H}\mathbf{H}+\mathbf{H}^T\mathbf{H}\mathbf{H}^T)\mathbf{I} + \frac{\bar{B}}{4} tr(\mathbf{H}\mathbf{H}+\mathbf{H}\mathbf{H}^T+\mathbf{H}^T\mathbf{H}+\mathbf{H}^T\mathbf{H}^T)\mathbf{H} \\
&+ \bar{B}\, tr(\mathbf{H})(\mathbf{H}\mathbf{H}+\mathbf{H}\mathbf{H}^T+\mathbf{H}^T\mathbf{H}) + \frac{\bar{B}}{2} tr(\mathbf{H}^T\mathbf{H})(\mathbf{H}+\mathbf{H}^T) + \bar{C}\, tr(\mathbf{H}) tr(\mathbf{H}^T\mathbf{H})\mathbf{I} + \bar{C}\big(tr(\mathbf{H})\big)^2\mathbf{H} \\
&+ \frac{1}{8}\bar{E}\, tr\left(\begin{array}{c} \mathbf{H}\mathbf{H}\mathbf{H}+\mathbf{H}\mathbf{H}\mathbf{H}^T+\mathbf{H}\mathbf{H}^T\mathbf{H}+\mathbf{H}\mathbf{H}^T\mathbf{H}^T \\ +\mathbf{H}^T\mathbf{H}\mathbf{H}+\mathbf{H}^T\mathbf{H}\mathbf{H}^T+\mathbf{H}^T\mathbf{H}^T\mathbf{H}+\mathbf{H}^T\mathbf{H}^T\mathbf{H}^T \end{array}\right)\mathbf{I} + \frac{3\bar{E}}{4} tr(\mathbf{H})\cdot(\mathbf{H}\mathbf{H}+\mathbf{H}\mathbf{H}^T+\mathbf{H}^T\mathbf{H}+\mathbf{H}^T\mathbf{H}^T) \\
&+ \frac{1}{2}\bar{F}\, tr(\mathbf{H}) tr(\mathbf{H}\mathbf{H}+\mathbf{H}\mathbf{H}^T+\mathbf{H}^T\mathbf{H}+\mathbf{H}^T\mathbf{H}^T)\mathbf{I} + \bar{F}\big(tr(\mathbf{H})\big)^2(\mathbf{H}+\mathbf{H}^T) + \frac{\bar{G}}{2} tr(\mathbf{H}\mathbf{H}+\mathbf{H}\mathbf{H}^T+\mathbf{H}^T\mathbf{H}+\mathbf{H}^T\mathbf{H}^T)\cdot(\mathbf{H}+\mathbf{H}^T) \\
&+ \bar{H}\left(4\big(tr(\mathbf{H})\big)^3+4\big(tr(\mathbf{H})\big)^2 tr(\mathbf{H}^T\mathbf{H})+tr(\mathbf{H})\big(tr(\mathbf{H}^T\mathbf{H})\big)^2\right)\mathbf{I}. \tag{10}
\end{aligned}$$

The balance of linear momentum and boundary conditions for the stress free plate shown in Figure 1 are

$$Div(\mathbf{T}_R) = \rho\,\ddot{\mathbf{u}}, \quad \mathbf{T}_R\cdot\mathbf{n}_3 = \mathbf{0}, \quad at\ X_3 = \pm h, \tag{11}$$

where ρ is the referential material density and $\mathbf{n}_3$ is the unit normal of the plate surface. Consider the interaction of two collimated plate wave modes $\mathbf{u}^{(a)}$ and $\mathbf{u}^{(b)}$, for which the frequency-wavenumber are (ω_a, k_a) and (ω_b, k_b), respectively. The wave-wave scattering in the weakly nonlinear material produce higher harmonic waves of mixed frequencies. The total displacement field in the plate up to third order is

$$\begin{aligned}
\mathbf{u} &= \mathbf{u}^{(a)} + \mathbf{u}^{(b)} + \mathbf{u}^{(aa)} + \mathbf{u}^{(bb)} + \mathbf{u}^{(ab)} \\
&+ \mathbf{u}^{(aaa)} + \mathbf{u}^{(bbb)} + \mathbf{u}^{(aab)} + \mathbf{u}^{(abb)}, \tag{12}
\end{aligned}$$

and for perturbation analysis, we assume that

$$\begin{aligned}
&|\mathbf{u}^{(aa)}|, |\mathbf{u}^{(bb)}|, |\mathbf{u}^{(ab)}|, |\mathbf{u}^{(aaa)}|, |\mathbf{u}^{(bbb)}|, |\mathbf{u}^{(aab)}|, |\mathbf{u}^{(abb)}| \\
&\ll |\mathbf{u}^{(a)}|, |\mathbf{u}^{(b)}|, \tag{13}
\end{aligned}$$

where $\mathbf{u}^{(aa)}$ and $\mathbf{u}^{(bb)}$ are second harmonics due to the self interaction of $\mathbf{u}^{(a)}$ and $\mathbf{u}^{(b)}$ at quadratic nonlinearity, respectively. $\mathbf{u}^{(ab)}$ is the sum or difference harmonics due to the mutual interaction of $\mathbf{u}^{(a)}$ and $\mathbf{u}^{(b)}$ at quadratic nonlinearity. We denote $\mathbf{u}^{(aa)}$, $\mathbf{u}^{(bb)}$, and $\mathbf{u}^{(ab)}$ as quadratic harmonics.

$\mathbf{u}^{(aaa)}$ and $\mathbf{u}^{(bbb)}$ are third harmonics due to the cubic self interaction of $\mathbf{u}^{(a)}$ and $\mathbf{u}^{(b)}$, respectively. $\mathbf{u}^{(aab)}$ and $\mathbf{u}^{(abb)}$ are cubic sum and difference harmonics due to the mutual interactions of $\mathbf{u}^{(a)}$ and $\mathbf{u}^{(b)}$ at cubic nonlinearity, for which the frequencies are centered at $|2\omega_a\pm\omega_b|$ or $|\omega_a\pm2\omega_b|$. We denote $\mathbf{u}^{(aaa)}$, $\mathbf{u}^{(bbb)}$, $\mathbf{u}^{(aab)}$, and $\mathbf{u}^{(abb)}$ as cubic harmonics.

The first Piola-Kirchhoff stress $\mathbf{T}_R$ can be rewritten by substituting Eq. (12) into Eq. (7)

$$\begin{aligned}
\mathbf{T}_R &= \mathbf{T}_R^L\big(\mathbf{u}^{(a)}\big) + \mathbf{T}_R^L\big(\mathbf{u}^{(b)}\big) + \mathbf{T}_R^L\big(\mathbf{u}^{(aa)}\big) + \mathbf{T}_R^L\big(\mathbf{u}^{(bb)}\big) \\
&+ \mathbf{T}_R^L\big(\mathbf{u}^{(ab)}\big) + \mathbf{T}_R^L\big(\mathbf{u}^{(aaa)}\big) + \mathbf{T}_R^L\big(\mathbf{u}^{(bbb)}\big) + \mathbf{T}_R^L\big(\mathbf{u}^{(aab)}\big) \\
&+ \mathbf{T}_R^L\big(\mathbf{u}^{(abb)}\big) + \mathbf{T}_R^Q\big(\mathbf{u}^{(a)}, \mathbf{u}^{(b)}, 2, 0\big) + \mathbf{T}_R^Q\big(\mathbf{u}^{(a)}, \mathbf{u}^{(b)}, 0, 2\big) \\
&+ \mathbf{T}_R^Q\big(\mathbf{u}^{(a)}, \mathbf{u}^{(b)}, 1, 1\big) + \mathbf{T}_R^C\big(\mathbf{u}^{(a)}, \mathbf{u}^{(b)}, 3, 0\big) \\
&+ \mathbf{T}_R^C\big(\mathbf{u}^{(a)}, \mathbf{u}^{(b)}, 0, 3\big) + \mathbf{T}_R^C\big(\mathbf{u}^{(a)}, \mathbf{u}^{(b)}, 1, 2\big) \\
&+ \mathbf{T}_R^C\big(\mathbf{u}^{(a)}, \mathbf{u}^{(b)}, 2, 1\big), \tag{14}
\end{aligned}$$

where $\mathbf{T}_R^L\big(\mathbf{u}^{(a)}\big)$, $\mathbf{T}_R^L\big(\mathbf{u}^{(b)}\big)$, $\mathbf{T}_R^L\big(\mathbf{u}^{(aa)}\big)$, $\mathbf{T}_R^L\big(\mathbf{u}^{(bb)}\big)$, $\mathbf{T}_R^L\big(\mathbf{u}^{(ab)}\big)$, $\mathbf{T}_R^L\big(\mathbf{u}^{(aaa)}\big)$, $\mathbf{T}_R^L\big(\mathbf{u}^{(bbb)}\big)$, $\mathbf{T}_R^L\big(\mathbf{u}^{(aab)}\big)$, and $\mathbf{T}_R^L\big(\mathbf{u}^{(abb)}\big)$ are the linear parts of the first Piola-Kirchhoff stress due to the linear Hooke's Law. $\mathbf{T}_R^Q\big(\mathbf{u}^{(a)}, \mathbf{u}^{(b)}, 2, 0\big)$ and $\mathbf{T}_R^Q\big(\mathbf{u}^{(a)}, \mathbf{u}^{(b)}, 0, 2\big)$ correspond to the quadratic terms of nonlinear stress due to self interaction of $\mathbf{u}^{(a)}$ and $\mathbf{u}^{(b)}$, respectively. $\mathbf{T}_R^Q\big(\mathbf{u}^{(a)}, \mathbf{u}^{(b)}, 1, 1\big)$

is the nonlinear stress due to the quadratic mutual interaction of the two modes. $\mathbf{T}_R^C\big(\mathbf{u}^{(a)},\mathbf{u}^{(b)},3,0\big)$ and $\mathbf{T}_R^C\big(\mathbf{u}^{(a)},\mathbf{u}^{(b)},0,3\big)$ are cubic nonlinear stresses caused by the cubic self interaction of $\mathbf{u}^{(a)}$ and $\mathbf{u}^{(b)}$, respectively. $\mathbf{T}_R^C\big(\mathbf{u}^{(a)},\mathbf{u}^{(b)},1,2\big)$ and $\mathbf{T}_R^C\big(\mathbf{u}^{(a)},\mathbf{u}^{(b)},2,1\big)$ are cubic nonlinear stresses due to the two modes mutual interactions. $\mathbf{T}_R^C\big(\mathbf{u}^{(a)},\mathbf{u}^{(b)},1,2\big)$ is caused by mode $\mathbf{u}^{(a)}$ interacting one time and mode $\mathbf{u}^{(b)}$ two times, while $\mathbf{T}_R^C\big(\mathbf{u}^{(a)},\mathbf{u}^{(b)},2,1\big)$ is caused by mode $\mathbf{u}^{(a)}$ interacting two times and mode $\mathbf{u}^{(b)}$ once. All other terms of nonlinear stress contain (i) fourth or higher order terms of fundamental displacements, or (ii) terms of secondary displacements that can be disregarded according to the perturbation assumption (Eq. (13)).

Substituting Eq. (14) into Eq. (11), two linear boundary problems and seven secondary boundary problems can be formulated. In this article, we focus on the generation of cubic harmonics. The secondary boundary problems formulated for cubic nonlinear waves interactions are as follows:

$$Div\Big(\mathbf{T}_R^L\big(\mathbf{u}^{(C)}\big)\Big) - \rho\ddot{\mathbf{u}}^{(C)} = -\mathbf{f}^C\big(\mathbf{u}^{(a)},\mathbf{u}^{(b)},N_a,N_b\big)$$
$$\Big(\mathbf{T}_R^L\big(\mathbf{u}^{(C)}\big) + \mathbf{T}_R^C\big(\mathbf{u}^{(a)},\mathbf{u}^{(b)},N_a,N_b\big)\Big)\cdot\mathbf{n}_3 = \mathbf{0}, at\, X_3 = \pm h,$$
$$(15)$$

where $\mathbf{u}^{(C)}$ $(C = aaa, bbb, aab, abb)$ is the third harmonic displacement field. $\mathbf{f}^C\big(\mathbf{u}^{(a)},\mathbf{u}^{(b)},N_a,N_b\big) = Div\big(\mathbf{T}_R^C\big(\mathbf{u}^{(a)},\mathbf{u}^{(b)},N_a,N_b\big)\big)$ is denoted as the cubic nonlinear body forces which are due to a mutual interaction that mode a participates N_a $(N_a = 0, 1, 2, 3)$ times and mode b interacts N_b $(N_b = 0, 1, 2, 3)$ times, where $N_a + N_b = 3$.

The cubic interaction problems defined by Eq. (15) can be solved with the modal expansion approach[27] as in de Lima and Hamilton.[9] The third harmonic fields can be expressed as a summation of all of the referential third harmonic components

$$\dot{\mathbf{u}}^{(C)}(X_1,X_3,t) = \sum_m a_m^C(X_1)\mathbf{v}_m(X_3),\qquad(16)$$

$$\mathbf{T}^{(C)}(X_1,X_3,t) = \sum_m a_m^C(X_1)\mathbf{T}_m(X_3).\qquad(17)$$

Notice that the third harmonic particle velocity $\mathbf{v}_m$ and stress $\mathbf{T}_m$ include both RL and SH wave fields. Here, a_m^C is the cubic modal participation factor, which is determined from the ordinary differential equation

$$4P_{mn}\left(\frac{\partial}{\partial X_1} - ik_n^*\right)a_m^C(X_1) = p_n^C e^{i(N_a k_a \pm N_b k_b)X_1},\qquad(18)$$

where

$$P_{mn} = -\frac{1}{16}\int_{-h}^{h}\Big(\mathbf{v}_n^*(X_3)\cdot\mathbf{T}_m(X_3) + \mathbf{v}_m(X_3)\cdot\mathbf{T}_n^*(X_3)\Big)\cdot\mathbf{n}_1 dX_3,\qquad(19)$$

$$p_n^C = \frac{1}{2}\left(\begin{array}{c}\int_{-h}^{h}\mathbf{v}_n^*(X_3)\cdot\mathbf{f}^C\big(\mathbf{u}^{(a)},\mathbf{u}^{(b)},N_a,N_b\big)dX_3\\[2mm] -\mathbf{v}_n^*(X_3)\cdot\mathbf{t}_R^C\big(\mathbf{u}^{(a)},\mathbf{u}^{(b)},N_a,N_b\big)\Big|_{-h}^{h}\end{array}\right),\qquad(20)$$

where P_{mn} is the complex power flux in the wave propagation direction and k_n^* is the wavenumber of the unique mode such that $P_{mn} \neq 0$. Here, $\mathbf{t}_R^C\big(\mathbf{u}^{(a)},\mathbf{u}^{(b)},N_a,N_b\big)$ is the nonlinear surface traction, which is given by the dot product of the cubic nonlinear stress $\mathbf{T}_R^C\big(\mathbf{u}^{(a)},\mathbf{u}^{(b)},N_a,N_b\big)$ and the referential surface unit normal $\mathbf{n}_3$. p_n^C is the cubic nonlinear power flux due to the cubic nonlinear forcing terms $\mathbf{f}^C\big(\mathbf{u}^{(a)},\mathbf{u}^{(b)},N_a,N_b\big)$ and $\mathbf{t}_R^C\big(\mathbf{u}^{(a)},\mathbf{u}^{(b)},N_a,N_b\big)$. Equation (18) was derived using complex reciprocity[27]

The solution to Eq. (18) is

$$a_m^C(X_1) = \frac{ip_n^C\left(e^{i(N_a k_a \pm N_b k_b)X_1} - e^{ik_n^*X_1}\right)}{4P_{mn}\left(k_n^* - (N_a k_a \pm N_b k_b)\right)}\quad\text{for } k_n^* \neq N_a k_a \pm N_b k_b,$$
$$(21)$$

$$a_m^C(X_1) = \frac{p_n^C e^{i(N_a k_a \pm N_b k_b)X_1}}{4P_{mn}}X_1,\quad\text{for } k_n^* = N_a k_a \pm N_b k_b.\quad(22)$$

A cumulative cubic harmonic mode, having linearly increasing amplitude with propagation distance, therefore, requires that: (i) $k_n^* = N_a k_a \pm N_b k_b$ (phase matching), (ii) $p_n^C \neq 0$ (non-zero power flux). These two conditions are driven by Eqs. (21) and (22) and taken together comprise internal resonance. In Sec. III, we will comment on which modes, if any, have a cumulative nature given the cubic interaction patterns of modes a and b.

III. CUMULATIVE NATURE OF CUBIC HARMONIC FIELDS

The cubic nonlinear stress components from Eq. (10) are used to assess the cumulative nature of the third harmonic fields due to the interaction of two collimated plate wave modes. The nonzero components of the cubic nonlinear stress for primary SH wave self interactions can be obtained by considering the primary displacement field $\mathbf{u}^{(\alpha)}$, where $\alpha = a$ or b, to have zero $u_1^{(\alpha)}$ and $u_3^{(\alpha)}$ components and to be independent of X_2. Similarly, the nonzero components of the cubic nonlinear stress for primary RL wave self interactions can be obtained by considering primary displacement field $\mathbf{u}^{(\alpha)}$ to have zero $u_2^{(\alpha)}$ component and to be independent of X_2. These expressions are rather lengthy, so they are provided in the Appendix.

The expression of the nonlinear stress $\mathbf{T}_R^C\big(\mathbf{u}^{(a)},\mathbf{u}^{(b)},N_a,N_b\big)$ resulting from cubic mutual interactions (which requires $N_a \neq 0$, $N_b \neq 0$, and $N_a + N_b = 3$) can be obtained by substituting $\mathbf{u}^{(a)} + \mathbf{u}^{(b)}$ into Eqs. (A1)–(A9). These expressions are extremely lengthy and have a similar form as Eqs. (A1)–(A9), thus, they are not written out here.

Cubic self interaction resulting in third harmonics is just a special case of the cubic mutual interactions. A total of 16 combinations of cubic nonlinear interaction must be considered, which is determined by the number of times the

primary wave interacts (N_a and N_b) and the nature of the primary waves, i.e., SH or RL type. Let $S(X_3)$ and $A(X_3)$ denote generic symmetric and antisymmetric functions through the thickness of the plate, respectively. Further, let *SSH*, *ASH*, *SRL*, and *ARL* denote symmetric SH waves, antisymmetric SH waves, symmetric RL waves, and antisymmetric RL waves, respectively. The parity of $\mathbf{T}_R^C\big(\mathbf{u}^{(a)}, \mathbf{u}^{(b)}, N_a, N_b\big)$ and $\mathbf{f}^C\big(\mathbf{u}^{(a)}, \mathbf{u}^{(b)}, N_a, N_b\big)$ for the 16 interaction combinations are obtained from Eqs. (A1) to (A9), and are presented in Table I.

With the parity of cubic nonlinear forcing terms $\mathbf{T}_R^C\big(\mathbf{u}^{(a)}, \mathbf{u}^{(b)}, N_a, N_b\big)$ and $\mathbf{f}^C\big(\mathbf{u}^{(a)}, \mathbf{u}^{(b)}, N_a, N_b\big)$ given in Table I, the power flux from two arbitrary primary modes to a prescribed type of cubic harmonic field can be examined. Take a *SSH-SSH-SSH* primary mode interaction for example, and examine a third order particle velocity field having the parity $\mathbf{v} = \{0, S, 0\}$ for a *SSH* third harmonic. The power flux to the *SSH* third harmonic field is given by Eq. (20) to be

$$
p_n^C = \frac{1}{2}\left(\int_{-h}^{h} \{0, v_2^*[S], 0\} \cdot \begin{Bmatrix} 0 \\ f_2^C[S] \\ 0 \end{Bmatrix} dX_3 \\ -\{0, v_2^*[S], 0\} \begin{bmatrix} 0 & T_{R12}^C[S] & 0 \\ T_{R21}^C[S] & 0 & T_{R23}^C[A] \\ 0 & T_{R32}^C[A] & 0 \end{bmatrix} \begin{Bmatrix} 0 \\ 0 \\ 1 \end{Bmatrix}\Big|_{-h}^{h} \right)
$$

$$
= \frac{1}{2}\left(\int_{-h}^{h} v_2^*[S] f_2^C[S]\, dX_3 - v_2^*[S] T_{R23}^C[A]\Big|_{-h}^{h} \right). \tag{23}
$$

Table I indicates that the same result is obtained for a *SSH-ASH-ASH* interaction. Note that Eq. (23) is in general non-zero (although it could be zero for some special primary-cubic mode pairs at special frequencies).

Now consider an *ASH* type of cubic harmonic field, where the parity of the particle velocity field is $\mathbf{v}$

$= \{0, A, 0\}$. Examining the same *SSH-SSH-SSH* primary mode interaction, the power flux to the cubic *ASH* type harmonic field is given by Eq. (20) to be

$$
p_n^C = \frac{1}{2}\left(\int_{-h}^{h} \{0, v_2^*[A], 0\} \cdot \begin{Bmatrix} 0 \\ f_2^C[S] \\ 0 \end{Bmatrix} dX_3 \\ -\{0, v_2^*[A], 0\} \begin{bmatrix} 0 & T_{R12}^C[S] & 0 \\ T_{R21}^C[S] & 0 & T_{R23}^C[A] \\ 0 & T_{R32}^C[A] & 0 \end{bmatrix} \begin{Bmatrix} 0 \\ 0 \\ 1 \end{Bmatrix}\Big|_{-h}^{h} \right)
$$

$$
= \frac{1}{2}\left(\int_{-h}^{h} v_2^*[A] f_2^C[S]\, dX_3 - v_2^*[A] T_{R23}^C[A]\Big|_{-h}^{h} \right) = 0. \tag{24}
$$

Again, the same result is obtained for a *SSH-ASH-ASH* primary mode interaction. Parity requires that Eq. (24) is always zero, which means no power flows to an *ASH* type third harmonic field from either *SSH-SSH-SSH* or *SSH-ASH-ASH* type primary mode interactions. Thus, an *ASH* type cubic harmonic field cannot be in resonance with either *SSH-SSH-SSH* or *SSH-ASH-ASH* type primary wave fields. All the possible cumulative third harmonic fields due to cubic mode interactions are analyzed in this fashion and the results are tabulated in Table II.

IV. PHASE AND GROUP VELOCITY MATCHING OF THIRD HARMONICS

In this section, we investigate the phase and group velocity matching conditions for cumulative third harmonic generation from cubic self interaction (i.e., a single mode

TABLE II. Possible cumulative cubic harmonic field due to two collimated wave interactions.

Primary interactions	Type of third harmonic field			
	SSH	*ASH*	*SRL*	*ARL*
SSH-SSH-SSH *SSH-ASH-ASH* *SSH-SRL-SRL* *SSH-ARL-ARL*	Y^a	N^a	N	N
ASH-SSH-SSH *ASH-ASH-ASH* *ASH-SRL-SRL* *ASH-ARL-ARL*	N	Y	N	N
SRL-SRL-SRL *SRL-ARL-ARL* *SRL-SSH-SSH* *SRL-ASH-ASH*	N	N	Y	N
ARL-SRL-SRL *ARL-ARL-ARL* *ARL-SSH-SSH* *ARL-ASH-ASH*	N	N	N	Y

[a]"*Y*" means the cubic harmonic field is cumulative, "*N*" indicates that the cubic harmonic field is not cumulative.

TABLE I. Parity properties of cubic nonlinear stress $\mathbf{T}_R^C$ and body force $\mathbf{f}^C$ due to cubic interactions of two collimated wave modes in plates. The primary mode type shown participates an odd number of times in the interaction.

Primary Mode Type	$\mathbf{T}_R^C$	$\mathbf{f}^C$
SSH	$\begin{bmatrix} 0 & S & 0 \\ S & 0 & A \\ 0 & A & 0 \end{bmatrix}$	$\begin{Bmatrix} 0 \\ S \\ 0 \end{Bmatrix}$
ASH	$\begin{bmatrix} 0 & A & 0 \\ A & 0 & S \\ 0 & S & 0 \end{bmatrix}$	$\begin{Bmatrix} 0 \\ A \\ 0 \end{Bmatrix}$
SRL	$\begin{bmatrix} S & 0 & A \\ 0 & S & 0 \\ A & 0 & S \end{bmatrix}$	$\begin{Bmatrix} S \\ 0 \\ A \end{Bmatrix}$
ARL	$\begin{bmatrix} A & 0 & S \\ 0 & A & 0 \\ S & 0 & A \end{bmatrix}$	$\begin{Bmatrix} A \\ 0 \\ S \end{Bmatrix}$

'*S*' and '*A*' represent symmetric and antisymmetric relative to X_3, respectively.

excitation). This parallels the analysis of matching conditions for second harmonics investigated by Müller *et al.*,[11] Liu *et al.*,[12] and Matsuda and Biwa.[14] The potentially cumulative harmonic fields due to cubic wave interactions have been determined by the parity analysis of the nonlinear forcing terms and third harmonic wave structures. By examining the self interaction cases in Table II, we conclude that the third harmonics which receive nonzero power flux have the same nature as the corresponding primary wave field. First, SH modes are analyzed, and then RL modes. Herein, c_L and c_T represent the longitudinal and shear wave speeds, and

$$p^2 = \left(\frac{\omega}{c_L}\right)^2 - k^2, \quad q^2 = \left(\frac{\omega}{c_T}\right)^2 - k^2. \quad (25)$$

A. Primary SH modes and third harmonic SH modes

The dispersion relation for SH modes is given by[28]

$$qh = \frac{n\pi}{2}, \quad (26)$$

where $n = 0, 2, 4, \ldots$ for symmetric SH modes and $n = 1, 3, 5, \ldots$ for antisymmetric SH modes. The third harmonic SH modes are given by

$$3qh = \frac{m\pi}{2}, \quad (27)$$

where m is an integer. Synchronized SH modes must satisfy both Eqs. (26) and (27), which gives

$$m = 3n. \quad (28)$$

Notice that the SH dispersion relation has an infinite number of solutions, which means the condition $m = 3n$ can always be satisfied. Thus, phase matching occurs for all SH wave modes at any frequency; a primary SH wave of mode number n always phase matches with a third harmonic of mode number $3n$.

SH wave phase velocity dispersion curves are shown in Figure 2 for a steel plate. Primary modes are labeled with upper case letters while third harmonic modes are labeled in lower case letters. Third harmonics are plotted as if the abscissa scale is 3 times the frequency. Clearly, the third harmonic modes entirely overlap primary modes.

Next, consider group velocity matching for SH wave modes. Rose gives the expression for group velocity of primary SH modes[27]

$$c_g(\omega h) = c_T \sqrt{1 - \frac{(n/2)^2}{[\omega h/(\pi c_T)]^2}}. \quad (29)$$

Substituting the phase-matched third harmonic SH waves into Eq. (29) yields

$$c_g(3\omega h) = c_T \sqrt{1 - \frac{(m/2)^2}{[3\omega h/(\pi c_T)]^2}} = c_g(\omega h), \quad (30)$$
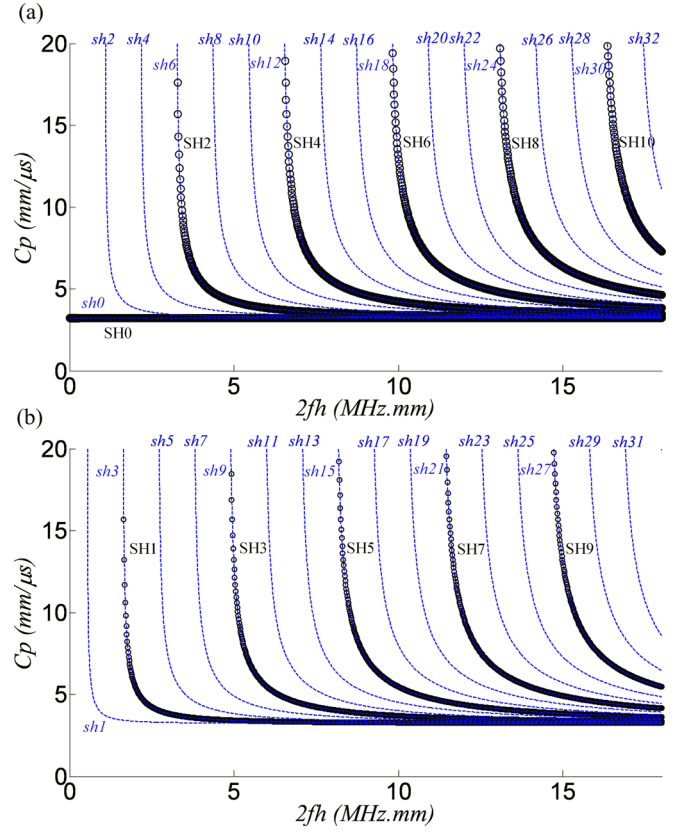
FIG. 2. Phase velocity dispersion curves for (a) SSH modes and (b) ASH modes in a steel plate. Primary and third harmonic modes are labeled with upper and lower case letters, respectively. $c_L = 5.96\,\text{mm}/\mu s$. $c_T = 3.23\,\text{mm}/\mu s$.

which indicates that the group velocity matching condition is met for all SH wave modes at all frequencies.

In summary, primary and third harmonic SH wave modes always exhibit both phase and group velocity matching, thus, we say that SH wave fields are holo-internal-resonant. The mode group number of primary (n) and third harmonic (m) SH wave mode are related by $m = 3n$.

B. Primary RL modes and third harmonic RL modes

The RL dispersion relations are given by[28]

$$\frac{\tan qh}{\tan ph} = -\left(\frac{4k^2pq}{(q^2 - k^2)^2}\right)^{\pm 1}, \quad (31)$$

where the plus and minus exponents correspond to symmetric and antisymmetric modes, respectively. Presume that in order for a primary mode (ω, k) to generate a cumulative third harmonic, that (3ω, $3k$) must also correspond to a mode; i.e., it satisfies the dispersion relation. Moreover, as a consequence of Eq. (22), we seek harmonics that are synchronized to the phase velocity of the fundamental mode. Substituting 3ω for ω and $3k$ for k into Eq. (25) for p and q gives $p \rightarrow 3p$ and $q \rightarrow 3q$, which gives the dispersion relations for the synchronized third harmonic RL modes:

$$\frac{\tan 3qh}{\tan 3ph} = -\left(\frac{4k^2pq}{(q^2 - k^2)^2}\right)^{\pm 1}. \quad (32)$$

Equating Eqs. (31) and (32) gives the synchronized condition for RL modes. Both symmetric and antisymmetric modes lead to

$$\sin 3qh \cos 3ph \cos qh \sin ph$$
$$- \cos 3qh \sin 3ph \sin qh \cos ph = 0, \qquad (33)$$

which can in turn be rewritten as

$$\sin(ph + qh)\sin(ph - qh)\sin ph \cos ph \sin qh \cos qh = 0. \qquad (34)$$

There are five possible solutions

$$\sin ph = 0 \rightarrow ph = n\pi,$$
$$\cos ph = 0 \rightarrow ph = \frac{(2n+1)\pi}{2},$$
$$\sin qh = 0 \rightarrow qh = n\pi, \qquad (35)$$
$$\cos qh = 0 \rightarrow qh = \frac{(2n+1)\pi}{2},$$
$$\sin(ph \pm qh) = 0 \rightarrow ph \pm qh = n\pi,$$

where n is an arbitrary whole number. The possible solutions given in Eq. (35) hold true for all phase velocity regions, namely, $c_p > c_L$ (p, q are both real), $c_L \geq c_p > c_T$ (p is imaginary, while q is real), and $c_p \leq c_T$ (p, q are both imaginary). The analysis has to be undertaken in several cases to identify all of the modes that meet the synchronism conditions.

Case 1: $ph = n\pi$, with $qh \neq n\pi$, but q may be 0

For symmetric primary and third order modes, substitution into Eq. (31) with the positive exponent leads to

$$(q^2 - k^2)^2 = 0$$
$$\Rightarrow q^2 = k^2 \qquad (36)$$
$$\Rightarrow c_p = \sqrt{2}c_T.$$

Equation (36) represents a group of waves known as Lamé modes that have a group velocity of $c_g = \frac{c_T}{\sqrt{2}}$,[14] therefore, group velocity matching also occurs. The corresponding synchronized frequencies can be obtained by substituting $c_p = \sqrt{2}c_T$ into $ph = n\pi$, which gives

$$\omega = \frac{\sqrt{2}n\pi c_L c_T}{h\sqrt{2c_T^2 - c_L^2}}, \qquad (37)$$

and requires that $\sqrt{2}c_T > c_L$.

For antisymmetric primary and third order modes, substitution into Eq. (31) with the negative exponent leads to

$$4k^2 pq = 0 \Rightarrow \begin{cases} p = 0 \Rightarrow c_p = c_L \\ q = 0 \Rightarrow c_p = c_T, \\ k = 0 \end{cases} \qquad (38)$$

where for the three possible solutions: no mode exists for $p = 0$, no mode satisfies $q = 0$, and $k = 0$ occurs at the mode cut-offs. The corresponding synchronized frequency is obtained by substituting $k = 0$ into $ph = n\pi$, which gives

$$\omega = \frac{n\pi c_L}{h}. \qquad (39)$$

The group velocity at all mode cut-off converges to zero, resulting in trivial group velocity matching.

Case 2: $ph = (2n + 1)\pi/2$, with $qh \neq (2n + 1)\pi/2$

The analysis for symmetric primary and third order modes results in Eq. (38). Similarly, $p = 0$ is not possible since $ph = (2n + 1)\pi/2$, no mode satisfies $q = 0$, and the mode cutoffs are again obtained for $k = 0$. The corresponding synchronized frequency is

$$\omega = \frac{(2n+1)\pi c_L}{2h}. \qquad (40)$$

For the analysis of antisymmetric primary and third order modes, substituting into Eq. (31) leads to the synchronized Lamé modes ($c_p = \sqrt{2}c_T$). The corresponding synchronized frequencies are

$$\omega = \frac{\sqrt{2}(2n+1)\pi c_L c_T}{2h\sqrt{2c_T^2 - c_L^2}}. \qquad (41)$$

Again, this requires that $\sqrt{2}c_T > c_L$.

Case 3: $qh = n\pi$, and $ph \neq n\pi$, but p may be 0

For symmetric primary and third order modes, substituting into Eq. (31) leads to $4k^2 pq = 0$. The three possible solutions are discussed below.

(i) $p = 0 \Rightarrow c_p = c_L$, the corresponding synchronized frequencies are obtained by substituting $c_p = c_L$ into $qh = n\pi$, which gives

$$\omega = \frac{n\pi c_L c_T}{h\sqrt{c_L^2 - c_T^2}}. \qquad (42)$$

Müller *et al.*[11] proved that the group velocities of symmetric RL modes at longitudinal velocity are identical and only depend on the material's elastic properties

$$c_g = \frac{c_L c_T^2 (c_L^2 + 2c_T^2)^2}{12c_L^2 c_T^4 - 4c_L^4 c_T^2 + c_L^6 - 8c_T^6}, \qquad (43)$$

therefore, the group velocities also match.

(ii) $q = 0 \Rightarrow c_p = c_T$, but no mode satisfies this condition.

(iii) For $k = 0$, we get the mode cut-offs. The modes are synchronized at

$$\omega = \frac{n\pi c_T}{h}. \qquad (44)$$

For antisymmetric primary and third order modes, Eq. (31) leads to the modes synchronized at the Lamé wave velocity ($c_p = \sqrt{2}c_T$), with the corresponding synchronized frequencies

$$\omega = \frac{\sqrt{2}n\pi c_T}{h}. \qquad (45)$$

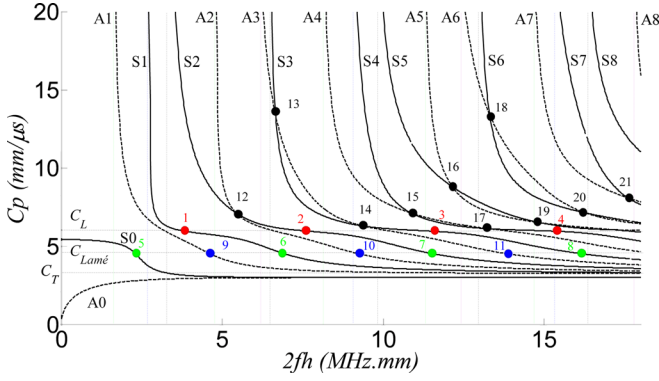**Case 4: $qh = (2n + 1)\pi/2$, with $ph \neq (2n + 1)\pi/2$**

FIG. 3. Phase velocity dispersion curves with synchronism points marked for third harmonic generation for SRL modes (black solid lines) and ARL modes (black dashed lines) in a steel plate. Points 1–4: synchronized SRL modes at longitudinal wave speed; points 5–8: synchronized SRL modes at Lamé wave velocity; points 9–11 denote phased matched ARL modes at Lamé wave velocity; points 12–21: synchronized points at primary mode intersections. The vertical lines represent the synchronized modes at mode cut-offs.

For symmetric primary and third order modes, we get $(q^2 - k^2)^2 = 0 \rightarrow c_p = \sqrt{2}c_T$, which are Lamé modes at the frequencies

$$\omega = \frac{\sqrt{2}(2n+1)\pi c_T}{2h}. \tag{46}$$

For antisymmetric modes, we again get Eq. (38) and the possible solutions are discussed below.

(i)   No mode satisfies $p = 0$.
(ii) The potential solution that $q = 0$, is not possible since $qh = (2n+1)\pi/2$.
(iii) The mode cutoffs occur when $k = 0$, which gives the frequencies

$$\omega = \frac{(2n+1)\pi c_T}{2h}. \tag{47}$$

Case 5: $ph \pm qh = n\pi$
Substituting into Eq. (42) results in

$$\frac{\tan qh}{\tan ph} = \pm 1 = \frac{4k^2 pq}{(q^2 - k^2)^2}$$
$$\rightarrow \frac{(q^2 - k^2)^2}{4k^2 pq} = \pm 1 = \frac{\tan qh}{\tan ph}, \tag{48}$$

for both symmetric and antisymmetric modes, thus, these points are intersections of primary symmetric and antisymmetric modes. Müller *et al.*[11] showed that the group velocities match at these intersection points.

The RL dispersion curves marked with synchronism points for a steel plate are shown in Figure 3. To summarize synchronism of RL modes, the analytical examination of the RL dispersion relations enabled us to identify four types of modes that satisfy both phase and group velocity matching for primary and third order modes. They are: symmetric RL modes at the longitudinal wave speed, symmetric and antisymmetric modes at the Lamé wave speed, symmetric and antisymmetric mode intersections, and symmetric and antisymmetric modes at cut-off frequencies. The synchronism points are tabulated for both SH and RL waves in Table III.

V. CONCLUSION

A mathematical approach has been employed to predict the cumulative behavior of the third order harmonics due to the nonlinear interaction of SH and RL waves in a homogeneous, isotropic plate. It has been shown that both SH and RL modes can be potentially generated as cumulative third order harmonics with a specific type of primary wave interaction,

TABLE III. Phase and group velocity matching mode pairs for third harmonic generation of SH and RL waves.

Primary modes	Third harmonic Modes	Phase velocity	Group velocity	Frequency, ω	Comments
SSH	*SSH*	ALL	ALL	ALL	$m = 3n$
ASH	*ASH*	ALL	ALL	ALL	$m = 3n$
SRL	*SRL*	$\sqrt{2}c_T$	$\dfrac{c_T}{\sqrt{2}}$	$\dfrac{\sqrt{2}n\pi c_L c_T}{h\sqrt{2c_T^2 - c_L^2}}$	*Provided $\sqrt{2}c_T > c_L$*
		$\sqrt{2}c_T$	$\dfrac{c_T}{\sqrt{2}}$	$\dfrac{\sqrt{2}(2n+1)\pi c_T}{2h}$	...
		c_L	$\dfrac{c_L c_T^2 (c_L^2 + 2c_T^2)^2}{12 c_L^2 c_T^4 - 4 c_L^4 c_T^2 + c_L^6 - 8 c_T^6}$	$\dfrac{n\pi c_L c_T}{h\sqrt{c_L^2 - c_T^2}}$	...
		∞	0	$\dfrac{n\pi c_T}{h}$ or $\dfrac{(2n+1)\pi c_L}{2h}$	*Mode cutoffs*
		$> c_L$	...	...	*SRL-ARL intersections*
ASL	*ASL*	$\sqrt{2}c_T$	$\dfrac{c_T}{\sqrt{2}}$	$\dfrac{\sqrt{2}(2n+1)\pi c_L c_T}{2h\sqrt{2c_T^2 - c_L^2}}$	*Provided $\sqrt{2}c_T > c_L$*
		$\sqrt{2}c_T$	$\dfrac{c_T}{\sqrt{2}}$	$\dfrac{\sqrt{2}n\pi c_T}{h}$	...
		∞	0	$\dfrac{(2n+1)\pi c_T}{2h}$ or $\dfrac{n\pi c_L}{h}$	*Mode cutoffs*
		$> c_L$	...	...	*SRL-ARL intersections*

and that these modes can be either symmetric or antisymmetric. It should be pointed out that the mutual interaction of waves is useful for characterizing localized material degradation. An analytical investigation was conducted for the synchronism analysis, which led to the identification of primary SH and RL modes that generate internally resonant third harmonics. Results indicate that primary SH modes are holo-internal-resonant with third harmonic SH wave fields, which has great potential for laboratory and field measurements. This work provides theoretical guidance for primary mode selection in order to generate third order harmonics to characterize material microstructural changes.

ACKNOWLEDGMENTS

APPENDIX: CUBIC NONLINEAR STRESS COMPONENTS

The nonzero components of the cubic nonlinear stress for primary SH wave self interactions are

$$T_{R\,12}^{CSH} = C_1^{SH}\left(\frac{\partial u_2^{(\alpha)}}{\partial X_1}\frac{\partial u_2^{(\alpha)}}{\partial X_1}\frac{\partial u_2^{(\alpha)}}{\partial X_1} + \frac{\partial u_2^{(\alpha)}}{\partial X_1}\frac{\partial u_2^{(\alpha)}}{\partial X_3}\frac{\partial u_2^{(\alpha)}}{\partial X_3}\right), \quad (A1)$$

$$T_{R\,21}^{CSH} = C_2^{SH}\left(\frac{\partial u_2^{(\alpha)}}{\partial X_1}\frac{\partial u_2^{(\alpha)}}{\partial X_1}\frac{\partial u_2^{(\alpha)}}{\partial X_1} + \frac{\partial u_2^{(\alpha)}}{\partial X_1}\frac{\partial u_2^{(\alpha)}}{\partial X_3}\frac{\partial u_2^{(\alpha)}}{\partial X_3}\right), \quad (A2)$$

$$T_{R\,23}^{CSH} = C_2^{SH}\left(\frac{\partial u_2^{(\alpha)}}{\partial X_1}\frac{\partial u_2^{(\alpha)}}{\partial X_1}\frac{\partial u_2^{(\alpha)}}{\partial X_3} + \frac{\partial u_2^{(\alpha)}}{\partial X_3}\frac{\partial u_2^{(\alpha)}}{\partial X_3}\frac{\partial u_2^{(\alpha)}}{\partial X_3}\right), \quad (A3)$$

$$T_{R\,32}^{CSH} = C_1^{SH}\left(\frac{\partial u_2^{(\alpha)}}{\partial X_1}\frac{\partial u_2^{(\alpha)}}{\partial X_1}\frac{\partial u_2^{(\alpha)}}{\partial X_3} + \frac{\partial u_2^{(\alpha)}}{\partial X_3}\frac{\partial u_2^{(\alpha)}}{\partial X_3}\frac{\partial u_2^{(\alpha)}}{\partial X_3}\right). \quad (A4)$$

Similarly, the nonzero components of the cubic nonlinear stress for primary RL wave self interactions are

$$T_{R\,11}^{CRL} = C_1^{RL}\left(\frac{\partial u_1^{(\alpha)}}{\partial X_1}\frac{\partial u_1^{(\alpha)}}{\partial X_3}\frac{\partial u_1^{(\alpha)}}{\partial X_3} + \frac{\partial u_1^{(\alpha)}}{\partial X_1}\frac{\partial u_1^{(\alpha)}}{\partial X_1}\frac{\partial u_1^{(\alpha)}}{\partial X_1}\right)$$
$$+ C_2^{RL}\frac{\partial u_1^{(\alpha)}}{\partial X_1}\frac{\partial u_1^{(\alpha)}}{\partial X_1}\frac{\partial u_3^{(\alpha)}}{\partial X_3} + C_3^{RL}\frac{\partial u_1^{(\alpha)}}{\partial X_1}\frac{\partial u_3^{(\alpha)}}{\partial X_3}\frac{\partial u_3^{(\alpha)}}{\partial X_3}$$
$$+ C_4^{RL}\frac{\partial u_1^{(\alpha)}}{\partial X_3}\frac{\partial u_3^{(\alpha)}}{\partial X_1}\frac{\partial u_3^{(\alpha)}}{\partial X_3} + C_5^{RL}\frac{\partial u_1^{(\alpha)}}{\partial X_1}\frac{\partial u_1^{(\alpha)}}{\partial X_1}\frac{\partial u_1^{(\alpha)}}{\partial X_1}$$
$$+ C_6^{RL}\left(\frac{\partial u_1^{(\alpha)}}{\partial X_3}\frac{\partial u_1^{(\alpha)}}{\partial X_3}\frac{\partial u_3^{(\alpha)}}{\partial X_3} + \frac{\partial u_3^{(\alpha)}}{\partial X_1}\frac{\partial u_3^{(\alpha)}}{\partial X_1}\frac{\partial u_3^{(\alpha)}}{\partial X_3}\right)$$
$$+ C_7^{RL}\frac{\partial u_1^{(\alpha)}}{\partial X_1}\frac{\partial u_3^{(\alpha)}}{\partial X_3}\frac{\partial u_3^{(\alpha)}}{\partial X_1} + C_8^{RL}\frac{\partial u_3^{(\alpha)}}{\partial X_3}\frac{\partial u_3^{(\alpha)}}{\partial X_3}\frac{\partial u_3^{(\alpha)}}{\partial X_3}, \quad (A5)$$

$$T_{R\,13}^{CRL} = C_1^{RL}\left(\frac{\partial u_1^{(\alpha)}}{\partial X_1}\frac{\partial u_1^{(\alpha)}}{\partial X_1}\frac{\partial u_1^{(\alpha)}}{\partial X_3} + \frac{\partial u_1^{(\alpha)}}{\partial X_3}\frac{\partial u_3^{(\alpha)}}{\partial X_3}\frac{\partial u_3^{(\alpha)}}{\partial X_3}\right)$$
$$+ C_4^{RL}\frac{\partial u_1^{(\alpha)}}{\partial X_1}\frac{\partial u_3^{(\alpha)}}{\partial X_1}\frac{\partial u_3^{(\alpha)}}{\partial X_3} + 2C_6^{RL}\frac{\partial u_1^{(\alpha)}}{\partial X_1}\frac{\partial u_1^{(\alpha)}}{\partial X_3}\frac{\partial u_3^{(\alpha)}}{\partial X_3}$$
$$+ \frac{C_7^{RL}}{2}\left(\frac{\partial u_1^{(\alpha)}}{\partial X_1}\frac{\partial u_1^{(\alpha)}}{\partial X_1}\frac{\partial u_1^{(\alpha)}}{\partial X_1} + \frac{\partial u_3^{(\alpha)}}{\partial X_1}\frac{\partial u_3^{(\alpha)}}{\partial X_3}\frac{\partial u_3^{(\alpha)}}{\partial X_3}\right)$$
$$+ C_9^{RL}\left(3\frac{\partial u_1^{(\alpha)}}{\partial X_3}\frac{\partial u_1^{(\alpha)}}{\partial X_3}\frac{\partial u_3^{(\alpha)}}{\partial X_1} + \frac{\partial u_3^{(\alpha)}}{\partial X_1}\frac{\partial u_3^{(\alpha)}}{\partial X_1}\frac{\partial u_3^{(\alpha)}}{\partial X_1}\right)$$
$$+ C_{10}^{RL}\frac{\partial u_1^{(\alpha)}}{\partial X_3}\frac{\partial u_1^{(\alpha)}}{\partial X_3}\frac{\partial u_1^{(\alpha)}}{\partial X_3} + C_{11}^{RL}\frac{\partial u_1^{(\alpha)}}{\partial X_3}\frac{\partial u_3^{(\alpha)}}{\partial X_1}\frac{\partial u_3^{(\alpha)}}{\partial X_1}, \quad (A6)$$

$$T_{R\,22}^{CRL} = C_8^{RL}\left(\frac{\partial u_1^{(\alpha)}}{\partial X_1}\frac{\partial u_1^{(\alpha)}}{\partial X_1}\frac{\partial u_1^{(\alpha)}}{\partial X_1} + \frac{\partial u_3^{(\alpha)}}{\partial X_3}\frac{\partial u_3^{(\alpha)}}{\partial X_3}\frac{\partial u_3^{(\alpha)}}{\partial X_3}\right)$$
$$+ C_{12}^{RL}\left(\begin{array}{c}\frac{\partial u_1^{(\alpha)}}{\partial X_1}\frac{\partial u_1^{(\alpha)}}{\partial X_3}\frac{\partial u_1^{(\alpha)}}{\partial X_3} + \frac{\partial u_1^{(\alpha)}}{\partial X_1}\frac{\partial u_3^{(\alpha)}}{\partial X_1}\frac{\partial u_3^{(\alpha)}}{\partial X_1} \\ + \frac{\partial u_1^{(\alpha)}}{\partial X_3}\frac{\partial u_1^{(\alpha)}}{\partial X_3}\frac{\partial u_3^{(\alpha)}}{\partial X_3} + \frac{\partial u_3^{(\alpha)}}{\partial X_1}\frac{\partial u_3^{(\alpha)}}{\partial X_1}\frac{\partial u_3^{(\alpha)}}{\partial X_3}\end{array}\right)$$
$$+ C_{13}^{RL}\left(\frac{\partial u_1^{(\alpha)}}{\partial X_1}\frac{\partial u_1^{(\alpha)}}{\partial X_3}\frac{\partial u_3^{(\alpha)}}{\partial X_1} + \frac{\partial u_1^{(\alpha)}}{\partial X_3}\frac{\partial u_3^{(\alpha)}}{\partial X_1}\frac{\partial u_3^{(\alpha)}}{\partial X_3}\right)$$
$$+ C_{14}^{RL}\left(\frac{\partial u_1^{(\alpha)}}{\partial X_1}\frac{\partial u_1^{(\alpha)}}{\partial X_1}\frac{\partial u_3^{(\alpha)}}{\partial X_3} + \frac{\partial u_1^{(\alpha)}}{\partial X_1}\frac{\partial u_3^{(\alpha)}}{\partial X_3}\frac{\partial u_3^{(\alpha)}}{\partial X_3}\right), \quad (A7)$$

$$T_{R\,31}^{CRL} = C_1^{RL}\left(\frac{\partial u_1^{(\alpha)}}{\partial X_1}\frac{\partial u_1^{(\alpha)}}{\partial X_1}\frac{\partial u_3^{(\alpha)}}{\partial X_1} + \frac{\partial u_3^{(\alpha)}}{\partial X_1}\frac{\partial u_3^{(\alpha)}}{\partial X_3}\frac{\partial u_3^{(\alpha)}}{\partial X_3}\right)$$
$$+ C_4^{RL}\frac{\partial u_1^{(\alpha)}}{\partial X_1}\frac{\partial u_1^{(\alpha)}}{\partial X_3}\frac{\partial u_3^{(\alpha)}}{\partial X_3} + 2C_6^{RL}\frac{\partial u_1^{(\alpha)}}{\partial X_1}\frac{\partial u_1^{(\alpha)}}{\partial X_1}\frac{\partial u_3^{(\alpha)}}{\partial X_3}$$
$$+ \frac{C_7^{RL}}{2}\left(\frac{\partial u_1^{(\alpha)}}{\partial X_1}\frac{\partial u_1^{(\alpha)}}{\partial X_1}\frac{\partial u_1^{(\alpha)}}{\partial X_3} + \frac{\partial u_1^{(\alpha)}}{\partial X_3}\frac{\partial u_3^{(\alpha)}}{\partial X_3}\frac{\partial u_3^{(\alpha)}}{\partial X_3}\right)$$
$$+ C_9^{RL}\left(3\frac{\partial u_1^{(\alpha)}}{\partial X_3}\frac{\partial u_3^{(\alpha)}}{\partial X_1}\frac{\partial u_3^{(\alpha)}}{\partial X_1} + \frac{\partial u_1^{(\alpha)}}{\partial X_3}\frac{\partial u_1^{(\alpha)}}{\partial X_3}\frac{\partial u_1^{(\alpha)}}{\partial X_3}\right)$$
$$+ C_{10}^{RL}\frac{\partial u_3^{(\alpha)}}{\partial X_1}\frac{\partial u_3^{(\alpha)}}{\partial X_1}\frac{\partial u_3^{(\alpha)}}{\partial X_1} + C_{11}^{RL}\frac{\partial u_1^{(\alpha)}}{\partial X_3}\frac{\partial u_1^{(\alpha)}}{\partial X_3}\frac{\partial u_3^{(\alpha)}}{\partial X_1},$$
$$(A8)$$

$$T_{R\,33}^{CRL} = C_1^{RL}\left(\frac{\partial u_1^{(\alpha)}}{\partial X_3}\frac{\partial u_1^{(\alpha)}}{\partial X_3}\frac{\partial u_3^{(\alpha)}}{\partial X_3} + \frac{\partial u_3^{(\alpha)}}{\partial X_1}\frac{\partial u_3^{(\alpha)}}{\partial X_1}\frac{\partial u_3^{(\alpha)}}{\partial X_3}\right)$$
$$+ C_2^{RL}\frac{\partial u_1^{(\alpha)}}{\partial X_1}\frac{\partial u_3^{(\alpha)}}{\partial X_3}\frac{\partial u_3^{(\alpha)}}{\partial X_3} + C_3^{RL}\frac{\partial u_1^{(\alpha)}}{\partial X_1}\frac{\partial u_1^{(\alpha)}}{\partial X_1}\frac{\partial u_3^{(\alpha)}}{\partial X_3}$$
$$+ C_4^{RL}\frac{\partial u_1^{(\alpha)}}{\partial X_1}\frac{\partial u_1^{(\alpha)}}{\partial X_3}\frac{\partial u_3^{(\alpha)}}{\partial X_1} + C_5^{RL}\frac{\partial u_3^{(\alpha)}}{\partial X_3}\frac{\partial u_3^{(\alpha)}}{\partial X_3}\frac{\partial u_3^{(\alpha)}}{\partial X_3}$$
$$+ C_6^{RL}\left(\frac{\partial u_1^{(\alpha)}}{\partial X_1}\frac{\partial u_1^{(\alpha)}}{\partial X_3}\frac{\partial u_1^{(\alpha)}}{\partial X_3} + \frac{\partial u_1^{(\alpha)}}{\partial X_1}\frac{\partial u_3^{(\alpha)}}{\partial X_1}\frac{\partial u_3^{(\alpha)}}{\partial X_1}\right)$$
$$+ C_7^{RL}\frac{\partial u_1^{(\alpha)}}{\partial X_3}\frac{\partial u_3^{(\alpha)}}{\partial X_1}\frac{\partial u_3^{(\alpha)}}{\partial X_3} + C_8^{RL}\frac{\partial u_1^{(\alpha)}}{\partial X_1}\frac{\partial u_1^{(\alpha)}}{\partial X_1}\frac{\partial u_1^{(\alpha)}}{\partial X_1}. \quad (A9)$$

The coefficients C_i^{SH} ($i = 1, 2$) and C_j^{RL} ($j = 1, 2, ..., 14$) are linear combinations of the Lamé's constants λ, μ, the third order elastic constants $\bar{A}$, $\bar{B}$, and $\bar{C}$, and the fourth order elastic constants $\bar{E}$, $\bar{F}$, $\bar{G}$, and $\bar{H}$, that is

$$C_1^{SH} = \frac{\bar{A}}{4} + \frac{\bar{B}}{2} + \bar{G},$$

$$C_2^{SH} = \frac{\lambda}{2} + \mu + \frac{\bar{A}}{2} + \bar{B} + \bar{G},$$

(A10)

$$C_1^{RL} = \frac{\lambda}{2} + \mu + \frac{5\bar{A}}{4} + \frac{7\bar{B}}{2} + \bar{C} + \frac{3\bar{E}}{2} + \bar{F} + 2\bar{G},$$

$$C_2^{RL} = 3\bar{B} + 3\bar{C} + 3\bar{E} + 6\bar{F} + 12\bar{H},$$

$$C_3^{RL} = \frac{\lambda}{2} + 2\bar{B} + 2\bar{C} + 4\bar{F} + 4\bar{G} + 12\bar{H},$$

$$C_4^{RL} = \mu + \bar{A} + 2\bar{B} + 3\bar{E} + 2\bar{F},$$

$$C_5^{RL} = \frac{\lambda}{2} + \mu + 2\bar{A} + 6\bar{B} + 2\bar{C} + 4\bar{E} + 4\bar{F} + 4\bar{G} + 4\bar{H},$$

$$C_6^{RL} = \frac{\bar{A}}{2} + 2\bar{B} + \bar{C} + \frac{3\bar{E}}{2} + \bar{F},$$

$$C_7^{RL} = \frac{3\bar{A}}{2} + 3\bar{B} + 3\bar{E} + 2\bar{F} + 4\bar{G},$$

$$C_8^{RL} = \bar{B} + \bar{C} + \bar{E} + 2\bar{F} + 4\bar{H},$$

$$C_9^{RL} = \frac{\bar{A}}{4} + \frac{\bar{B}}{2} + \bar{G},$$

$$C_{10}^{RL} = \frac{\lambda}{2} + \mu + \frac{\bar{A}}{2} + \bar{B} + \bar{G},$$

$$C_{11}^{RL} = \frac{\lambda}{2} + \frac{\bar{A}}{2} + \bar{B} + 3\bar{G},$$

$$C_{12}^{RL} = \bar{B} + \bar{C} + \frac{3\bar{E}}{4} + \bar{F},$$

$$C_{13}^{RL} = \bar{B} + \frac{3\bar{E}}{2} + 2\bar{F},$$

$$t\,C_{14}^{RL} = \bar{C} + 2\bar{F} + 12\bar{H}.$$

(A11)

[1]A. Hikata, B. B. Chick, and C. Elbaum, Appl. Phys. Lett. **3**, 195 (1963).
[2]J. H. Cantrell and W. T. Yost, Int. J. Fatigue **23**, 487 (2001).
[3]J. H. Cantrell, J. Appl. Phys. **105**, 043520 (2009).
[4]J. H. Cantrell and W. T. Yost, J. Appl. Phys. **81**, 2957 (1997).
[5]J. H. Cantrell and W. T. Yost, Appl. Phys. Lett. **77**, 1952 (2000).
[6]J. Y. Kim, J. Qu, L. J. Jacobs, and J. W. Littles, J. Acoust. Soc. Am. **120**, 1266 (2006).
[7]M. Deng, J. Appl. Phys. **84**, 3500 (1998).
[8]M. Deng, J. Appl. Phys. **85**, 3051 (1999).
[9]W. J. N. de Lima and M. F. Hamilton, J. Sound Vib. **265**, 819 (2003).
[10]A. Srivastava and F. Lanza di Scalea, J. Sound Vib. **323**, 932 (2009).
[11]M. F. Müller, J. Y. Kim, J. Qu, and L. J. Jacobs, J. Acoust. Soc. Am. **127**, 2141 (2010).
[12]Y. Liu, V. Chillara, and C. J. Lissenden, J. Sound Vib. **332**, 4517 (2013).
[13]V. Chillara and C. J. Lissenden, J. Appl. Phys. **111**, 124909 (2012).
[14]N. Matsuda and S. Biwa, J. Appl. Phys. **109**, 094903 (2011).
[15]M. Deng and J. Pei, Appl. Phys. Lett. **90**, 121902 (2007).
[16]C. Bermes, J. Y. Kim, J. Qu, and L. J. Jacobs, Appl. Phys. Lett. **90**, 021901 (2007).
[17]C. Pruell, J. Y. Kim, J. Qu, and L. J. Jacobs, Appl. Phys. Lett. **91**, 231911 (2007).
[18]K. H. Matlack, J. Y. Kim, L. J. Jacobs, and J. Qu, J. Appl. Phys. **109**, 014905 (2011).
[19]Y. Xiang, M. Deng, F. Xuan, and C. Liu, J. Appl. Phys. **111**, 104905 (2012).
[20]A. Srivastava and F. Lanza di Scalea, J. Sound Vib. **329**, 1499 (2010).
[21]Y. Liu, E. Khajeh, C. J. Lissenden, and J. L. Rose, J. Acoust. Soc. Am. **133**, 2541 (2013).
[22]A. Hikata and C. Elbaum, Phys. Rev. **144**, 469 (1966).
[23]A. Hikata and C. Elbaum, Phys. Rev. **151**, 442 (1966).
[24]F. D. Murnaghan, *Finite Deformation of an Elastic Solid* (John Wiley and Sons, Inc., New York, 1951).
[25]L. D. Landau and E. M. Lifshitz, *Theory of Elasticity* (Pergamon, New York, 1986).
[26]M. F. Hamilton, Y. A. Ilinskii, and E. A. Zabolotskaya, J. Acoust. Soc. Am. **116**, 41 (2004).
[27]B. A. Auld, *Acoustic Fields and Waves in Solids* (Robert E. Krieger Publishing Company, Malabar, Florida, 1990), Vol. II.
[28]J. L. Rose, *Ultrasonic Waves in Solid Media* (Cambridge University Press, Cambridge, 1999).

Interaction of torsional and longitudinal guided waves in weakly nonlinear circular cylinders

Yang Liu, Ehsan Khajeh, Cliff J. Lissenden,[a] and Joseph L. Rose
Department of Engineering Science and Mechanics, The Pennsylvania State University, University Park, Pennsylvania 16802

The nonlinear forcing terms for the wave equation in general curvilinear coordinates are derived based on an isotropic homogeneous weakly nonlinear elastic material. The expressions for the nonlinear part of the first Piola-Kirchhoff stress are specialized for axisymmetric torsional and longitudinal fundamental waves in a circular cylinder. The matrix characteristics of the nonlinear forcing terms and secondary mode wave structures are manipulated to analyze the higher harmonic generation due to the guided wave mode self-interactions and mutual interactions. It is proved that both torsional and longitudinal secondary wave fields can be cumulative by a specific type of guided wave mode interactions. A method for the selection of preferred fundamental excitations that generate strong cumulative higher harmonics is formulated, and described in detail for second harmonic generation. Nonlinear finite element simulations demonstrate second harmonic generation by $T(0,3)$ and $L(0,4)$ modes at the internal resonance points. A linear increase of the normalized modal amplitude ratio A_2/A_1^2 over the propagation distance is observed for both cases, which indicates that mode $L(0,5)$ is effectively generated as a cumulative second harmonic. Counter numerical examples demonstrate that synchronism and sufficient power flux from the fundamental mode to the secondary mode must occur for the secondary wave field to be strongly cumulative.
© 2013 Acoustical Society of America. [http://dx.doi.org/10.1121/1.4795806]

I. INTRODUCTION

Linear ultrasonic guided waves are generally sensitive to gross defects, i.e., open cracks and large scale corrosion. However, it is highly desirable to detect damage at the smallest scale possible to maintain the best achievable structural integrity. Nonlinear ultrasonics has been shown to have the capability to provide sensitivity to microstructural changes.[1–3] Cantrell and Yost[4] used nonlinear bulk waves to characterize fatigue damage and developed a model between the acoustic nonlinearity and dislocation dipoles. Likewise, Cantrell[5] studied the harmonic generation in cyclically stressed wavy slip metals and correlated the nonlinearity parameter β with the percentage of total life expended. The higher harmonic generation of guided waves in plates has been studied by Deng,[6,7] de Lima and Hamilton,[8] Srivastava and Lanza di Scalea,[9] and Müller *et al.*[10] These studies formulated the general conditions for the generation of cumulative higher harmonics in plate, such as nonzero power flux from the fundamental to the secondary wave fields and a phase matching condition. Müller *et al.*[10] also considered group velocity matching as a necessary condition for cumulative second harmonic generation. Experimental results have confirmed the cumulative nature of higher harmonics and demonstrated their sensitivity to material microstructure.[11–14]

Axisymmetric guided waves can propagate large distances in cylinders with little energy loss. They have been

successfully applied in pipeline inspections.[15–17] However, there has been little study of higher harmonic generation of guided waves in cylindrical waveguides. de Lima and Hamilton[18] studied the higher harmonic generation of waves in waveguides having arbitrary cross-section and gave examples of cylindrical rods and shells. They solved the nonlinear wave equation by a normal mode expansion method using a perturbation analysis, and then they investigated the cumulative condition for the longitudinal modes. Srivastava and Lanza di Scalea[19] studied the higher harmonic generation of longitudinal modes in rods, and found that the nature of the primary generating modes restricts the mode circumferential orders that can be generated as higher harmonics. Srivastava *et al.*[20] and Nucera and Lanza di Scalea[21] then proposed a nonlinear semi-analytical finite element method to numerically evaluate higher harmonic generation in nonlinear waveguides with generic cross-sections. Cumulative growth of the phase matched secondary modes are observed in their studies.

The present work contributes by formulating the nonlinear forcing terms in general curvilinear coordinates and giving the expressions for the nonlinear part of the first Piola-Kirchhoff stress for axisymmetric torsional and longitudinal fundamental modes in particular. Higher harmonic generation due to the fundamental mode self-interactions and mutual interactions are studied. The internal resonance plots for the selection of the preferred fundamental excitations are created and discussed in detail for second harmonic generation. Nonlinear finite element models are constructed for axisymmetric torsional and longitudinal

[a]Author to whom correspondence should be addressed. Electronic mail: cjl9@psu.edu

types of fundamental wave fields in a weakly nonlinear material (steel) to confirm the mode selection method. Combining a cumulative higher harmonic with the penetration power of guided waves could be very beneficial for a nondestructive evaluation and eventually structural health monitoring.

II. NONLINEAR FORCING TERMS IN CURVILINEAR COORDINATES

Before beginning the analysis, it is worth noting that all the derivations are undertaken in the reference configuration. Assume two sets of reference coordinate systems in Euclidean space, one is Cartesian coordinates (X^1, X^2, X^3) with basis vectors $(\mathbf{i}, \mathbf{j}, \mathbf{k})$, another is an arbitrary curvilinear coordinate system (Y^1, Y^2, Y^3) with covariant basis vectors $(\mathbf{e}_1, \mathbf{e}_2, \mathbf{e}_3)$. The transformation between the two coordinate systems is given by $Y = X(X^1, X^2, X^3)$, and $X = Y(Y^1, Y^2, Y^3)$ is the corresponding inverse transformation.

In the absence of body forces, the equation of motion for an isotropic, homogeneous, weakly nonlinear waveguide[18] in a general curvilinear coordinate system, is given by

$$\mu u_{i;j}{}^j + (\lambda + \mu) u_{j;i}{}^j + \bar{f}_i = \rho_0 \ddot{u}_i. \tag{1}$$

The stress free boundary condition

$$(T_{ij}^{R-L} + \bar{T}_{ij})n^j = 0 \quad \text{on } \chi, \tag{2}$$

where $u_i = u_i(Y^1, Y^2, Y^3, t)$ is the particle displacement given in the reference configuration, and $u_{i;j}$ is the covariant derivative of u_i with respect to Y^j. T_{ij}^{R-L} and $\bar{T}_{ij}$ are the linear and nonlinear parts of the first Piola-Kirchhoff stress, respectively, while $\bar{f}_i$ is the divergence of $\bar{T}_{ij}$. All of the nonlinear terms are contained in $\bar{T}_{ij}n^j$ and $\bar{f}_i$, which are often referred to as the nonlinear surface traction and the nonlinear body force, respectively. n^j is the outward unit normal of the boundary surface χ. λ and μ are Lamé's constants, and ρ_0 is the referential material density.

de Lima and Hamilton[8] showed that the secondary wave field is generated due to the power flux from the fundamental wave field through nonlinear stress $\bar{T}_{ij}$ and nonlinear body force $\bar{f}_i$. Gol'dberg[22] provided the expressions of the nonlinear forcing terms for weakly nonlinear media in Cartesian coordinates. However, Cartesian tensor equations derived through partial differentiation are generally invalid in curvilinear coordinates. In this section, the nonlinear forcing terms in general curvilinear coordinates will be formulated by using covariant derivatives.

The Green strain tensor in general curvilinear coordinates is given by

$$E_{ij} = \frac{1}{2}(u_{i;j} + u_{j;i} + u^k{}_{;i} u_{k;j}), \tag{3}$$

where the covariant derivative $u_{i;j}$ is defined as

$$u_{i;j} = \frac{\partial u_i}{\partial Y^j} - u_k \Gamma_{ij}^k. \tag{4}$$

Here, Γ_{ij}^k is the Euclidean Christoffel symbol, which is given by a linear combination of the partial derivatives of the metric tensor g_{ij},

$$\Gamma_{ij}^k = \frac{1}{2} g^{km} \left(\frac{\partial g_{mj}}{\partial Y^i} + \frac{\partial g_{im}}{\partial Y^j} - \frac{\partial g_{ij}}{\partial Y^m} \right). \tag{5}$$

The covariant metric tensor g_{ij} is given by

$$g_{ij} = \delta_{mn} \frac{\partial X^m}{\partial Y^i} \frac{\partial X^n}{\partial Y^j} = \mathbf{e}_i \cdot \mathbf{e}_j, \tag{6}$$

where δ_{mn} is the Kronecker delta. g_{ij} has a contravariant counterpart g^{ij}, which is given by its inverse.

The hyperelastic strain energy function proposed by Landau and Lifshitz[23] can be written for a general curvilinear coordinate system by

$$S_E = \frac{1}{2} \lambda (E_k{}^k)^2 + \mu E_{ij} E^{ji} + \frac{1}{3} C(E_k{}^k)^3$$
$$+ B E_k{}^k E_{ij} E^{ji} + \frac{1}{3} A E_{ij} E^j{}_k E^{ki} + O\left((E_i{}^i)^4\right), \tag{7}$$

up to and including the third order terms in strain multiples where A, B, and C are Landau and Lifshitz third order elastic constants. The second Piola-Kirchhoff stress T_{ij}^{RR} is a referential measure of stress that is paired with the Green strain tensor through the strain energy function, Eq. (7), which gives

$$T_{ij}^{RR} = \frac{\partial S_E}{\partial E^{ij}}. \tag{8}$$

Writing the second Piola-Kirchhoff stress T_{ij}^{RR} in terms of $u_{i;j}$ leads to

$$T_{ij}^{RR} = \lambda u_{l;}{}^l g_{ij} + \frac{\lambda}{2} u_{k;l} u^{k;l} g_{ij} + \mu(u_{i;j} + u_{j;i}) + \mu u_{k;i} u^k{}_{;j}$$
$$+ C(u_{l;}{}^l)^2 g_{ij} + B u_{l;}{}^l (u_{i;j} + u_{j;i})$$
$$+ \frac{B}{2} (u_{l;k} u^{k;l} + u_{k;l} u^{k;l}) g_{ij}$$
$$+ \frac{A}{4} (u_{i;k} u^k{}_{;j} + u_{k;i} u_{j;}{}^k + u_{i;k} u_{j;}{}^k + u_{k;i} u^k{}_{;j})$$
$$+ O\left((u_{i;j})^3\right). \tag{9}$$

The second Piola-Kirchhoff stress can be decomposed into a linear part T_{ij}^{RR-L} and nonlinear part T_{ij}^{RR-NL}, where

$$T_{ij}^{RR-L} = \lambda u_{l;}{}^l g_{ij} + \mu(u_{i;j} + u_{j;i}), \tag{10}$$

$$T_{ij}^{RR-NL} = \frac{\lambda}{2} u_{k;l} u^{k;l} g_{ij} + \mu u_{k;i} u^k{}_{;j} + C(u_{l;}{}^l)^2 g_{ij}$$
$$+ \frac{B}{2} (u_{l;k} u^{k;l} + u_{k;l} u^{k;l}) g_{ij} + B u_{l;}{}^l (u_{i;j} + u_{j;i})$$
$$+ \frac{A}{4} (u_{i;k} u^k{}_{;j} + u_{k;i} u_{j;}{}^k + u_{i;k} u_{j;}{}^k + u_{k;i} u^k{}_{;j})$$
$$+ O\left((u_{i;j})^3\right). \tag{11}$$

The first Piola-Kirchhoff stress T_{ij}^R is related to the second Piola-Kirchhoff stress T_{ij}^{RR} by

$$T_{ij}^R = T_{ij}^{RR} + T_{ik}^{RR} u^k_{;j}. \tag{12}$$

Substituting the linear and nonlinear parts of the second Piola-Kirchhoff stress into Eq. (12) and grouping all the nonlinear terms leads to the nonlinear part of first Piola-Kirchhoff stress

$$\bar{T}_{ij} = T_{ij}^{RR-NL} + T_{ik}^{RR-L} u^k_{;j} + T_{ik}^{RR-NL} u^k_{;j}. \tag{13}$$

Furthermore, substituting Eqs. (10) and (11) into Eq. (13), the nonlinear part of the first Piola-Kirchhoff stress $\bar{T}_{ij}$ can be obtained by

$$\bar{T}_{ij} = \frac{\lambda}{2} u_{k;l} u^{k;l} g_{ij} + (\lambda + B) u_{l;}{}^l u_{i;j} + C(u_{l;}{}^l)^2 g_{ij}$$
$$+ \frac{B}{2}(u_{l;k} u^{k;l} + u_{k;l} u^{k;l}) g_{ij} + B u_{l;}{}^l u_{j;i} + \frac{A}{4} u_{k;i} u_{j;}{}^k$$
$$+ \left(\mu + \frac{A}{4}\right)(u_{i;k} u^k_{;j} + u_{k;i} u^k_{;j} + u_{i;k} u_{j;}{}^k) + O\left((u_{i;j})^3\right). \tag{14}$$

Finally, the nonlinear body force is given by the divergence of the nonlinear stress

$$\bar{f}_i = \bar{T}_{ij;}{}^j. \tag{15}$$

Equations (14) and (15) give the nonlinear forcing terms in general curvilinear coordinates, which can be easily adopted to a specific curvilinear coordinate system such as cylindrical coordinates by using the metric tensor and Christoffel symbols in the corresponding coordinates. The nonzero terms of the nonlinear stress in cylindrical coordinates for axisymmetric longitudinal and torsional fundamental modes are given in the Appendix.

III. CUMULATIVE HARMONIC GENERATION DUE TO MODE INTERACTIONS

Consider the interaction of two guided wave modes $\mathbf{u}^{(a)}$ and $\mathbf{u}^{(b)}$ propagating in the cylinder. The total displacement field can be decomposed into fundamental and secondary wave fields

$$\mathbf{u} = \mathbf{u}^{(a)} + \mathbf{u}^{(b)} + \mathbf{u}^{(aa)} + \mathbf{u}^{(bb)} + \mathbf{u}^{(ab)}, \tag{16}$$

where $\mathbf{u}^{(aa)}$ and $\mathbf{u}^{(bb)}$ are the secondary wave fields due to the self-interaction of mode a and mode b, respectively, and $\mathbf{u}^{(ab)}$ is the displacement field due to the mutual interaction of the two modes. Following a similar method of de Lima and Hamilton,[18] the axisymmetric torsional and longitudinal mode interaction problem can be solved by the normal mode expansion technique of Auld.[24] The secondary particle velocity field $\mathbf{v}^{(2)}(R, Z, t)$ is given by

$$\mathbf{v}^{(2)}(R, Z, t) = \frac{1}{2} \sum_m \frac{i(p_n^{\mathrm{surf}} + p_n^{\mathrm{vol}})}{4 P_{mn}[k_n^* - (k_a \pm k_b)]} \mathbf{v}_m(R)$$
$$\times \left(e^{i(k_a \pm k_b)Z} - e^{ik_n^* Z}\right)$$
$$\times e^{-i(\omega_a \pm \omega_b)t} + \mathrm{c.c.}, \quad k_n^* \neq k_a \pm k_b, \tag{17}$$

$$\mathbf{v}^{(2)}(R, Z, t) = \frac{1}{2} \sum_m \frac{(p_n^{\mathrm{surf}} + p_n^{\mathrm{vol}})Z}{4 P_{mn}} \mathbf{v}_m(R)$$
$$\times e^{i\{(k_a \pm k_b)Z - (\omega_a \pm \omega_b)t\}} + \mathrm{c.c.}, \quad k_n^* = k_a \pm k_b, \tag{18}$$

where

$$P_{mn} = -\frac{\pi}{8} \int_{R_i}^{R_o} (\mathbf{v}_n^* \cdot \mathbf{T}_m + \mathbf{v}_m \cdot \mathbf{T}_n^*) \cdot \mathbf{n}_Z R dR, \tag{19}$$

$$p_n^{\mathrm{surf}} = \pi R_o \left(\mathbf{v}_n^*(R_o) \cdot \bar{\mathbf{T}}(R_o) \cdot \mathbf{n}_R\right)$$
$$- \pi R_i \left(\mathbf{v}_n^*(R_i) \cdot \bar{\mathbf{T}}(R_i) \cdot \mathbf{n}_R\right), \tag{20}$$

$$p_n^{\mathrm{vol}} = \pi \int_{R_i}^{R_o} \mathbf{v}_n^* \cdot \bar{\mathbf{f}} \cdot R dR, \tag{21}$$

where $\mathbf{v}_m$ is the particle velocity of the mth secondary wave mode at $\omega_a \pm \omega_b$, and P_{mn} is the complex power flux in the propagation direction. Also, k_n^* is the wavenumber of the unique mode such that $P_{mn} \neq 0$, p_n^{surf}, and p_n^{vol} are interpreted as power fluxes through the surface and through the volume, respectively, due to the nonlinear surface traction and body force exerted by the fundamental waves in the cylinders. R_i and R_o are the inner and outer radii of the cylinder, respectively. Notice that these equations have a similar form to secondary Lamb waves in a plate.[8] As indicated in Eq. (16), the nonlinear terms $\bar{\mathbf{T}}$ and $\bar{\mathbf{f}}$ contain terms corresponding to mode self-interactions and mutual interactions. Sections III A and III B will discuss details of each case.

A. Guided wave mode self-interactions

The expressions of the nonlinear stress for axisymmetric longitudinal and torsional waves in the reference configuration are given in the Appendix. For both types of fundamental wave fields $\bar{\mathbf{T}}$ and $\bar{\mathbf{f}}$ can be written in matrix form as

$$\bar{\mathbf{T}} = \begin{bmatrix} \bar{T}_{RR} & 0 & \bar{T}_{RZ} \\ 0 & \bar{T}_{\Theta\Theta} & 0 \\ \bar{T}_{ZR} & 0 & \bar{T}_{ZZ} \end{bmatrix}, \tag{22}$$

$$\bar{\mathbf{f}} = \begin{Bmatrix} \bar{f}_R \\ 0 \\ \bar{f}_Z \end{Bmatrix}, \tag{23}$$

which enables the determination of the possible types of cumulative secondary wave fields due to guided wave mode self-interactions.

With regards to axisymmetric torsional mode secondary wave fields, the power flux from an arbitrary fundamental mode to a prescribed torsional secondary mode via the nonlinear stress is given by

J. Acoust. Soc. Am., Vol. 133, No. 5, May 2013

Liu *et al.*: Noninteraction of waves in cylinders   2543

$$p_n^{\text{surf}-T} = \pi R_o \left\{ \{0, v_\Theta^*(R_o), 0\} \cdot \begin{bmatrix} \bar{T}_{RR}(R_o) & 0 & \bar{T}_{RZ}(R_o) \\ 0 & \bar{T}_{\Theta\Theta}(R_o) & 0 \\ \bar{T}_{ZR}(R_o) & 0 & \bar{T}_{ZZ}(R_o) \end{bmatrix} \cdot \begin{Bmatrix} 1 \\ 0 \\ 0 \end{Bmatrix} \right\}$$

$$-\pi R_i \left\{ \{0, v_\Theta^*(R_i), 0\} \cdot \begin{bmatrix} \bar{T}_{RR}(R_i) & 0 & \bar{T}_{RZ}(R_i) \\ 0 & \bar{T}_{\Theta\Theta}(R_i) & 0 \\ \bar{T}_{ZR}(R_i) & 0 & \bar{T}_{ZZ}(R_i) \end{bmatrix} \cdot \begin{Bmatrix} 1 \\ 0 \\ 0 \end{Bmatrix} \right\} = 0. \qquad (24)$$

Additionally, the power flux resulting from the nonlinear body force is given by

$$p_n^{\text{vol}-T} = \pi \int_{R_i}^{R_o} \{0, v_\Theta^*(R), 0\} \cdot \begin{Bmatrix} \bar{f}_R(R) \\ 0 \\ \bar{f}_Z(R) \end{Bmatrix} R\,dR = 0, \qquad (25)$$

thus the total power flux from the fundamental wave fields to a torsional type secondary wave field due to mode self-interactions is

$$p_n^{\text{total}-T} = p_n^{\text{surf}-T} + p_n^{\text{vol}-T} = 0. \qquad (26)$$

Considering the resulting axisymmetric longitudinal mode secondary wave field, the power flux from an arbitrary fundamental mode to a prescribed longitudinal secondary mode via the nonlinear stress is given by

$$p_n^{\text{surf}-L} = \pi R_o \left\{ \{v_R^*(R_o), 0, v_Z^*(R_o)\} \cdot \begin{bmatrix} \bar{T}_{RR}(R_o) & 0 & \bar{T}_{RZ}(R_o) \\ 0 & \bar{T}_{\Theta\Theta}(R_o) & 0 \\ \bar{T}_{ZR}(R_o) & 0 & \bar{T}_{ZZ}(R_o) \end{bmatrix} \cdot \begin{Bmatrix} 1 \\ 0 \\ 0 \end{Bmatrix} \right\}$$

$$-\pi R_i \left\{ \{v_R^*(R_i), 0, v_Z^*(R_i)\} \cdot \begin{bmatrix} \bar{T}_{RR}(R_i) & 0 & \bar{T}_{RZ}(R_i) \\ 0 & \bar{T}_{\Theta\Theta}(R_i) & 0 \\ \bar{T}_{ZR}(R_i) & 0 & \bar{T}_{ZZ}(R_i) \end{bmatrix} \cdot \begin{Bmatrix} 1 \\ 0 \\ 0 \end{Bmatrix} \right\}$$

$$= \pi R_o \{v_R^*(R_o)\bar{T}_{RR}(R_o) + v_Z^*(R_o)\bar{T}_{ZR}(R_o)\} - \pi R_i \{v_R^*(R_i)\bar{T}_{RR}(R_i) + v_Z^*(R_i)\bar{T}_{ZR}(R_i)\}, \qquad (27)$$

and the power flux resulting from the nonlinear body force is given by

$$p_n^{\text{vol}-L} = \pi \int_{R_i}^{R_o} \{v_R^*(R), 0, v_Z^*(R)\} \cdot \begin{Bmatrix} \bar{f}_R(R) \\ 0 \\ \bar{f}_Z(R) \end{Bmatrix} R\,dR$$

$$= \pi \int_{R_i}^{R_o} \left(v_R^*(R)\bar{f}_R(R) + v_Z^*(R)\bar{f}_Z(R) \right) R\,dR. \qquad (28)$$

Thus the total power flux from the fundamental wave field to the prescribed longitudinal secondary wave field due to mode self-interactions is given by

$$p_n^{\text{total}-L} = \pi R_o \{v_R^*(R_o)\bar{T}_{RR}(R_o) + v_Z^*(R_o)\bar{T}_{ZR}(R_o)\}$$
$$- \pi R_i \{v_R^*(R_i)\bar{T}_{RR}(R_i) + v_Z^*(R_i)\bar{T}_{ZR}(R_i)\}$$
$$+ \pi \int_{R_i}^{R_o} \left(v_R^*(R)\bar{f}_R(R) + v_Z^*(R)\bar{f}_Z(R) \right) R\,dR. \qquad (29)$$

Equation (29) gives the power flux intensity from an arbitrary fundamental wave field to prescribed longitudinal type secondary modes due to mode self-interactions, which is in general nonzero. Thus for the case of guided wave mode self-interactions, only axisymmetric longitudinal secondary wave fields can be in internal resonance with the fundamental modes. Either type of fundamental mode (longitudinal or torsional) can generate a cumulative longitudinal secondary wave field. While torsional mode secondary fields receive no power flux from either type of fundamental mode, no cumulative secondary torsional modes can be generated by a unitary excitation.

B. Guided wave mode mutual interactions

The nonlinear forcing terms for mode mutual interaction problems can be obtained by substituting $\mathbf{u}^{(a)}$ and $\mathbf{u}^{(b)}$ into Eqs. (14) and (15), while retaining terms up to the second order for the nonlinear stress and the nonlinear body forces. By doing so the nonlinear stress for the mode mutual interaction in general curvilinear coordinates is given by

$$\bar{T}_{ij}^{M} = \lambda u^{(a)}{}_{k;}{}^{k} u^{(b)}{}_{i;j} + \lambda u^{(b)}{}_{l;}{}^{l} u^{(a)}{}_{i;j} + \frac{\lambda}{2} \left(u^{(a)}{}_{k;l} u^{(b)k}{}_{;l} + u^{(b)}{}_{k;l} u^{(a)k}{}_{;l} \right) g_{ij}$$

$$+ \mu u^{(a)}{}_{i;k} \left(u^{(b)k}{}_{;j} + u^{(b)}{}_{j;}{}^{k} \right) + \mu u^{(b)}{}_{i;k} \left(u^{(a)k}{}_{;j} + u^{(a)}{}_{j;}{}^{k} \right) + \mu \left(u^{(a)}{}_{k;i} u^{(b)k}{}_{;j} + u^{(b)}{}_{k;i} u^{(a)k}{}_{;j} \right)$$

$$+ 2C u^{(a)}{}_{k;}{}^{k} u^{(b)}{}_{l;}{}^{l} g_{ij} + B u^{(a)}{}_{k;}{}^{k} \left(u^{(b)}{}_{i;j} + u^{(b)}{}_{j;i} \right) + B u^{(b)}{}_{l;}{}^{l} \left(u^{(a)}{}_{i;j} + u^{(a)}{}_{j;i} \right)$$

$$+ \frac{B}{2} \left(u^{(a)}{}_{l;k} u^{(b)k}{}_{;l} + u^{(b)}{}_{l;k} u^{(a)k}{}_{;l} + u^{(a)}{}_{k;l} u^{(b)k}{}_{;l} + u^{(b)}{}_{k;l} u^{(a)k}{}_{;l} \right) g_{ij}$$

$$+ \frac{A}{4} \left(u^{(a)}{}_{i;k} u^{(b)k}{}_{;j} + u^{(b)}{}_{i;k} u^{(a)k}{}_{;j} + u^{(a)}{}_{k;i} u^{(b)}{}_{j;}{}^{k} + u^{(b)}{}_{k;i} u^{(a)}{}_{j;}{}^{k} \right.$$

$$\left. + u^{(a)}{}_{k;i} u^{(b)k}{}_{;j} + u^{(b)}{}_{k;i} u^{(a)k}{}_{;j} + u^{(a)}{}_{i;k} u^{(b)}{}_{j;}{}^{k} + u^{(b)}{}_{i;k} u^{(a)}{}_{j;}{}^{k} \right) + O\left(\left(u^{(a)}{}_{i;j} \right)^{3} \right) + O\left(\left(u^{(b)}{}_{i;j} \right)^{3} \right), \tag{30}$$

and the nonlinear body force for the mode mutual interaction is given by

$$\bar{f}_{i}^{M} = \bar{T}_{ij;}^{Mj}. \tag{31}$$

By examining the matrix characteristics of Eqs. (30) and (31), two sub-cases exist for the mutual interaction between two fundamental mode excitations: (1) $\mathbf{u}^{(a)}$ and $\mathbf{u}^{(b)}$ are the same mode type and (2) $\mathbf{u}^{(a)}$ is a different mode type from $\mathbf{u}^{(b)}$. For case (1) either both modes are longitudinal or both are torsional. For this case, the matrix forms of the nonlinear forcing terms are exactly the same as Eqs. (22) and (23). The nonlinear forcing terms can be obtained via Eqs. (30) and (31) by considering cylindrical coordinates with either $u_{R}^{(a)} \neq 0$, $u_{\Theta}^{(a)} = 0$, $u_{Z}^{(a)} \neq 0$, $u_{R}^{(b)} = u_{Z}^{(b)} = 0$, $u_{\Theta}^{(b)} \neq 0$ or $u_{R}^{(a)} = u_{Z}^{(a)} = 0$, $u_{\Theta}^{(a)} \neq 0$, $u_{R}^{(b)} \neq 0$, $u_{\Theta}^{(b)} = 0$, $u_{Z}^{(b)} \neq 0$, and u_{i} is independent of Θ.[28] The matrix form of the nonlinear forcing terms for these two subcases is

$$\bar{\mathbf{T}}^{M} = \begin{bmatrix} \bar{T}_{RR}^{M} & \bar{T}_{R\Theta}^{M} & \bar{T}_{RZ}^{M} \\ \bar{T}_{\Theta R}^{M} & \bar{T}_{\Theta\Theta}^{M} & \bar{T}_{\Theta Z}^{M} \\ \bar{T}_{ZR}^{M} & \bar{T}_{Z\Theta}^{M} & \bar{T}_{ZZ}^{M} \end{bmatrix}, \tag{32}$$

$$\bar{\mathbf{f}}^{M} = \begin{Bmatrix} \bar{f}_{R}^{M} \\ \bar{f}_{\Theta}^{M} \\ \bar{f}_{Z}^{M} \end{Bmatrix}, \tag{33}$$

where the superscript M indicates the mode mutual interaction problem.

1. Longitudinal-longitudinal (L-L) or torsional-torsional (T-T) mutual interactions

When the two mutually interacting fundamental excitations are the same mode type, i.e., L-L or T-T mode mutual interactions, the nonlinear forcing terms will have the same matrix formats as mode self-interaction. Thus, the cumulative second harmonic generation will also have a similar pattern as the single mode excitation case; that is cumulative higher harmonics only occur for the secondary longitudinal wave field for the same mode type mutual interaction. No axisymmetric torsional secondary mode can be internally resonant given this kind of mutual interaction.

2. Longitudinal-torsional (L-T) mutual interaction

The power flux from L-T mutual interaction fundamental fields to a prescribed torsional secondary mode via the nonlinear stress is given by

$$p_{n}^{\text{surf}-T-M} = \pi R_{o} \left\{ \{0, v_{\Theta}^{*}(R_{o}), 0\} \cdot \begin{bmatrix} \bar{T}_{RR}^{M}(R_{o}) & \bar{T}_{R\Theta}^{M}(R_{o}) & \bar{T}_{RZ}^{M}(R_{o}) \\ \bar{T}_{\Theta R}^{M}(R_{o}) & \bar{T}_{\Theta\Theta}^{M}(R_{o}) & \bar{T}_{\Theta Z}^{M}(R_{o}) \\ \bar{T}_{ZR}^{M}(R_{o}) & \bar{T}_{Z\Theta}^{M}(R_{o}) & \bar{T}_{ZZ}^{M}(R_{o}) \end{bmatrix} \cdot \begin{Bmatrix} 1 \\ 0 \\ 0 \end{Bmatrix} \right\}$$

$$- \pi R_{i} \left\{ \{0, v_{\Theta}^{*}(R_{i}), 0\} \cdot \begin{bmatrix} \bar{T}_{RR}^{M}(R_{i}) & \bar{T}_{R\Theta}^{M}(R_{i}) & \bar{T}_{RZ}^{M}(R_{i}) \\ \bar{T}_{\Theta R}^{M}(R_{i}) & \bar{T}_{\Theta\Theta}^{M}(R_{i}) & \bar{T}_{\Theta Z}^{M}(R_{i}) \\ \bar{T}_{ZR}^{M}(R_{i}) & \bar{T}_{Z\Theta}^{M}(R_{i}) & \bar{T}_{ZZ}^{M}(R_{i}) \end{bmatrix} \cdot \begin{Bmatrix} 1 \\ 0 \\ 0 \end{Bmatrix} \right\}$$

$$= \pi R_{o} v_{\Theta}^{*}(R_{o}) \bar{T}_{\Theta R}^{M}(R_{o}) - \pi R_{i} v_{\Theta}^{*}(R_{i}) \bar{T}_{\Theta R}^{M}(R_{i}), \tag{34}$$

and the power flux via the nonlinear body forces is

$$p_n^{\text{vol}-T-M} = \pi \int_{R_i}^{R_o} \{0, v_\Theta^*(R), 0\} \cdot \begin{Bmatrix} \bar{f}_R^M(R) \\ \bar{f}_\Theta^M(R) \\ \bar{f}_Z^M(R) \end{Bmatrix} R dR = \pi \int_{R_i}^{R_o} v_\Theta^*(R) \bar{f}_\Theta^M(R) R dR. \tag{35}$$

Thus the total power flux resulting from *L-T* mutual-interaction fundamental fields to a prescribed torsional secondary mode is given by

$$p_n^{\text{total}-T-M} = \pi R_o v_\Theta^*(R_o) \bar{T}_{\Theta R}^M(R_o) - \pi R_i v_\Theta^*(R_i) \bar{T}_{\Theta R}^M(R_i) + \pi \int_{R_i}^{R_o} v_\Theta^*(R) \bar{f}_\Theta^M(R) R dR. \tag{36}$$

The right side of Eq. (36) is in general nonzero, which indicates that the secondary torsional mode can be cumulative along the propagation distance provided fundamental *L-T* mutual interaction occurs, and the cumulative secondary torsional wave fields will exist at sum or difference frequencies $\omega_a \pm \omega_b$.

The power flux from *L-T* mutual interaction fundamental fields to a prescribed longitudinal secondary mode via the non-linear stress is given by

$$
\begin{aligned}
p_n^{surf-L-M} = \pi R_o &\left\{ \{v_R^*(R_o), 0, v_Z^*(R_o)\} \cdot \begin{bmatrix} \bar{T}_{RR}^M(R_o) & \bar{T}_{R\Theta}^M(R_o) & \bar{T}_{RZ}^M(R_o) \\ \bar{T}_{\Theta R}^M(R_o) & \bar{T}_{\Theta\Theta}^M(R_o) & \bar{T}_{\Theta Z}^M(R_o) \\ \bar{T}_{ZR}^M(R_o) & \bar{T}_{Z\Theta}^M(R_o) & \bar{T}_{ZZ}^M(R_o) \end{bmatrix} \cdot \begin{Bmatrix} 1 \\ 0 \\ 0 \end{Bmatrix} \right\} \\
- \pi R_i &\left\{ \{v_R^*(R_i), 0, v_Z^*(R_i)\} \cdot \begin{bmatrix} \bar{T}_{RR}^M(R_i) & \bar{T}_{R\Theta}^M(R_i) & \bar{T}_{RZ}^M(R_i) \\ \bar{T}_{\Theta R}^M(R_i) & \bar{T}_{\Theta\Theta}^M(R_i) & \bar{T}_{\Theta Z}^M(R_i) \\ \bar{T}_{ZR}^M(R_i) & \bar{T}_{Z\Theta}^M(R_i) & \bar{T}_{ZZ}^M(R_i) \end{bmatrix} \cdot \begin{Bmatrix} 1 \\ 0 \\ 0 \end{Bmatrix} \right\} \\
= \pi R_o &\{v_R^*(R_o) \bar{T}_{RR}^M(R_o) + v_Z^*(R_o) \bar{T}_{ZR}^M(R_o)\} - \pi R_i \{v_R^*(R_i) \bar{T}_{RR}^M(R_i) + v_Z^*(R_i) \bar{T}_{ZR}^M(R_i)\},
\end{aligned} \tag{37}
$$

and the power flux via the nonlinear body forces is given by

$$
\begin{aligned}
p_n^{\text{vol}-L-M} &= \pi \int_{R_i}^{R_o} \{v_R^*(R), 0, v_Z^*(R)\} \cdot \begin{Bmatrix} \bar{f}_R^M(R) \\ \bar{f}_\Theta^M(R) \\ \bar{f}_Z^M(R) \end{Bmatrix} R dR \\
&= \pi \int_{R_i}^{R_o} \left(v_R^*(R) \bar{f}_R^M(R) + v_Z^*(R) \bar{f}_Z^M(R) \right) R dR.
\end{aligned} \tag{38}
$$

Thus the total power flux resulting from an arbitrary *L-T* mutual interaction fundamental field to a prescribed longitudinal secondary mode is given by

$$
\begin{aligned}
p_n^{\text{total}-L-M} = &\pi R_o \{v_R^*(R_o) \bar{T}_{RR}^M(R_o) + v_Z^*(R_o) \bar{T}_{ZR}^M(R_o)\} \\
&- \pi R_i \{v_R^*(R_i) \bar{T}_{RR}^M(R_i) + v_Z^*(R_i) \bar{T}_{ZR}^M(R_i)\} \\
&+ \pi \int_{R_i}^{R_o} \left(v_R^*(R) \bar{f}_R^M(R) + v_Z^*(R) \bar{f}_Z^M(R) \right) R dR.
\end{aligned} \tag{39}
$$

In summary, cumulative higher harmonics can be generated by either mode self-interactions or mode mutual interactions. Only longitudinal secondary wave fields can be cumulative for mode self-interactions, *T-T* mutual interaction or *L-L* mutual interaction. However, both torsional and longitudinal secondary wave fields can be cumulative for *L-T* mutual interaction. Table I lists all the possible cumulative secondary fields due to mode interactions.

IV. EXCITATION OF STRONG CUMULATIVE SECOND HARMONICS

In this section, a method is illustrated for the selection of fundamental excitations that generate strong cumulative second harmonics. This method can be generalized for the

TABLE I. Possible cumulative secondary wave fields due to interacting fundamental torsional and longitudinal modes in cylinders.

Fundamental wave field		Secondary wave mode	
		T[a]	L[a]
Self-interaction	L	N[b]	Y[b]
	T	N	Y
Mutual interaction	T-T	N	Y
	L-L	N	Y
	L-T	Y	Y

[a]*L* and *T* represent longitudinal and torsional modes, respectively.
[b]Y means that the secondary mode is cumulative and N indicates that the secondary field is not cumulative.

selection of other order of strongly cumulative higher harmonic generations. The generation of second harmonics is limited to mode self-interactions in this section. The amplitude of the second harmonic grows linearly with propagation distance, as indicated by Eq. (18), provided it has twice the wave number of the fundamental mode (thus the phase velocities are synchronized) and $p_n^{\text{surf}} + p_n^{\text{vol}} \neq 0$ (thus the power flux is nonzero). This is known as the internal resonance condition for second harmonics, and the cumulative nature of the internal resonant second harmonics is useful in experiments. Hence, fundamental wave modes that generate strongly cumulative second harmonics with reasonably good excitability will be sought. The dimensions and properties of a steel cylinder analyzed here for illustrative purposes are given in Table II.

Dispersion curves for axisymmetric fundamental torsional and longitudinal modes are shown in Figs. 1(a) and 1(b), respectively, as colored lines. The color scale represents the normalized power flux intensity to the $L(0,5)$ secondary wave field. Also shown are dashed lines that represent potential secondary wave modes plotted at their half-frequency so that synchronism points can be easily identified. The synchronism points are the intersection points of the fundamental and secondary wave fields and are marked with circles. A limited number of synchronism points occur when the phase velocities are equal to (1) the longitudinal wave speed C_L, (2) the shear wave speed C_T, (3) the Rayleigh wave speed C_R, and (4) the Lamé mode wave speed $C_{\text{Lamé}}$ ($\sqrt{2}C_T$); or (5) the crossing points of fundamental modes. Müller et al.[10] and Matsuda and Biwa[27] manipulated the dispersion relations for plates to show mathematically that the synchronism points for a plate occur at any of the aforementioned conditions. While that type of analysis is not performed here, Figs. 1(a) and 1(b) demonstrate that the same synchronism points exist for axisymmetric guided waves in cylinders. In addition to the above synchronism points, which are the same for plates and cylinders, new synchronism points are possible for cylinders. These points occur for $L(0,1)$ and $T(0,1)$ in low frequency range near the vicinity of where the phase velocity of the secondary $L(0,1)$ experiences a sharp drop. This drop of the phase velocity for the pipe, used in this article with $s = 0.15$ (s is the ratio of pipe thickness to pipe mean radius), occurs around 80 kHz.

Figures 1(a) and 1(b) are termed internal resonance plots, because they show both the synchronism points and the normalized power flux intensity [obtained by Eq. (29)] from the fundamental modes to a prescribed secondary wave
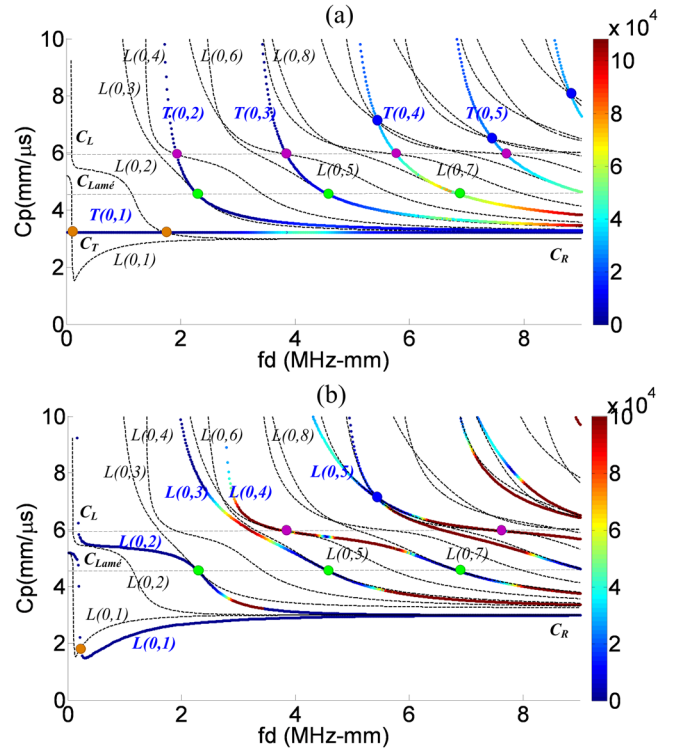

FIG. 1. (Color online) Internal resonance plots: (a) Fundamental axisymmetric torsional modes to secondary $L(0,5)$ mode, and (b) fundamental axisymmetric longitudinal modes to secondary $L(0,5)$ mode. Color scaled lines represent the fundamental modes superimposed with normalized power flux intensity to the secondary $L(0,5)$ mode. The black dashed lines are the possible cumulative secondary modes and the small circles indicate the synchronism points.

field, $L(0,5)$ in this case. The internal resonance plots enable the selection of synchronism points that have a higher power flux to a prescribed secondary wave field, which implies the preferred fundamental excitations. Table III lists the power flux from fundamental excitation points to corresponding secondary wave fields for some synchronism mode pairs. Notice that high power flux occurs from the longitudinal fundamental modes to $L(0,5)$ and $L(0,9)$, while low power flux

TABLE III. Normalized power flux intensity for some synchronism mode pairs for steel pipe dimensions and material properties given in Table II.

Synchronism fundamental mode types			Secondary wave field	fd value (MHz-mm)	Normalized power flux intensity
Torsional modes		$T(0,1)$	$L(0,1)$	0.06	1.62×10^{-6}
	C_T	$T(0,1)$	$L(0,2)$	1.72	1.29×10^2
	$C_{\text{Lamé}}$	$T(0,2)$	$L(0,3)$	2.28	1.23×10^1
		$T(0,3)$	$L(0,6)$	4.56	2.36×10^2
	C_L	$T(0,2)$	$L(0,4)$	1.92	4.10×10^3
		$T(0,3)$	$L(0,5)$	3.85	1.27×10^4
		$T(0,4)$	$L(0,7)$	5.78	5.47×10^4
Longitudinal modes		$L(0,1)$	$L(0,1)$	0.15	2.68×10^{-6}
	$C_{\text{Lamé}}$	$L(0,2)$	$L(0,3)$	2.28	1.35×10^{-3}
		$L(0,3)$	$L(0,6)$	4.56	2.18×10^{-2}
		$L(0,4)$	$L(0,8)$	6.84	3.63×10^2
	C_L	$L(0,4)$	$L(0,5)$	3.85	2.81×10^4
		$L(0,5)$	$L(0,9)$	7.70	1.36×10^5

TABLE II. Input parameters for the finite element models.

Dimensions		Material properties[a]					
R_i (mm)	R_o (mm)	ρ (kg/m³)	λ (GPa)	μ (GPa)	A (GPa)	B (GPa)	C (GPa)
9	10.5	7932	116.2	82.7	−325	−310	−800

[a] A, B, and C are obtained from Rushchitsky (Ref. 25). A conversion between Landau and Lifshitz third order elastic constants and Murnaghan constants can be found in Norris (Ref. 26).

occurs to $L(0,1)$, $L(0,3)$, $L(0,6)$, and $L(0,8)$. $L(0,5)$ and $L(0,9)$ correspond to symmetric Lamb modes in the plate, while $L(0,1)$, $L(0,3)$, $L(0,6)$, and $L(0,8)$ correspond to antisymmetric Lamb modes. In plates, antisymmetric secondary modes receive no power flux due to their symmetry properties.[9,10] However, in cylinders the mode shapes are neither exactly symmetric nor antisymmetric, thus nonzero power flux occurs at all longitudinal modes, albeit it is small to those modes that correspond to antisymmetric Lamb modes in the plate. This analysis holds for torsional fundamental modes as well. The synchronism points with higher power flux provide a stronger potential for a nonlinear ultrasonic guided wave nondestructive evaluation of cylindrical structures. Due to this consideration of the power flux and the modal excitability, $T(0,3)$-$L(0,5)$ and $L(0,4)$-$L(0,5)$ mode pairs are selected for finite element simulation.

V. FINITE ELEMENT SIMULATION OF WEAKLY NONLINEAR CYLINDERS

To demonstrate that internal resonance plots enable selection of preferred fundamental excitations, finite element simulations of nonlinear circular cylinders are performed. Srivastava et al.[20] and Nucera and Lanza di Scalea[21] developed a nonlinear semi-analytical finite element modeling approach, based on which they successfully performed the dispersion analysis of waveguides with arbitrary cross sections and investigated the modal generation of second harmonics. The nonlinear finite element simulations we present in this section directly solve the transient dynamics nonlinear wave propagation problem based upon the applied loading. The internally resonant mode pairs identified in Sec. IV are investigated along with counter examples. Nonlinear finite element models based on Eqs. (3), (7), and (8) and the input parameters given in Table II have been constructed. To guarantee convergent solutions in the time domain and adequately accurate solutions in the spatial domain during wave propagation simulations of second harmonic generation, two criteria must be satisfied: (1) The maximum length of each element in the wave propagation direction should be less than $\lambda_{2f}/8$, where λ_{2f} is the wavelength of the secondary mode, (2) the time step Δt must be selected according to the ratio of the smallest element length ΔL_{min} in the wave propagation direction and the fastest group velocity C_g that exists in the simulation, i.e., $\Delta t \leq \Delta L_{min}/C_g$.

Simulation results are presented for longitudinal mode excitation where the received signal is u_Z for both fundamental and secondary modes, as well as for torsional mode excitation where the received signals are u_Θ for the fundamental mode and u_Z for the secondary mode. In each case sets of results are provided for propagation distances of 5λ to 25λ.

A. Longitudinal mode fundamental excitation

Two numerical simulations of longitudinal mode excitation are presented to show second harmonic generation and whether it is cumulative. The first simulation involves excitation of the $L(0,4)$ mode at the longitudinal wave speed, which is a cumulative case shown in Table III. A six-

element interdigital transducer (IDT) that wraps around the circumference of the pipe is simulated by applied surface tractions. A 15-cycle tone burst excitation of the shear traction component in the axial direction with a central frequency of $f_0 = 2.569$ MHz is applied. The IDT element spacing is equivalent to the half wavelength, and the element width is half of this spacing. For the $L(0,4)$ mode at the longitudinal wave speed the wavelength is $\lambda_1 = 2.318$ mm. The second simulation is excitation of the $L(0,2)$ mode at $f_0 = 1$ MHz ($fd = 1.5$ MHz-mm), which is not synchronized with any secondary modes. A similar IDT is used for the excitation of $L(0,2)$, with the appropriate modifications to specific transducer parameters. That is, the IDT element spacing and width are adjusted according to the $L(0,2)$ mode wavelength, $\lambda_2 = 5.264$ mm.

Before presenting simulation results, the influence of the window type used to transform to the frequency domain is investigated. Window selection influences the resulting amplitude of the harmonics and the small side lobes in the Fourier transform. The preferred analysis decreases the side lobes to enhance isolation of the higher harmonics. Various windows of identical length are applied to the single wave packet in the time domain shown in Fig. 2(a): Tukey, Hamming, Blackman, Chebyshev, Rectangular, and Blackman-Harris. Three Tukey windows numbered by decreasing taper-to-constant section ratios (0.9, 0.6, and 0.2) are used. The results indicate that window type affects the amplitudes for the harmonics, as shown in Fig. 2(b). However, the normalized spectra in Fig. 2(c) show that the ratio of the secondary peak to the fundamental peak is insensitive to the window type. The normalized spectra indicate that Tukey1, with the cosine-tapered ratio of 0.9, provides a
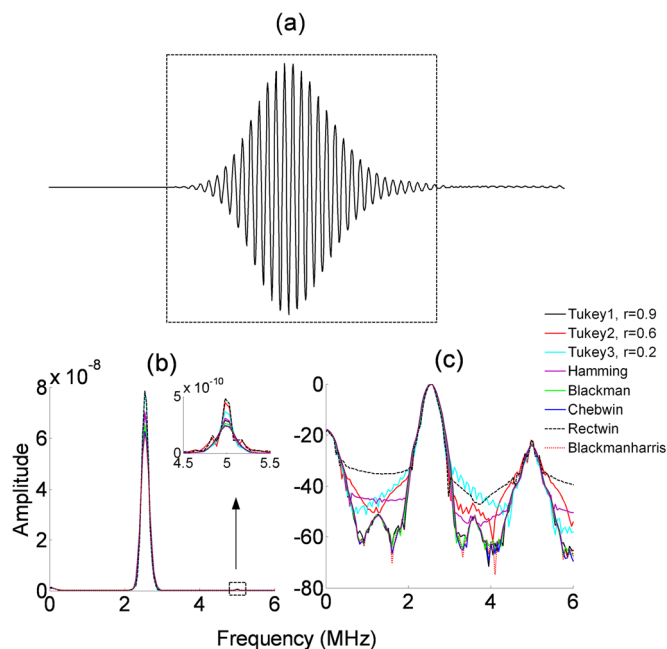

FIG. 2. (Color online) (a) A wave packet in the time domain with a central frequency of 2.569 MHz; dashed lines indicate a window size of 12 μs. (b) Frequency spectra obtained from different window types result in different amplitudes. (c) Normalized frequency spectra show that the window type does not affect the secondary-to-fundamental amplitude ratio.
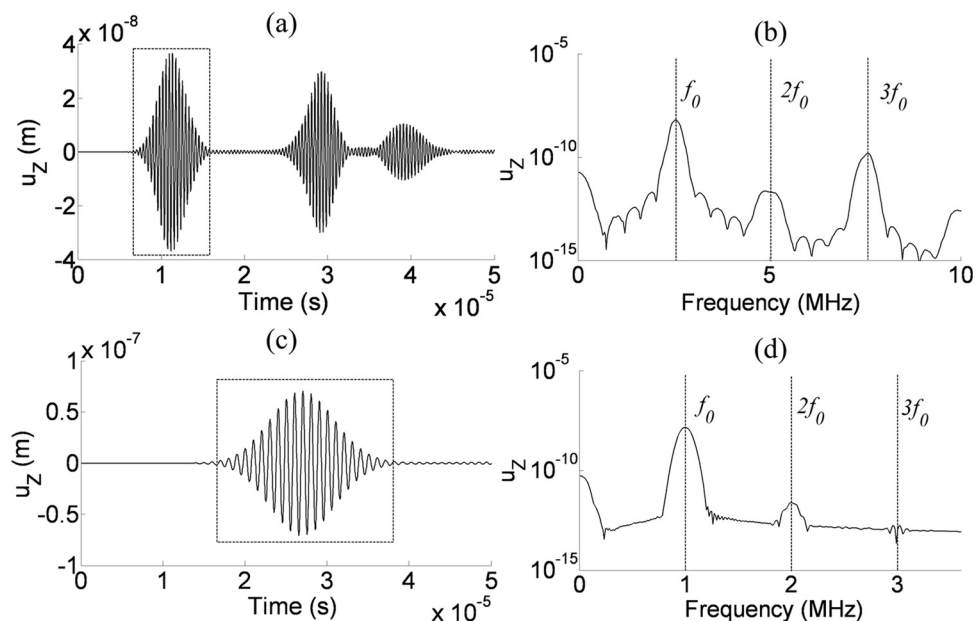
Liu *et al.*: Noninteraction of waves in cylinders

FIG. 3. Signals received from fundamental longitudinal mode excitation at a propagation distance of 10λ. (a) Received time domain signal for the $L(0,4)$ mode excitation and (b) the frequency spectrum for the windowed waveform in (a). (c) Time domain signal for the $L(0,2)$ mode excitation and (d) the frequency spectrum for the windowed waveform in (c).
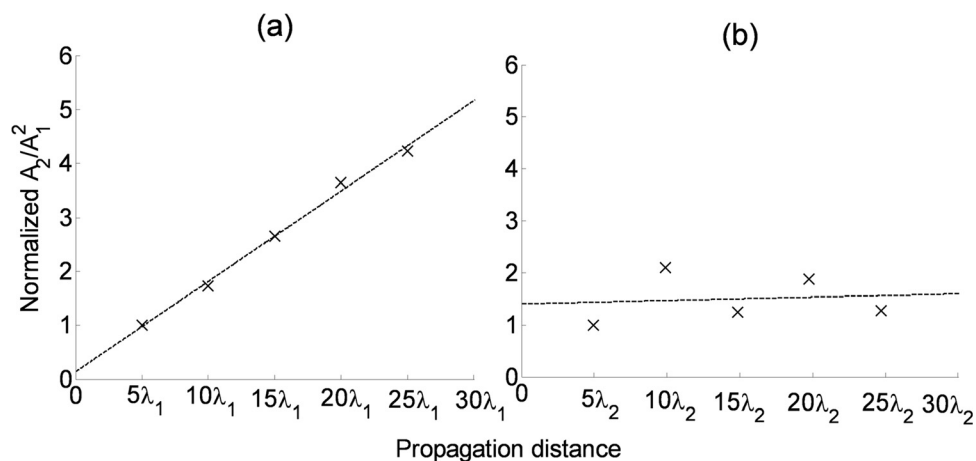

FIG. 4. The normalized modal amplitude ratio A_2/A_1^2 as a function of propagation distance for longitudinal mode excitation. (a) Fundamental $L(0,4)$ mode excitation and (b) fundamental $L(0,2)$ mode excitation. A_1 is the modal amplitude at the excitation frequency, while A_2 is the amplitude at double the excitation frequency. The dotted lines are regressed to the data points. $\lambda_1 = 2.318$ mm, $\lambda_2 = 5.264$ mm.
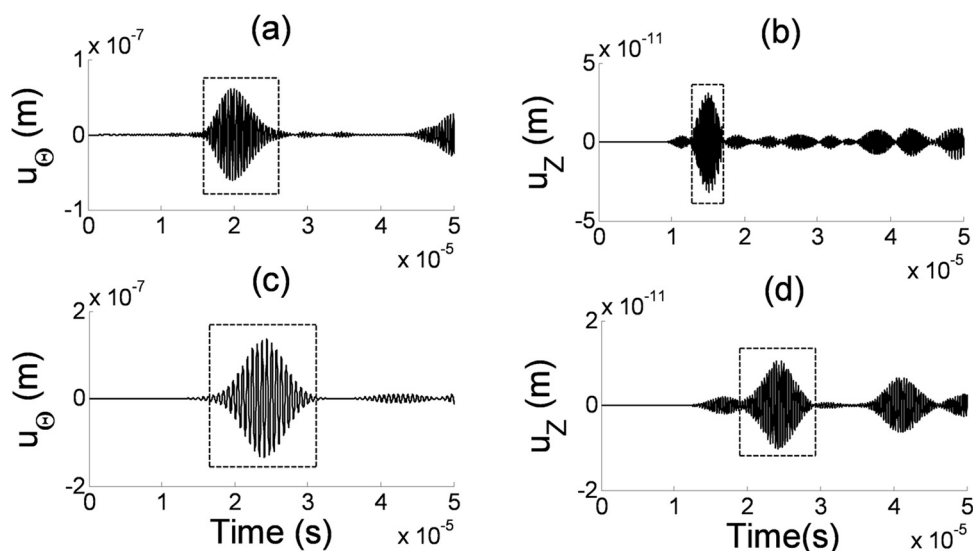

FIG. 5. Time domain signals from torsional mode fundamental excitations. (a) The displacement u_Θ component, and (b) the displacement u_Z component for fundamental $T(0,3)$ mode excitation at propagation distance of $10\lambda_3$. (c) The displacement u_Θ component, and (d) the displacement u_Z component for fundamental $T(0,2)$ mode excitation at propagation distance of $10\lambda_4$. The dotted rectangles indicate the time domain window for the Fourier transform.
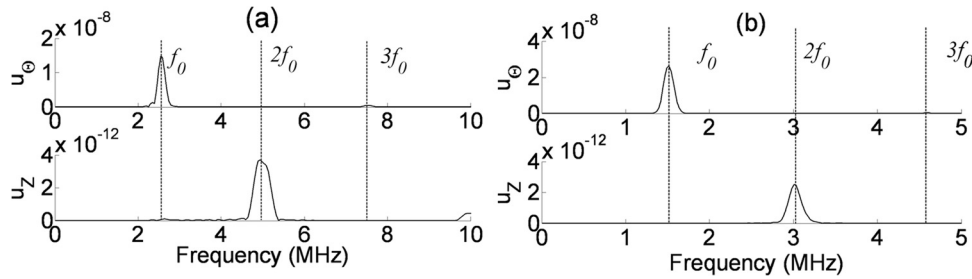
FIG. 6. Frequency spectra from torsional mode fundamental excitations. The fast Fourier transform results of the first receiving wave packet of both the u_Θ displacement component and u_Z displacement component are shown. (a) Shows the frequency spectra for $T(0,3)$ mode excitation and (b) gives the frequency spectra for $T(0,2)$ mode excitation.

good resolution of the peaks in the frequency domain relative to the other window types. Thus, all simulation data are analyzed by a Tukey window with a cosine-tapered ratio of 0.9 and a fixed window size for each data set.

To make the results of the two simulations comparable, the data is acquired at multiples of the corresponding fundamental wavelength. Measurements are reported for propagation distances from 5λ to 25λ, in increments of 5λ. The time domain signals received for 10λ propagation distances are shown in Figs. 3(a) and 3(c) for $L(0,4)$ and $L(0,2)$ excitations, respectively. A Tukey window has been applied to extract the first received wave packet for the Fourier transform. The other waveforms in the received signal in Figs. 3(a) and 3(c) are primarily from back wall reflections and mode conversion. The wave packet for higher harmonics analysis must be isolated from other wave packets. Figures 3(b) and 3(d) show the frequency spectra for the corresponding $L(0,4)$ and $L(0,2)$ excitations.

The modal amplitude ratio, A_2/A_1^2, where A_1 and A_2 are the amplitudes of the fundamental (f_0) and second harmonic ($2f_0$), respectively, were determined for different propagation distances to assess whether the second harmonic is cumulative. Afterward, these ratios were normalized with respect to the ratio for the 5λ propagation distance and plotted in Fig. 4. It is evident from Fig. 4(a) that the normalized modal amplitude ratio A_2/A_1^2, which is a relative measure of the nonlinearity parameter β, increases linearly with propagation distance for the $L(0,4)$ fundamental excitation. Thus, we conclude that the $L(0,4)$-$L(0,5)$ mode pair is cumulative and has internal resonance, while on the other hand, the normalized ratio for the $L(0,2)$ mode, shown in Fig. 4(b), exhibits a

behavior that can be describe as bounded oscillation along propagation distance.

B. Torsional mode fundamental excitation

The third finite element simulation is of excitation of the fundamental $T(0,3)$ mode. A six-element IDT with elements spaced at the half wavelength ($\lambda_3 = 2.349$ mm) is used in this simulation. A tone burst tangential traction in the circumferential direction with a central frequency 2.569 MHz is applied. As a counter example, a fourth simulation of the torsional mode [$T(0,2)$ at 1.520 MHz] is also presented. While this point synchronizes with the $L(0,3)$ mode, its power flux is very low as shown in Table III. The corresponding wavelength for this torsional mode is $\lambda_4 = 3.022$ mm, and the IDT elements are also spaced at half of this wavelength.

Figures 5(a) and 5(b) show the received time domain signals of the u_Θ and u_Z displacement components from the $T(0,3)$ excitation for a 10λ propagation distance, while Figs. 5(c) and 5(d) present the same displacement components for the $T(0,2)$ excitation. The circumferential component of the displacement field, u_Θ [shown in Figs. 5(a) and 5(c)] corresponds to the particle displacement of torsional waves. Figures 5(b) and 5(d) correspond to the axial component of the displacement field u_Z, which is generated due to the material nonlinearity.

Tukey windows, indicated by the dashed lines in Fig. 5, were applied to extract the wave packets to determine the frequency spectra presented in Fig. 6. This latter figure, Fig. 6(a), shows the frequency spectra of the u_Θ and u_Z received signals from the $T(0,3)$ fundamental excitation, while
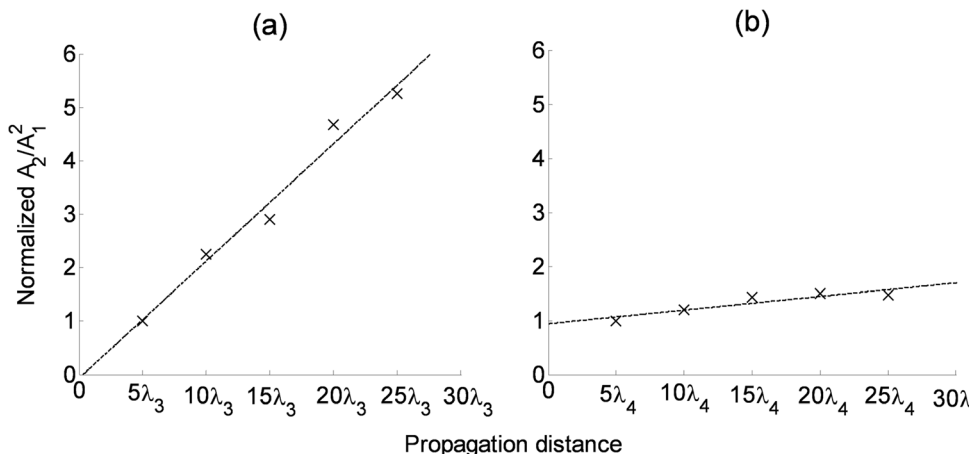

FIG. 7. The normalized modal amplitude ratio A_2/A_1^2 for torsional mode fundamental excitations as a function of propagation distance. (a) is the result of fundamental $T(0,3)$ excitation, and (b) shows the modal amplitude ratio for fundamental $T(0,2)$ excitation. Notice that A_1 is the modal amplitude of u_Θ displacement component at fundamental frequency, while A_2 is the amplitude of u_Z displacement component at double frequency. The best fit lines of the data points are included. $\lambda_3 = 2.349$ mm, $\lambda_4 = 3.022$ mm.

Liu *et al.*: Noninteraction of waves in cylinders

Fig. 6(b) represents the same components for $T(0,2)$. Both cases display a u_Θ peak at the fundamental frequency of the respective modes, while a u_Z peak exists at the double frequency. As indicated by Eq. (26), no torsional type second harmonic is generated, while as indicated by Eq. (29), longitudinal type second harmonics are generated.

In the same fashion that the modal amplitude A_2/A_1^2 was normalized with respect to the ratio obtained at 5λ for longitudinal modes in Fig. 4, the normalized modal amplitude ratios are plotted for the torsional modes in Fig. 7. With this latter figure, the normalized modal amplitude ratio (A_2/A_1^2) is where A_1 and A_2 are the amplitudes of the fundamental torsional mode (u_Θ at f_0) and second harmonic (u_Z at $2f_0$), respectively. A linear increase of the normalized amplitude ratio with propagation distance is observed for $T(0,3)$ mode fundamental excitation, shown in Fig. 7(a), which implies $L(0,5)$ is effectively generated as a cumulative second harmonic as indicated in Table III. Conversely, the counterexample shown in Fig. 7(b) exhibits no significant increase in A_2/A_1^2 with propagation distance. Thus as expected, the $T(0,2)$ mode does not generate a strongly cumulative second harmonic due to insufficient power flux.

VI. CONCLUSION

The generation of higher harmonics due to weakly nonlinear mode interactions of axisymmetric torsional and longitudinal modes in isotropic homogeneous cylinders has been investigated. A strong cumulative higher harmonic generation is achieved by satisfying (1) high power flux from the fundamental mode to the secondary wave field and (2) the synchronism condition. The ability to select fundamental modes and frequencies based on theory, which has been demonstrated herein through finite element simulations, is expected to lead to successful experiments. However, without the benefit of the theory, experiments would have only a slim chance of success. For higher harmonic generation of axisymmetric modes in cylindrical waveguides we conclude the following:

(1) Cumulative axisymmetric torsional mode secondary wave fields can only be generated by fundamental L-T mutual interaction, and they occur at sum and difference frequencies. Secondary longitudinal modes can be cumulative over the propagation length for any type of fundamental wave field. Both axisymmetric longitudinal and torsional fundamental wave fields have the potential to generate cumulative secondary wave fields. The analysis of axisymmetric longitudinal modes agrees with that of de Lima and Hamilton,[18] as well as Srivastava and Lanza di Scalea,[19] while the analysis of torsional mode self-interaction and torsional-longitudinal mode mutual interactions are new.

(2) Synchronism points for cumulative second harmonics in cylinders have been identified graphically. Only a finite number of fundamental excitation points meet the synchronism condition; some are points with special phase velocities (longitudinal wave speed C_L, shear wave speed C_T, Rayleigh wave speed C_R, or Lamé wave speed $C_{\text{Lamé}}$); or are the crossing points of fundamental wave modes. These synchronism points are shared by axisymmetric guided waves in cylinders and plate waves. Additional synchronism points exist solely for cylinders, which occur for $T(0,1)$ and $L(0,1)$ at very low frequencies.

(3) Internal resonance plots that explicitly present synchronism points and power flux intensity to a prescribed secondary wave field have been created. These plots aid mode and frequency selection of fundamental modes capable of generating strong cumulative second harmonics. Preferred fundamental excitation can be achieved by selecting the synchronism points in high power flux intensity areas.

(4) Nonlinear finite element analysis has demonstrated that the $L(0,4)$-$L(0,5)$ mode pair at the longitudinal wave speed, which is internally resonant, results in a cumulative second harmonic generation that increases linearly over propagating distances of 5λ to 25λ. The counter example of $L(0,2)$ mode excitation with a wavelength of $\lambda = 5.264$ mm does not exhibit an increase in second harmonic amplitude over comparable propagation distances, 5λ to 25λ.

(5) The $T(0,3)$ mode at the longitudinal wave speed has been excited in a finite element simulation. The normalized amplitude ratio of the $L(0,5)$ secondary mode is cumulative, indicating that the $T(0,3)$-$L(0,5)$ mode pair at the longitudinal wave speed is internally resonant. This is the first time a torsional wave fundamental excitation has been used to generate a cumulative second harmonic in a cylindrical waveguide. A counter example of the $T(0,2)$-$L(0,3)$ mode pair at the Lamé wave speed does not have sufficient power flux to give a strong cumulative second harmonic.

ACKNOWLEDGMENT

APPENDIX: NONLINEAR FORCING TERMS IN CYLINDRICAL COORDINATES

In cylindrical coordinates, that is $(Y^1, Y^2, Y^3) = (R, \Theta, Z)$, the nonzero components of the covariant metric tensor and the Christoffel symbols are

$$g_{11} = 1, \quad g_{22} = R^2, \quad g_{33} = 1, \tag{A1}$$

$$\Gamma_{22}^1 = -R, \quad \Gamma_{12}^2 = \Gamma_{21}^2 = \frac{1}{R}. \tag{A2}$$

The nonlinear forcing terms for axisymmetric longitudinal modes can be obtained via Eqs. (14) and (15) by considering the fundamental displacement field u_i to have zero circumferential component and to be independent of Θ.[28] The nonzero terms of the nonlinear part of the first Piola-Kirchhoff stress for axisymmetric longitudinal mode fundamental wave fields are given by

$$\bar{T}_{RR} = \left(\frac{3\lambda}{2} + 3\mu + A + 3B + C\right)\frac{\partial u_R}{\partial R}\frac{\partial u_R}{\partial R} + \left(\frac{\lambda}{2} + B + C\right)\frac{\partial u_Z}{\partial Z}\frac{\partial u_Z}{\partial Z} + \left(\frac{\lambda}{2} + B + C\right)\left(\frac{u_R}{R}\frac{u_R}{R} + 2\frac{\partial u_R}{\partial R}\frac{u_R}{R} + 2\frac{\partial u_R}{\partial R}\frac{\partial u_Z}{\partial Z}\right)$$
$$+ 2C\frac{u_R}{R}\frac{\partial u_Z}{\partial Z} + \left(\frac{\lambda}{2} + \mu + \frac{A}{4} + \frac{B}{2}\right)\left(\frac{\partial u_R}{\partial Z}\frac{\partial u_R}{\partial Z} + \frac{\partial u_Z}{\partial R}\frac{\partial u_Z}{\partial R}\right) + \left(\mu + \frac{A}{2} + B\right)\frac{\partial u_R}{\partial Z}\frac{\partial u_Z}{\partial R}, \tag{A3}$$

$$\bar{T}_{RZ} = \left(\mu + \frac{A}{2} + B\right)\left(\frac{\partial u_R}{\partial R}\frac{\partial u_R}{\partial Z} + \frac{\partial u_R}{\partial Z}\frac{\partial u_Z}{\partial Z}\right) + (\lambda + B)\frac{\partial u_Z}{\partial R}\frac{u_R}{R} + B\frac{\partial u_R}{\partial Z}\frac{u_R}{R} + \left(\lambda + 2\mu + \frac{A}{2} + B\right)\left(\frac{\partial u_R}{\partial Z}\frac{\partial u_Z}{\partial R} + \frac{\partial u_Z}{\partial R}\frac{\partial u_Z}{\partial Z}\right), \tag{A4}$$

$$\bar{T}_{\Theta\Theta} = \left(\frac{3\lambda}{2} + 3\mu + A + 3B + C\right)\frac{u_R}{R}\frac{u_R}{R} + B\frac{\partial u_R}{\partial Z}\frac{\partial u_Z}{\partial R} + \left(\frac{\lambda}{2} + B + C\right)\left(\frac{\partial u_R}{\partial R}\frac{\partial u_R}{\partial R} + 2\frac{\partial u_R}{\partial R}\frac{u_R}{R} + 2\frac{\partial u_Z}{\partial Z}\frac{u_R}{R} + \frac{\partial u_Z}{\partial Z}\frac{\partial u_Z}{\partial Z}\right)$$
$$+ \left(\frac{\lambda}{2} + \frac{B}{2}\right)\left(\frac{\partial u_R}{\partial Z}\frac{\partial u_R}{\partial Z} + \frac{\partial u_Z}{\partial R}\frac{\partial u_Z}{\partial R}\right) + 2C\frac{\partial u_R}{\partial R}\frac{\partial u_Z}{\partial Z}, \tag{A5}$$

$$\bar{T}_{ZR} = \left(\mu + \frac{A}{2} + B\right)\left(\frac{\partial u_R}{\partial R}\frac{\partial u_Z}{\partial R} + \frac{\partial u_Z}{\partial R}\frac{\partial u_Z}{\partial Z}\right) + (\lambda + B)\frac{\partial u_R}{\partial Z}\frac{u_R}{R} + \left(\lambda + 2\mu + \frac{A}{2} + B\right)\left(\frac{\partial u_R}{\partial Z}\frac{\partial u_R}{\partial R} + \frac{\partial u_R}{\partial Z}\frac{\partial u_Z}{\partial Z}\right) + B\frac{\partial u_Z}{\partial R}\frac{u_R}{R}, \tag{A6}$$

$$\bar{T}_{ZZ} = \left(\frac{3\lambda}{2} + 3\mu + A + 3B + C\right)\frac{\partial u_Z}{\partial Z}\frac{\partial u_Z}{\partial Z} + \left(\mu + \frac{A}{2} + B\right)\frac{\partial u_R}{\partial Z}\frac{\partial u_Z}{\partial R} + \left(\frac{\lambda}{2} + \mu + \frac{A}{4} + \frac{B}{2}\right)\left(\frac{\partial u_Z}{\partial Z}\frac{\partial u_Z}{\partial Z} + \frac{\partial u_R}{\partial R}\frac{\partial u_Z}{\partial Z}\right)$$
$$+ 2C\frac{\partial u_R}{\partial R}\frac{u_R}{R} + \left(\frac{\lambda}{2} + B + C\right)\left(\frac{\partial u_R}{\partial R}\frac{\partial u_R}{\partial R} + \frac{u_R}{R}\frac{u_R}{R} + 2\frac{\partial u_R}{\partial R}\frac{\partial u_Z}{\partial Z} + 2\frac{u_R}{R}\frac{\partial u_Z}{\partial Z}\right). \tag{A7}$$

The nonlinear forcing terms for axisymmetric torsional mode fundamental wave fields are obtained through Eqs. (14) and (15) by letting $u_R = u_Z = 0, u_\Theta \neq 0$, and requiring u_i to be independent of Θ.[28] The nonzero terms of the nonlinear stress for axisymmetric torsional mode fundamental wave fields are given by

$$\bar{T}_{RR} = \left(\frac{\lambda}{2} + \mu + \frac{A}{4} + \frac{B}{2}\right)\left(\frac{\partial u_\Theta}{\partial R}\frac{\partial u_\Theta}{\partial R} + \frac{u_\Theta}{R}\frac{u_\Theta}{R}\right) + \left(\frac{\lambda}{2} + \frac{B}{2}\right)\frac{\partial u_\Theta}{\partial Z}\frac{\partial u_\Theta}{\partial Z} - \left(\mu + \frac{A}{2} + B\right)\frac{\partial u_\Theta}{\partial R}\frac{u_\Theta}{R}, \tag{A8}$$

$$\bar{T}_{RZ} = \left(\mu + \frac{A}{4}\right)\frac{\partial u_\Theta}{\partial R}\frac{\partial u_\Theta}{\partial Z} - \frac{A}{4}\frac{\partial u_\Theta}{\partial Z}\frac{u_\Theta}{R}, \tag{A9}$$

$$\bar{T}_{\Theta\Theta} = \left(\frac{\lambda}{2} + \mu + \frac{A}{4} + \frac{B}{2}\right)\left(\frac{\partial u_\Theta}{\partial R}\frac{\partial u_\Theta}{\partial R} + \frac{u_\Theta}{R}\frac{u_\Theta}{R} + \frac{\partial u_\Theta}{\partial Z}\frac{\partial u_\Theta}{\partial Z}\right) - \left(\mu + \frac{A}{2} + B\right)\frac{\partial u_\Theta}{\partial R}\frac{u_\Theta}{R}, \tag{A10}$$

$$\bar{T}_{ZR} = \left(\mu + \frac{A}{4}\right)\frac{\partial u_\Theta}{\partial R}\frac{\partial u_\Theta}{\partial Z} - \left(\mu + \frac{A}{4}\right)\frac{\partial u_\Theta}{\partial Z}\frac{u_\Theta}{R}, \tag{A11}$$

$$\bar{T}_{ZZ} = \left(\frac{\lambda}{2} + \frac{B}{2}\right)\left(\frac{\partial u_\Theta}{\partial R}\frac{\partial u_\Theta}{\partial R} + \frac{u_\Theta}{R}\frac{u_\Theta}{R}\right) + \left(\frac{\lambda}{2} + \mu + \frac{A}{4} + \frac{B}{2}\right)\frac{\partial u_\Theta}{\partial Z}\frac{\partial u_\Theta}{\partial Z} - B\frac{\partial u_\Theta}{\partial R}\frac{u_\Theta}{R}. \tag{A12}$$

[1]G. E. Dace, R. B. Thompson, L. J. H. Brasche, D. K. Rehbein, and O. Buck, "Nonlinear acoustics, a technique to detection microstructural changes in materials," Rev. Prog. Quant. Nondestr. Eval. **10B**, 1685–1692 (1991).

[2]J. H. Cantrell, "Nonlinear dislocation dynamics at ultrasonic frequencies," J. Appl. Phys. **106**, 043520 (2009).

[3]J. Y. Kim, L. J. Jacobs, J. Qu, and J. W. Littles, "Experimental characterization of fatigue damage in a nickel-base superalloy using nonlinear ultrasonic waves," J. Acoust. Soc. Am. **120**, 1266–1273 (2006).

[4]J. H. Cantrell and W. T. Yost, "Nonlinear ultrasonic characterization of fatigue microstructures," Int. J. Fatigue **23**, 487–490 (2001).

[5]J. H. Cantrell, "Substructural organization, dislocation plasticity and harmonic generation in cyclically stressed wavy slip metals," Proc. R. Soc. London, Ser. A **460**, 757–780 (2004).

[6]M. Deng, "Cumulative second-harmonic generation accompanying nonlinear shear horizontal mode propagation in a solid plate," J. Appl. Phys. **84**, 3500–3505 (1998).

[7]M. Deng, "Cumulative second-harmonic generation of Lamb-mode propagation in a solid plate," J. Appl. Phys. **85**, 3051–3058 (1999).

[8]W. J. N. de Lima and M. F. Hamilton, "Finite-amplitude waves in isotropic elastic plates," J. Sound. Vib. **265**, 819–839 (2003).

[9]A. Srivastava and F. Lanza di Scalea, "On the existence of antisymmetric or symmetric Lamb waves at non-linear higher harmonics," J. Sound. Vib. **323**, 932–943 (2009).

[10]M. F. Müller, J. Y. Kim, J. Qu, and L. J. Jacobs, "Characteristics of second harmonic generation of Lamb waves in nonlinear elastic plates," J. Acoust. Soc. Am. **127**, 2141–2152 (2010).

[11]M. Deng, P. Wang, and X. Lv, "Experimental observation of cumulative second-harmonic generation of Lamb-wave propagation in an elastic plate," J. Phys. D: Appl. Phys. **38**, 344–353 (2005).

[12]C. Bermes, J. Y. Kim, J. Qu, and L. J. Jacobs, "Experimental characterization of material nonlinearity using Lamb waves," Appl. Phys. Lett. **90**, 021901 (2007).

[13]C. Pruell, J. Y. Kim, J. Qu, and L. J. Jacobs, "Evaluation of plasticity driven material damage using Lamb waves," Appl. Phys. Lett. **91**, 231911 (2007).

[14]K. H. Matlack, J. Y. Kim, L. J. Jacobs, and J. Qu, "Experimental characterization of efficient second harmonic generation of Lamb waves in a nonlinear elastic isotropic plate," J. Appl. Phys. **109**, 014905 (2011).

[15]M. J. S. Lowe, D. N. Alleyne, and P. Cawley, "Defect detection in pipes using guided waves," Ultrasonics **36**, 147–154 (1998).

[16]H. Kwun and K. A. Bartels, "Magnetostrictive sensor technology and its applications," Ultrasonics **36**, 171–178 (1998).

[17]J. Li and J. L. Rose, "Implementing guided wave mode control by use of a phased transducer array," IEEE Trans. Ultrason. Ferroelectr. Freq. Control **49**, 1720–1729 (2001).

[18]W. J. N. de Lima and M. F. Hamilton, "Finite amplitude waves in isotropic elastic waveguides with arbitrary constant cross-sectional area," Wave Motion **41**, 1–11 (2005).

[19]A. Srivastava and F. Lanza di Scalea, "On the existence of longitudinal or flexural waves in rods at nonlinear higher harmonics," J. Sound. Vib. **329**, 1499–1506 (2010).

[20]A. Srivastava, I. Bartoli, and F. Lanza di Scalea, "Higher harmonic generation in nonlinear waveguides of arbitrary cross-section," J. Acoust. Soc. Am. **127**, 2790–2796 (2010).

[21]C. Nucera and F. Lanza di Scalea, "Higher harmonic generation analysis in complex waveguides via a nonlinear semi-analytical finite element algorithm," Math. Probl. Eng. **2012**, 365630 (2012).

[22]Z. A. Gol'dberg, "Interaction of plane longitudinal and transverse elastic waves," Sov. Phys. Acoust. **6**, 306–310 (1961).

[23]L. D. Landau and E. M. Lifshitz, *Theory of Elasticity* (Pergamon, New York, 1986), Chap. 3, pp 87–107.

[24]B. A. Auld, *Acoustic Fields and Waves in Solids, Vol. II* (Robert E. Krieger Publishing Company, Malabar, FL, 1990), Chap. 10, pp. 63–220.

[25]J. J. Rushchitsky, "Quadratically nonlinear cylindrical hyperelastic waves: Primary analysis of evolution," Int. Appl. Mech. **41**, 770–777 (2005).

[26]A. N. Norris, "Finite amplitude waves in solids," in *Nonlinear Acoustics*, edited by M. F. Hamilton and D. T. Blackstock (Academic Press, San Diego, 1998), Chap. 9, pp. 263–277.

[27]N. Matsuda and S. Biwa, "Phase and group velocity matching for cumulative harmonic generation in Lamb waves," J. Appl. Phys. **109**, 094903 (2011).

[28]J. L. Rose, *Ultrasonic Waves in Solid Media* (Cambridge University Press, Cambridge, 1999), pp. 101–261.

J. Acoust. Soc. Am., Vol. 133, No. 5, May 2013

Liu *et al.*: Noninteraction of waves in cylinders   2553